Solar Photoelectrochemical Energy Storage: Materials and Devices

João Azevedo
MAP-FIS doctoral Program in Physics
Physics Department of UP
2016

Supervisor
João Pedro Esteves de Araújo, Professor Doutor, FCUP
co-Supervisor
Adélio Miguel Magalhães Mendes, Professor Doutor, FEUP
co-Supervisor
Célia Tavares de Sousa, Doutora, FCUP

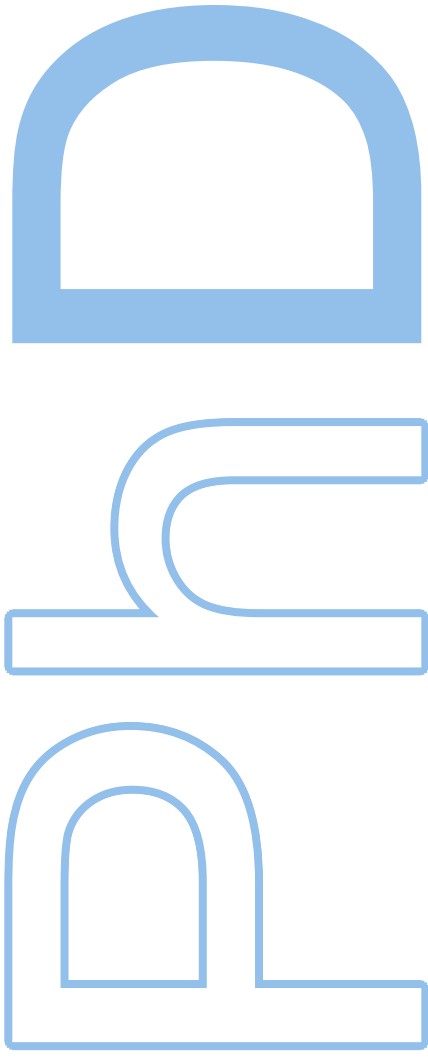

João Carlos Almeida Monteiro Azevedo

Solar Photoelectrochemical Energy Storage: Materials and Devices

Supervisor: *Prof. Doutor João Pedro Esteves de Araújo*

co-Supervisor: *Prof. Doutor Adélio Miguel Magalhães Mendes*

co-Supervisor: *Doutora Célia Tavares de Sousa*

Thesis submitted to the Faculty of Sciences of the University of Porto in partial fulfilment of the requirements for the degree of Doctor in Physics

Department of Physics and Astronomy
Faculty of Sciences of the University of Porto
2016

This thesis was developed in the following institutions:

Funding:

To my parents,
my sister
and Teresa.

Acknowledgments

The work presented in this thesis results from a collaboration between the research group of Prof. João Pedro Araújo from the Instituto de Física dos Materiais da Universidade do Porto (IFIMUP and IN – Institute of Nanoscience and Nanotechnology), and the research group of Prof. Adélio Mendes from Laboratory for Process Engineering, Environment, Biotechnology and Energy (LEPABE). As a research work, it thus results from the collaboration between several people to whom I am deeply thankful.

I would like to take this opportunity to thank all my supervisors.

I would like to thank Professor João Pedro Araújo for everything he did for me. For the opportunity he gave me by accepting me into his group. I have to thank him all the motivation and guidance that led me where I am today and for his scientific insights that were crucial in the development of this work.

I would also like to thank Professor Adélio Mendes for receiving me in his group. His never-ending efforts and ideas were a true motivation and example on how to be a scientist. I have to acknowledge all the hours he spent with this work. I would also like to thank the opportunity he gave me on working on solar redox flow batteries. His perseverance and enthusiasm are the only reasons I was able to accomplish the results presented in this thesis.

Last but not least, I would like to thank Doctor Célia Sousa. She was always present to help and support my work. From laboratory colleague to work coordinator she did everything. I feel that my work would not have been the same without her collaboration. Besides a supervisor, she was also a friend and for that I will always be deeply thankful.

I also want the express my gratitude to all members of IFIMUP and LEPABE for the warm welcome, support and friendship. It has been an honor to be able to work among such brilliant scientists and professionals. This thesis would be twice as long if I wrote the proper acknowledgments to all of you.

At IFIMUP, to João Ventura I would like to acknowledge his support and dedication to my work. Also, thank you for all the good conversations. I would like to thank Professor Joaquim Agostinho Moreira for Raman measurements. To Gonçalo Oliveira I am thankful for XRD expertise and for a crucial help in LaTeX. To Maria Paz for collaboration and dedication (her knowledge in magnetism and X-ray absorption were essential). To Arlete Apolinário for her collaboration and dedication but most of all for her kindness. To Mariana Proença and Joel Puga for their collaboration in the three-dimensional alumina structures and a special thanks to Mariana for all her help around the laboratory. To José Miguel for his help in X-ray absorption measurements. To Bernardo Bordalo and Pedro Fernandes for their knowledge in numerical simulations. I also would like to thank

the rest of the team, in particular, Diogo, João Horta, Marcelo, André, Catarina, Luís, Daniel, João Amaral, Luís Custódio, Francisco Carpinteiro, Florbela, Dra. Armanda Sá and Dra. Isabel Alves.

At LEPABE, to Luísa Andrade for her welcoming and dedication. To Tânia Lopes for her kindness and important inputs in electrical impedance. To Rui Cruz and José Nogueira for their help and upmost interesting discussions. To Verena for her collaboration and willingness to help. To Paula for her collaboration. To Marta Boaventura for her availability. To Roberto for his help and patience. To André Monteiro for his collaboration and conversations. To Sandra and Márcia for their help in the laboratory (specially with resorcinol resin). To Jorge for his good mood and engineering knowledge. To Dª Fátima Faustino for her patience and help. I also would like to thank Joana, Isabel, Ali, Sérgio, António, Rute, Pedro, Cláudio, Andreia, Ana and the rest of the solar group.

I have to acknowledge the importance my stay at École polytechnique fédérale de Lausanne (EPFL) had in this thesis, particularly on the research of cuprous oxide. I am mostly grateful to Professor Michael Grätzel for accepting me into his group and for his precious insights on my work. I have no words to thank Professor David Tilley. For his kindness, efforts, availability, mentorship, motivation and brilliance I am eternally thankful. I would also like to thank the whole team I worked with: Morgan Stefik, Marcel Schreier, Matthew Mayer, Ludmilla Steier for their support.

I would like to acknowledge the importance of the collaboration with Professor Anders Bentien and his group in the solar redox flow battery work. To Professor Anders Bentien I thank his great ideas and motivation. To Kristina Wedege I thank the company during the long hours in the laboratory and the wonderful brainstormings. I am looking forward to get to know the rest of the group better.

My gratitude goes to Fraunhofer Institute, especially Doctor Jens Burfeind and Thorsten Seipp for their contribution and knowledge in redox flow batteries; to Instituto de Nanociencia de Aragón, especially César Magén for STEM measurements and help; to CEMUP, especially Professor Carlos Sá and Rui Rocha for their help in SEM measurements and training.

For all of those that I have met during conferences, workshops and seminars, I also want to thank all your contributions to improve my knowledge, all your help during my PhD, and your friendship.

I would like to thank FCT (Fundação para a Ciência e a Tecnologia) for their funding of my doctoral years (SFRH/BD/79207/2011) and of research projects and conference attendances. This work is also supported by the following projects: BI-DSC (grant agreement no. 321315) funded by European Research Council; PECDEMO project co-funded by Europe's Fuel Cell and Hydrogen Joint Undertaking (FCH JU) under Grant Agreement No. 621252); NORTE-070124-FEDER-000070 Multifunctional Nanomaterials funded by FEDER and CCDRN as well as other projects.

I have to thank to all my friends for providing me non-work related fun hours. To my physics classmates for their companionship. To the volleyball teammates for enabling

me to enjoy one of my passions.

I would also like to thank my family for eternal support and patience. To my parents I only wish they know how important they are to me and that my greatest desire is to make them proud. I could not have asked for better parents. To my sister that is always present for me in the good and bad times. To the memory of my grandfathers.

To my three “brothers” (Álvaro Vaz, João Barros and José Sousa) who grew up by my side a warm thank you.

To Teresa goes a very special thank you. For being my best friend, for the patience and guidance, for making me a better person; for all the laughs and tears; for everything; for you I am truly and deeply thankful.

Resumo

O aumento de consumo de energia e as emissões crescentes de dióxido de carbono para a atmosfera, resultantes da utilização de combustíveis fósseis, são a grande motivação para desenvolver tecnologias para aproveitar fontes de energia renováveis. A energia solar tem o potencial de sustentar todas as necessidades energéticas da humanidade mas, dada a sua natureza intermitente, necessita de armazenamento. As células fotoelectroquímicas para produção de combustíveis solares, utilizando materiais baratos e seguros, são consideradas uma solução promissora para armazenar energia solar. Embora esta via para armazenar energia solar seja muito atrativa ainda existem muitos desafios a superar. O foco desta tese são alguns dos desafios principais na produção fotoeletroquímica de combustíveis solares.

Células fotoelectroquímicas para produção de hidrogénio, através de hidrólise solar da água, são dos dispositivos para captação e armazenamento de energia solar mais estudados. O desafio mais crítico em hidrólise solar da água é encontrar um semiconductor que cumpra os requisitos necessários para um dispositivo eficiente, barato e estável. Apenas alguns foram considerados adequados e o óxido cuproso é um dos mais promissores, com uma eficiência alcançável máxima de conversão luz para hidrogénio de 18 %. No entanto, é um material instável em meios aquosos, fazendo da melhoria da estabilidade um desenvolvimento importante. Esta tese reporta o trabalho desenvolvido na melhoria da estabilidade do óxido cuproso, para produção de hidrogénio por hidrólise solar da água, utilizando um inovador tratamento a vapor e uma nova camada protetora de óxido de estanho, alcançando estabilidades recorde de 57 h.

Dadas as perdas de eficiência energética na junção semicondutor/liquido devido a sobrepotenciais necessários para levar a cabo as reações de evolução de hidrogénio e oxigénio, a energia necessária para a fotoeletrólise é frequentemente reportada perto dos 1.9 eV por par electrão-lacuna gerado. Pares redox alternativos com sobrepotenciais mais baixos e cinéticas mais rápidas são desejados. Esta tese estuda um inovador conceito de armazenamento de energia solar baseado em células fotoelectroquímicas e baterias redox de fluxo – bateria redox de fluxo solar. A primeira bateria redox de fluxo solar sem bias é demonstrada utilizando fotoeletrodos de sulfeto de cádmio e pares redox de vanádio. A estratégia para carregar esta bateria utilizando apenas energia solar foi estudada. A questão de baixa estabilidade do sulfeto de cádmio é explorada com diferentes camadas protetoras e seleneto de cádmio revelou-se como uma boa camada possibilidade. Outros electrólitos foram estudados dado o ambiente com baixo pH e instabilidade do sulfeto de cádmio. Uma bateria redox de fluxo utilizando

pares redox orgânicos e inorgânicos num eletrólito alcalino foi escolhida por permitir a utilização de um fotoeletrodo de hematite, um semicondutor eficiente e estável. O dispositivo desenvolvido mostrou-se eficiente e carregou parcialmente, usando apenas luz solar.

A morfologia de nanotubo tem sido amplamente explorada para aplicações em células fotoelectroquímicas. Exibindo uma arquitetura unidimensional, demonstrou ser vantajosa num semicondutor para um transporte de carga eficiente (eletrões e lacunas). Para além de resultados reportados, áreas superficiais maiores e paredes ultra finas deveriam melhorar o desempenho dos fotoeletrodos. Nesta tese um método inovador de fabrico de nanotubos de hematite complexos é demonstrado, baseado na conversão de nanofios de ferro a nanotubos de hematite. A electrodeposição é um método simples e barato para criar nanofios homogéneos e a otimização de um método de electrodeposição assistido por molde para sintetize de nanofios de ferro ultralongos é apresentada. A transformação do nanofios em nanotubos é descrita pela primeira vez e nanotubos de dupla parede de hematite, com paredes suaves e altas áreas superficiais, altamente reprodutíveis são obtidos. A aplicabilidade do processo de fabrico a outros metais é demonstrado. A versatilidade de usar alumina nanoporosa como molde também é demonstrada utilizando poros modulados e fabricando estruturas tridimensionais com nanofios ou nanotubos interligados, aumentando a área superficial e tornando estas novas estruturas muito promissoras para aplicação em células solares.

Abstract

The increasing demand of energy and the higher levels of carbon dioxide in the atmosphere, result of the intensive use of fossil fuels, are the driving force for the development of technologies for harvesting energy from renewable sources. Solar energy has the potential to supply humanity's energy requirements; however, there is a need for storage given its intermittent nature. A promising solution to store solar energy relies on photoelectrochemical cells for solar fuel production, using low cost and safe materials. Although this route to store solar energy is very attractive, there are many challenges to overcome. This thesis addresses some of the key challenges of photoelectrochemical solar fuel production.

Photoelectrochemical cells for water splitting are one of the most studied devices to store solar energy. The most critical challenge in solar water splitting is to find a suitable semiconductor that fulfills all the necessary requirements for an efficient, low cost and stable device. Only few semiconductor materials have been considered suitable and, with a thermodynamic maximum light-to-hydrogen conversion efficiency of 18 %, cuprous oxide is one of the most promising possibilities. Nevertheless, it is unstable in aqueous environments, which has driven significant efforts to improve its stability. This thesis reports the work developed on cuprous oxide stability enhancement for hydrogen production from solar water splitting using a novel steam treatment and a new protective layer of tin oxide, achieving stabilities up to 57 h.

Given the energy efficiency losses at semiconductor/liquid junctions due to overpotentials needed to drive the hydrogen and oxygen evolution reactions in solar water splitting, the energy required for photoelectrolysis is frequently reported to be ca. 1.9 eV per electron-hole pair generated. Alternative redox pairs with lower overpotentials and faster kinetics would be desirable. In this thesis an innovative concept of solar energy storage is studied based on photoelectrochemical cells and redox flow batteries - solar redox flow battery. The first unbiased solar redox flow battery is demonstrated using cadmium sulfide photoelectrodes and all vanadium redox pairs. The strategy to charge this battery using only solar energy was studied. The low stability of cadmium sulfide was addressed assessing different protective layers; cadmium selenide proved to be an acceptable option. Given the low pH environment and instability of cadmium sulfide other electrolytes were studied. A redox flow battery using an organic and an inorganic redox pairs in an alkaline electrolyte was chosen since it allows the use of hematite photoelectrode, an efficient and stable semiconductor. The developed device proved to be quite energy efficient and to partially charge the redox battery unbiased.

The nanotube morphology has been widely exploited for applications in photo-

electrochemical cells. Displaying a one-dimensional architecture, they have shown to be quite advantageous for an efficient charge transport (electrons and holes) in semiconductors. Beyond previous reports, higher surface areas and ultra thin walls would improve the performance of the photoelectrodes. In this thesis, a novel method to fabricate complex hematite nanotube structures is described, based on the conversion of iron nanowires into iron oxide nanotubes. Electrodeposition is a simple and low cost method to create homogeneous nanowires and optimization of a template assisted electrodeposition method of ultra-long iron nanowires is presented. The transformation of nanowires into nanotubes is described and highly reproducible hematite double walled nanotubes were obtained with smooth walls and high surface areas. The fabrication process was demonstrated to be applicable to other metals. The versatility of using porous anodic alumina as template was also demonstrated with pore modulation and fabrication of three dimensional structures with interconnected nanowires or nanotubes, increasing thus the surface area and making these new nanostructures very promising for solar cells applications.

Contents

Acknowledgments **ix**

Resumo **xiii**

Abstract **xv**

Contents **xx**

List of Figures **xxx**

List of Tables **xxxi**

List Of Abbreviations **xxxiii**

Thesis Outline **1**

1 Introduction **5**

1.1 Motivation 5

1.2 Solar Water Splitting 7

1.2.1 Basic Concepts 7

1.2.2 Cuprous oxide photocathode 9

1.2.3 Cuprous oxide photocorrosion 11

1.3 Solar Redox Flow Batteries 15

1.3.1 Hydrogen alternative 15

1.3.2 Redox Flow Batteries 16

1.3.3 Solar Charging 17

1.4 Nanostructured Photoelectrodes 19

1.4.1 Hematite Nanotubes 21

2 Stability Enhancement of Cuprous Oxide by Low Temperature Steam Treatment **25**

2.1 Background 25

2.2 Experimental details 27

2.2.1 Electrodeposition of Cuprous Oxide 27

2.2.2 Overlayer Deposition 27

2.2.3 Steam Treatment Optimization 28

2.2.4 Co-Catalyst deposition . . . 28
2.2.5 Thin Film Characterization . . . 29
2.2.6 Photoelectrochemical measurements . . . 30
2.3 Results and Discussion . . . 30
2.3.1 Steam Treatment Optimization . . . 30
2.3.2 Crystallographic Characterization . . . 32
2.3.3 Electrical Properties . . . 35
2.3.4 Surface modification . . . 36
2.4 Conclusions . . . 40

3 Tin Oxide as Stable Protective Layer for Cuprous Oxide 41
3.1 Background . . . 41
3.2 Experimental details . . . 43
3.2.1 Sample Preparation . . . 43
3.2.2 Thin Film Characterization . . . 43
3.2.3 Photoelectrochemical Measurements . . . 44
3.2.4 Faradaic Efficiency . . . 44
3.3 Results and Discussion . . . 45
3.3.1 SnO_2 Protective Layer . . . 45
3.3.2 Quantum Efficiency and Crystallographic Characterization . . . 47
3.3.3 Thickness Variation and Steam Treatment . . . 49
3.3.4 ZnO interfacial layer . . . 50
3.4 Conclusions . . . 52

4 Photoelectrochemical redox flow battery 55
4.1 Background . . . 55
4.2 Experimental details . . . 57
4.2.1 Substrate preparation . . . 57
4.2.2 CdS thin film fabrication . . . 58
4.2.3 Under and overlayers deposition . . . 58
4.2.4 Thin Film Characterization . . . 59
4.2.5 Preparation of vanadium solutions . . . 59
4.2.6 Flow cell construction and cycling analysis . . . 59
4.2.7 Solar battery characterization . . . 60
4.2.8 Tandem system . . . 62
4.3 Results and Discussion . . . 62
4.3.1 CdS Photoanodes . . . 62
4.3.2 Battery Solar Charge . . . 64
4.3.3 Overlayers . . . 67
4.3.4 Tandem System . . . 69
4.4 Conclusions . . . 71

5 Alkaline Solar Redox Flow Battery **73**
5.1 Background . . . 73
5.2 Experimental details . . . 76
5.2.1 Hematite photoanodes preparation . . . 76
5.2.2 Hematite post synthetic annealing . . . 76
5.2.3 Polyaniline electrodeposition . . . 76
5.2.4 Cyclic voltammetry and charging/discharging in redox flow cell . . . 77
5.2.5 Photoelectrochemical cells . . . 78
5.2.6 Optical and morphological characterization . . . 79
5.2.7 Prolonged illumination UV test . . . 80
5.3 Results and Discussion . . . 80
5.3.1 Surface Modification . . . 80
5.3.2 Onset Improvement . . . 83
5.3.3 Efficiency . . . 86
5.4 Conclusions . . . 87

6 Ultra-long Iron Nanowires Electrodeposition **89**
6.1 Background . . . 89
6.2 Experimental Details . . . 91
6.2.1 Porous Anodic Alumina Membranes Fabrication . . . 91
6.2.2 Iron Electrodeposition . . . 91
6.2.3 Sample Characterization . . . 92
6.3 Results and Discussion . . . 93
6.3.1 Rest Pulse Duration . . . 94
6.3.2 Electrolyte Molar Concentration . . . 98
6.3.3 Temperature . . . 100
6.3.4 Stirring . . . 101
6.3.5 Barrier Layer Thickness . . . 102
6.3.6 Deposition Pulse Current Density . . . 103
6.3.7 Cross Parameter influence . . . 105
6.4 Conclusions . . . 108

7 High Surface Area Double Walled Hematite Nanotubes **109**
7.1 Background . . . 109
7.2 Experimental details . . . 110
7.2.1 Sample preparation . . . 110
7.2.2 Sample Characterization . . . 111
7.3 Results and Discussion . . . 113
7.3.1 Double walled hematite nanotubes . . . 113
7.3.2 Magnetic properties . . . 117
7.3.3 Growth Mechanism . . . 120

7.4 Conclusions 122

8 Main Conclusions and Perspectives **123**

List of Publications **127**

Bibliography **130**

Appendices **155**

A Porous Anodic Alumina Templates **157**
A.1 Fabrication Process 157
A.1.1 Mild Anodization 157
A.1.1.1 Two-step anodization process 160

B Alumina Template Pore Modulation **163**
B.1 Hard anodization 163
B.2 Pore Modulation 164

C Three-dimensional Template for Conductive Substrates **169**
C.1 3D interconnected nanoporous alumina templates 169
C.2 3D interconnected nanowire arrays 169
C.2.1 Au Nanowires 169
C.2.2 Free-standing interconnected nanowire arrays 171

List of Figures

1.1 Sunlight can be harnessed and converted into fuel or electricity by 3 energy-conversion strategies: photosynthesis, phototovoltaics and photoelectrochemical cells. The semiconducting material (blue) and metal electrode (green) (Extracted from 7). 6

1.2 Schematic representation of a conventional PEC cell using a photoanode as WE. Water splitting chemical reactions are represented. 8

1.3 Energy band positions for various semiconductors at pH 14 (Extracted from 5). 10

1.4 a) Bandgap transitions; b) incident photon-to-current efficiency (IPCE) of an electrodeposited Cu_2O photocathode for water splitting (Extracted from 43). 11

1.5 Diagram with various possibilities for thermodynamic stability of a semiconductor in water (Extracted from 53). 12

1.6 Positions of band edges and decomposition thermodynamic decomposition potentials for different oxide and non-oxide semiconductors at pH 0. Cu_2O is the first one and is marked in red (Adapted from 52). 12

1.7 a) Schematic representation and b) top SEM view of a composite photocathode Cu_2O/AZO/TiO_2/Pt (Extracted from 40). 13

1.8 Energy diagram of a composite photocathode Cu_2O/AZO/TiO_2 with TiO_2 different deposition temperatures (Extracted from 40). 14

1.9 Chronoamperometric stability measurement of a Cu_2O photocathode with RuO_2 catalyst biased at 0 V_{RHE} in pH 5.0 phosphate–sulfate electrolyte under light chopping (Extracted from 32). 14

1.10 Simple schematic diagram of a redox flow battery. The electron transport in the circuit, ion transport in the electrolyte and across the membrane and mass transport in the electrolyte are represented. 16

1.11 Schematic representation of various redox-flow systems (the values give the potential of the redox couple). a) All vanadium, b) vanadium/ bromine, c) iron/chromium, d) Fe-EDTA/bromine, e) zinc/ cerium, f) bromine/ polysulphide, g) nonaqueous ruthenium/ bipyridine, h) nonaqueous vanadium/ acetylacetonate, i) nonaqueous chromium/ acetylacetonate (Extracted from 56). 17

1.12 Distribution of high-throughput screened quinone/hydroquinone redox couples. (a) A histogram of theoretically predicted E^0 (V vs. SHE). Number of bins and width of the histogram are 130 and 0.1 V, respectively. (b) E^0 windows for the different classes of quinones. The orange crosses show the mean values of E0 for each class. Redox potentials of the conventional inorganic AFB redox couples are noted for comparison (Extracted from 78). 18

1.13 Conceptual sketch of a Solar-RFB: PEC cell on the roof for direct solar charging a redox flow battery coupled with a thermal system. 19

1.14 Expected evolution of photogenerated current with morphology and surface chemistry control in $\alpha - Fe_2O_3$ photoanodes (Extracted from 106). . . 21

1.15 Different generations of anodic iron oxide: a) nanoporous and b) nanotubes arrays (Adapted from 117 and 99). 21

1.16 Schematic diagram of the processes used for the synthesis of the $\alpha - Fe_2O_3$ nanotube arrays on PAA template (Adapted from 124). 23

2.1 Cross-sectional SEM image of a photocathode with respective ALD layer thicknesses. 27

2.2 Current-voltage characteristics at extreme temperature and duration of steam treatment conditions: a) 180 °C for 1 h; b) 5 h at 150 °C. 29

2.3 Stability variation with steam treatment temperature (°C) and duration (h). Stability is evaluated–under continuous illumination measurement conditions–as the time it takes for the initial photocurrent to drop to 90 % of its initial value (a 10 % loss). The black lines represent prediction profiles extracted from a statistical analysis on performed measurements and the blue dashed lines represent the corresponding confidence intervals. 32

2.4 Analysis of variance of the modeled stability response with the respective R^2. 33

2.5 Current-voltage characteristics of a composite Cu_2O photocathode: a) comparison between the performance of a photocathode as prepared and with steam treatment at 150 °C for 3h, b) linear sweep of the photocathode with steam treatment before and after 45 h stability measurement under light chopping and c) chronoamperometric stability measurement biased at 0 V_{RHE}. All measurements were carried out in pH 5.0 phosphate–sulfate electrolyte under light chopping. 33

2.6 X-ray diffraction patterns with corresponding layer Bragg reflections (left) and Raman spectra with phonon modes of Cu_2O and TiO_2 of steam treatment samples with different conditions (right). 34

2.7 a) GIXRD on a TiO_2 (100 nm), deposited on glass substrate, after the steam treatment at 150 °C for 3 h; b) Ellipsometry measurements of TiO_2 film on a silicon wafer before and after steam treatment at 150 °C for 3 h. . 34

2.8 TEM analysis on the hydrothermally treated sample compared to the reference sample. a) Bright field image of the hydrothermal treatment electrode cross-section (from top to bottom: amorphous carbon/TiO_2/AZO/Cu_2O). The inset shows the area selected by the aperture for the diffraction pattern shown at the bottom of (c). b) Dark field image of the position marked in red in (a) and obtained from spot B in the diffraction pattern in (c). Crystalline domains are visible in the TiO_2 layer and small crystallites in the ZnO layer underneath. c) Top: Energy-dispersive X-ray spectroscopy (EDX) analysis of the TiO_2 layer showing homogenous coverage trough the film. Bottom: Selected area diffraction pattern of TiO_2 shown in the inset of (a). Spot B (anatase (105) plane) was used for the dark field image in (b). d) Dark field image of the reference sample without hydrothermal treatment obtained from Spot A in the inset. 35

2.9 Mott-Schottky plot of TiO_2 films prepared with hydrogen peroxide precursor on FTO, measured in 1 M NaOH electrolyte. Steam conditions were 150 °C for 3 h. 36

2.10 Surface morphology of the TiO_2 overlayer (left) and TEM cross-section (right) of an as prepared sample (a,c) and a sample with steam treatment at 150 °C for 3 h (b,d). It is clear that the surface experienced major morphological changes upon steam treatment. The TiO_2 thickness was measured in different places of both samples and the larger thicknesses (boundaries) are marked in red and lower thicknesses (tips) marked in yellow. 37

2.11 Photocathode SEM top view after RuO_x electrodeposition a) no steam treatment and b) after steam treatment at 150 °C for 3 h. 38

2.12 SEM top view a, b) TiO_2 after steam treatment at 150 °C for 3 h; c, d) photo-assisted electrodeposited RuO_x catalyst; e, f) active area after 20 h under illumination conditions. 39

2.13 Current-voltage characteristics of a composite Cu_2O photocathode after steam treatment at 150 °C for 3 h: a) comparison between performance of a photocathode with RuO_x and Pt as catalyst; chronoamperometric stability measurement biased at 0 V_{RHE} in pH 5.0 phosphate–sulfate electrolyte under light chopping b) with RuO_x and c) Pt as catalyst. 40

3.1 A digital photograph of a representative Au/Cu_2O/SnO_2/RuO_2 photocathode. 43

3.2 a) Cross-sectional SEM image of a photocathode with respective ALD layer thicknesses. b) Current-potential characteristics of a composite $Cu_2O/SnO_2/RuO_2$ photocathode under chopped simulated sunlight illumination: performance comparison between a photocathode after 2 h activation and 30 h stability measurement (biased at 0 V_{RHE} in pH = 5.0 phosphate-sulfate electrolyte). c) Chronoamperometric stability measurement biased at 0 V_{RHE} under continuous illumination. The inset shows small fluctuations in the measured current due to gas bubble evolution, trapping (loss of surface area), and eventual escape (surface area recovered). 45

3.3 SEM top view of a photocathode with photo-assisted electrodeposited RuO_2 catalyst a) as deposited, b) after 3 h and c) 27 h under illumination at 0 V_{RHE} bias. 46

3.4 a) Current-voltage characteristics of a composite $Cu_2O/SnO_2/RuO_2$ photocathode with different SnO_2 thicknesses: comparison between the performance of the photocathodes with SnO_2 layer thicknesses of 20, 50 and 100 nm; b) corresponding stability measurements under illumination and 0 V_{RHE} bias. All measurements were carried out in pH 5.0 phosphate–sulfate electrolyte. 47

3.5 IPCE of a photocathode biased at 0 V_{RHE} in standard pH 5.0 electrolyte. Integration of the IPCE values with the solar AM 1.5 spectrum gives the same photocurrent value as is typically observed under simulated one sun illumination. 47

3.6 a) X-ray diffraction patterns with corresponding layer Bragg reflections; b) grazing angle XRD for 50 nm of ALD SnO_2 grown at 110 °C atop on optically polished silicon; c) Raman spectra with phonon modes of Cu_2O and SnO_2 of a photocathode with Cu_2O/SnO_2 configuration. 48

3.7 a) Cross-sectional SEM image of a photocathode and b) respective SnO_2 layer thickness distribution along the sample. Average thickness of 53 nm and maximum (red) and minimum (blue) thicknesses occur at the marked positions in (a). 49

3.8 a) Current-potential characteristics of composite $Cu_2O/SnO_2/RuO_2$ photocathode samples with different steam treatment conditions: without treatment and with steam treatment at temperatures of 100, 125 and 150 °C. (b) Corresponding stability measurements under continuous illumination and biased at 0 V_{RHE}. All measurements were carried out in pH 5.0 phosphate–sulfate electrolyte. 50

3.9 Pourbaix diagram for a) TiO_2 and b) SnO_2 in 0.5 M Na_2SO_4 electrolyte at T = 25 °C, for $[Ti^{2+}] = [Sn^{2+}] = 10\ \mu M$. Generated using Medusa (http://www.kemi.kth.se/medusa/). 51

3.10 Faradaic efficiency measurement for a $Cu_2O/SnO_2/RuO_2$ photocathode under continuous illumination at 0 V_{RHE} in standard pH 5.0 electrolyte, which confirms 100 % Faradaic efficiency for hydrogen generation. 51

3.11 Photoelectrochemical characteristics of composite photocathodes. a) Current-potential comparison between the performance of a photocathode with ($Cu_2O/ZnO/SnO_2/RuO_2$) and without ($Cu_2O/SnO_2/RuO_2$) ZnO layer. b) Chronoamperometric stability measurements under continuous illumination and biased at 0 V_{RHE}. All measurements were carried out in pH 5.0 phosphate–sulfate electrolyte. 52

4.1 Schematic diagram of a) all vanadium solar redox flow battery charged with a CdS photoanode and b) Energy diagram of the system, including the standard redox reactions. 57

4.2 Charge–discharge curves and b) Efficiencies of V3V3 RFB at current density of 1 $mA{\cdot}cm^{-2}$ at 20 $ml{\cdot}min^{-1}$. 60

4.3 Home-made solar redox flow battery cell design. 61

4.4 Nernst equation for V^{3+}/V^{4+} and V^{3+}/V^{3+} configurations, according to reference 158. 61

4.5 Cross-sectional a) and surface b) SEM micrograph of a CdS photoanode. Inset shows an amplified view of the surface; c) X-ray diffraction patterns of CdS photoanode. Different crystalline phases are marked with the corresponding miller indexes. Orange circles mark the TCO diffraction peaks; d) The UV–VIS spectra of CdS thin films. 63

4.6 CdS films deposited at different potentials with respect to reference electrode saturated Ag/AgCl: a) -0.75 V, b) -0.8 V, c) -0.85 V, d) -0.9 V and e) -0.95 V. 64

4.7 Pourbaix diagram for V^{3+} at T = 25 °C, for $[V^{3+}]$ = 0.4 M. Generated using Medusa (http://www.kemi.kth.se/medusa/). 65

4.8 a) Photocurrent–photovoltage characteristics under 1.5 AM light and dark conditions (in 0.4 M V3/V3 / 2 M H_2SO_4 electrolyte) of the best performing CdS photoanodes. Inset shows stability. 65

4.9 a) Photocurrent–photovoltage characteristics under chopped 1.5 AM light CdS photoanode at different SOC values in V3/V3; b) Absorption spectra of V^{3+}-VO^{2+} mixtures at different SOC and for the parent V^{3+} and VO^{2+} solutions. 66

4.10 A generalized band position diagram for the multilayer photocathode and redox levels of the involved chemical reactions. 68

4.11 Photocurrent-photovoltage characteristics of the best performing CdS/CdSe sample. Inset shows stability. 69

4.12 a) Schematic representation of a tandem device comprising a DSC and a CdS photoanode to charge a vanadium RFB; Photocurrent–photovoltage characteristics of a tandem system composed by c) CdS(s)/DSC|VO^{2+}, $VO_2{}^{+}$||V^{3+}, V^{2+}|Carbon Felt(s). 70

4.13 a) Experimental results J–V and power curves; b) The UV–VIS absorption spectra of the DSC. 71

5.1 Energy diagram of the PEC/RF cell for solar charging of redox pairs connected to a RF cell for discharge. Desired electron-hole pathways under light exposure are shown with full blue arrows. Undesirable back-electron transfer is shown in red dotted arrows. 74

5.2 Potential as a function of time when performing the polyaniline electrode-position for two representative hydrothermally treated samples; (inset) Polyaniline deposition (20 min, 5 μA·cm^{-2}) on TCO glass after dipping half the sample in 1 M NaOH. 77

5.3 a) Assembled cell, side-view and b) carbon felt and gaskets inside the cell. 78

5.4 a) PEC battery cell and b) UV Standard curve for 0.2 M ferrocyanide/-ferricyanide solution in 1 M NaOH diluted 100 times for peaks at 420 nm referenced to 1 M NaOH 79

5.5 SEM top view of different prepared samples a) bare b) annealed and c) coated. 81

5.6 Absorption measurements for bare TCO glass polyaniline directly on TCO glass, bare, annealed and coated sample. 81

5.7 a) CVs of AQDS (red line) and $Fe(CN)_6^{4-}$ (blue line) 1 mM in 1 M NaOH at scan rate 100 mV·s^{-1} on a GC electrode; b) Charge-discharge curves in a 25 cm^2 RF cell with a constant current density of 20 mA·cm^{-2} and redox pair concentration 0.1M AQDS and 0.2M ferrocyanide in 1 M NaOH; c) Efficiency data for the 10 cycles in b). 82

5.8 a) *J-E* curves under 1 sun illumination (left) and in the dark (right) in the three-electrode PEC cell for 3 surface treated hematite samples from batch A in 0.2 M $K_4Fe(CN)_6$, 1 M NaOH. b) Average $E_{on,photo}$ and standard deviation for all samples from batch A from *J-E* measurements with varying $Fe(CN)_6^{3-}$ concentration and a constant concentration of 0.2 M $K_4Fe(CN)_6$ and semi-logarithmic fits with slopes 122 mV (bare, R^2 = 0.997), 122mV (annealed, R^2 = 0.999) and 73 mV (coated, R^2 = 0.936), respectively. 82

5.9 a)+b) *J-E* chopped (1 sun illumination/dark) curves recorded in the PEC cell at different SOC for two representative samples from batch B a) bare and b) coated at a recording interval of 5 mV at scan rate of 10 $mV \cdot s^{-1}$. c) Average $E_{on,photo}$ (red and blue) and $E_{on,dark}$ (black and grey) for bare hematite samples (circles) and coated (squares) with standard deviation obtained from chopped *J-E* curves recorded in the PEC cell and semi-logarithmic regressions (see Table 5.1). 84

5.10 *J-E* curves for water splitting in 1 M NaOH in the light and in the dark for hematite bare sample, annealed and coated – samples from the same batch. 85

5.11 Illustration of possible mechanism for increased electron harvesting in the hematite-PANI photoelectrode under visible light illumination (Adapted from 186). 86

5.12 Incident solar-to-chemical conversion efficiency of a coated hematite sample as a function of current density. 87

5.13 a) The absorbance of the ferrocyanide side of the PEC/RF cell as a function of unbiased solar charging time of 40-400 min under 1 sun illumination. b) The absorbance of a 0 % SOC solution ferrocyanide left under 1 sun illumination in a separate transparent container (cuvette) with same light area-to-volume ratio for the same time as a). 87

6.1 Stages of nanowire growth embedded in PAA template: (a) V_{dep} and j_{dis}, (b) dV_{dep}/dt and (c) layout of the stages of nanowires growth. 93

6.2 Deposition profiles taken during the electrodeposition: a) 0.3 s, b) 0.5 s, c) 0.7 s, d) 0.9 s and e) 1.2 s. For each curve the point where the NWs reach the top of the template is marked (red line). 95

6.3 Top SEM images of electrodeposited PAA templates with iron in different rest pulse durations: a) 0.3 s, b) 0.5 s, c) 0.6 s, d) 0.7 s, e) 0.9 s and e) 1.2 s. 96

6.4 Filled percentage dependence on rest pulse duration. The solid line is a guide to the eye. 96

6.5 X-ray diffraction pattern of the Fe NWs in an amorphous alumina matrix for different rest pulse durations. The Bragg reflection corresponds to 110. 97

6.6 Grain size dependence on rest pulse duration. The solid line is a guide to the eye. 97

6.7 Geometry and conditions used in the simulation. 98

6.8 Concentration before each deposition pulse for different rest pulse durations. 99

6.9 (a) Effect of $FeSO_4 \cdot 7H_2O$ concentration on f_p and V_0. The PED parameters used are the standard values (T, stirring, t_{rest}, j and δ_b of 20 °C, 0 rpm, 0.7 s, 70 mA·cm^{-2} and 10.4 nm, respectively). The solid lines are a guide to the eye. (b) Surface SEM images of samples electrodeposited at 0.01 M, 0.1 M, 0.5 M and 1 M. 99

6.10 (a) f_p and filling time dependence on electrodeposition temperature with corresponding surface SEM images. The PED parameters used are the standard values (C, stirring, t_{rest}, j and δ_b of 0.43 M , 0 rpm, 0.7 s, 70 mA·cm^{-2} and 10.4 nm, respectively). The solid lines are a guide to the eye; (b) Grain size *vs* temperature and Fe (110) Bragg diffraction peak (inset) for different electrodeposition temperature. Error bars contained within experimental points. The solid line is a guide to the eye. 101

6.11 Dependence of f_p and V_0 on stirring velocity. The PED parameters used are the standard values (C, T, t_{rest}, j and δ_b of 0.43 M, 20 °C, 0.7 s, 70 mA·cm^{-2} and 10.4 nm, respectively). The solid lines are a guide to the eye. 102

6.12 (a) Deposition profiles for different δ_b and corresponding dendrites filling times (t_d); (b) Dependence of f_p with δ_b. The PED parameters used are the standard values (C, T, stirring, t_{rest}, j of 0.43 M, 20 °C, 0 rpm, 0.7 s and 70 mA·cm^{-2}, respectively). The solid lines are a guide to the eye. . . . 103

6.13 (a) Deposition profiles, with increasing j, taken during electrodeposition (initial stages are shown in detail in the inset); (b) V_{dep} dependence on j. The PED parameters used are the standard values (C, T, stirring, t_{rest}, and δ_b of 0.43 M, 20 °C, 0 rpm, 0.7 s and 10.4 nm, respectively). 104

6.14 (a) Filled percentage dependence on the current density; (b) Grain size *vs* j. Error bars contained within experimental points. The PED parameters used are the standard values (C, T, stirring, t_{rest}, and δ_b of 0.43 M, 20 °C, 0 rpm, 0.7 s and 10.4 nm, respectively). The solid lines are a guide to the eye. 104

6.15 Prediction profiles for each studied electrodeposition parameter and corresponding confidence intervals (blue dashed lines). For each parameters, the desirability plot is presented under the prediction profile. The solid lines are a guide to the eye and the dashed lines represent the confidence intervals. 106

6.16 (a) Filled percentage dependence on template thickness for reference, optimized from individual studies and RSM optimized parameters. The solid line is a guide to the eye.; (b) SEM cross section image of a 50 μm PAA filled sample; (c) top view without milling: the white mushroom structures correspond to the deposits once the nanowires reach the template surface; (d) SEM top view image of a 50 μm PAA filled sample after 5 μm milling. 107

7.1 (a) Top view SEM images showing the high-density of Fe nanowire array. (b) Cross section reveals the vertical alignment of the NWs. 113
7.2 X-ray diffraction patterns with corresponding layer Bragg reflections of nanoparticles in template and after alumina template removal. Peak values were compared to reference – Table 7.1. 114
7.3 a) STEM side-view image of a single double walled nanotube; (b) STEM-EELS chemical profile across α-Fe_2O_3 double wall NT along the green line in a); c) STEM side-view of another double walled nanotube with composition on inset. 115
7.4 a) Raman spectra of three most common iron oxide phases; b) Raman spectra of double walled nanotubes (peaks fit well with hematite); c) X-ray diffraction patterns of double walled nanotubes. Different crystalline phases of α-Fe_2O_3 are marked with the corresponding miller indexes. Peak values were compared to reference – Table 7.2. 116
7.5 Experimental Fe K-edge XANES spectrum for double walled nanotube sample (orange line) measured at room temperature together with the fit (blue circles) - see text. A weighted sum of Fe (10.54 %) and α-Fe_2O_3 (89.91 %) was employed to describe the experimental XANES of the sample. The spectra of α-Fe_2O_3 (red) and α–Fe (black) that were employed for the weighted sum (see text) are also shown at the bottom for clarity. 116
7.6 Magnetization versus temperature after zero field cooling (ZFC) and field cooling (FC) conditions of the double walled NTs. Both were taken under a magnetic field of 100 Oe. Arrows indicate the measurement direction in reference to temperature variation. The dotted vertical line show the T_S. . 117
7.7 a) Hysteresis loops measured at several temperatures; b) Temperature dependence of H_{ex} and H_c obtained from *M(H)* hysteresis loops. 118
7.8 a) Arrott plots for double wall NTs in the temperature range of 5 – 350 K; b) temperature dependence of spontaneous magnetization (The solid line shows the fit to Bloch's $T^{3/2}$ law). 119
7.9 Morphology evolution of the nanostructures: SEM and STEM images of the products obtained a) as prepared in template, b) after template removal and c) after annealing. 120
7.10 STEM images of a) modulated Fe NTs (inset shows SEM image of original Fe NW, prior to annealing); b) Ni NTs formed using the same technique. . 121

A.1 Illustration of the principal stages of pore formation in a nanoporous alumina membrane. 157
A.2 Current density transient monitored during a first and second anodization in 0.3 M oxalic acid at 2 °C and with a constant applied potential of 40 V. . 159

A.3 SEM images obtained with different acidic solutions: top surface and cross section images of anodizations with (a), (d) sulphuric acid; (b), (e) oxalic acid and (c), (f) phosphoric acid (Adapted from 268). 159
A.4 Schematic drawings of two step anodization method and correspondent SEM images. 160

B.1 (a) Comparison between the thickness of PAA for MA (40 V) and HA (140 V) as a function of time, using oxalic acid; Top (b) and cross-section (c) SEM views of a PAA template made by HA at 140 V for 4 h. 164
B.2 a) and b) 1D Pore modulation with different diameters (Extracted from 242); c) and d) 3D template (Extracted from 279). 165
B.3 a) Pore modualted template abrication process and b) pulsed anodization pulse shape (Adapted from 242). 166
B.4 Current density profile of a series of tailor pulses (a) and the amplified view of one pulse (b) marked with a red rectangle. U_1 = 80 V; U_2 = 140 V; U_3 = 160 V; τ_1 = 144 s; τ_2 = 0.2 s. 167
B.5 Current density profile of a series of tailor pulses for a prolonged time. . . 167
B.6 Different modulation patterns. U_1, U_2, U_3, τ_1 and τ_2 values are: a) 80, 140, 160, 144, 0.2; b) 80, 140, 160, 36, 0.2; c) 80, 140, 160, 200, 0.2; d) 80, 140, 160, 400, 0.2; e) 80, 140, 160, 144, 5; f) 50, 140, 160, 144, 0.2. Bar corresponds to 1 μm. 168

C.1 Sequence of the applied anodization potential/current pulses for the formation of diameter modulated pores. SEM cross-sectional images of the 3D interconnected nanoarchitectures formed in the nanoporous alumina templates. 170
C.2 Different three dimensional templates. 170
C.3 SEM cross-sectional images of 3D interconnected arrays of Au nanowires electrodeposited in 3D porous alumina templates, illustrating diameter modulations with different spacings and the breaking of the interconnected wires during deposition in some segments (upper right). At the bottom: photographs of the alumina membranes (around 1 cm in diameter) after the electrodeposition process in the central area (with around 0.5 cm in diameter) taken at different angles, illustrating the different optical reflections of the 3D interconnected network of nanowires. The scheme at the bottom right, extracted from reference 280, illustrates the same effect. 171
C.4 SEM top views of free-standing Au nanowire arrays after template removal: a) 3D interconnected NW arrays, and b) NW arrays with no interconnected structures. 171

List of Tables

1.1 Comparison of hematite different fabrication methods. 22

2.1 CCD factors and respective levels. 29
2.2 Observed values of process responses. Stability is evaluated under continuous illumination measurement conditions. 31
2.3 Comparison of electrical properties of the TiO_2 films with/ without steam treatment. Flatband and donor density extracted according to the Mott–Schottky equation[31]. [a] Reference values from reference 32. 36

4.1 Structural parameters calculated from the XRD patterns and literature values for the diffracting planes[161]. 64
4.2 Summary of PEC performance for the different ALD layers investigated. . 67

5.1 Data for semi-logarithmic fits from Figure 5.9c. 84

6.1 CCD values and respective levels. 92
6.2 Optimum electrodeposition parameters obtained from RSM analysis and experimental results. 106

7.1 Structural parameters of α-Fe calculated from the XRD patterns and literature values for the diffracting planes. 112
7.2 Structural parameters of α-Fe_2O_3 calculated from the XRD patterns and literature values for the diffracting planes. 112

A.1 Anodization conditions and pore characteristics. 160

B.1 Different pulses applied during anodization. 166
B.2 Range of different modulation features. 168

List Of Abbreviations

- AC, Alternate Current
- AFM, Antiferromagnetic
- ALD, Atomic Layer Deposition
- AM, Air Mass
- ANOVA, Analysis of Variance
- AQDS, Anthraquinone-2,7-disulphonate
- AR, Anodization Rate
- AZO, Aluminum Doped Zinc Oxide
- C, Molar Concentration
- CCD, Central Composite Design
- CE, Counter Electrode
- CV, Cyclic Voltammogram
- DC, Direct Current
- DF, Dark Field
- D_{int}, Interpore Distance
- D_p, Pore Diameter
- DSC, Dye Sensitized Solar Cell
- e^-, Electron
- E, Applied Voltage
- EB, Exchange Bias
- E_{CB}, Conduction Band Energy
- EDX, Energy-dispersive X-ray spectroscopy
- E_g, Band Gap Energy
- EELS, Electron Energy Loss Spectroscopy
- E_{VB}, Valence Band Energy
- FC, Field Cooling
- FIB, Focused Ion Beam
- FM, Ferromagnetic
- f_p, Pore Filling Percentage
- FTO, Fluorine-doped Tin Oxide
- GIXRD, Grazing-Incidence X-ray Diffraction
- h^+, Hole
- H, Magnetic Field
- HAADF, High Angle Annular Dark Field
- H_C, Coercive Field
- HER, Hydrogen Evolution Reaction
- H_{ex}, Exchange Bias Field
- HOMO, Highest Occupied Molecular Orbital
- HRTEM, High-Resolution Transmission Electron Microscopy
- IPCE, Incident Photon-to-Current Efficiency
- J, Photocurrent Density
- j, Deposition Pulse Current Density
- J_0, Initial Photocurrent Density
- j_{dis}, Discharge Current Density
- LUMO, Lowest Unoccupied Molecular Orbital
- M, Magnetization
- $M(H)$, Magnetization versus Magnetic Field
- M_S, Saturation Magnetization
- $M(T)$, Magnetization versus Temperature
- NHE, Normal Hydrogen Electrode
- NT, Nanotube

- NW, Nanowire
- NZEB, Nearly Zero Energy Building
- OCV, Open Circuit Voltage
- OER, Oxygen Evolution Reaction
- P, Porosity
- PAA, Porous Anodic Alumina
- PEC, Photoelectrochemical
- PED, Pulsed Electrodeposition
- PV, Photovoltaic
- RE, Reference Electrode
- RFB, Redox Flow Battery
- RHE, Reversible Hydrogen Electrode
- RSM, Response Surface Method
- SADP, Selected Area Diffraction Pattern
- SCLJ, Semiconductor-liquid Junction
- SEM, Scanning Electron Microscopy
- SOC, State-of-Charge
- SQUID, Superconducting Quantum Interference Device
- STEM, Scanning Transmission Electron Microscopy
- STP, Standard Temperature and Pressure
- T, Temperature
- t, Time
- T_B, Blocking Temperature
- TEM, Transmission Electron Microscopy
- t_{rest}, Rest Pulse Duration
- T_S, Saturation Temperature
- V_0, First Deposition Pulse Potential
- V_{dep}, Deposition Potential
- WE, Working Electrode
- XANES, X-ray Absorption Near Edge Structure
- XAS, X-ray Absorption Spectroscopy
- XRD, X-ray Diffraction
- ZFC, Zero Field Cooling
- δ_b, Barrier Layer Thickness
- φ_{ox}, Thermodynamic Oxidation Potential
- φ_{re}, Thermodynamic Reduction Potential

Thesis Outline

The PhD has been performed in collaboration between the research group of Professor João Pedro Araújo, at Instituto de Física dos Materiais da Universidade do Porto (IFIMUP-IN) and the research group of Professor Adélio Mendes, at Laboratory for Process, Environment, Biotechnology and Energy Engineering (LEPABE). Nevertheless, it is important to emphasize the number and intensity of collaborations with other research groups. Especially, Professor Michael Grätzel's group at Laboratory of Photonics and Interfaces (LPI) with whom the cuprous oxide work was developed and Professor Anders Bentien group at Aarhus University with whom the solar redox flow batteries work was developed. Other important mentions are the team at Energy storage laboratories from Fraunhofer UMSICHT who helped in understanding redox flow batteries operational principles and stack fabrication and Instituto de Nanociencia de Aragón for transmission electron microscopy measurements.

The work developed in this thesis was only possible after the implementation and development of several experimental techniques. In particular, hard anodization, modulated templates and three-dimensional alumina nanostructures were implemented at IFIMUP-IN within the framework of this thesis. Treatments on surface nano defect patching and cuprous oxide photocathode new configurations were implemented at LPI. Redox flow batteries (RFB) and solar RFB were developed and tested at LEPABE, initiating a new line of research in this group.

This thesis is structured in eight chapters, comprising an introduction, six chapters reporting on the main results and discussions on the topics addressed in this thesis and a chapter with conclusions and future perspectives. Only works that resulted in scientific publications (either published or under submission) are discussed here. A brief summary of each chapter is given here:

- Chapter 1 introduces the field of photoelectrochemical (PEC) cells, focusing on solar water splitting. Cu_2O photocathode is reviewed and the topic of photocorrosion is addressed. An innovative concept, solar RFB is discussed together with the basic principles of RFB. A brief introduction on nanostruturing advantages is given together with a small review on previous reported hematite morphologies.

- The Chapter 2 studies performed an innovative low temperature steam treatment for improving the stability of Cu_2O-based photoelectrodes protected with amorphous TiO_2 layers. Low temperature steam post-synthetic treatments were implemented and demonstrated greatly enhanced stabilities compared with non-treated samples. Photocurrents over -5 $mA{\cdot}cm^{-2}$ were achieved with only 10 %

loss over its initial photocurrent value during more than 50 h of light chopping (biased at 0 V_{RHE}).

- Chapter 3 is dedicated to a novel strategy for protecting cuprous oxide from photocorrosion, wherein a thin SnO_2 overlayer enables increased stability over previous reports using TiO_2 protective layers. This strategy can be applied to other materials as well as a TiO_2 replacement. It was demonstrated that performance and stability are influenced by the film thickness, post-deposition steam treatment, and the nature of the heterojunction interface. A maximum stability of 57 h of photoelectrochemical water reduction, maintaining 90 % of its initial photocurrent, was achieved.

- Chapter 4 proposes the direct conversion of sunlight into electrochemical energy stored in a redox flow battery. A photoelectrochemical cell was used to charge a vanadium redox flow cell (CdS(s)|V^{3+}, VO^{2+}||V^{3+}, V^{2+}|Carbon Felt(s), E° = 0.6 V_{NHE}). A CdS thin film photoelectrode was prepared to directly charge the cell redox pairs, V^{3+}/VO^{2+}. CdS photoanode exhibits competitive photocurrents, when compared with other photoelectrochemical devices, and yields enough photovoltage to charge the vanadium battery up to 75 % with no external bias. An overlayer of CdSe was able to improve the performance of CdS with current densities up to ca. 1.4 $mA{\cdot}cm^{-2}$. Finally, a tandem configuration was tested using a dye-sensitized solar cell and a CdS photoanoade producing 1.3 V of photovoltage. This tandem arrangement proved to allow charging conventional all vanadium redox cell (DSC/CdS(s)|VO^{2+}, VO_2^+ ||V^{3+}, V^{2+}|Carbon Felt(s), E° = 1.2 V_{NHE}) without external bias.

- In Chapter 5 the first solar alkaline redox flow battery using low cost and environmentally safe materials is demonstrated. The redox pairs are ferrocyanide (negative pole) and anthraquinone-2,7-disulphonate (positive pole) in sodium hydroxide solution yielding a cell potential of 0.74 V. A thin film hematite photoanode was used to charge the battery. Photovoltage enhancement strategies were demonstrated for the ferrocyanide-hematite junction by employing an annealing treatment and depositing an organic layer of conductive polymer polyaniline on the electrode surface thereby combating electron-hole recombination.

- Chapter 6 addresses the electrodeposition of iron nanowires in porous anodic alumina templates. The effect of electrolyte molar concentration, temperature and stirring, pulse shape and barrier layer thickness on the deposition quality was investigated. The electrodeposition temperature and current density were also found to be determinant parameters affecting NWs crystallography. A methodology of surface response design of experiment was conducted to retrieve the optimum values for the deposition parameters. With the determined optimized

process, it was possible to obtain filling ratios up to 93 % and aspect ratios over 10 times higher than previous reports for an alternating current method.

- Chapter 7 studies double walled hematite nanotube structures. A novel method to prepare nanotubes based on the conversion of Fe NWs developed in Chapter 6 into hematite NTs is presented. Highly reproducible hematite double walled nanotubes were obtained with smooth walls and high surface areas. The fabrication process was demonstrated to be applicable to other metals. The versatility of using porous anodic alumina as template was also demonstrated with pore modulation. Scanning transmission electron microscopy was used to characterize the samples and understand the formation mechanism of the nanotubes. Magnetic properties are also discussed.

- Finally, the Main Conclusions and Perspectives are summarized in Chapter 8.

CHAPTER 1

Introduction

1.1 Motivation

With the escalation of energy consumption, consequent carbon dioxide footprint and fossil fuel reserves depletion, the worldwide nations are increasingly aware of the necessity to take advantage of renewable energy sources. Also, in the last years, new energy policies are being developed and some were already enforced aiming at more energy-sustainable behavior. For example, urban building energy management will change over the next decade to a new concept of Nearly Zero Energy Building (NZEB) under European directive (Directive 2010/31/EU) - in which the building should have nearly zero net energy consumption and nearly zero carbon emissions over the course of one year. This means that over the next decade, the energy supply of buildings will be increasingly dominated by renewable sources perfectly integrated in buildings, aiming at energy generation where it is consumed.

Among the different renewable energy sources, solar energy can easily provide enough power for all of human needs if it can be efficiently harvested[1]. In fact, to produce the predicted 43 TW needed by 2100, one would need 10 % efficient devices with a total area of approximately 24 % of the Sahara desert[2]. Also, in large and populated cities, solar energy is probably the most locally available renewable energy resource, not needing proximity to water nor specific geographic conditions for optimum wind benefit. Extensive research is ongoing to develop low-cost and environmentally friendly solutions towards a new generation of efficient solar cells with diversified and tailored optoelectronic properties. In Europe, Portugal is one of the countries with the highest solar incidence making it reasonable to invest in the development of solar harvesting technologies[3].

Three different ways of obtaining energy from solar radiation can be used: photosynthesis, phototovoltaics (PV) and photoelectrochemical (PEC) cells - Figure 1.1. Using photosynthesis plants convert sunlight, carbon dioxide and water into sugars (fuel) and oxygen. Commonly, PV cells are used to convert solar to electric energy. However, solar radiation is intermittent and unpredictable by nature and cannot be dispatched like fossil energy. A building with 100 % renewable energy support system may have large mismatches between the availability of the renewable sources and the

intended consumption, existing some periods of overpower and others of insufficient power generation. An effective method to store energy for later dispatch is therefore needed. Compared to other storage systems, such as conventional batteries, gravity or mechanical-based and supercapacitors, that can be used for the applications requiring moderate energy capacities and high power densities, chemical fuels are very attractive for their high energy density and because the necessary infrastructure can be adapted from fossil fuels[4–6]. Chemical fuels can also be used for mobile applications solving the most unattractive feature of batteries - long recharge time.

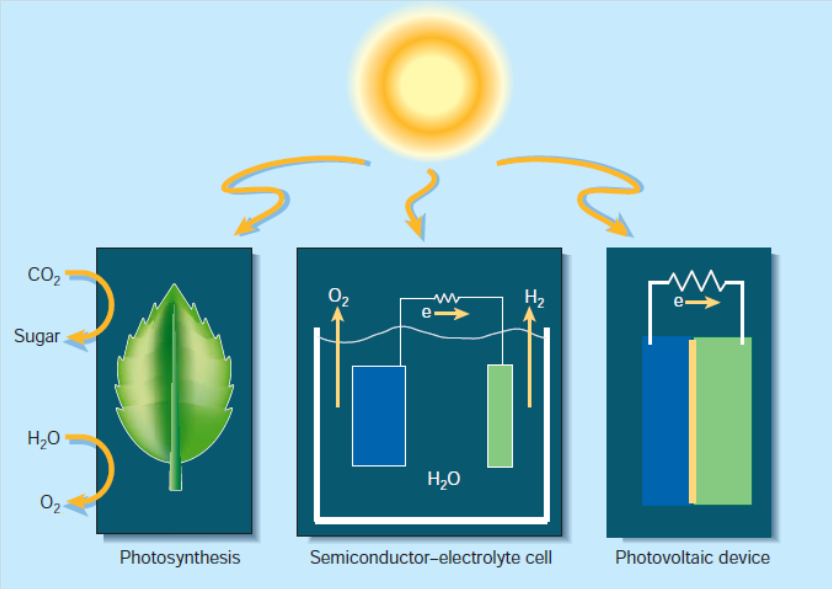

Figure 1.1 – Sunlight can be harnessed and converted into fuel or electricity by 3 energy-conversion strategies: photosynthesis, phototovoltaics and photoelectrochemical cells. The semiconducting material (blue) and metal electrode (green) (Extracted from 7).

A simple way to convert solar energy into chemical energy is through light-induced electrochemical processes in a PEC cell. Simply put, by direct use of sunlight, a PEC cell produces current in a PV cell or a photoelectrode and transforms a chemical entity (H_2O for example) into useful chemical energy (such as H_2) using that current. The most widely researched solar fuels are products of carbon dioxide reduction[8–10] and hydrogen[11–13]. It is clear that the development of low cost, efficient and environmentally safe PEC cells will have a major impact in our future energy needs.

This thesis focus on solar energy production and storage solutions using solar water splitting and solar redox flow batteries. First, cuprous oxide stability is improved for solar water splitting. Afterwards, a solar battery concept, based on photoelectrochemical cells and redox flow batteries, is explored. Finally, novel nanostructures are discussed and synthesized for solar energy applications.

1.2 Solar Water Splitting

1.2.1 Basic Concepts

Water splitting can be achieved by PV modules connected directly to electrolyzers. Water splitting PEC cells simplicity lies on immersing a semiconductor in water avoiding external connections. Usually they are low cost materials and easily create an electric field at the semiconductor/liquid interface (semiconductor-liquid junction - SCLJ)[5,14]. To perform stand-alone water splitting, i.e. without any external bias being supplied to the system, a semiconductor must produce enough voltage to promote the necessary electrochemical reactions. Until today, no semiconductor was able to do so efficiently and an external bias is necessary[15]. An elegant solution is combining PV and PEC cell in a tandem arrangement. In this arrangement the PV cell feeds electric current directly to the PEC cell instead of an electrolyzer, avoiding external bias. To preserve the necessary area of solar exposure, PV and PEC cells are placed on top of each other thus partially blocking sunlight to one of them and reducing the overall performance. Although great efforts have been made in these kinds of devices[11,13,16–19], an unbiased monolithic approach still is the most elegant and desired solution for solar water splitting. Besides being a clean and efficient energy carrier, PEC hydrogen production has the advantage that solar energy harvesting, conversion and storage are made in a single simple device.

Unbiased PEC devices can be divided into single and multiple photo-system arrangements[5,15]. The possible single photo-systems are:

1. n-type semiconductor photoanode and a counter-electrode;
2. p-type semiconductor photocathode and a counter-electrode;
3. p-n junction.

And the multiple photo-system arrangements are:

1. n- and p-type semiconductors (acting as photoanodes and photocathodes, respectively), wired or linked by an ohmic contact;
2. composite photoelectrodes of several semiconductor films stacked on top of each other.

Given its simplicity, throughout this thesis, the focus will be on the single photo-system, considered the *holy grail* of solar energy conversion and storage.

A typical PEC, as depicted in Figure 1.2, for water splitting, consists of three electrodes immersed in an electrolyte solution, namely the working electrode (WE), counter electrode (CE), and reference electrode (RE). Using an n-type semiconductor as example, the WE, also called photoanode, absorbs photons and, if they have sufficient energy to excite electrons from the valence to the conduction band, electron-hole pairs

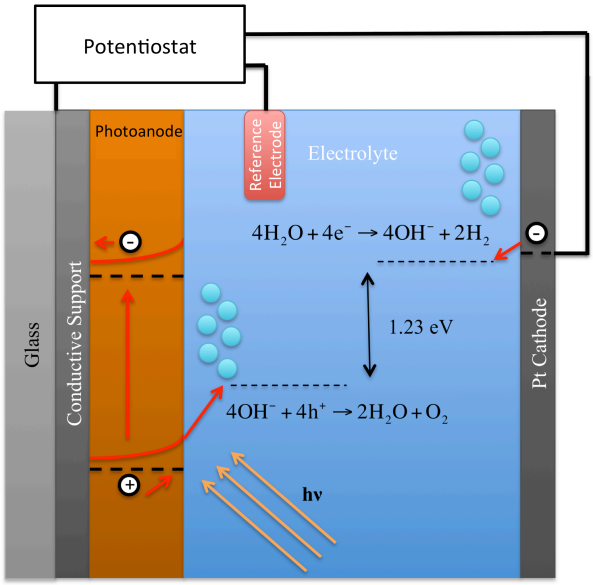

Figure 1.2 – Schematic representation of a conventional PEC cell using a photoanode as WE. Water splitting chemical reactions are represented.

are created. The electrons travel to the conductive support and are transported to the CE (or cathode) typically a corrosion resistant metal, commonly platinum, to prevent dissolution products from the counter electrode contaminating the solution; there they reduce water to form hydrogen gas. The holes that remain in the valence band migrate to the surface of the photoanode where they recombine with the electrolyte anions generated at the counter-electrode to oxidize water to form oxygen gas, thus closing the cycle. The equations that govern these reactions, in alkaline medium, are here presented[5]:

$$2H_2O + 2e^- \rightarrow H_2 + 2OH^- \quad E^0 = -0.828\ V_{NHE}, \tag{1.1}$$

$$2OH^- + 2h^+ \rightarrow H_2O + \frac{1}{2}O_2 \quad E^0 = 0.401\ V_{NHE}, \tag{1.2}$$

Where NHE stands for Normal Hydrogen Electrode. For an acidic environment, reactions 1.1 and 1.2 change to:

$$2H^+ + 2e^- \rightarrow H_2 \quad E^0 = 0.000\ V_{NHE}, \tag{1.3}$$

$$H_2O + 2h^+ \rightarrow H^+ + \frac{1}{2}O_2 \quad E^0 = 1.229\ V_{NHE}, \tag{1.4}$$

For either case, the overall water splitting reaction is the same:

$$H_2O + 2h\nu \rightarrow H_2 + \frac{1}{2}O_2\ . \tag{1.5}$$

The process is very similar if the photoanode is replaced by a photocathode: the majority charge carrier changes from electrons to holes that travel to the back contact and are transported to the CE (in this case, the anode) and electrons flow to the surface of the

semiconductor to reduce water.

The molar free energy change for the conversion of H_2O to H_2 under standard temperature and pressure (STP) conditions is $\triangle G$ = 237.2 kJ/mol, which, according to the Nernst equation, corresponds to $\triangle E^0$ = 1.23 V per electron transferred[5]. For a semiconductor to be able to achieve this reaction with light, the same must absorb radiant light with photon energies > 1.23 eV (corresponding to wavelengths of 1000 nm and shorter). In the ideal case, a single semiconductor material having a band gap energy (E_g) large enough to split water, and having a conduction band-edge energy (E_{CB}) and valence band-edge energy (E_{VB}) that straddles the electrochemical potentials E^0 (H^+/H_2) and E^0 (O_2/H_2O), can drive water splitting reaction under illumination. However, given the energy losses at SCLJ due to the concentration and kinetic overpotentials needed to drive the hydrogen evolution reaction (HER) and the oxygen evolution reaction (OER), the energy required for photoelectrolysis is frequently reported as 1.6 - 2.4 eV per electron-hole pair generated[20]. Besides adequate band edge positions, a semiconductor should meet several criteria, such as high chemical stability, strong light absorption, efficient charge transport (of both electrons and holes), low overpotentials and, ideally, low cost and safe[5,20,21].

1.2.2 Cuprous oxide photocathode

The solar water-splitting phenomenon was first reported in 1972 in a pioneering work by Fujishima and Honda, using TiO_2 as photoanode[22]. Since that date the process of H_2 generation has been profoundly studied and today it is well understood, including the separation, the mobility and the lifetime of photogenerated electrons and holes, as well as the comprehensive insights into the correlation between the structure and composition of a photoeletrode and their performances. Much research effort has been dedicated to the preparation semiconductor materials to enhance their performance.

Today there are several possible semiconductors being investigated for solar water splitting, ranging from metal oxides (α–Fe_2O_3[23–25], TiO_2[26,27], WO_3[19,28], $BiVO_4$[13,18,29], Cu_2O[30–32], etc.) and non-metal oxide semiconductors (e.g. CdSe[33,34], CdS[35,36], Ta_3N_5[37,38], etc.) - Figure 1.3. The energy levels for several semiconductors are represented in Figure 1.3, together with the water splitting energy levels. Different fabrication methods (spray pyrolysis[39], electrodeposition[40], chemical vapor deposition[41], atomic layer deposition[42], etc.) have been used to fine-tune the composition and morphology of the semiconductor under study, in the hope of finding an efficient and stable photoelectrode.

Hematite (α–Fe_2O_3) and cuprous oxide (Cu_2O) stand out as two possible candidates for solar water splitting. Hematite will be discussed later on in this chapter. Being copper one of the most abundant materials on planet Earth, Cu_2O is a low cost and environmentally safe material[40,43]. Cu_2O is one of the most thermodynamically stable form of copper oxide. The copper and oxygen atoms in Cu_2O arrange in a cubic lattice

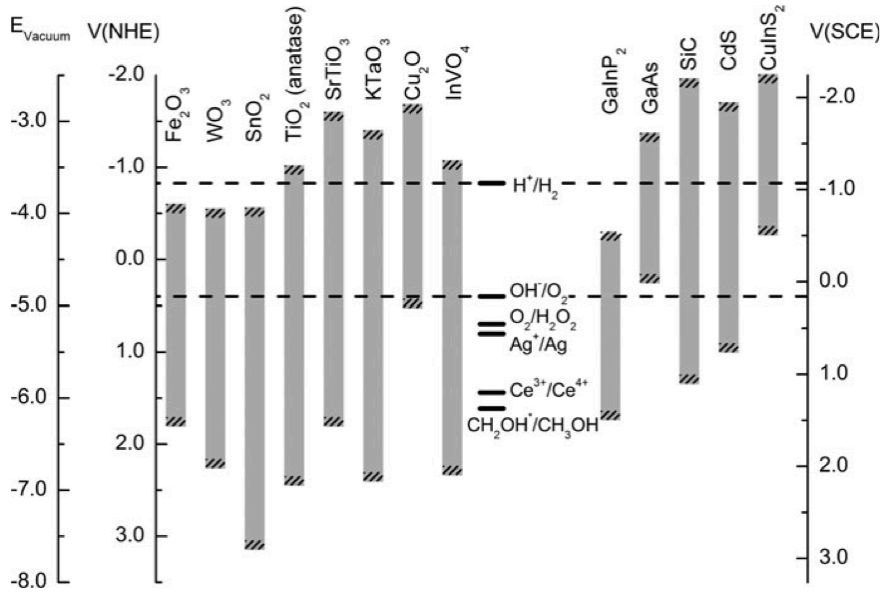

Figure 1.3 – Energy band positions for various semiconductors at pH 14 (Extracted from 5).

with space group $Pn\bar{3}m$ and lattice constant 4.2696 Å[43]. It is a widely studied p-type semiconductor in H_2 generations, in lithium ion batteries and in PV applications in heterojunction with ZnO[44]. It is accepted that copper vacancies, acting as electron acceptors, are at the origin of the p-type nature of this material[45–47]. In fact, binding energy calculations for both donors and acceptors in Cu_2O reveal that it is in fact easier to make p-type than n-type Cu_2O (266 meV and 156 meV donor and acceptor binding energy, respectively), although examples of n-type doping have been reported[48].

With 2 eV bandgap[49], corresponding to a maximum achievable photocurrent density, based on optical absorption limits, of -14.7 $mA \cdot cm^{-2}$ and a light-to-hydrogen conversion efficiency of 18 % based on the Air Mass (AM) 1.5, Cu_2O is suitable for water splitting[40]. The E_{CB} is placed 0.7 V above the hydrogen evolution potential and the E_{VB} very close and below to oxygen evolution potential - Figure 1.3. With no overpotential available for oxygen evolution, Cu_2O can drive half of the water splitting reaction but an external bias is required to conduct the other half reaction (that can be applied from a PV device)[40].

In low grain size Cu_2O (such as electrodeposited Cu_2O that will be discussed in chapters 2 and 3 of this thesis) have charge carrier collection lengths less than 1 μm[50]. This means that in order to collect charge carriers produced by longer wavelength photons nanostruturing is necessary otherwise recombination will limit the efficiency.

Given the band structure of Cu_2O, a direct band gap of 2.0-2.1 eV is present. However, the lowest fundamental absorption transitions at the Γ-point of the Brillouin zone ($\Gamma_8^+ \rightarrow \Gamma_6^+$ and $\Gamma_7^+ \rightarrow \Gamma_6^+$) are parity forbidden[48]. The next allowed optical transitions are ($\Gamma_7^+ \rightarrow \Gamma_8^-$ and $\Gamma_8^+ \rightarrow \Gamma_8^-$). This limits the absorption efficiency of Cu_2O, even below the bandgap wavelengths, as can be seen in Figure 1.4.

Furthermore, the limiting factor of Cu_2O as an effective water-splitting photoelec-

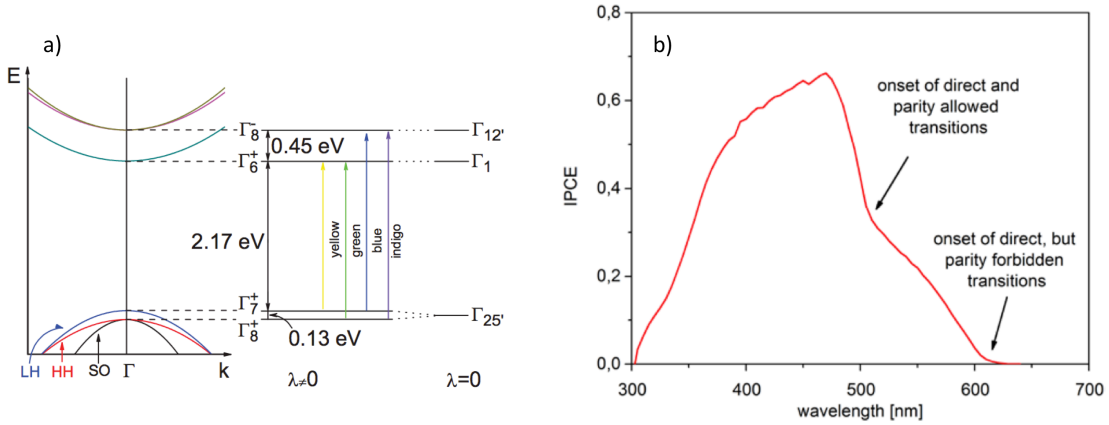

Figure 1.4 – a) Bandgap transitions; b) incident photon-to-current efficiency (IPCE) of an electrodeposited Cu_2O photocathode for water splitting (Extracted from 43).

trode is clearly the long-term stability[40,51]. When a semiconductor electrode is placed in contact with an electrolyte solution under illumination some reactions may occur, for instance ionic oxidation or reduction of the semiconductor – this is called photocorrosion[52].

1.2.3 Cuprous oxide photocorrosion

A semiconductor MX (e.g., M = Zn, Ga, Ti and X = S, N, O_2 in ZnS, GaN, TiO_2) used as the n-type photoanode may have a favorable E_{VB} alignment with O_2/H_2O oxidation potential, but the photogenerated holes (h^+) can oxidize the semiconductor first, rather than the water, causing the semiconductor corrosion[52],

$$MX + zh^+ + \rightleftharpoons M^{z+} + X. \quad (1.6)$$

Also the photogenerated electrons (e^-) in the p-type photocathode MX may reduce itself:

$$MX + ze^- + \rightleftharpoons X^{z-} + M. \quad (1.7)$$

These two reactions define two potentials for holes and electrons: thermodynamic oxidation potential φ_{ox} and reduction potential φ_{re}, respectively[53]. Depending on the positions of these potentials regarding the valence and conduction bands, the semiconductor might be stable or unstable - Figure 1.5. If the φ_{ox} is below the valence band maximum, no anodic decomposition can occur. Conversely, φ_{re} is above the conduction band minimum, no cathodic photocorrosion can occur. Figure 1.6 shows some decomposition potentials for various semiconductors used to carry out the water splitting reaction under solar radiation. Although these diagrams do not show all the factors regarding (for example, reaction kinetics is not taken into account), both thermodynamic potentials for oxidation and reduction of Cu_2O lie within the bandgap and, as experimentally tested, this semiconductor is unstable for long-term water

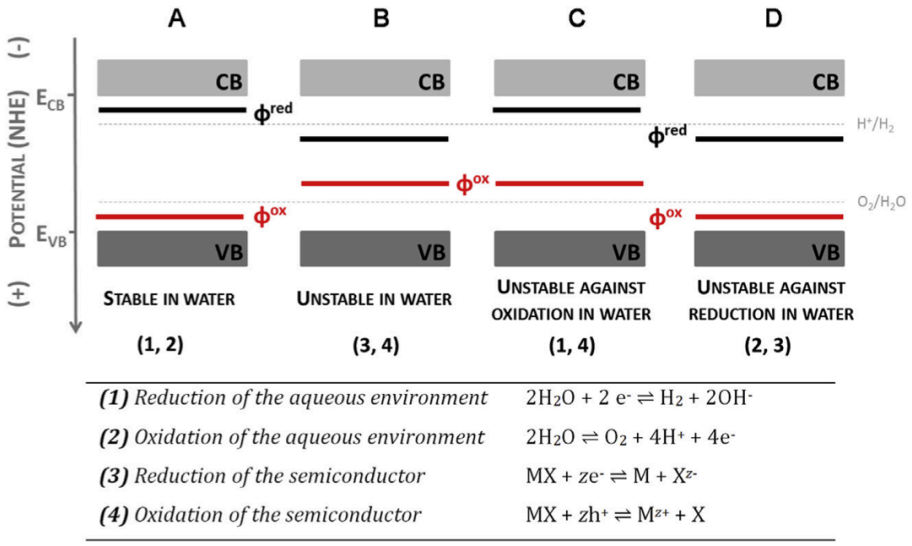

Figure 1.5 – Diagram with various possibilities for thermodynamic stability of a semiconductor in water (Extracted from 53).

splitting[40].

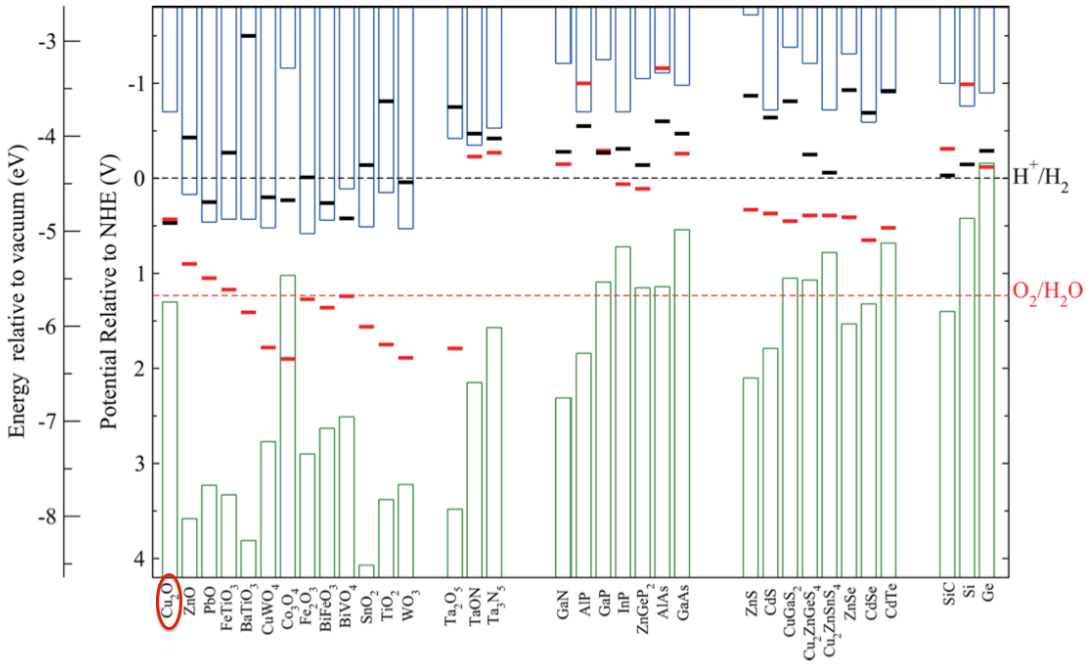

Figure 1.6 – Positions of band edges and decomposition thermodynamic decomposition potentials for different oxide and non-oxide semiconductors at pH 0. Cu_2O is the first one and is marked in red (Adapted from 52).

One possible way to overcome this limitation is to cover the Cu_2O with a protective layer, given that it fulfills a set of criteria: since it is the intermediate material between the photoabsorber and the electrolyte, it must have a staggered type-II band offset when interfaced with Cu_2O in order to inject charge carriers in the correct direction for water reduction (electrons to the electrolyte and holes to the counter electrode); this is the case

for some n-type semiconductors with sufficiently high conduction band edge; second, the surface of the protective layer should have an electrochemical reaction rate suitable with water reduction to H_2, which can usually be achieved using a suitable catalyst; finally, no corrosive side reactions should occur at potentials in the bandgap[40].

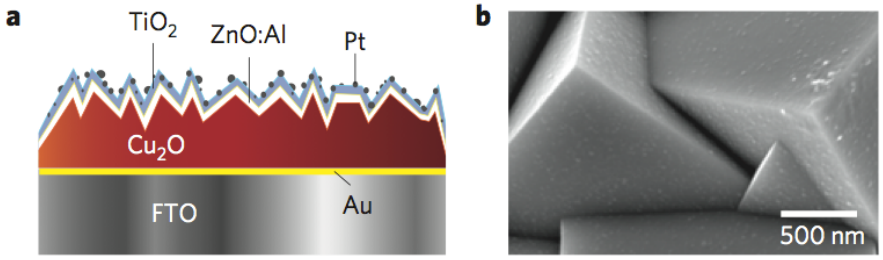

Figure 1.7 – a) Schematic representation and b) top SEM view of a composite photocathode Cu_2O/AZO/TiO_2/Pt (Extracted from 40).

Probably the most well known work on protected Cu_2O photocathode for solar water splitting belongs to Paracchino *et al.*[40]. In this work, Cu_2O was conformally coated with Al:ZnO (AZO) covered by a thin TiO_2 layer - Figure 1.7. The resulting composite photoeletrode reported hydrogen-evolving photocurrents of -7.6 mA·cm^{-2} at an applied bias of 0 V_{RHE} in pH 5 electrolyte. The Cu_2O was deposited using a low cost technique (electrodeposition) and the overlayers were deposited using atomic layer deposition (ALD) to guarantee a compact and defect free layer. The authors realized that the AZO middle layer was essential to stabilize the photoeletrode, providing a good seed layer to improve the nucleation and conformity of the subsequent TiO_2 layer. Also, AZO created a p-n buried junction improving the overall photovoltage of the device. Stability tests were conducted on this composite photoeletrode over 20 minutes in chopped light at 0 V_{RHE} and no corrosion of the underlying photovoltaic material was observed by either XPS and XRD. The photocurrent decrease with time was attributed to recombination of electrons trapped in TiO_2 as Ti^{3+}. The same authors were able to further improve the stability of this photoelectrode by controlling the deposition temperature of the TiO_2 (changed from 120 °C to 150 °C), which shifts the flatband potential from +0.3 V to -0.1 V - Figure 1.8[51]. This shift flattened the TiO_2 band reducing electron trapping and increasing stability.

In the previous mentioned reports, Pt was used as catalyst. Some efforts were made to find suitable alternatives. Tilley *et al.* investigated the use of RuO_2, best known as an effective water oxidation catalyst, but also a very effective hydrogen evolution catalyst[32]. For a current density of 10 mA·cm^{-2} - a realistic value of what one could obtain with a 2 eV bandgap (Cu_2O) and AM 1.5 solar illumination - RuO_2 requires only an additional 30 mV of overpotential compared to Pt, the best known hydrogen-evolving catalyst. RuO_2 was electrodeposited under 1.5 AM illumination onto TiO_2. Plateau photocurrents of -5 mA·cm^{-2} at +0.55 V_{RHE} were observed and vastly improved stability with 94 % of photocurrent remaining after 8 hours of light chopping when biasing at

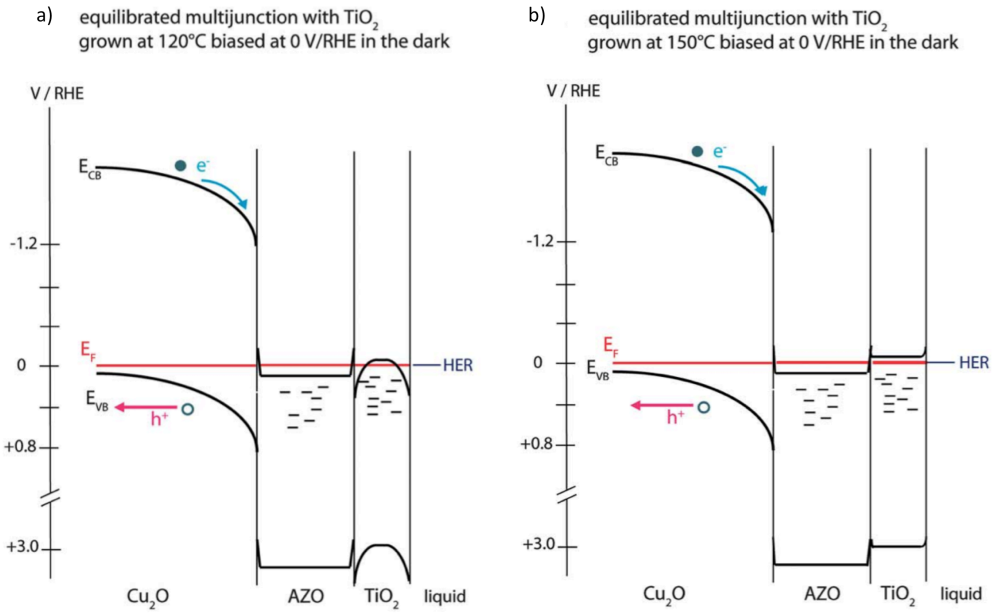

Figure 1.8 – Energy diagram of a composite photocathode $Cu_2O/AZO/TiO_2$ with TiO_2 different deposition temperatures (Extracted from 40).

0 V_{RHE} - Figure 1.9. Additionally, a new catalyst was tested yielding great results based on molybdenum sulphide[31]. This catalyst extended the pH operating range of the Cu_2O photocathode, revealing an extraordinary -5.5 $mA{\cdot}cm^{-2}$ photocurrent at 0 V_{RHE} and pH = 1.21. The reported stability for pH = 5 was 10 h but with smaller current densities than before. These works proved that through improvement of the protective layers, major stability enhancement could be achieved.

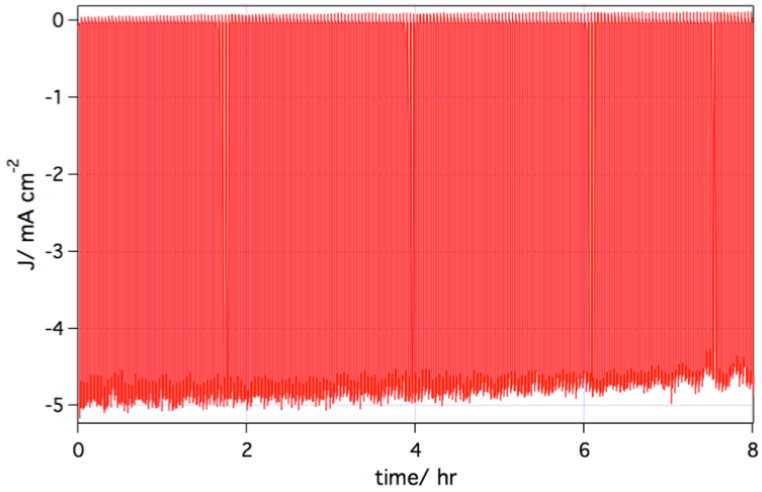

Figure 1.9 – Chronoamperometric stability measurement of a Cu_2O photocathode with RuO_2 catalyst biased at 0 V_{RHE} in pH 5.0 phosphate–sulfate electrolyte under light chopping (Extracted from 32).

Chapter 2 develops an understanding on the influence of TiO_2 synthesis conditions on the photocathode stability. A simple low-cost solution was developed based on a steam treatment that can patch surface nano defects and improve stability by a factor of

6. Chapter 3 explores a new protective layer alternative to TiO_2. This study represents the first demonstration of SnO_2 as a photocathode protection layer. Record breaking stabilities were achieved up to 57 h.

1.3 Solar Redox Flow Batteries

1.3.1 Hydrogen alternative

For the past two decades, energy storage using solar water splitting has been one of the most investigated technologies, as discussed in section 1.2. Much effort was devoted to fabricate and optimize PEC cells for water splitting offering the prospect of clean, dispatchable, abundant, and affordable energy. However, hydrogen is a very low-density gas requiring high-end technology for storage and transport. Also, its production via PEC cells route still presents many unsolved challenges, in particular low conversion efficiency[54,55]. PEC cells require an abundant semiconductor material with E_g large enough to split water and a E_{CB} and E_{VB} that straddles the electrochemical potentials for generation of hydrogen ($E^0_{H^+/H_2}$) and oxygen ($E^0_{O_2/H_2O}$)[20]. This requirement limits the possibilities to a handful of semiconductor materials. Since the positions of both the band edges of most interesting semiconductors and $E^0_{H^+/H_2}/E^0_{O_2/H_2O}$ shift with -59 mV per pH unit[5], pH-tuning strategies to match energy levels are not effective.

In a PEC cell, the photo induced free charge carriers migrate to a semiconductor/liquid junction reacting with electroactive species directly at the semiconductor interface. Given the energy efficiency losses at semiconductor/liquid junctions due to the concentration and kinetic overpotentials needed to drive the hydrogen and oxygen evolution reactions, the energy required for photoelectrolysis is frequently reported to have values around 2 eV per electron-hole pair generated[5,20]. Considering the significant amount of research in the field for the past two decades, identification of semiconductors that enable unbiased and efficient single photoelectrode solar water splitting appears unlikely.

There are several battery technologies that can be used for electric power storage but redox flow batteries (RFBs) are a very attractive solution for their low cost, high charge-discharge energy efficiency, fast response time, modularity and flexibility[56]. RFB separate power and energy: the stack size controls the power while energy is stored in the electrolytes which volume controls the stored energy amount. This modular design enables easy transportation and simplifies construction and maintenance. Also, the system can be optimized over a greater range of variables and storage can be increased with relatively ease and minimal cost compared to the stack. RFBs are expected to be the cheapest devices for storing electricity at stationary local level with foreseen costs of 3 ¢/kWh[57] of electricity stored per cycle in 2050. This technology is expected to be a great contributor for the European directive NZEBs as well as enabling easy fuel for electric transportation.

1.3.2 Redox Flow Batteries

Redox flow batteries are an attractive alternative to conventional batteries with low cost, very little maintenance and modularity[56,58,59]. RFB consists of an assembly of power cells in which the electrolytes are separated by an ion exchange membrane, as depicted in Figure 1.10. During the charging step, a redox reaction is driven by electrical power, similarly to the PEC cell, promoting the reduction/oxidation (depending on polarization of the electrode) of a chemical species (charging it) and the charged electrolytes are stored in separate tanks. When electric power is needed, the flux of the electrolytes is inverted and electrons are provided from the reverse reactions to an external circuit.

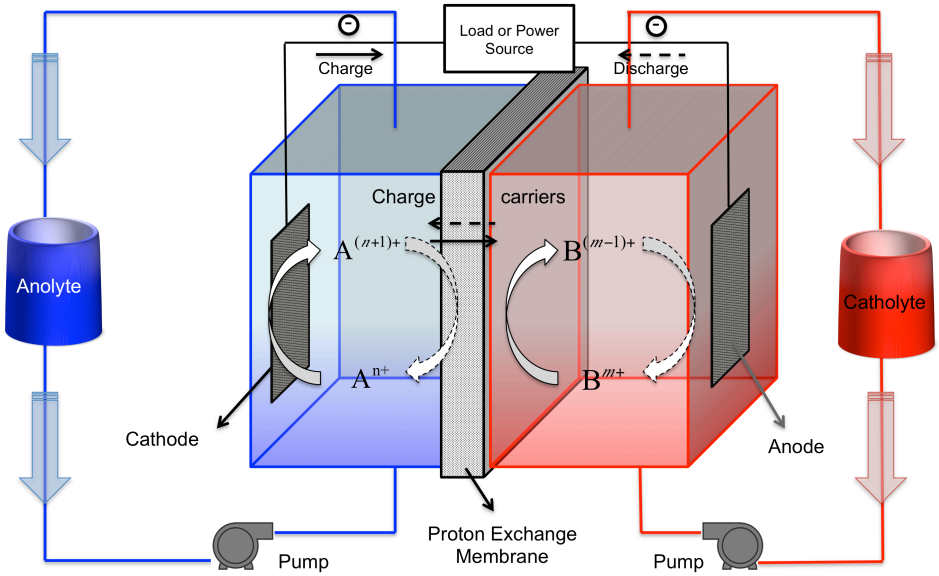

Figure 1.10 – Simple schematic diagram of a redox flow battery. The electron transport in the circuit, ion transport in the electrolyte and across the membrane and mass transport in the electrolyte are represented.

In 1985 Maria Skyllas-Kazacos described a RFB using vanadium electrolytes[58]. This battery has been widely studied over the last few years and is one of the few configurations with present industrial application[60–70]. A key component of RFBs is the ability to separate power and energy. The stack controls the power while the energy is separately stored in the electrolyte. Due to this independence RFBs can be tailored to fit the specific demands of an application controlling the energy with minimal cost since the stack is the most expensive system component.

There are several other RFB configurations with different electrolytes - Figure 1.11. One of the most interesting redox couple for RFBs is the polysulfide/bromine for its high cycle efficiency (over 80 %) at ambient temperature, readily available materials and high solubility that reduces the volume per energy amount, making it the cheapest and most promising energy storage technology suitable for applications from 10 to 100 MW with duration up to 12 h[71–73].

More recently, in order to substitute redox-active metals and nobel-metal electrocat-

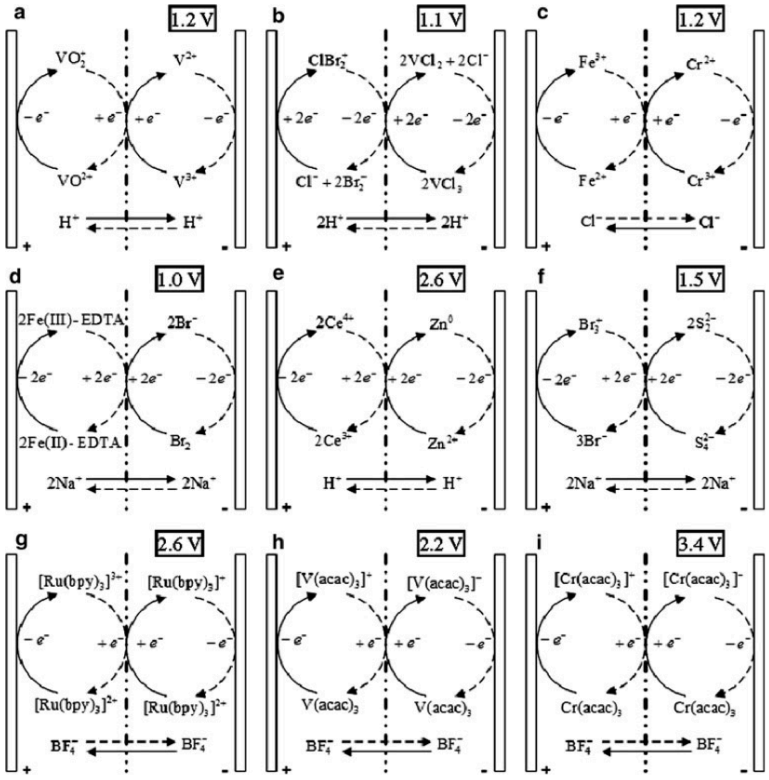

Figure 1.11 – Schematic representation of various redox-flow systems (the values give the potential of the redox couple). a) All vanadium, b) vanadium/ bromine, c) iron/chromium, d) Fe-EDTA/bromine, e) zinc/ cerium, f) bromine/ polysulphide, g) nonaqueous ruthenium/ bipyridine, h) nonaqueous vanadium/ acetylacetonate, i) nonaqueous chromium/ acetylacetonate (Extracted from 56).

alysts[74,75], several organic RFB have been under active study[76–78]. The first reports date back to 2007 and more recently by Huskinson *et al.* on 9,10-anthraquinone-2,7-disulphonic acid (AQDS) with bromine in sulfuric acid[76]. They demonstrated equivalent efficiencies when compared to state-of-the-art RFBs such as all vanadium, yielding a peak galvanic power density exceeding 0.6 W cm^{-2} at 1.3 A·cm^{-2}. Cycling of this quinone–bromide flow battery showed >99 % storage capacity retention per cycle. The biggest advantages of quinone based RFB are the low cost, high efficiency, safety and tunability. In fact, there is a big family of quinones that can be used with different redox potentials and pH tolerances, offering prospects of high efficiency and low cost RFBs - Figure 1.12[76–81].

1.3.3 Solar Charging

In the work developed in this thesis, it is proposed an innovative storage system, based on the combination of RFB with PEC cells – Solar-RFB. This system is inspired in one of nature most common mechanisms: photosynthesis - Figure 1.1. The photosynthesis process allows plants to absorb and store solar energy in the form of chemical energy. During the day, plants absorb sunlight and convert it to adenosine triphosphate that transports chemical energy within cells for metabolism, which is stored until needed –

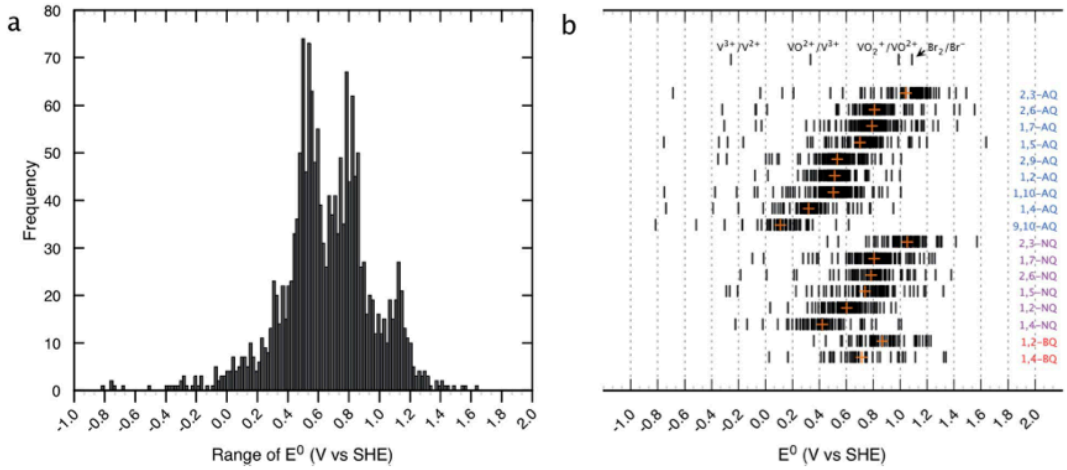

Figure 1.12 – Distribution of high-throughput screened quinone/hydroquinone redox couples. (a) A histogram of theoretically predicted E^0 (V vs. SHE). Number of bins and width of the histogram are 130 and 0.1 V, respectively. (b) E^0 windows for the different classes of quinones. The orange crosses show the mean values of E0 for each class. Redox potentials of the conventional inorganic AFB redox couples are noted for comparison (Extracted from 78).

photosynthetic stage[82]. When that energy is needed, the plant metabolism obtains it breaking down energy storing compounds – respiratory stage. The simplicity and self-sufficiency of this mechanism makes photosynthesis an ideal solar energy harvesting mechanism. The proposed technology mimics the photosynthetic/respiratory stages of plants with potential high efficiencies. PEC panels convert sunlight into electrochemical energy (in the form of dissolved redox pairs) and harvest heat. The charged and heated electrolytes are stored in reservoirs and can exchange heat with sanitary waters and central heating for thermal comfort – Figure 1.13. When needed, electricity could be generated by discharging the electrolytes.

Solar electrochemical energy storage systems were initially explored in the 1980s[83]. The focus was investigation of semiconductor-electrolyte junctions in combined conversion and storage cells using both liquid and semisolid redox systems. The research paused due to technical challenges such as lack of efficient, stable and cheap photoelectrodes and issues with membrane selectivity. Other attempts have been made more recently by two different research groups. Wu *et al.* combined a dye sensitized TiO_2 photoelectrode and a lithium based battery describing the advantages of having a photoassisted battery charging[84,85]. On the other hand, Liu *et al.* integrated an all vanadium RFB with a TiO_2 photoelectrode with high Faradaic efficiencies[86,87]. Despite the reported advantages, none was able to demonstrate the possibility of charging a RFB to high states-of-charge with no external bias, lacking a good fit between electrolytes redox potentials and semiconductor energy band positions.

Chapter 4 describes the first unbiased solar RFB for solar energy solutions. Based on acid all-vanadium RFB and CdS photoelectrodes, the concept was demonstrated with reasonable current densities. Given the low pH environment and instability of

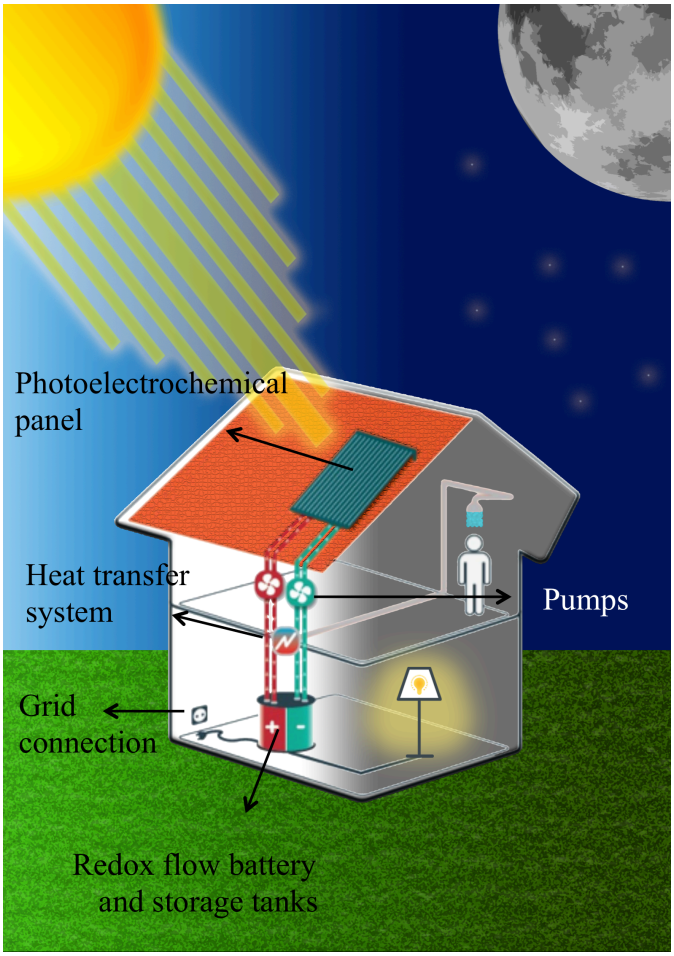

Figure 1.13 – Conceptual sketch of a Solar-RFB: PEC cell on the roof for direct solar charging a redox flow battery coupled with a thermal system.

CdS, alkaline electrolytes are approached in chapter 5. Organic-inorganic alkaline electrolytes are presented in a novel RFB and, in combination with hematite photoelectrode, solar charging was achieved. The kinetics in a hole scavenger environment were also improved for the first time.

1.4 Nanostructured Photoelectrodes

Nanotechnology created many amazing opportunities in a wide range of applications. From electronics[88], sensor devices[89], optoelectronics[90], photovoltaic[91] and photocatalysis[92], nanostructured materials such as nanoparticles[93], nanowires[94], nanotubes[95], nanorods[96] and nanobelts[97] are being used and intensely investigated.

In chapter 5 hematite thin film photoeletrodes were used. Hematite is one of the best examples that illustrate how much nanostruturing can influence the performance of a photoeletrode[14,98,99]. With a reported bandgap of 2.0 - 2.2 eV, it has the potential to offer conversion efficiencies ranging from 12.7 - 16.8 %, the achievement of which would mark a major breakthrough in this field[100]. Since the first report by Bard *et al.* in

1976[101], significant research has been conducted to study hematite for PEC devices. Although much progress have been made the best operating hematite based devices still work at considerably lower efficiencies than the theoretical limit[102].

A look at the energy levels of hematite when in contact with an aqueous solution should help us understand some limitations of hematite. As shown in Figure 1.6, the conduction band edge is measured at 4.71 eV (vs. vacuum) or 0.21 V (vs. normal hydrogen electrode, NHE)[103]. A key challenge is immediately obvious: the significant mismatch of hematite's conduction and valence band edge positions and the oxidation energy levels of several electrolytes. Thus, a reduction potential needs to be provided at the counter electrode. In principle, forming multi-quantum systems may solve this problem[17,104].

Some other important limitations of hematite can be understood by examining the expression that describes the quantum efficiency of the photoelectrochemical process at a semiconductor/liquid interface[105],

$$\eta = \frac{1 - e^{-\alpha W} + \frac{L_K}{L_{K+\alpha^{-1}}} e^{-\alpha W}}{1 + \frac{k}{k_\varepsilon}\left(\frac{L_D}{\sqrt{2\nu_0}} + \frac{L_K}{e^{\nu_0}}\right)} \tag{1.8}$$

where α is the light absorption coefficient at a given wavelength, W is the depletion width, L_d is the Debye length, L_K is the recombination distance, k is the recombination rate of charges within hematite, k_ε is the faradaic rate constant, and ν_0 is the degree of band bending. We see from this equation that good light absorption, long hole diffusion distance (hence long recombination distance), low charge recombination in the bulk, and fast charge transfer across the surface are desired for high quantum efficiencies. Unfortunately, the intrinsic properties of hematite satisfy none of these considerations (we note that although hematite's absorption in the short wavelength region ($\sim 10^3$ cm^{-1})[106], it drops rapidly near the band edge where the photons are most abundant in the solar spectrum). The small (ca. 10 nm) space charge layer (present in highly doped hematite) and the short (ca. 4 nm) diffusion length of minority carriers[107] suggests that the ideal morphology of a $\alpha-Fe_2O_3$ photoanode would be one where all of the hematite is within 10-20 nm of the semiconductor/liquid junction. The simplest way to do this is deposit a 10 nm layer of hematite on a transparent substrate using a traditional deposition method and by stacking multiple films in tandem, the poor absorptivity would be overcome. In fact, this solution was proposed by Itoh in 1984[108]. But it is very expensive to implement and presents other problems as high hole recombination[106]. A logical move would be to try to modify various aspects of hematite properties selectively. One alternative is to dope the hematite by adding impurities such as Ti[109,110], Si[111], or Sn[107,112], among others, that increase the carrier density and improve the conductivity. This approach, however, depends a great deal on the detailed synthetic methods, and as a result, is progressing at a slow pace.

In addition to changing compositions, innovations in the design of morphologies

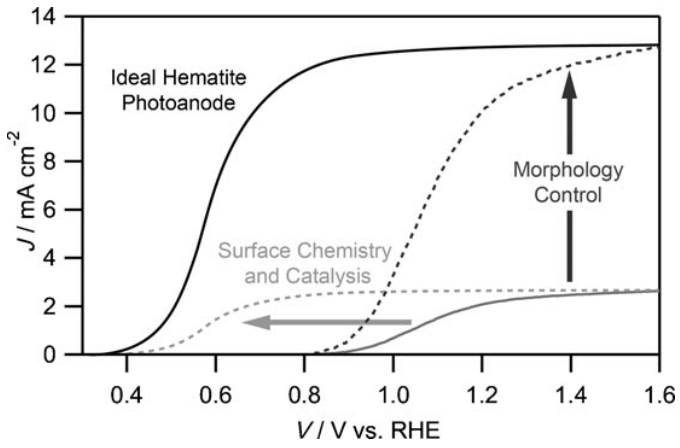

Figure 1.14 – Expected evolution of photogenerated current with morphology and surface chemistry control in $\alpha - Fe_2O_3$ photoanodes (Extracted from 106).

shows to be a promising alternative. For example, nanostructured hematite, like cauliflowers[111], nanorods[113,114] or nanowires[107], may address the poor minority charge carrier diffusion issue - see Figure 1.14. α–Fe_2O_3 nanostructures with anisotropic morphologies can take advantage that light is absorbed along the longitudinal direction (which can be hundreds of nanometres to microns long) and charges are separated along the transverse direction (which is typically in the nanometre range). As such, the numerator in Equation 1.8 will be close to unity and no longer depends on α.

1.4.1 Hematite Nanotubes

There are many different techniques to prepare $\alpha - Fe_2O_3$ nanostructures (see Table 1.1). Among these, nanotubes (NTs) rapidly emerged with ultra-thin walls, improved charge transport properties and excellent photoactivity compared to other structures[99,115]. Also, the low feature size has been reported to have upward shift of the conduction band due to quantum confinement[116]. The most common method to prepare $\alpha - Fe_2O_3$ NTs is Fe electrochemical anodization[99,117,118].

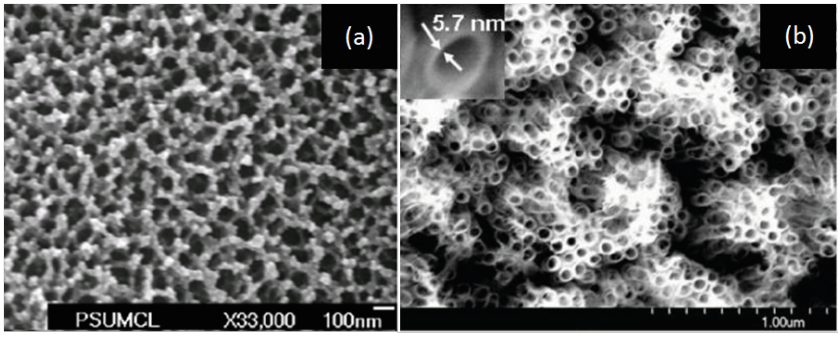

Figure 1.15 – Different generations of anodic iron oxide: a) nanoporous and b) nanotubes arrays (Adapted from 117 and 99).

Technique	Feature size/ Thickness	Dopant/ Treatment	PEC conditions	Photoresponse (at 1.23 V_{RHE})	Ref./ Date
Single Crystal	um	Nb/None	1 M NaOH; 100 W/Hg arc lamp (20 mW·cm^{-2})	135 μA·cm^{-2} and IPCE 37 % at 370 nm	119/1988
Sintered polycrystalline disk	um	Si/None	1 M NaOH; AM 1.5 G (100 mW·cm^{-2})	125 μA·cm^{-2} and IPCE 34 % at 400 nm	120/1982
Solution-based Colloidal	500 nm	Ru	1 M NaOH; AM 1.5 G (100 mW·cm^{-2})	5.7 mA·cm^{-2} and IPCE 82 % at 320 nm (bare: 0.31 mA·cm^{-2})	121/2015
APCVD	700 nm	Si (TEOS)/IrO_2 co-catalyst	1 M NaOH; AM 1.5 G (100 mW·cm^{-2})	3.0 mA·cm^{-2} and IPCE 50 % at 320 nm	14/2010
Electrodeposition	20 – 50 nm	Mo/None	1 M NaOH, 410 mW·cm^{-2}	1.5 mA·cm^{-2} and IPCE 8 % at 400 nm	122/2008
ALD	32 nm	None/Ga_2O_3 underlayer + $Ni(OH)_2$ co-catalyst	1 M NaOH; AM 1.5 G (100 mW·cm^{-2})	0.7 mA·cm^{-2}	123/2014
Solution-based nanowires	700 nm	Sn	1 M NaOH; AM 1.5 G (100 mW·cm^{-2})	1.2 mA·cm^{-2} and IPCE 16 % at 400 nm	107/2011
Potentiostatic anodization	um	None	1 M KOH; AM 1.5 G (87 mW·cm^{-2})	1.0 mA·cm^{-2}	99/2009

Table 1.1 – Comparison of hematite different fabrication methods.

The first researcher to report hematite nanostructures by simple and low cost Fe electrochemical anodization process was Grimes[117] - Figure 1.15a. Highly organized nanoporous were obtained using 1 % HF + 0.2 % HNO_3 + NH_4F (0.5 wt % and 1 wt %) in glycerol media, at different temperatures (4 and 10 °C) and applied potential (40, 60 and 90 V). The nanopores could be tuned by varying the applied potential and after annealing photocurrent density of 0.26 mA·cm^{-2} at 0.6 V vs Ag/AgCl (in 1M NaOH solution) under simulated AM 1.5 sunlight were obtained. Later, Mistra *et al.* reported NTs structures using sonoelectrochemical anodization of a Fe foil at room temperature[99] - Figure 1.15b. Smooth NTs with pore diameters of 50-55 nm and 3-4 μm long could be produced and after annealing showed 1.41 mA·cm^{-2} at 0.5 V vs Ag/AgCl, respectively (under AM 1.5 illumination in 1M KOH solution).

More recently, another research group used porous anodic alumina (PAA) templates to grow vertically aligned hematite NTs[124]. PAA templates are very attractive because they are cheap and easy to synthesize with highly tunable pore dimensions (anodization steps are described in appendix A. The process required several steps to synthesize the $\alpha - Fe_2O_3$ nanotube structure: besides the PAA template, a gold layer was deposited, then the template was filled with polyaniline and, after the pore widening, Fe was electrodeposited in the gaps between polyaniline and PAA forming NTs - Figure 1.16. Only after annealing and PAA removal would the final $\alpha - Fe_2O_3$ NTs be ready. Although the tubes were organized, the performance was rather low (less than 1 mA·cm^{-2} at 0.4 V vs Ag/AgCl).

Higher surface areas and ultra thin walls should improve the performance of α – Fe_2O_3 NT photoanodes. In this thesis a novel method to fabricate complex nanotube structures is demonstrated. Chapter 6 optimizes the electrodeposition of ultra-long iron NWs in PAA. Electrodeposition is simple and low cost method to create homogeneus

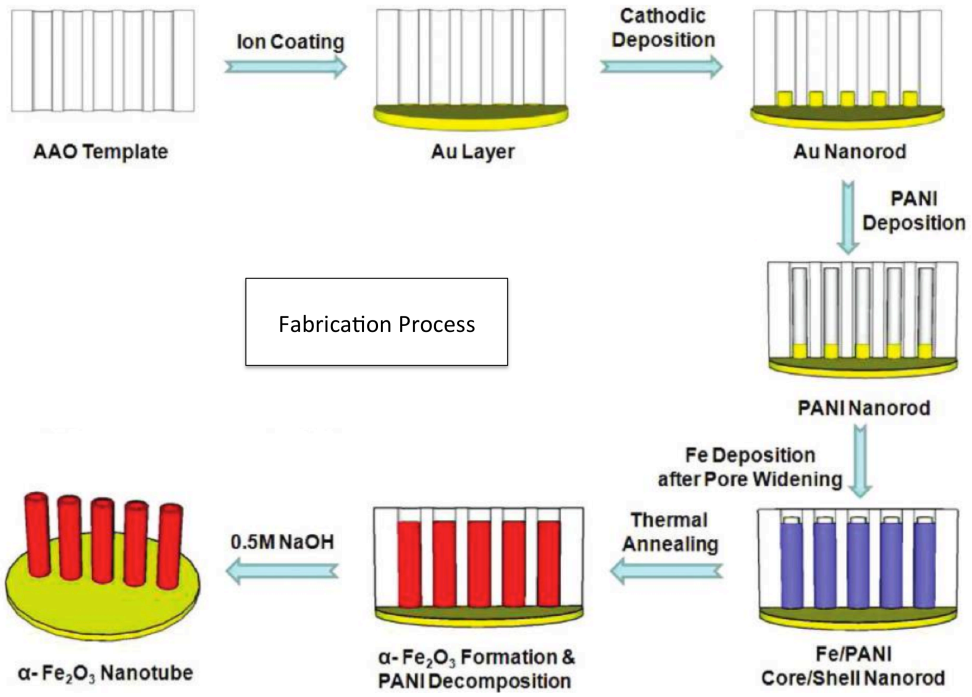

Figure 1.16 – Schematic diagram of the processes used for the synthesis of the $\alpha - Fe_2O_3$ nanotube arrays on PAA template (Adapted from 124).

NWs. These same NWs are then converted into $\alpha - Fe_2O_3$ double walled NTs in a simple annealing treatment - chapter 5. The PAA templates were fine tuned to provide high surface areas and novel features to the NTs.

CHAPTER 2

On the stability enhancement of cuprous oxide water splitting photocathodes by low temperature steam annealing

This chapter is dedicated to the studies on an innovative low temperature steam treatment for improving the stability of Cu_2O-based photoelectrodes protected with amorphous TiO_2 layers. Low temperature steam post-synthetic treatments were implemented and demonstrated greatly enhanced stabilities compared with non-treated samples. Photocurrents over –5 mA·cm^{-2} were achieved with only 10 % loss over its initial photocurrent value during more than 50 h of light chopping (biased at 0 V_{RHE}).

This chapter is adapted from the published work:
J. Azevedo, L. Steier, P. Dias, M. Stefik, C. T. Sousa, J. P. Araújo, A. Mendes, M. Graetzel and S. D. Tilley, *Energy & Environmental Science*, 2014, 7, 4044-4052.

The author contributed to the planning and execution of all the experiments described in this chapter, except: TEM measurements which were carried out by Steier, L; XRD, Raman, SEM and Ellipsometry measurements which were carried out by Stefik, M and Tilley, S.D. The author was also involved on the discussion and interpretation of all results, as well as on the preparation of the manuscript.

2.1 Background

Cuprous oxide, Cu_2O, is abundant, cheap and environmentally friendly and it absorbs a significant part of the solar spectrum with a 2 eV bandgap, with favorable energy band positions for water cleavage. It has good p-type conductivity and it can be processed with low-cost methods such as electrodeposition[40], thus meeting all the necessary criteria for a promising photocathode, except for one - stability in aqueous environment.

Recently a multilayer configuration was presented, using Cu_2O as the photoactive material, which addressed the instability problem of this material under working conditions[40,51]. The samples were prepared on gold coated F:SnO_2 (FTO) glass substrates. The photoelectrode consisted of a photovoltaic p–n junction of p-type Cu_2O and n-type Al:ZnO (AZO) coated with a TiO_2 protective layer, and activated for hydrogen evolution

with electrodeposited Pt nanoparticles, producing photocurrents up to -7.6 mA·cm^{-2}, under simulated solar AM 1.5 illumination when biased at 0 V_{RHE}[40]. Despite the conformal protective layer of TiO_2 deposited by atomic layer deposition (ALD), a decay of performance over the first 20 minutes was observed. No evidence of Cu_2O degradation was observed and the photocurrent decline was attributed to electron traps in the protective TiO_2 aggravated by its amorphous state. Although stability was still far from ideal, this configuration revealed a new strategy that inspired the investigation to improve overlayers for better stability.

In a first approach, higher deposition temperature of the TiO_2 ALD deposited layer revealed stability improvements[51]. In that work, deposition of the TiO_2 layer at 150 °C enhanced the stability of the resulting photocathode when compared to the lower deposition temperature (120 °C). Furthermore, in recent work, given the detachment of the platinum from the surface of the photocathode upon illumination, RuO_x as a co-catalyst was investigated[32]. RuO_x is more resistant to heavy metal ion poisoning from impurities[125] in the electrolyte and the porous electrodeposited film provides a high surface area that is crucial for an efficient charge extraction from the TiO_2 underlayer[32]. This co-catalyst yielded a stable photocurrent of -5 mA·cm^{-2} when biased at 0 V_{RHE} during 8 h of light chopping[32]. The improved catalyst/TiO_2 interface allowed a record-breaking stability of Cu_2O-based photocathodes for water reduction.

From these previous reports, an understanding of the influence of the TiO_2 synthesis conditions on the photocathode stability was developed. An alternative approach for further improving the photoelectrode stability targets improving the quality of the TiO_2 protective layer with post-synthetic treatments. Heating the samples at high temperatures ($\sim$ 400 °C) could convert the amorphous TiO_2 to a crystalline phase, which is expected to be more stable in the slightly acidic aqueous electrolyte. However, as annealing temperatures increase above 200 °C, the performance of the photocathode is diminished, perhaps due to loss of the doping in the cuprous oxide, which is based on copper vacancies.

In this chapter, a new low temperature steam treatment for improving the stability of Cu_2O-based photoelectrodes protected with largely amorphous TiO_2 layers is addressed. Post-synthetic treatments at temperatures not higher than 150 °C revealed large improvements in the photocathode stability with no loss in performance. Morphological and crystallographic properties were investigated to understand the steam treatment influence on the materials. This treatment was tested with different co-catalysts and reproducible results were observed. Photocurrents over -5 mA·cm^{-2} were achieved with only 10 % loss over its initial photocurrent value during more than 50 h of light chopping (biased at 0 V_{RHE}).

2.2 Experimental details

2.2.1 Electrodeposition of Cuprous Oxide

The working electrodes were fabricated on Au-coated TEC-15 F:SnO_2 substrates (FTO, NSG glass). FTO-glass was cut into 1 x 3 cm^2 pieces and then cleaned by sonication sequentially in soapy water (15 min), acetone (15 min), ethanol (15 min), and finally distilled water (15 min). The substrates were then dried under a stream of compressed air gas to remove any liquid and a 10 nm chromium adhesion layer was deposited by sputtering followed by a 150 nm layer of gold. These thin layers serve as better interface for the semiconductor deposition and form a desirable ohmic contact with Cu_2O.

The Cu_2O thin films were electrodeposited from a basic solution of lactate-stabilized copper sulphate (pH = 12) at 30 °C, as described previously[50]. A 1 x 1 cm^2 area was left un-deposited to serve as electric contact for the experimental characterizations. The deposition conditions were optimized previously and a galvanostatic electrodeposition was performed using a two-electrode configuration with Pt mesh as counter electrode for 105 min at -0.1 $mA{\cdot}cm^{-2}$, resulting in a Cu_2O thickness of roughly 500 nm, as confirmed by cross sectional scanning electron microscope (SEM) – Figure 2.1.

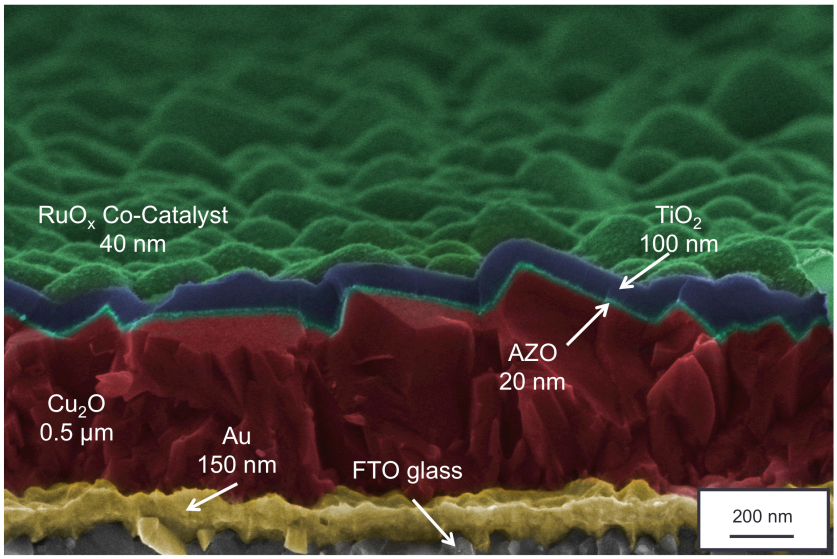

Figure 2.1 – Cross-sectional SEM image of a photocathode with respective ALD layer thicknesses.

2.2.2 Overlayer Deposition

Very thin n-type oxide overlayers were deposited on top of the Cu_2O using a thermal ALD system (Savannah 100, Cambridge Nanotech). The exposed Au substrate was masked with Kapton® tape and the samples were rinsed in DI water and dried with compressed air prior to the deposition. The AZO (20 nm) and TiO_2 (100 nm) were deposited as described previously[32]. Briefly, AZO was deposited on a substrate temperature of 120 °C using diethylzinc, trimethylaluminum and H_2O as the Zn, Al and O precursors,

respectively. Each precursor was held in the chamber for 2.0 seconds, followed by a 15.0 second nitrogen purge. For each cycle of trimethylaluminum and water there were 20 cycles of diethylzinc and water. TiO_2 was deposited on a substrate temperature of 150 °C using tetrakis(dimethylamino)titanium, TDMAT (99.99 %, Aldrich), at a precursor temperature of 75 °C, and hydrogen peroxide (50 % in water, stabilized, Aldrich) at room temperature. TiO_2 was deposited in pulse mode under a nitrogen flow of 5 sccm, with a pulse length of 0.1 s and wait period of 10 seconds for both precursors.

2.2.3 Steam Treatment Optimization

The steam treatment was carried out in a 100 ml Teflon autoclave. To identify the optimum conditions for the annealing of Cu_2O (500 nm)/AZO (20 nm)/TiO_2 (100 nm) samples to increase stability, a systematic study of the effect of multiple variables was carried out. The amount of water, treatment duration and annealing temperature were varied and an optimum range of values identified. The samples were very sensitive to the amount of water in the autoclave, and they would easily dissolve at high temperatures. A small volume (200 μL) of water was added to the autoclave and the sample was suspended in the vapor phase to avoid direct contact with water.

In order to identify the range of temperature and duration of the steam treatment, a screening design was conducted between temperature, T, $\in$ [100, 300] °C and time, t, $\in$ [1, 8] h. Prior to the response surface methodology (RSM) analysis, screening samples were created to identify the limit values for water content in the autoclave and the maximum temperature and time for the annealing. Different volumes of water were tested (0.2 to 30 mL) with the sample in direct contact with the water. Upon removal from the autoclave, the samples were completely deteriorated and in the cases of higher water content, only the gold remained in the FTO substrate. We therefore suspended the sample in the autoclave, using a small flask and a cork, and for the smaller water vapour pressures the samples remained macroscopically unchanged. For temperatures above 150 °C and durations longer than 3 h the performance of the photocathodes was impaired (see examples in Figure 2.2). For lower temperature and duration, no significant change was observed when compared to untreated samples. A careful variation of the T and t intervals with no sample deterioration was conducted with T between 100 °C and 150 °C and t between 1 h and 3 h. Table 2.1 shows the parameter values for each experiment. The heating and cooling ramps were fixed at 6 °C·min^{-1}.

2.2.4 Co-Catalyst deposition

For the photoelectrochemical tests, RuO_x and Pt catalysts were used, as described previously[32]. Briefly, RuO_x was deposited by galvanostatic photodeposition using a 1.3 mM aqueous solution of $KRuO_4$ and a current density of -28.3 μA·cm^{-2} for 15 min under simulated one sun illumination. Pt was deposited using the same technique with 1

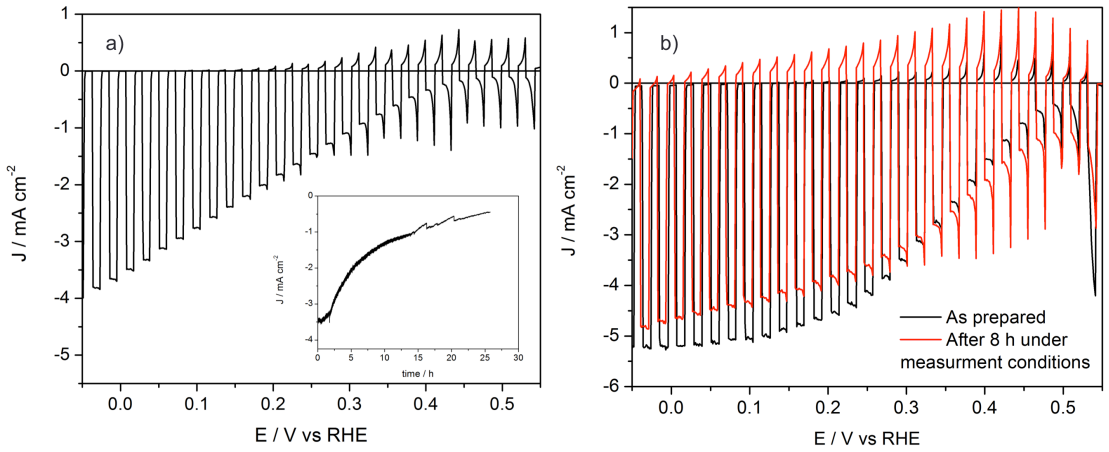

Figure 2.2 – Current-voltage characteristics at extreme temperature and duration of steam treatment conditions: a) 180 °C for 1 h; b) 5 h at 150 °C.

Table 2.1 – CCD factors and respective levels.

Run #	Actual values	
	T **(°C)**	***t*** **(h)**
1	150	2
2	125	1
3	100	3
4	125	2
5	125	2
6	125	3
7	150	1
8	100	1
9	100	2
10	150	3

mM solution of H_2PtCl_6 and a current density of -8.5 μA·cm^{-2} for 15 min under simulated one sun illumination.

2.2.5 Thin Film Characterization

High-resolution scanning electron microscopy (both a FEI XL30 SFEG and also a Zeiss Merlin instrument) with a field emission source operated at 5 kV and a through-the-lens detector for secondary electrons was used to study the morphology of the photocathodes. The crystallinity was evaluated with a Bruker D8 Discover diffractometer, using monochromatic Cu Kα1 radiation (1.540598 Å). The Bragg reflections were compared with values from the literature[126]. Raman scattering measurements were made using a 532 nm wavelength laser beam and were acquired with a Labram HR800 model of Jobin-Yvon Horiba spectrometer equipped with a microscope for collection of backscattered Raman signals and phonon modes compared with references[127,128]. The thickness and *n*, *k* parameters of the ALD titania layer were evaluated using spectroscopic ellipsometry (Sopra GES 5E). The range of photo energies used in the study was between 1.5 and 5.5 eV. The obtained spectra were fitted using a Tauc Lorentz dispersion law (WinELI software) to extract the thickness and *n*, *k* parameters

of the deposited TiO_2 layers. Transmission electron microscopy (TEM) measurements were carried out with a Technai Osisris (FEI, USA) in dark field and bright field mode. An acceleration voltage of 200 kV was applied. A 10 μm selected area aperture was used to obtain diffraction patterns of a single layer. The camera length was 330 mm. Cross-section lamellae for TEM were prepared with a Zeiss NVision 40 CrossBeam with focused ion beam (FIB). Diffraction patterns were simulated with JEMS (Version 4.1520, CIME, EPFL, Switzerland).

2.2.6 Photoelectrochemical measurements

The photoelectrochemical performance of the photocathodes was studied using an Ivium Potentiostat/Galvanostat to acquire the photoresponse under chopped irradiation from a 450 W Xe-lamp (Osram, ozone-free) equipped with an IR/UV filter (KG3 filter, 3 mm, Schott), calibrated with a silicon diode in order to simulate AM 1.5 illumination (100 $mW{\cdot}cm^{-2}$). A scan rate of 10 $mV{\cdot}s^{-1}$ in the cathodic direction was used to acquire the current-voltage data.

Measurements were carried out in a three-electrode configuration with the Cu_2O photocathodes as working electrode, a Pt wire as counter-electrode and Ag/AgCl/Sat. KCl as reference electrode, in an electrolyte solution of 0.5 M Na_2SO_4 and 0.1 M KH_2PO_4 at pH 5.0. The electrolyte was continuously sparged with nitrogen gas to remove dissolved oxygen.

2.3 Results and Discussion

2.3.1 Steam Treatment Optimization

TiO_2 proved to be an efficient protective overlayer for Cu_2O photocathodes in previous occasions[31,32,40]. Nevertheless, the stability of this photocathode is still far from that required for commercial implementation. The biggest limitation in these systems results from electron trapping in the amorphous TiO_2 layer, likely compensated by proton intercalation. It was hypothesized that a crystalline overlayer would be more robust, and thus fabrication of a system with a crystalline TiO_2 overlayer was sought. It is possible to grow crystalline TiO_2 by ALD[129]. However, heating the Cu_2O/AZO junction to these temperatures (over 200 °C) hinders the photoelectrochemical performance significantly[51]. Post-synthetic heat treatments on a hot plate or in a tubular furnace, in both atmospheric and inert environment led to similar deterioration of the performance. Thus a low temperature method to alter the overlayer protective properties without damaging the photovoltaic properties of the semiconductor underlayers was investigated.

Hydrothermal treatments have been proven to be useful in the crystallization of oxide films[130], including TiO_2[131], and commonly require temperatures less than 200 °C. Hydrothermal post-synthetic heat treatments were thus investigated. We

found that the oxide materials were sometimes partially or completely dissolved when completely submerged in water in the autoclave at modest temperatures (150 °C). We therefore experimented with steam treatments in which only small amounts of water were added, and care was taken to keep liquid water from contacting the photoelectrode. A systematic study on the temperature and duration of the steam treatment was performed and the key current-voltage characteristics presented in Table 2.2. The plateau photocurrent and onset potential show no specific trend with steam treatment conditions and the observed variations can be attributed to sample-to-sample variation. On the other hand, stability (hereafter evaluated in terms of the time necessary for the photocurrent to decrease by 10 % under continuous illumination conditions) reveals a clear relation with steam treatment parameters (Figure 2.3). An analysis of variance (ANOVA) was performed and parameters with p-values smaller than 0.05 were considered to have significant contribution for the model. The stability showed a correlation with the studied parameters with determination coefficient R^2 = 0.97 (Figure 2.4).

Table 2.2 – Observed values of process responses. Stability is evaluated under continuous illumination measurement conditions.

Run #	Plateau (mA·cm^{-2})	Onset (V_{RHE})	10 % loss (h)
1	5.5	0.55	18
2	4.6	0.53	2
3	5.5	0.61	15
4	4.7	0.58	10
5	5.2	0.50	12
6	5.7	0.57	16
7	5.7	0.63	14
8	4.8	0.58	1
9	4.8	0.61	5
10	5.4	0.52	27

Between 100 °C and 150 °C, a constant increase in stability with temperature and duration of steam treatment is observed (Figure 2.3). This is in accordance to what we expected since higher temperatures and annealing times should be related to a higher degree of crystallization. However, at temperatures greater than 150 °C or duration longer than 3 h a steep decrease in performance is observed due to the negative impact on the photovoltaic properties of the semiconducting underlayers. We believe that at high temperatures the doping levels of Cu_2O (which are based on copper vacancies) are altered, thus affecting the performance.

The highest stability was achieved at 150 °C for 3 h and the corresponding sample is characterized in Figure 2.5 and compared with a photocathode with no steam treatment. The onset is not significantly improved but a plateau photocurrent increase between 2 % and 10 % is observed in the steam treatment case (Figure 2.5a). We previously reported the activation of the photoelectrodeposited catalyst after a few linear sweeps, accompanied with a fill factor improvement[32]. With steam treatment, under measurement conditions, not only does the fill factor increase, with a steep photocurrent

increase at ~ 0.5 V_{RHE}, but also the onset is shifted anodically by 70 mV (Figure 2.5b). The stability is greatly enhanced, recording only 10 % loss over 50 h biased at 0 V_{RHE} in pH 5.0 phosphate–sulfate electrolyte under light chopping (Figure 2.5c). This is by far the most stable Cu_2O photocathode reported to date.

2.3.2 Crystallographic Characterization

These results motivated us to study the reason for the improved performance. Park *et al.* reported on the crystallization of semiconductor thin films with hydrothermal treatments[130]. Improved crystallinity in the TiO_2 would explain the superior performance as it is more resistant to electro trapping and/or etching in the slightly acidic medium. XRD and Raman spectra were obtained on photocathodes with different steam treatments to search for crystalline phases (Figure 2.6). XRD spectra were unable to identify any TiO_2 crystallization, even for samples that were subjected to extreme conditions, and were quite similar to photocathodes with no steam treatment[51]. Raman spectroscopy showed very broad bands at 397, 518 and 639 cm^{-1} that could correspond to anatase phase, but are too faint to suggest crystallinity of the TiO_2 unambiguously. Given the rough nature of the photocathode surface and the coincidental Bragg diffraction peaks of different layers, any crystallization of the TiO_2 protective layer is inconclusive. Therefore, grazing-incidence XRD (GIXRD) was performed on a TiO_2-coated quartz substrate (100 nm TiO_2) with the source tilted at 1 °C to eliminate any contribution from the remaining layers of the photocathode, and revealed that the TiO_2 was amorphous after the steam treatment at 150 °C for 3 h (Figure 2.7a).

These two techniques have proven that no major crystalline transition on the TiO_2 is obtained with these steam treatment conditions. Even so, small crystalline domains or a

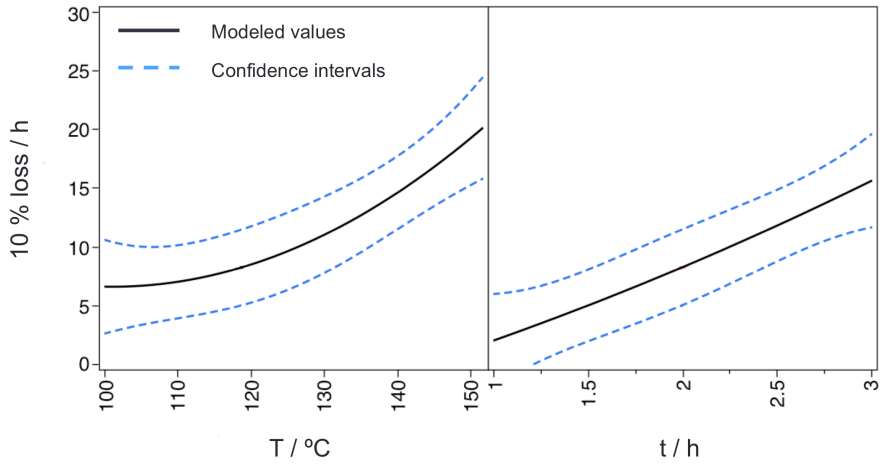

Figure 2.3 – Stability variation with steam treatment temperature (°C) and duration (h). Stability is evaluated–under continuous illumination measurement conditions–as the time it takes for the initial photocurrent to drop to 90 % of its initial value (a 10 % loss). The black lines represent prediction profiles extracted from a statistical analysis on performed measurements and the blue dashed lines represent the corresponding confidence intervals.

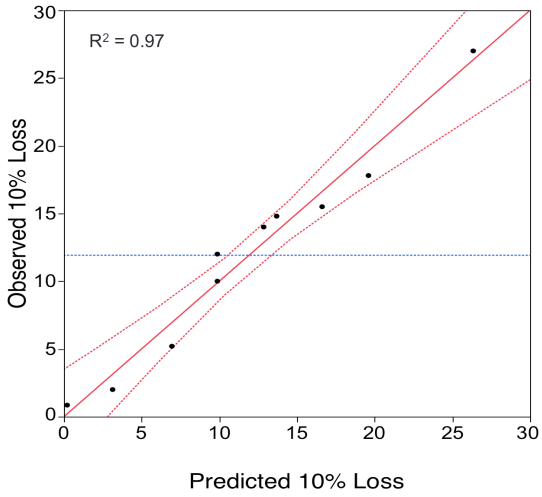

Figure 2.4 – Analysis of variance of the modeled stability response with the respective R^2.

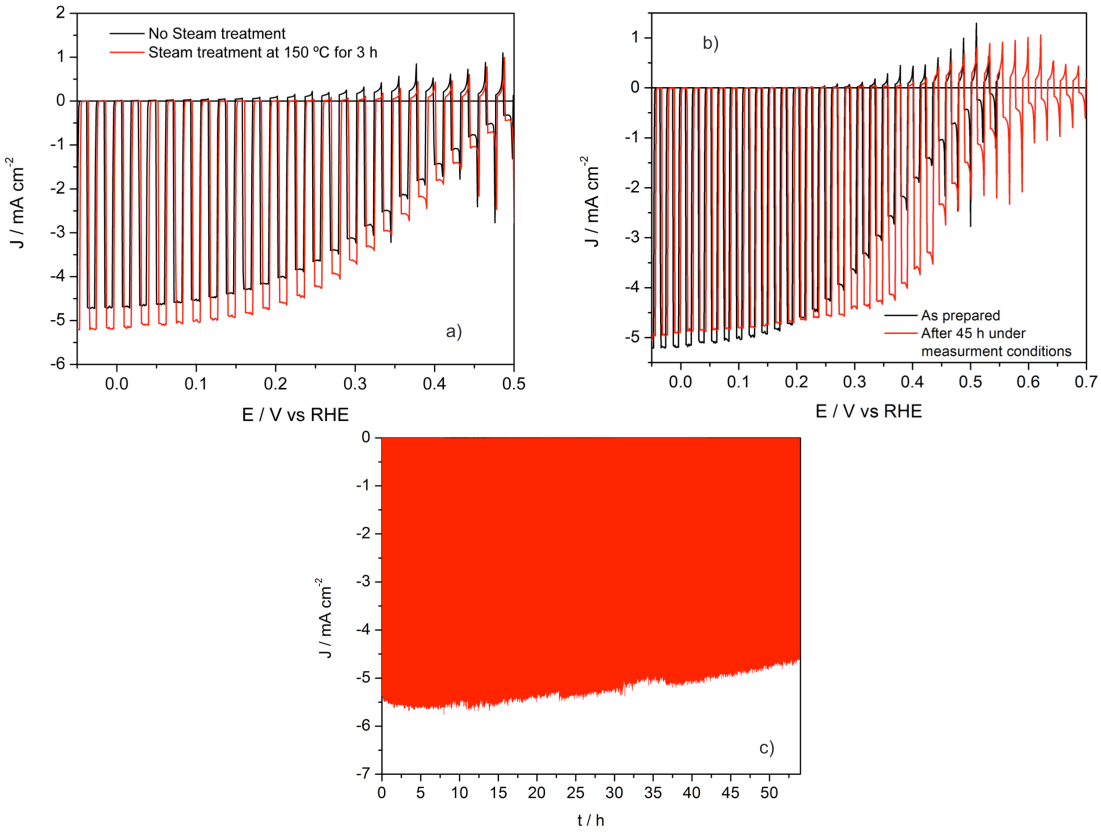

Figure 2.5 – Current-voltage characteristics of a composite Cu_2O photocathode: a) comparison between the performance of a photocathode as prepared and with steam treatment at 150 °C for 3h, b) linear sweep of the photocathode with steam treatment before and after 45 h stability measurement under light chopping and c) chronoamperometric stability measurement biased at 0 V_{RHE}. All measurements were carried out in pH 5.0 phosphate–sulfate electrolyte under light chopping.

surface crystallization (on the order of a few atomic layers) could be forming and not be detected by these techniques. Ellipsometry was performed on samples of 100 nm ALD TiO_2 on Si wafer substrates (Figure 2.7b) to search for density modifications usually

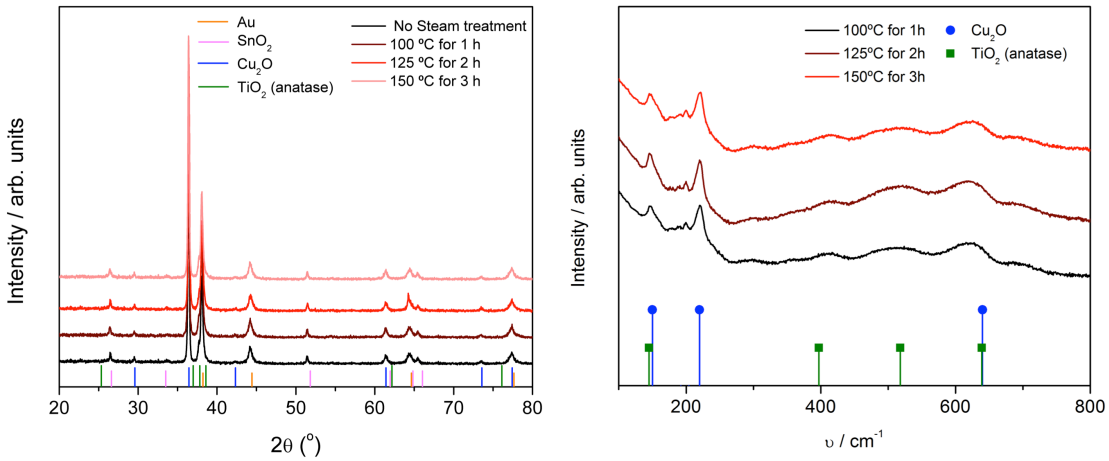

Figure 2.6 – X-ray diffraction patterns with corresponding layer Bragg reflections (left) and Raman spectra with phonon modes of Cu_2O and TiO_2 of steam treatment samples with different conditions (right).

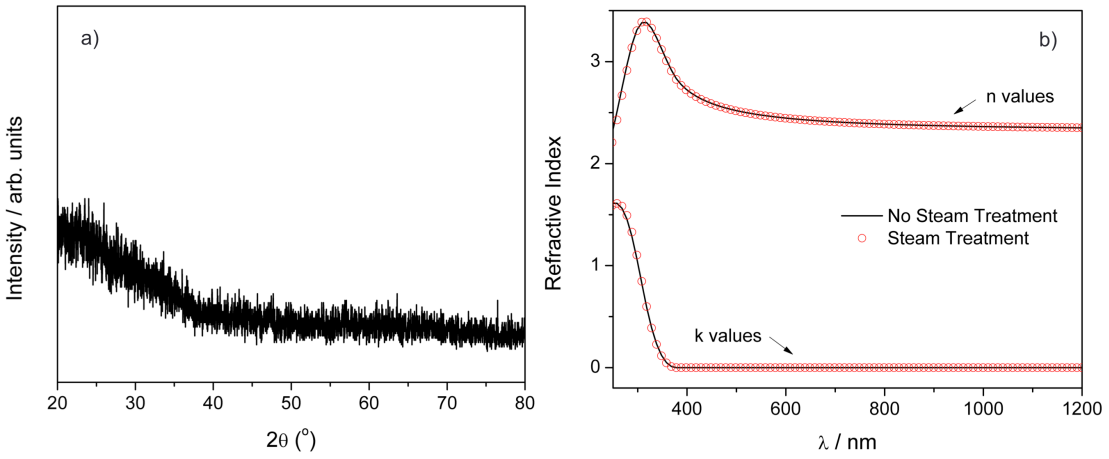

Figure 2.7 – a) GIXRD on a TiO_2 (100 nm), deposited on glass substrate, after the steam treatment at 150 °C for 3 h; b) Ellipsometry measurements of TiO_2 film on a silicon wafer before and after steam treatment at 150 °C for 3 h.

observed in crystallizations. No densification was observed with the steam treatment, expected for an amorphous to crystalline transition[51]. Since XRD measurements extract a diffraction pattern from all layers, we chose TEM to selectively investigate the TiO_2 layer more precisely. Figure 2.8a shows the bright field image of the hydrothermally treated electrode cross-section where the red circle marks the position seen in the dark field (DF) image (Figure 2.8b). The DF image was obtained from the selected area diffraction pattern (SADP) shown at the bottom of Figure 2.8c, and obtained from the selected area shown in the inset of Figure 2.8a. The SADP was analyzed using ring patterns simulated in JEMS. This analysis shows the presence of anatase as well as brookite, however, with these few reflections it is difficult to assign the rings accurately. The diffraction pattern confirms that the TiO_2 layer is largely amorphous and has only few crystalline domains. These crystalline domains visible in DF image (Figure 2.8b),

reveal crystallinity present in our hydrothermally treated TiO_2 overlayer, which could not be resolved in XRD nor in ellipsometric surface density measurements. However, following the same TEM analysis for the reference sample, a similar diffraction pattern was found (inset of Figure 2.8d) and crystalline domains are shown to be present as well in the DF image (Figure 2.8d). Thus, it could not be concluded that the steam treatment can largely crystallize our ALD grown TiO_2 overlayer. Since these crystalline domains have the size of the thickness of the layer it is most probable that they were grown epitaxial during the deposition.

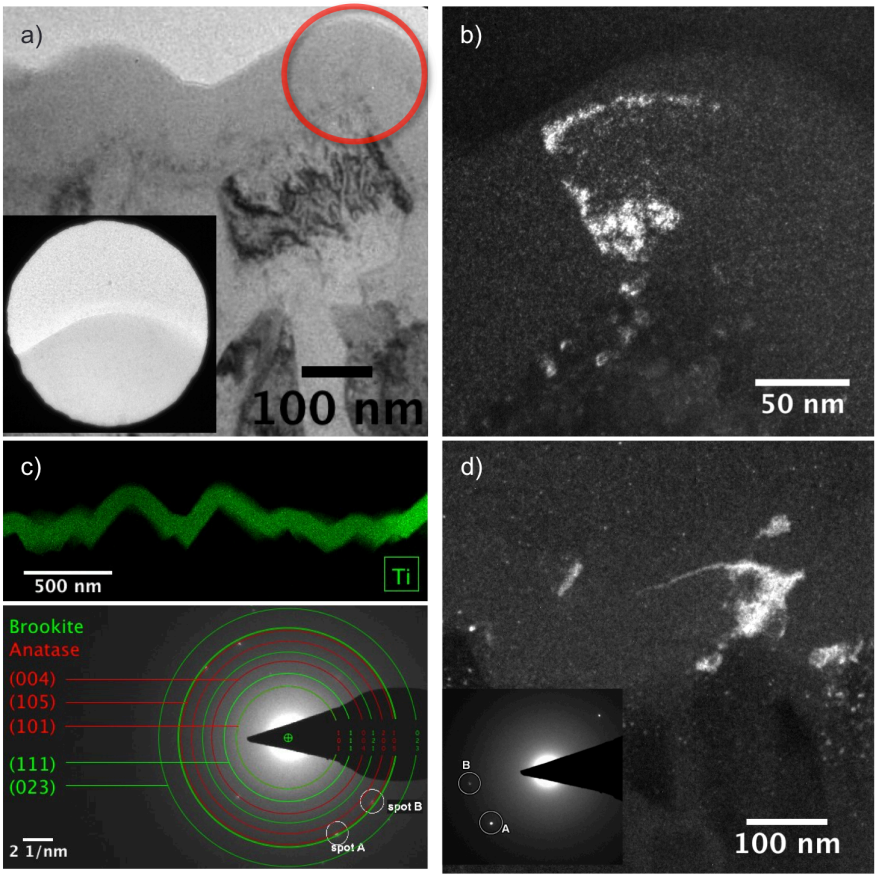

Figure 2.8 – TEM analysis on the hydrothermally treated sample compared to the reference sample. a) Bright field image of the hydrothermal treatment electrode cross-section (from top to bottom: amorphous carbon/TiO_2/AZO/Cu_2O). The inset shows the area selected by the aperture for the diffraction pattern shown at the bottom of (c). b) Dark field image of the position marked in red in (a) and obtained from spot B in the diffraction pattern in (c). Crystalline domains are visible in the TiO_2 layer and small crystallites in the ZnO layer underneath. c) Top: Energy-dispersive X-ray spectroscopy (EDX) analysis of the TiO_2 layer showing homogenous coverage trough the film. Bottom: Selected area diffraction pattern of TiO_2 shown in the inset of (a). Spot B (anatase (105) plane) was used for the dark field image in (b). d) Dark field image of the reference sample without hydrothermal treatment obtained from Spot A in the inset.

2.3.3 Electrical Properties

Previously, we showed that improvement of the electrical properties of the protective layers can enhance stability by decreasing recombination and electron traps[32,51]. In

TiO_2, oxygen vacancies are charge balanced by Ti^{3+} states that absorb light, and can act as recombination centers. In order to see if the steam treatment changes the defect chemistry of the TiO_2 by eliminating oxygen vacancies, we studied the donor density by Mott-Schottky (Figure 2.9). We can observe, from Table 2.3, that there is no significant difference in the flatband potential between samples with/without steam treatment. We note a slight decrease in the donor density after steam treatment, which is likely due to the filling of oxygen vacancies in the TiO_2 by oxygen in the autoclave during the annealing treatment. However, it is unclear how this relatively modest change could result in the dramatic improvements in the stability that we observe in the photocathodes.

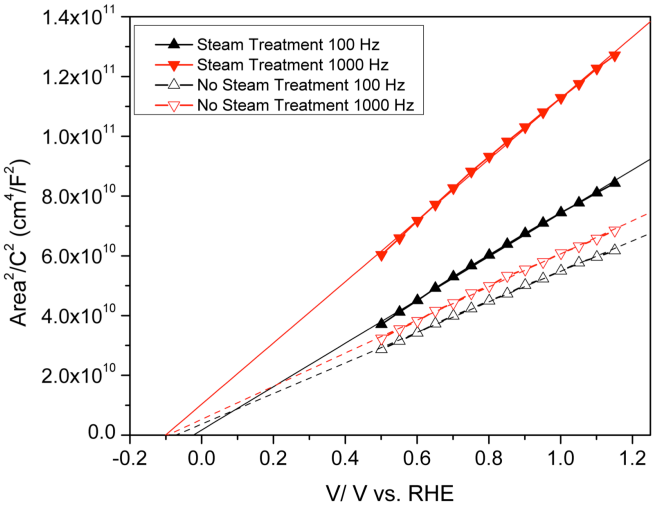

Figure 2.9 – Mott-Schottky plot of TiO_2 films prepared with hydrogen peroxide precursor on FTO, measured in 1 M NaOH electrolyte. Steam conditions were 150 °C for 3 h.

Table 2.3 – Comparison of electrical properties of the TiO_2 films with/ without steam treatment. Flatband and donor density extracted according to the Mott–Schottky equation[31]. [a] Reference values from reference 32.

Treatment	E_{FB} (V_{RHE})	N_D (cm^{-3})
No steam treatment[a]	-0.10	3.5×10^{19}
Steam treatment for 3 h at 150 °C	-0.09	2.2×10^{19}

2.3.4 Surface modification

With no clear changes in the crystallinity or the band alignment of the TiO_2 overlayer, we decided to take a closer look at the morphology. Under the conditions of the steam treatment (water vapor under pressure), the surface of the TiO_2 will undergo a continuous modification due to the repeated cleavage and condensation of Ti-O-Ti bonds in lesser-strained forms (surface relaxation). This bond modification is usually associated with a smoothing of the surface[131–133]. Figure 2.10 shows the surface morphology of the TiO_2 overlayer prior to and after a steam treatment. It is clear that a morphological change has occurred. Prior to treatment the TiO_2 reveals a significant

roughness with a grainy structure whereas the steam treatment gave a much more smooth surface. The thickness profile of the TiO_2 protective layer was also studied by cross-sectional TEM. Different thicknesses of the TiO_2 layer were measured along the surface and a clear trend was identified. In agreement with a previous literature report, the thickness of the TiO_2 on top of underlayer grain boundaries is larger and at the grain tips is smaller[134]. Before steam treatment, at the Cu_2O grain boundaries (represented in red in Figure 2.10c) the TiO_2 is thicker than at the grain tips with an average difference of 26 nm. After steam treatment the thickness is much more equally distributed with a thickness standard deviation of σ = 3 nm.

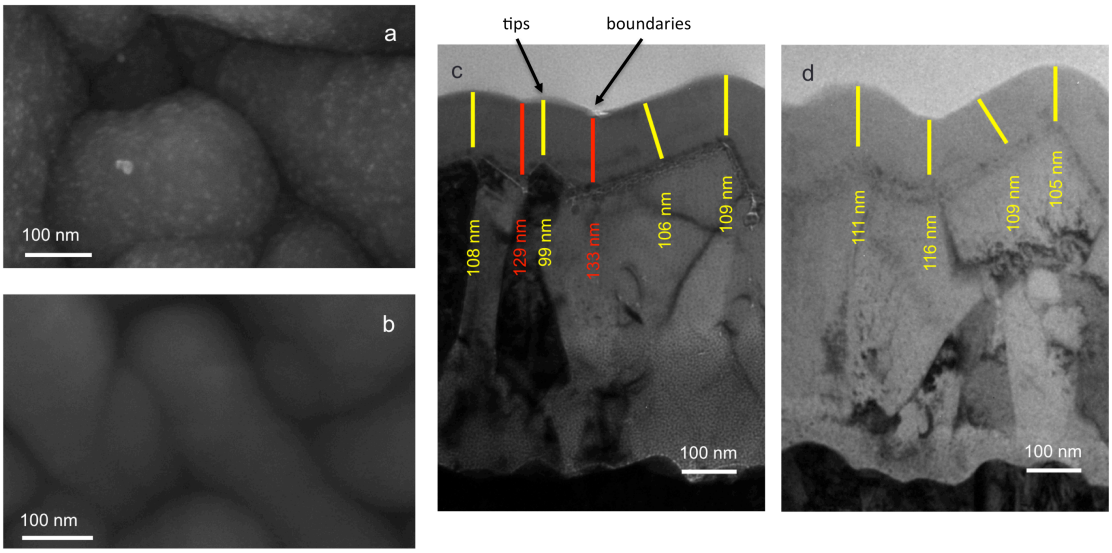

Figure 2.10 – Surface morphology of the TiO_2 overlayer (left) and TEM cross-section (right) of an as prepared sample (a,c) and a sample with steam treatment at 150 °C for 3 h (b,d). It is clear that the surface experienced major morphological changes upon steam treatment. The TiO_2 thickness was measured in different places of both samples and the larger thicknesses (boundaries) are marked in red and lower thicknesses (tips) marked in yellow.

This smoothing process likely patches any defects and cracks in the TiO_2 surface as well as improves the quality of the surface for a more homogeneous catalyst deposition. In our system, electrodeposition consists of the formation of a layer onto a conducting substrate occurring through the electrochemical reduction of higher valence ions dissolved in a suitable aqueous solvent. As electrons flow through the substrate they are transferred to the ions in solution near the surface promoting their reduction and precipitation forming a film. When the substrate is a conducting metal (resistivity on the order of 10^{-9} Ωm), electrons flow easily to the surface and are readily available to assist electrodeposition evenly across the surface. On the other hand, when the substrate is several orders of magnitude less conductive, thickness variations on the order of a few nanometers have a large influence on the potential distribution across the surface, resulting in heterogeneous electrodeposition, as the authors verified in previous reports[135–137]. Since TiO_2 is not a conductor ($\rho \sim 1 - 10$ Ωm)[138], the rough surface of the amorphous TiO_2 creates an irregular current density distribution across the surface,

yielding a granular RuO_x co-catalyst structure, typical in non-uniform electrodeposition (Figure 2.11a). As the surface smooths, the current distribution becomes more regular and the co-catalyst is more homogeneous (Figure 2.11b). Homogeneous deposition of catalyst on the surface ensures that injected photoelectrons in the TiO_2 will be efficiently extracted, thus minimizing the likelihood of electron trapping in the overlayer. Also, the smoothing and healing of small cracks in the overlayer prevent direct contact of the electrolyte with the Cu_2O layer, greatly increasing the stability of the system.

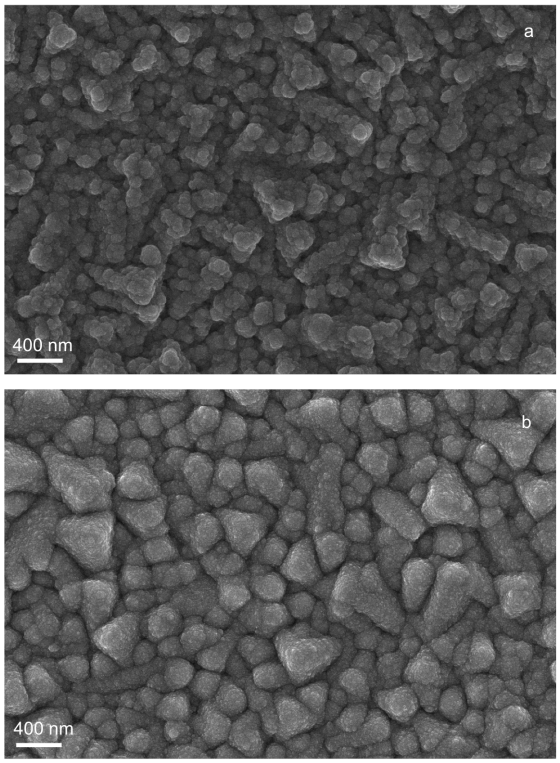

Figure 2.11 – Photocathode SEM top view after RuO_x electrodeposition a) no steam treatment and b) after steam treatment at 150 °C for 3 h.

The surface morphology of the photocathode is again modified upon deposition of the RuO_x (Figure 2.12) offering a higher surface area than the smooth TiO_2 layer, a clear advantage for catalysis. We also studied the morphology of the catalyst after a long term stability measurement. After 20 h under continuous illumination conditions, it appears that the catalyst has undergone a large morphological change, becoming pasty and cracked (Figure 2.12e and f). It appears that under extended hydrogen evolution conditions, the surface continues to rearrange and to smoothen. The cracks that are observed in the SEM images likely occur only after drying in the high vacuum conditions of the SEM.

To support our theory regarding homogeneous electrodeposition, we tested a Pt co-catalyst. Pt is expected to be less stable than RuO_x, as previous results indicated[32], but we expected that a more homogeneous catalytic layer of Pt on top of the TiO_2 would facilitate charge extraction and therefore increase stability. A comparison between both

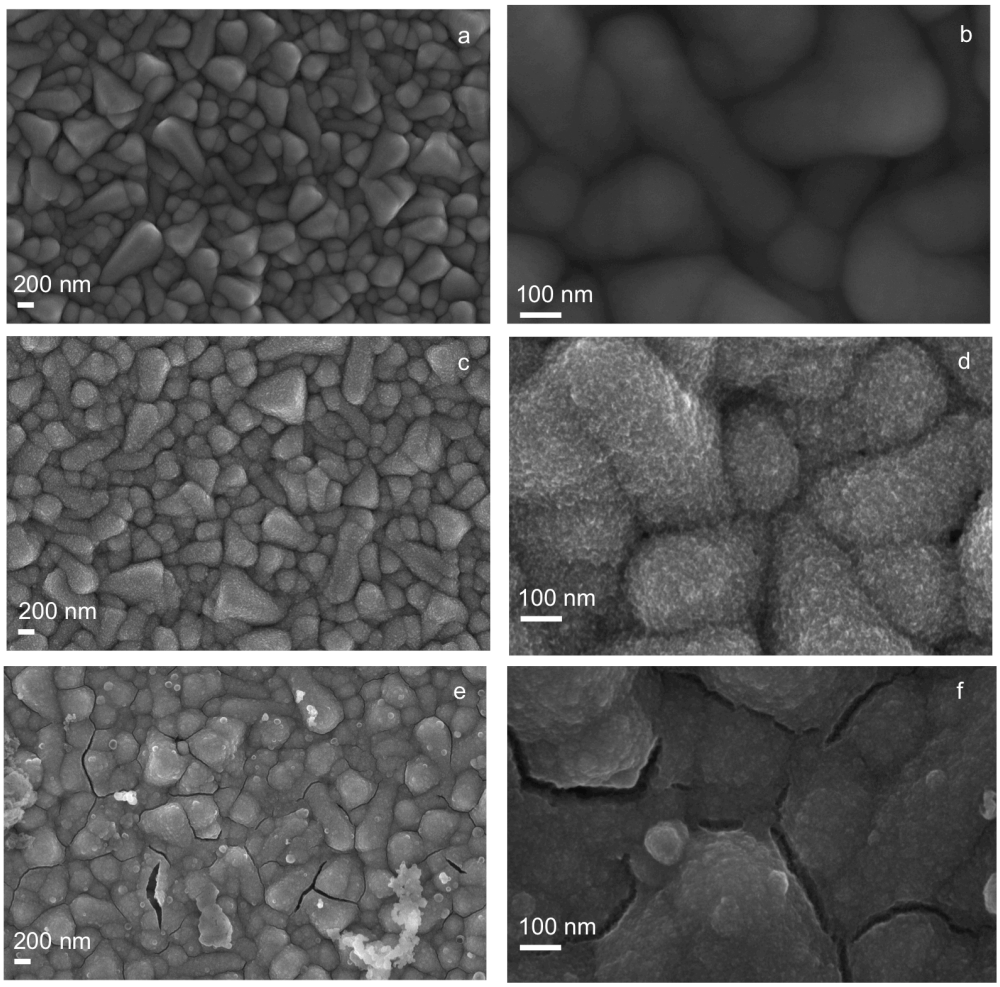

Figure 2.12 – SEM top view a, b) TiO_2 after steam treatment at 150 °C for 3 h; c, d) photo-assisted electrodeposited RuO_x catalyst; e, f) active area after 20 h under illumination conditions.

catalysts is represented in Figure 2.13. We observed an onset potential of +0.64 V_{RHE} and a plateau photocurrent of greater than –5.5 $mA{\cdot}cm^{-2}$ at 0 V_{RHE} (Figure 2.13a). With a plateau photocurrent 10 % greater than the RuO_x and a significant shift in the onset, this represents a major step forward for unbiased photoelectrochemical tandem systems. The stability for both catalysts is presented in Figure 2.13b and c. As expected, the Pt was less stable than the RuO_x catalyst, yet is vastly superior to previous photocathodes employing Pt catalyst. With 10 % loss after 20 h stability measurement biased at 0 V_{RHE} in pH 5.0 phosphate–sulfate electrolyte under light chopping, this level of stability represents an improvement of 2000 % over previous results[51].

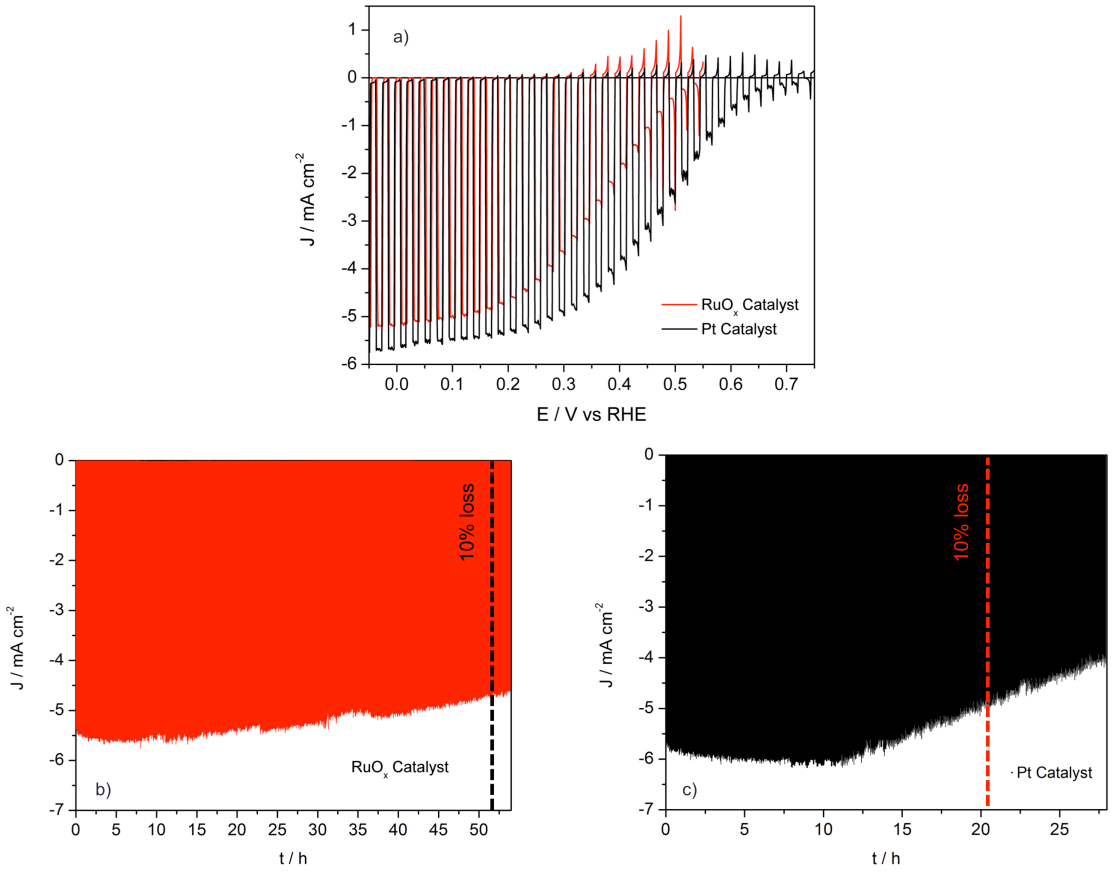

Figure 2.13 – Current-voltage characteristics of a composite Cu_2O photocathode after steam treatment at 150 °C for 3 h: a) comparison between performance of a photocathode with RuO_x and Pt as catalyst; chronoamperometric stability measurement biased at 0 V_{RHE} in pH 5.0 phosphate–sulfate electrolyte under light chopping b) with RuO_x and c) Pt as catalyst.

2.4 Conclusions

A simple low cost solution was developed to greatly enhance Cu_2O photocathode stability. Post-synthetic annealing under steam atmosphere was optimized for Cu_2O/AZO/TiO_2 composite photocathodes and 10 % photocurrent loss over its initial value during more than 50 h of light chopping (biased at 0 V_{RHE}) was achieved. Crystallographic and electronic analysis revealed no significant changes in the materials. TEM analysis shows a smoothness of the TiO_2 surface and healing of small cracks in the overlayer, providing a better protection for the underlying Cu_2O. This hypothesis was tested with two different co-catalysts (RuO_x and Pt) and both yielded better stabilities with the steam treated samples. Not only did we obtain record breaking stabilities in both cases, we also uncovered the critical importance of morphological changes of the surface in generating these high-stability photocathodes. The steam treatment should also be broadly applicable to materials other than TiO_2.

CHAPTER 3

Tin Oxide as Stable Protective Layer for Composite Cuprous Oxide Water-Splitting Photocathodes

This chapter is dedicated to a novel strategy for protecting cuprous oxide from photocorrosion, wherein a thin SnO_2 overlayer enables increased stability over previous reports utilizing TiO_2 protective layers. This strategy can be applied to other materials as well as a TiO_2 replacement. Performance and stability are influenced by the film thickness, post-deposition steam treatment, and the nature of the heterojunction interface. A maximum stability of 57 h of sustained photoelectrochemical water reduction, maintaining 90 % of its initial photocurrent, is achieved.

This chapter is adapted from the published work:
J. Azevedo, S. David Tilley, M. Schreier, M. Stefik, C. T. Sousa, J. P. Araújo, A. Mendes, M. Graetzel and M. T. Mayer, *Nano Energy*, 2016, 24, 10-16.

The author contributed to the planning and execution of all the experiments described in this chapter, except: XRD, Raman and SEM measurements which were carried out by Stefik, M and Mayer M.T. Faradaic efficiency measurements were carried out by Schreier M. The author was also involved on the discussion and interpretation of all results, as well as on the preparation of the manuscript.

3.1 Background

Since unprotected Cu_2O is highly unstable, different strategies have been investigated to protect this material[50,139–141]. Paracchino *et al.* reported a multilayer configuration consisting of a p-n junction between p-type Cu_2O and n-type AZO covered by a thin TiO_2 layer to prevent direct contact of the junction with the aqueous environment[40]. This configuration yielded stable photocurrents for 1 hour, upon which would decrease rapidly to near zero values. More recently, Tilley *et al.* were able to extend the stability of this photocathode by using an amorphous RuO_2 layer as a catalyst replacement for Pt[32]. This way, not only was it possible to sustain high photocurrents with $\sim$ 100 % Faradaic efficiency but also to extend the photocathode stability up to 4 h under

continuous illumination. Furthermore, in a subsequent report by the same authors, a simple steam treatment applied to the photocathode presented a ground-breaking stability enhancement; it preserved 90 % of initial photocurrent under chopped AM 1.5 illumination over 25 h (biased at 0 V_{RHE} in pH 5 electrolyte)[142].

These works proved that through improvement of the protective layers, major stability enhancements could be achieved. To be efficient, the protective layer needs to exhibit several characteristics, such as favorable energy band alignment with the Cu_2O, good electrochemical reaction rate and no corrosive side reactions should occur at potentials in the bandgap[40].

In theory, TiO_2 fulfills the necessary requirements for a good protective layer but, as observed by Paracchino *et al.*, the deposition of a TiO_2 on Cu_2O without any intermediate layer yields very low photocurrents and is highly unstable[40]. This indicates that TiO_2 does not by itself fully prevent the photocorrosion of the photocathode. Given the low photocurrent inherent to this Cu_2O/TiO_2 configuration, poor charge separation at the semiconductor interface must be promoting recombination and side reactions like Cu_2O reduction[51].

The usage of AZO interlayer provides a better interface (as evidenced by its use in heterojunction solar cells) with good charge extraction through the p-n junction between the p-type Cu_2O and n-type AZO. When annealed at 400 °C, a TiO_2 thin film shows excellent stabilities over days[143]. However, heating the Cu_2O/AZO junction over 200 °C decreases dramatically the photoelectrochemical performance[27]. A breakthrough is necessary to achieve much higher stabilities before Cu_2O photocathodes can be viable for commercial application.

The next step to enhance the stability of Cu_2O photocathodes is to implement protective layers different from the conventional TiO_2. Among semiconductors available that could conformably deposited by ALD, tin dioxide (SnO_2) gathers all the necessary requirements. SnO_2 is a wide band gap (3.6 eV) semiconductor with a low n-type resistivity, high transparency, earth abundant and easily applicable over large surfaces[144–146]. SnO_2 has been used as protective layer in other occasions but until now was not explored as a stand-alone protective layer for semiconductor photoelectrodes[147,148].

This chapter reports on the performance and stability of Cu_2O photocathodes protected by a SnO_2 layer for solar water splitting. Photocurrents over -4 $mA{\cdot}cm^{-2}$ were achieved and a seven-fold stability improvement over TiO_2 was observed. Furthermore, different treatments and thickness were tested to further improve the stability of this composite $Cu_2O/SnO_2/RuO_2$ photocathode and the interface between materials is discussed. A maximum stability of 57 h, with 10 % photocurrent drop used as reference, under continuous illumination conditions was achieved. The proposed approach has the potential to tackle the stability issue of other nonstable photoelectrodes and thus can make a significant contribution in the field of photoelectrochemical energy conversion.

3.2 Experimental details

3.2.1 Sample Preparation

Electrodeposited Cu_2O samples were prepared on FTO glass as described in chapter 2. Since Cu_2O suffers from severe photocorrosion in aqueous environments it was protected by n–type semiconductor overlayers deposited by ALD using a thermal ALD system (Savannah 100, Cambridge Nanotech). Prior to deposition, samples were cleaned with DI water and a small portion of the sample was covered with Kapton® tape to preserve the gold contact uncovered. Two different configurations were tested: $Cu_2O/ZnO/SnO_2/RuO_2$ and $Cu_2O/SnO_2/RuO_2$. The deposition parameters of ZnO are described in previous reports (single pulse was used in this work)[32,40]. SnO_2 was deposited at 110 °C using tetrakis(dimethylamino)tin(IV) (TDMASn, ABCR). The ALD procedure was adapted from previous reports on tin oxide[149]. The deposition was done in pulse mode under ultra pure nitrogen flow rate at 20 sccm. One single cycle of SnO_2 was made: close, 0.5 s TDMASn pulse, 10 s delay, open, 17 s delay, close, 0.015 s O_3 pulse, 10 s delay, open, 17 s delay. The growth rate was determined using spectroscopic ellipsometry (Sopra GES 5E) on samples grown on Si wafers. The range of photo energies used in the study was between 1.5 and 5.5 eV and the obtained spectra were fitted using Tauc Lorentz dispersion law (WinELI software) to extract the thickness. The growth per cycle of SnO_2 was estimated at 0.1 nm·cycle^{-1}. RuO_2 co-catalyst was electrodeposited as described in chapter 2. A digital photograph of a representative sample can be observed in Figure 3.1.

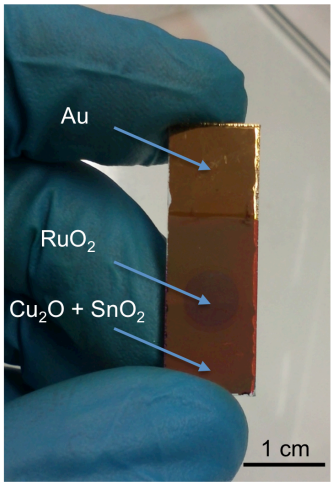

Figure 3.1 – A digital photograph of a representative $Au/Cu_2O/SnO_2/RuO_2$ photocathode.

3.2.2 Thin Film Characterization

A high-resolution scanning electron microscope (Xeiss Merlin) with a through-the-lens detector for secondary electrons was used to evaluate the morphology of the samples

using an accelerating voltage of 3 kV (surface) and 5 kV (cross section). The cross section images were taken on freshly cleaved samples. The crystallinity was evaluated with a Bruker D8 Discover diffractometer, using monochromatic Cu Kα1 radiation (1.540598 Å) at a scan rate of 0.06 deg·min^{-1} with step width of 0.02°, and the Bragg reflections matched with the American Mineralogist Crystal Structure Database. Raman spectra were made using a 532 nm wavelength laser beam and were acquired with a Labram HR800 model of Jobin–Yvon Horiba spectrometer equipped with a microscope for collection of backscattered Raman signals. Phonon modes were compared with literature.

3.2.3 Photoelectrochemical Measurements

The photoelectrode response of the photocathodes was measured in a standard three-electrode configuration using a Pt mesh as the counter electrode and an Ag/AgCl/Sat. KCl for reference electrode, connected to an Ivium Potentiostat/Galvanostat. The measurements were made in an electrolyte solution of 0.5 M Na_2SO_4 buffered with 0.1 M KH_2PO_4 to obtain pH = 5.

The photoresponse was measured under chopped irradiation using the light source described above. The scan rate for the linear sweep voltammetry was 10 mV·s^{-1} in the negative direction. The electrolyte was previously sparged in nitrogen and sparging was maintained during measurements to remove oxygen bubbles formed during the tests. In the long stability tests sparging was stopped to avoid electrolyte evaporation.

IPCE measurements were performed under light from a 300 W xenon lamp with integrated parabolic reflector (Cermax PE 300 BUV) passing through a monochromator (Bausch & Lomb, bandwidth 10 nm FWHM). Comparison with a calibrated Si photodiode allowed the calculation of the IPCE.

3.2.4 Faradaic Efficiency

Faradaic efficiency measurements were carried out in a custom-made gastight PEC cell, equipped with diaphragms (Metrohm, Switzerland) separating the counter and reference compartments from the working electrode compartment. A Ag/AgCl (KCl sat.) electrode (Metrohm, Switzerland) was used as reference and a Pt wire as counter electrode. The active sample surface was defined by covering excess sample surface with hot glue. Thus prepared samples were fixed into the cell that was mounted on a laboratory shaker (IKA KS 130 basic, 400 rpm) to improve equilibration between all phases in the system. The cell was filled with the pH 5 electrolyte described above and samples were polarized at 0 V_{RHE} using an Iviumstat Potentiostat (Ivium, Netherlands). The cell was illuminated by a collimated LED light source (Thorlabs MCWHL5) of which the photon flux in the absorption range of Cu_2O has been tuned to match the flux of the AM 1.5 spectrum. Ar (99.998 %, Carbagas, Switzerland) at a flow rate of 6.8 mL·min^{-1} was sparged into

the electrolyte solution and 5 mL aliquots of outflowing gas were periodically collected and analyzed by gas chromatography (Thermo Trace ULTRA, Restek ShinCarbon ST 80/100 2m, He carrier, PDD detector). Calibration was carried out by polarizing a flamed Pt wire at a series of galvanostatic currents.

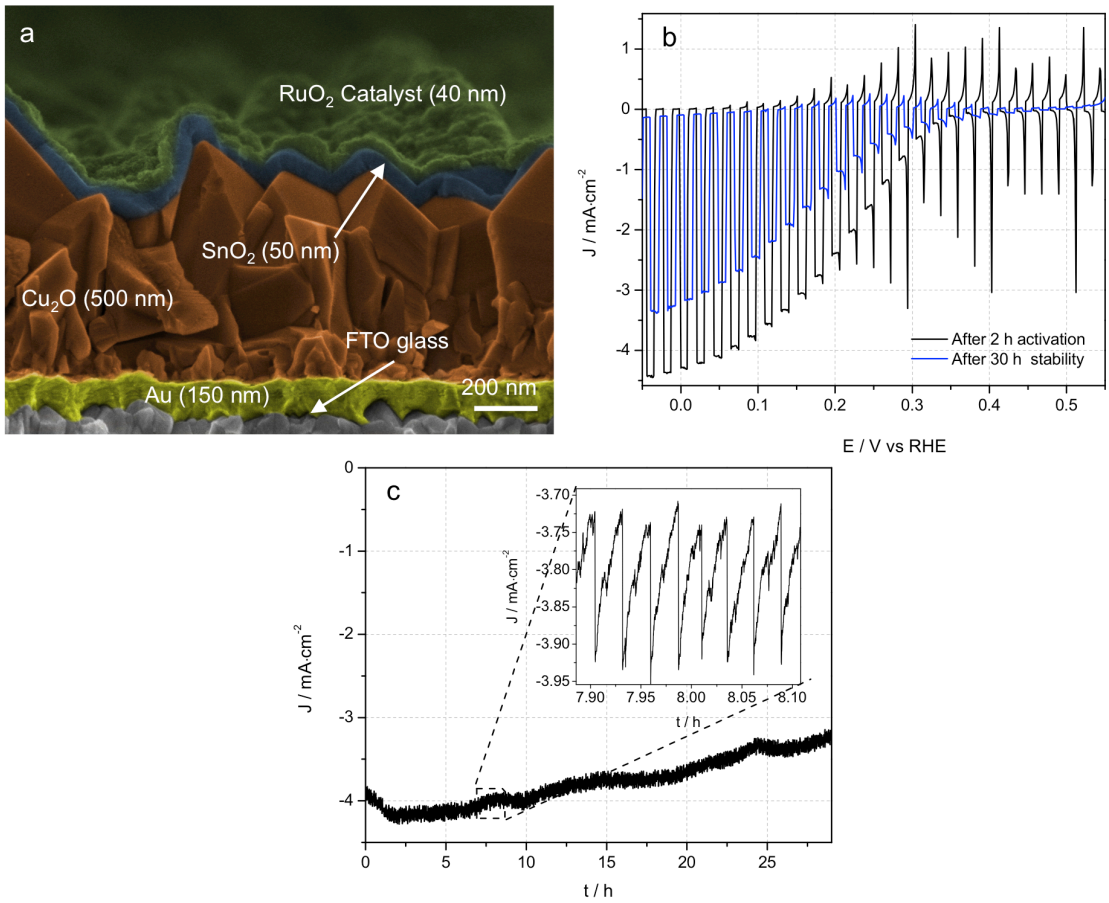

Figure 3.2 – a) Cross-sectional SEM image of a photocathode with respective ALD layer thicknesses. b) Current-potential characteristics of a composite $Cu_2O/SnO_2/RuO_2$ photocathode under chopped simulated sunlight illumination: performance comparison between a photocathode after 2 h activation and 30 h stability measurement (biased at 0 V_{RHE} in pH = 5.0 phosphate-sulfate electrolyte). c) Chronoamperometric stability measurement biased at 0 V_{RHE} under continuous illumination. The inset shows small fluctuations in the measured current due to gas bubble evolution, trapping (loss of surface area), and eventual escape (surface area recovered).

3.3 Results and Discussion

3.3.1 SnO_2 Protective Layer

From the SEM image of the cross section of the photocathode (Figure 3.2a) it is possible to observe that the SnO_2 overlayer is 50 nm thick and the deposition is homogeneous and dense, as expected from the ALD technique. A dense overlayer is crucial for protection as it provides better isolation from the electrolyte. The Cu_2O/SnO_2 configuration with RuO_x surface catalyst shows a plateau photocurrent close to -

4.5 mA·cm^{-2} at 0 V_{RHE} with an onset at +0.34 V_{RHE} (Figure 3.2b), corresponding to more than twice the photocurrent reported for a TiO_2 overlayer on top of Cu_2O[40].

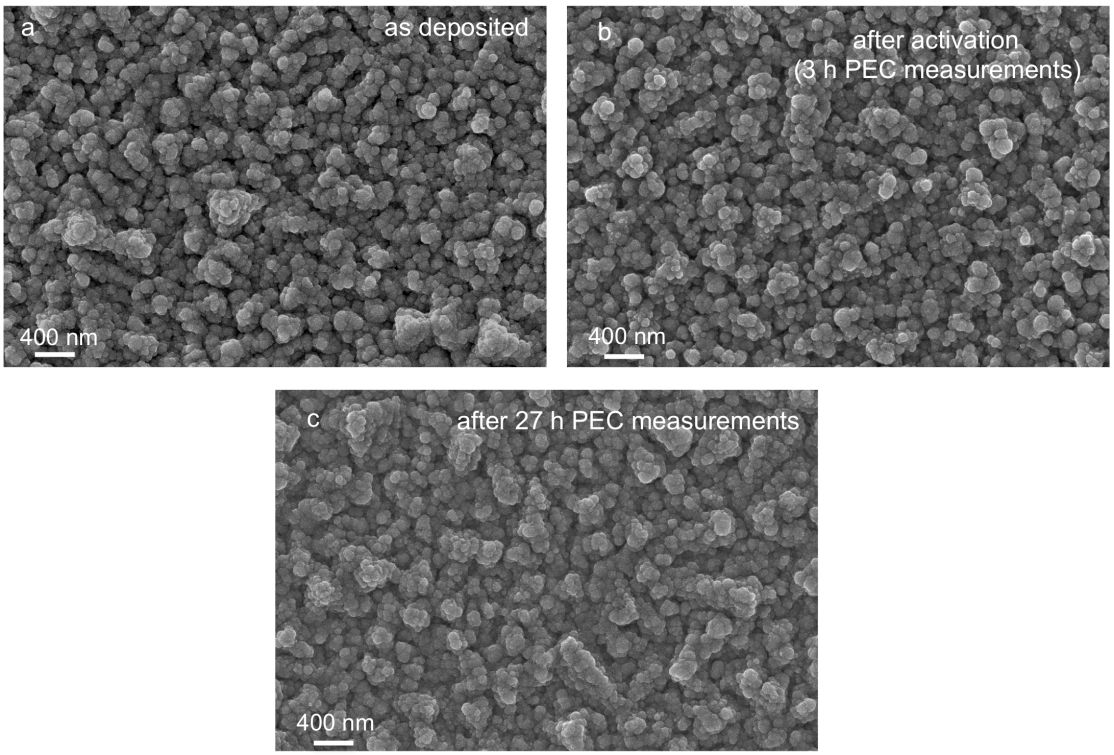

Figure 3.3 – SEM top view of a photocathode with photo-assisted electrodeposited RuO_2 catalyst a) as deposited, b) after 3 h and c) 27 h under illumination at 0 V_{RHE} bias.

The stability was assessed under 1 sun illumination during 30 h (Figure 3.2c). The noisy photocurrent during measurement results from the hydrogen evolution at the photocathode and temporary hydrogen bubbles accumulating on the photoelectrode surface (Figure 3.2c onset). After 30 h biased at 0 V_{RHE}, 90 % of the photoelectrode initial photocurrent is preserved (Figure 3.2b). This new protective overlayer is a major improvement over previous reported results with no need for an interfacial layer. To confirm the stability of the developed photocathode, the surface of the Cu_2O/SnO_2 samples was studied in SEM images taken at different stages of the stability test. Figure 3.3 shows images acquired after three different durations of stability testing; no significant morphologic differences can be observed besides a slight smoothing of the RuO_x surface after 27 h.

The current-voltage characteristics and stability curves of Cu_2O photocathodes coated with different SnO_2 overlayer thicknesses (20 nm, 50 nm and 100 nm) were compared (Figure 3.4). The samples with the 20 nm of SnO_2 show a current density decrease after the stability test of ca. 20 % and a later onset potential; whereas higher thicknesses present a higher current density and a much higher stability preserving 80 % of its initial plateau current after 45 h. These results show that SnO_2 can be optimized to improve stability by depositing thicker layers without losing performance.

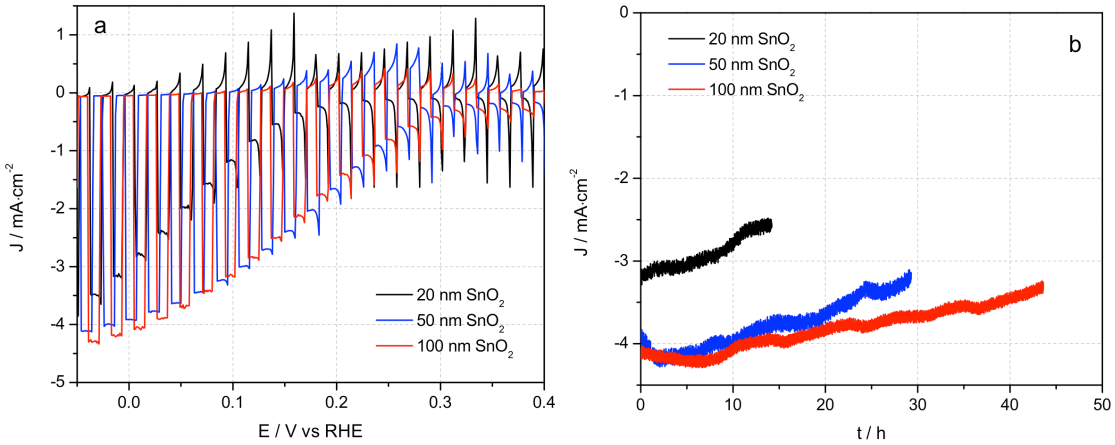

Figure 3.4 – a) Current-voltage characteristics of a composite $Cu_2O/SnO_2/RuO_2$ photocathode with different SnO_2 thicknesses: comparison between the performance of the photocathodes with SnO_2 layer thicknesses of 20, 50 and 100 nm; b) corresponding stability measurements under illumination and 0 V_{RHE} bias. All measurements were carried out in pH 5.0 phosphate–sulfate electrolyte.

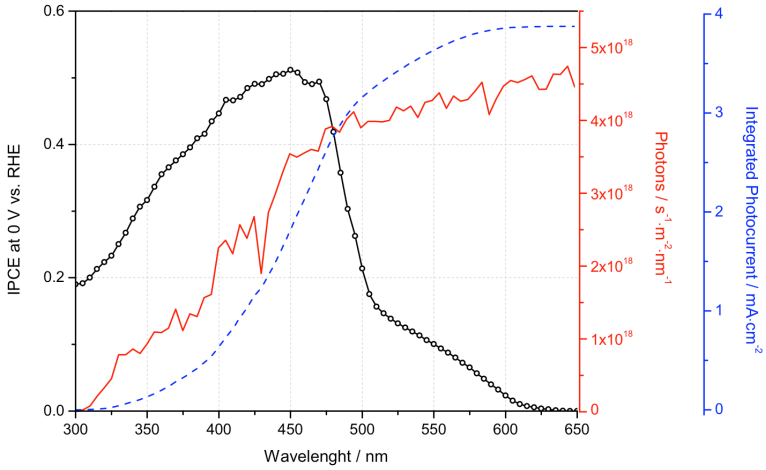

Figure 3.5 – IPCE of a photocathode biased at 0 V_{RHE} in standard pH 5.0 electrolyte. Integration of the IPCE values with the solar AM 1.5 spectrum gives the same photocurrent value as is typically observed under simulated one sun illumination.

3.3.2 Quantum Efficiency and Crystallographic Characterization

The IPCE of the most stable photocathode (with 100 nm SnO_2) was determined, as shown in Figure 3.5. In the visible region between 380 and 480 nm the IPCE exceeded 40 %. Above 480 nm the IPCE values drop quickly. This behavior is in accordance with the band structure of Cu_2O. The lowest fundamental absorption transition in Cu_2O is $\Gamma_7^+ \rightarrow \Gamma_6^+$ (2.0 eV), at the Γ-point of the Brillouin zone, corresponding to 620 nm, which is parity forbidden[48]. The integration of the IPCE spectrum yielded 3.8 mA·cm^{-2} , the same value obtained with the photoelectrode under simulated 1 sun illumination.

The SnO_2 layer was investigated to understand the stability improvements. The degree of crystallization was examined through XRD and Raman spectroscopy (Figure 3.6) and no clear indication of a SnO_2 crystalline phases in the protective layer was

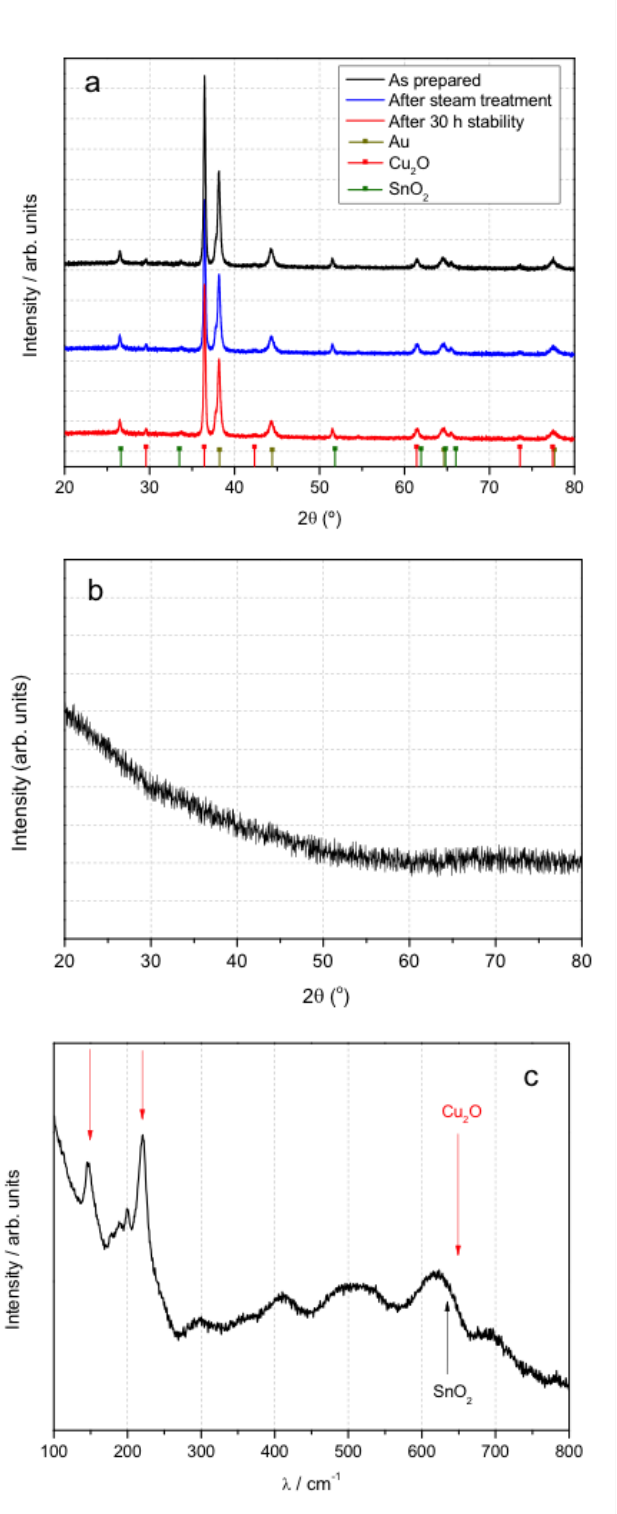

Figure 3.6 – a) X-ray diffraction patterns with corresponding layer Bragg reflections; b) grazing angle XRD for 50 nm of ALD SnO_2 grown at 110 °C atop on optically polished silicon; c) Raman spectra with phonon modes of Cu_2O and SnO_2 of a photocathode with Cu_2O/SnO_2 configuration.

observed. The multilayered structure of the photocathode makes it difficult to isolate the Bragg diffraction peaks of the different materials and we hypothesize that all SnO_2 Bragg

peaks identified in Figure 3.6a correspond actually to the FTO substrate. A grazing angle XRD (Figure 3.6b) was performed to eliminate the contribution from subjacent layers and also shows no sign of crystallinity, in agreement with the Raman results (Figure 3.6c). XRD results showed no signs of decomposition of the Cu_2O after the 30 h stability test, when compared to previous reports on unprotected samples where decomposition was observed by XRD[40].

3.3.3 Thickness Variation and Steam Treatment

Cross section images of the SnO_2 thin layer (Figure 3.7a) display a dense and crack-free coating, as expected from the ALD deposition. Although the thickness of the SnO_2

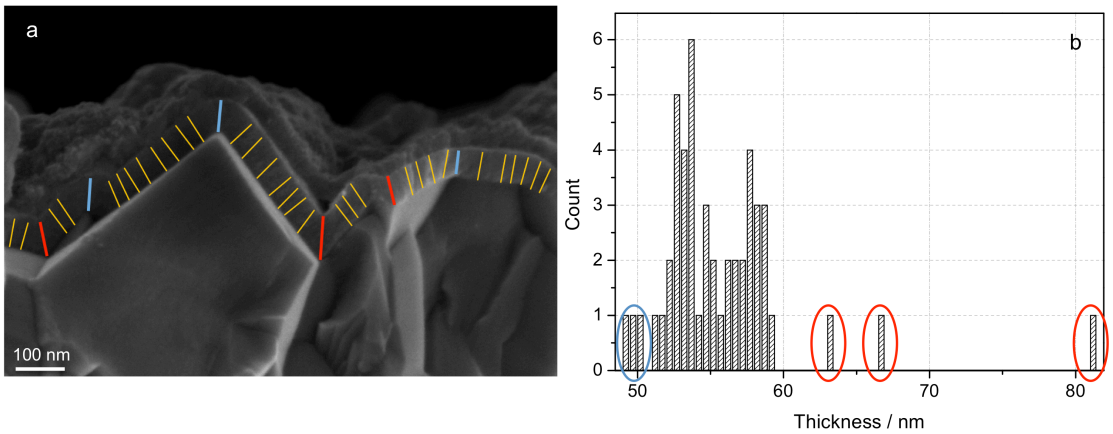

Figure 3.7 – a) Cross-sectional SEM image of a photocathode and b) respective SnO_2 layer thickness distribution along the sample. Average thickness of 53 nm and maximum (red) and minimum (blue) thicknesses occur at the marked positions in (a).

is very homogeneous a small variation is observed from the Cu_2O grain tips to the grain boundaries, typical in ALD deposition on a microcrystalline surface[134,142]. In fact, larger thicknesses at the grain boundaries and more constant thicknesses elsewhere are observed (Figure 3.7b). Previous reports show that a thickness variation, even small, does not offer optimum conditions for the electrodeposition of co-catalysts[142]. An easy way to reduce the thickness variation is by a simple low temperature steam treatment, as previously reported[142]. Three different temperatures were tested (100 °C, 125 °C and 150 °C) and their performances compared by current-voltage characteristics and stability curves – Figure 3.8. No significant changes in plateau photocurrent or onset were observed, as expected, since the sample did not suffer any major morphological or structural changes. At 100 °C there were no significant changes in stability attributed to the unaltered surface at such low temperature treatment. Nevertheless, as the steam temperature increases, the stability shows significant improvements and a maximum stability of 90 % of its initial plateau current after 57 h biased at 0 V_{RHE} was observed, with no loss in peak photocurrent or fill factor. This is a major improvement over previous reports with TiO_2 protective layer[32,40,51,142].

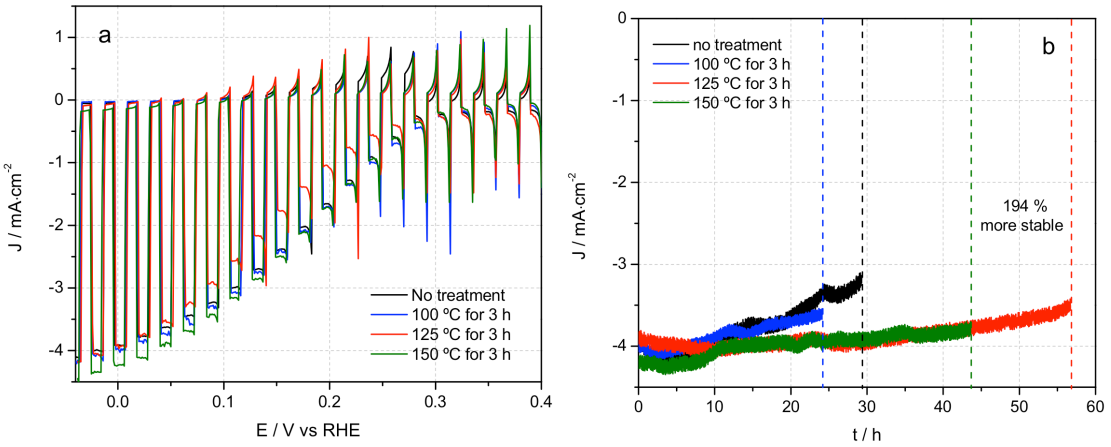

Figure 3.8 – a) Current-potential characteristics of composite $Cu_2O/SnO_2/RuO_2$ photocathode samples with different steam treatment conditions: without treatment and with steam treatment at temperatures of 100, 125 and 150 °C. (b) Corresponding stability measurements under continuous illumination and biased at 0 V_{RHE}. All measurements were carried out in pH 5.0 phosphate–sulfate electrolyte.

Predicted potential-pH phase diagrams shown in Figure 3.9 reveal the thermodynamic behaviors of Ti and Sn oxides under water reduction conditions. Both TiO_2 and SnO_2 are the predicted stable phases at 0 V_{RHE} in pH = 5 solutions, providing little insight into the reason for the observed stability enhancement of SnO_2. For both overlayer materials, post-deposition steam treatments led to significantly improved stabilities, treatments which are believed to decrease the density of defects such as cracks and pinholes and thereby better protect the underlying layers from corrosion[142]. It is therefore likely that the superior quality of ALD deposited and steam annealed SnO_2 contributed to the stability reported here. Further analysis of the degradation mechanisms of both device types is the topic of ongoing work. Nevertheless, we confirmed that the observed photocurrents corresponded to unity Faradaic yields for H_2 evolution, as measured by gas chromatography and presented in Figure 3.10.

3.3.4 ZnO interfacial layer

Another aspect that can be improved in the Cu_2O/SnO_2 configuration is the interface between the active semiconductor, Cu_2O, and the protective layer, SnO_2[40,150]. ZnO is known to provide a good interface between Cu_2O and TiO_2 probably providing a more hydroxylated surface for TiO_2 to grow on and forming a local electrostatic field at the Cu_2O/ZnO p–n junction assisting in extracting photogenerated electrons[40,51]. The significant improvements that a ZnO thin film implemented below the TiO_2 overlayer motivated us to test the same approach in the SnO_2 system. A single ALD pulse cycle of ZnO was applied between the two semiconductor layers and the samples were characterized – Figure 3.11.

The performance of the $Cu_2O/ZnO/SnO_2/RuO_2$ configuration was better with an onset at +0.55 V_{RHE} and a plateau photocurrent around -4.4 mA·cm^{-2} at 0 V_{RHE}

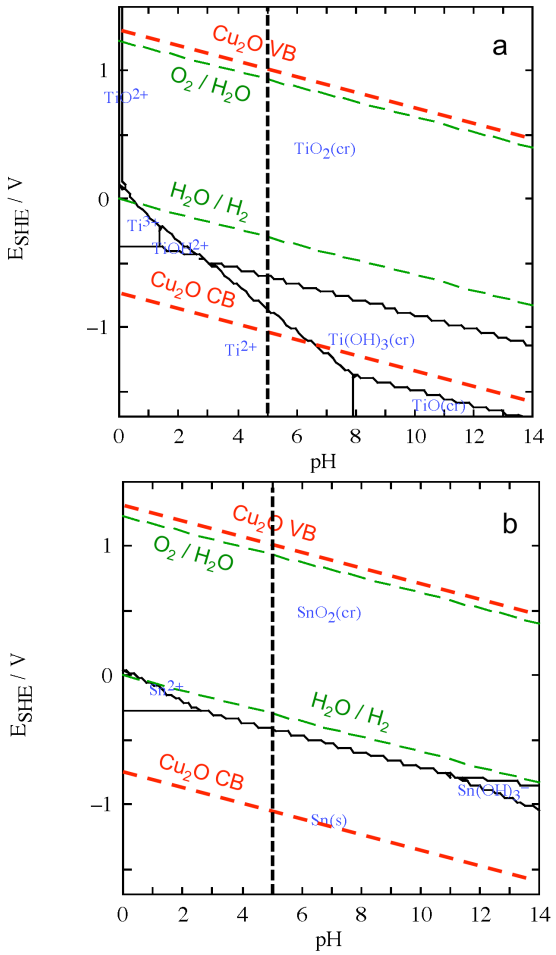

Figure 3.9 – Pourbaix diagram for a) TiO_2 and b) SnO_2 in 0.5 M Na_2SO_4 electrolyte at T = 25 °C, for $[Ti^{2+}] = [Sn^{2+}] = 10\ \mu M$. Generated using Medusa (http://www.kemi.kth.se/medusa/).

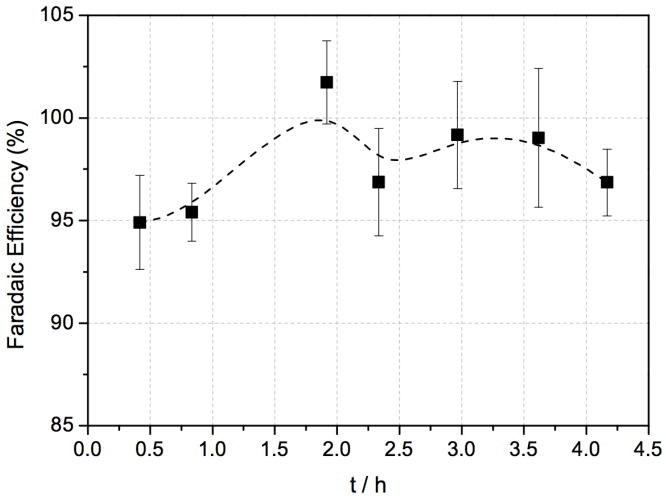

Figure 3.10 – Faradaic efficiency measurement for a $Cu_2O/SnO_2/RuO_2$ photocathode under continuous illumination at 0 V_{RHE} in standard pH 5.0 electrolyte, which confirms 100 % Faradaic efficiency for hydrogen generation.

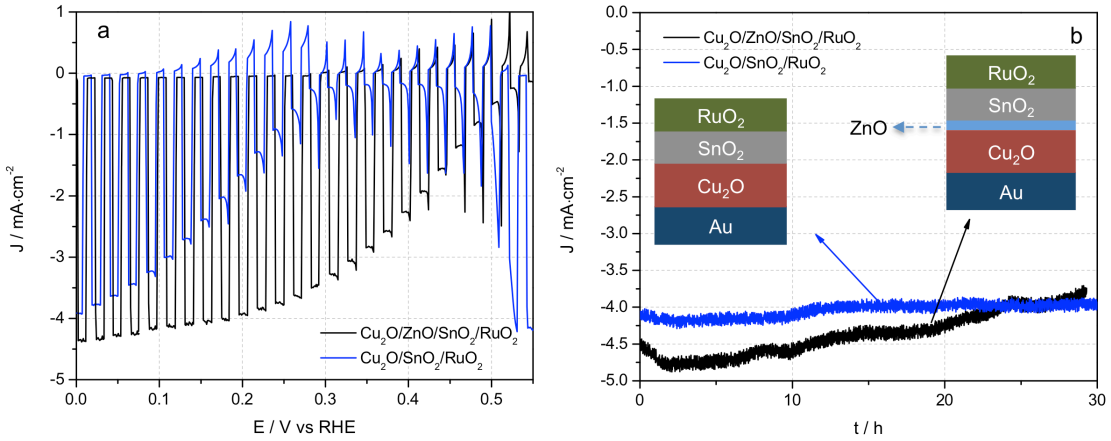

Figure 3.11 – Photoelectrochemical characteristics of composite photocathodes. a) Current-potential comparison between the performance of a photocathode with (Cu_2O/ZnO/SnO_2/RuO_2) and without (Cu_2O/SnO_2/RuO_2) ZnO layer. b) Chronoamperometric stability measurements under continuous illumination and biased at 0 V_{RHE}. All measurements were carried out in pH 5.0 phosphate–sulfate electrolyte.

(Figure 3.11a) showing that a single cycle of ZnO is enough to improve the interface with the protective layer. This enhanced onset over previous reports on composite Cu_2O photocathodes with RuO_2 co-catalyst is the same as observed with Pt co-catalyst[31,32,142].

When Cu_2O is exposed to atmosphere, a thin layer of CuO is formed given it is the stable phase of copper oxide at room temperature and pressure. Deposition of ZnO onto an oxidized Cu_2O interface can reduce the CuO layer without affecting the Cu_2O underneath, thus enhancing the open-circuit voltage of devices comprised of such heterojunctions[44,151]. The effect of a single ZnO pulse cycle reported here, a positive shift in photocurrent onset potential of over 200 mV, corresponds to a significant improvement of junction photovoltage achieved without the need for the thicker Al-doped ZnO layers employed in previous reports.

The stability test of the device featuring a ZnO interlayer is shown in Figure 3.11b. The initial photocurrent is higher than the Cu_2O/SnO_2/RuO_2 device, but degradation of the current is more pronounced. This behavior is presently under further study, but an initial hypothesis is that the SnO_2 overlayer is not as conformal when deposited onto ZnO, as compared to directly onto the Cu_2O, therefore making the device more susceptible to corrosion.

3.4 Conclusions

In this chapter it was observed that ALD deposited SnO_2 is a promising candidate overlayer for stabilizing photocathodes for hydrogen evolution. The performance and stability were influenced by the film thickness, post-deposition steam treatment, and the nature of the heterojunction interface. The optimized device exhibited great stability,

maintaining 90 % of its initial photocurrent after 57 h of sustained photoelectrochemical water reduction. Further study will include identification of the mechanism of slow degradation, optimization of the heterojunctions for improved performance, and exploration of photocathode operation in acidic or alkaline solutions, which are desirable for complete devices. To the best of our knowledge, this study represents the first demonstration of SnO_2 as a photocathode protection layer[152], and these findings should be widely applicable for use on other photoelectrode devices.

CHAPTER 4

Unbiased solar energy storage: Photoelectrochemical redox flow battery

This chapter proposes the direct conversion of sunlight into electrochemical energy stored in a redox flow battery. A photoelectrochemical cell is used to charge a vanadium redox flow cell (CdS(s)|V^{3+}, VO^{2+}||V^{3+}, V^{2+}|Carbon Felt(s), E° = 0.6 V_{NHE}). A CdS thin film photoelectrode is prepared to directly charge the cell, pairs V^{3+}/VO^{2+}. CdS photoanode exhibits competitive photocurrents, when compared to other photoelectrochemical devices, and yields enough photovoltage to charge the vanadium battery up to 75 % with no external bias. An overlayer of CdSe improves the performance of CdS with current densities up to ca. 1.4 mA·cm^{-2}. Finally, a tandem configuration is tested using a dye-sensitized solar cell and a CdS photoanoade creating 1.3 V of photovoltage. This tandem arrangement proves to charge conventional all vanadium redox cell (DSC/CdS(s)|VO^{2+}, VO_2^+ ||V^{3+}, V^{2+}|Carbon Felt(s), E° = 1.2 V_{NHE}) without external bias.

This chapter is adapted from the published work:
J. Azevedo, T. Seipp, J. Burfeind, C. T. Sousa, A. Bentien, J. P. Araújo, A. Mendes, *Nano Energy*, 2016, 22 396–405.

The author contributed to the planning and execution of all the experiments described in this chapter, except: dye sensitized solar cell fabrication which was conducted by Maçaira J. The author was also involved on the discussion and interpretation of all results, as well as on the preparation of the manuscript.

4.1 Background

The use of photoeletrodes for converting solar into electrochemical energy in a RFB arrangement is a disruptive approach that allows an efficient storage of solar energy. Contrary to water splitting, where oxidation and reduction potentials are unique, in the case of direct solar charging redox flow batteries it is potentially possible to find two redox pairs for a selected photoelectrode, fitting the redox potentials with the semiconductor band edges. Moreover, the round trip energy efficiency using redox pairs for storing electricity is very high, ca. 85 %, compared to hydrogen with round trip

energy efficiencies of 20 % - 50 %[153]. The direct solar charging of redox flow batteries is then viewed as a premium opportunity for the research on photoelectrochemical cells.

Preliminary experiments using a photoelectrode for charging redox pairs have been reported in the 80s but limited choice of redox pairs and membrane limitations made the combined PEC and RFB device unable to efficiently convert solar into electrochemical storable energy and research in this topic came to a halt for decades[83,154]. Compared to PEC water splitting, for solar-RFB there are multiple choices of the redox couples given a great flexibility for choosing suitable photoelectrodes. Semiconductors that are unsuitable for water splitting due to thermodynamic potential mismatch or corrosion may now be used for solar-RFB since the choice of redox pairs is quasi-unlimited with redox potentials varying almost continuously[56,78,155]. Furthermore, most of the charge transfer processes involving redox couples normally used in RFB have faster kinetics since they rely on single or double electron transfer processes[56,76,155,156]. Thus, the overall system of solar-RFB is very likely to be more efficient and the direct conversion of sunlight into electrochemical energy may potentially be a cost effective alternative to PV charged RFB.

While this work was being developed, two different research groups published work on the solar battery concept. Wu *et al.* combined a dye sensitized TiO_2 photoelectrode and a lithium based battery describing the advantages of having a photoassisted battery charging[84,85]. Despite the reported advantages, single photoelectrode unassisted photocharge is highly unlike for the reported system and a tandem arrangement is most probably not beneficial due to the photoanode broad absorption spectrum. Moreover, the energy storage capacity of a lithium based battery is limited by the size of the battery, making this technology unpractical for very large applications. Liu *et al.* integrated an all vanadium RFB with a TiO_2 photoelectrode with high Faradaic efficiencies[86,87]. RFBs are easily scalable, display high round trip efficiencies, long lifetimes and acceptable costs for large-scale electrical energy storage, when compared with lithium-based batteries[56,155,157]. The charging measurements of the all vanadium RFB, by Liu *et al.*, were conducted with discharged batteries and a voltage gain of less than 0.05 V is reported[87]. Contrarily to solar water splitting, where the redox potentials of the chemical species in solution are constant during electrochemical reactions (not accounting small pH changes), in RFB an intrinsic electrochemical potential variation is observed governed by the Nernst equation[158]. The battery was charged up to 5 % state of charge (SOC); beyond this point more potential is required from the photoanode to charge the battery, which the authors have not demonstrated to be possible with the proposed photoelectrode. Moreover, a TiO_2, which has a wide bang gap, can only absorb a small part of the solar spectrum, making TiO_2 based devices very energy inefficient.

Figure 4.1a is a schematic representation of the proposed solar RFB that consists in a cadmium sulfide (CdS) semiconductor electrode placed at the negative (photoanode) side of a RFB. The photogenerated electron/hole pairs conduct the necessary redox

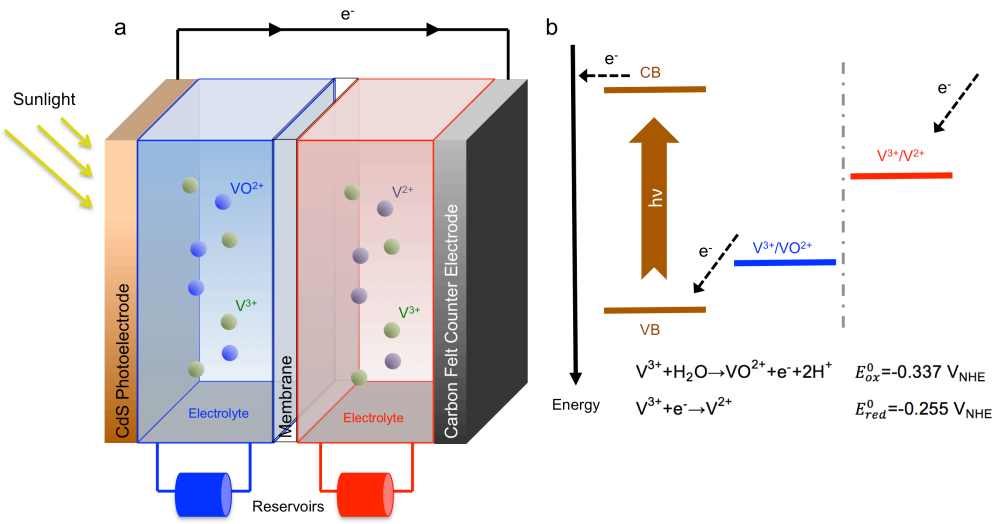

Figure 4.1 – Schematic diagram of a) all vanadium solar redox flow battery charged with a CdS photoanode and b) Energy diagram of the system, including the standard redox reactions.

reactions to charge the battery whereas the charged redox pairs are stored in two external tanks. Given that the photoelectrode provides enough voltage to charge the battery, direct charge can be conducted in a stand-alone device (with no external bias needed). The vanadium redox pairs were selected not only for their good kinetics or reversibility, but also for energy fit with the CdS band gap positioning – Figure 4.1b.

In this chapter, for the first time, it is demonstrated that the solar RFB, CdS(s)|V^{3+}, VO^{2+}||V^{3+}, V^{2+}|Carbon Felt(s), E^0 = 0.6 V_{NHE}, can be charged up to 75 % SOC without any external bias with photocurrents of ca. 1.4 mA·cm^{-2}. This was possible due to a good match between selected redox pair and semiconductor. In this work it is intended to prove the possibility to achieve easily unbiased charging of a RFB. In the future other redox pair/semiconductor combinations can be used to achieve higher efficiencies and energy densities. With the current developments in RFB technology[76,81,155,159] an even larger range of redox pairs could be available for energy fine-tuning between photo absorber and redox pairs.

4.2 Experimental details

4.2.1 Substrate preparation

Conducting fluorine doped tin oxide (F:SnO_2) glass was used as substrate (Solaronix TCO22-7). FTO-glass was cut into 1 x 3 cm^2 pieces and then cleaned by sonication sequentially in soapy water (15 min), acetone (15 min), ethanol (15 min), and finally in distilled water (15 min).

To obtain the best quality samples, the FTO substrate was delimited with an epoxy resin resistant to high temperatures (Araldite® Super Strength). The active area was measured from photographs of the samples with image analysis software[160], and found

to be 0.94 cm^2 ± 0.37 cm^2.

4.2.2 CdS thin film fabrication

CdS thin films can be prepared by different methods; here electrodeposition[161] has been chosen because the morphology and nanoparticle size of the films can be easily controlled by e.g. pH, temperature and deposition potential[135,162,163].

The chosen electrodeposition conditions of the CdS thin films were based on previous reports[164,165] and optimized for the present system. Briefly, CdS thin films were deposited in a plating bath containing 2 mM $CdSO_4$ (99 %, Sigma-Aldrich) and 100 mM $Na_2S_2O_3$ (98 %, Sigma-Aldrich), with a pH adjusted to 2.5 using 2 M H_2SO_4 (95-97 % Fluka). The bath was kept at 40 °C with stirring throughout the deposition. A three-electrode configuration cell with a ZENNIUM (Zahner Elektrik, Germany) electrochemical workstation was used at a constant potential of -0.8 V for 2 h for most of the samples. The counter-electrode was a 99.9 % pure platinum wire (Alfa Aesar, Germany) and the reference electrode was Ag/AgCl/Sat.KCl (Metrohm, Switzerland). After electrodeposition the samples were annealed at 450 °C for 30 min, in ambient atmosphere, under forced air flux. The films had a thickness of ca. 200 nm.

4.2.3 Under and overlayers deposition

Different configurations were tested in order to improve the performance of the CdS photoelectrodes. Layers of n-type semiconductors were deposited on top of CdS or directly on FTO such as TiO_2 and CdSe. Epoxy resin or Teflon tape was used to cover any exposed FTO substrate and delimit the active area.

Cadmium selenide (CdSe) was electrodeposited from a 2 mM aqueous solution of SeO_2 (99.8 %, Sigma-Aldrich) in 20 mM $CdSO_4$, at pH = 2. Galvanostatic deposition was done with 1 $mA{\cdot}cm^{-2}$ at 30 °C using the same three electrode configuration as described above. The deposition time was adjusted to 400 s to give a 200 nm thick film.

Titanium dioxide (TiO_2) overlayer films were deposited using atomic layer deposition (Beneq TFS 200) at a substrate temperature of 225 °C using titanium isopropoxide (99.99 %, Aldrich), at a precursor temperature of 45 °C, and water at room temperature. TiO_2 was deposited in pulse mode under a nitrogen flow of 0.250 $L_{STP}{\cdot}min^{-1}$, with a pulse length of 1 s and a purge time of 5 s for TiO_2 and a pulse length of 1 s and a purge time of 3 s for water. The growth per cycle of TiO_2 corresponded to 0.58 $Å{\cdot}cycle^{-1}$ at 225 °C. The samples were annealed at 500 °C for 15 min.

Underlayer of porous TiO_2 (denoted as TiO_2 paste) was deposited by doctor blade of a TiO_2 paste (Ti–Nanoxide T/SP from Solaronix) followed by drying at 80 °C for 20 minutes. The samples were annealed at 500 °C for 15 min. The thickness was approximately 5 μm.

Crystalline structure of underlayers and overlayers was checked by X-ray diffraction and energy-dispersive X-ray spectroscopy as described in section 4.2.4.

4.2.4 Thin Film Characterization

The morphology and surface topography of the films was characterized using a high-resolution scanning electron microscope (FEI Quanta 400 FEG ESEM) with a through-the-lens detector for secondary electrons. The acceleration voltage was 15 keV while an in-lens detector was employed with a working distance of about 10 mm. Cross-sectional images were acquired from freshly cleaved samples. The compositions of as-obtained thin films were studied by energy-dispersive X-ray spectrometry (EDAX Genesis X4M).

The crystalline structure of the samples was analyzed by X-ray diffraction (XRD) in a Rigaku MiniFlex 600 diffractometer in the $\theta - 2\theta$ geometry using the Cu – Kα line with wavelength λ = 1.540593 Å. The spectra were acquired by moving the detector between $2\theta = 20^\circ$ and $2\theta = 60^\circ$ at a scan rate of 0.6 deg·min^{-1} with a step width of 0.02°. The spectra peaks were fitted with Lorentzian functions to determine the average grain size according to Scherer equation, as described elsewhere[136]. Reflection patterns were matched literature values[161].

UV–VIS spectra were obtained on a Shimatzu UV-3600 UV-VIS-NIR spectrophotometer, equipped with a 150 mm integrating sphere and using $BaSO_4$ as 100 % reflectance standard. A quartz cuvette with path length of 1 cm was used for electrolyte absorption measurements.

4.2.5 Preparation of vanadium solutions

Vanadium electrolyte solution (AMG-GfE GmbH) containing 1.6 M vanadium in 2 M H_2SO_4 was used. The vanadium species were separated in V^{3+} and VO^{2+} using a flow cell at constant potential 1 V (see Equation 4.1), until a clear blue solution was observed on the cathode side and a dark green solution on the anode side, which indicates a good separation of both species. Prior to any test, the initial solutions were screened in the UV-VIS-NIR spectrophotometer to check the complete separation of V^{3+} and VO^{2+}. The obtained solutions were then diluted to 0.4 M using 2 M H_2SO_4.

4.2.6 Flow cell construction and cycling analysis

The flow cell used had 25 cm^2 active membrane area and a thickness of 3 mm. The RFB was assembled in a flow-through configuration. A Nafion^{TM} NM 117 (Quintech) membrane served as the separator. High surface area carbon felt electrodes were used (Sigratherm® GFA5 from SGL Technologies GmbH) with an uncompressed thickness of 6 mm and a specific weight of 500 g·m^{-2}. The carbon felt was heat-treated at 350 °C for 7 h, in oxygen atmosphere, prior testing for activation. The current collectors were graphite bipolar plates (Sigracet® TF6 from SGL). Contacts to the current collectors were

made with nickel-coated copper plates. Battery cycling studies were carried out with a ZENNIUM workstation in a two-electrode configuration. Charge-discharge cycles were recorded galvanostatically, with battery at 0 % SOC. All cycling measurements were conducted at current densities of 1 $mA{\cdot}cm^{-2}$. Further, all experiments were performed at room temperature with no active temperature control. Watson Marlow 323 pumps were used to maintain an electrolyte flow rate of 20 $mL{\cdot}min^{-1}$ during cycling measurements. Both reservoirs were argon purged before testing to minimize oxidation of the vanadium species. Charge/discharge cycles of Carbon Felt(s)$|V^{3+}$, $VO^{2+}||V^{3+}$, $V^{2+}|$Carbon Felt(s), E^0 = 0.6 V_{NHE} are represented – Figure 4.2.

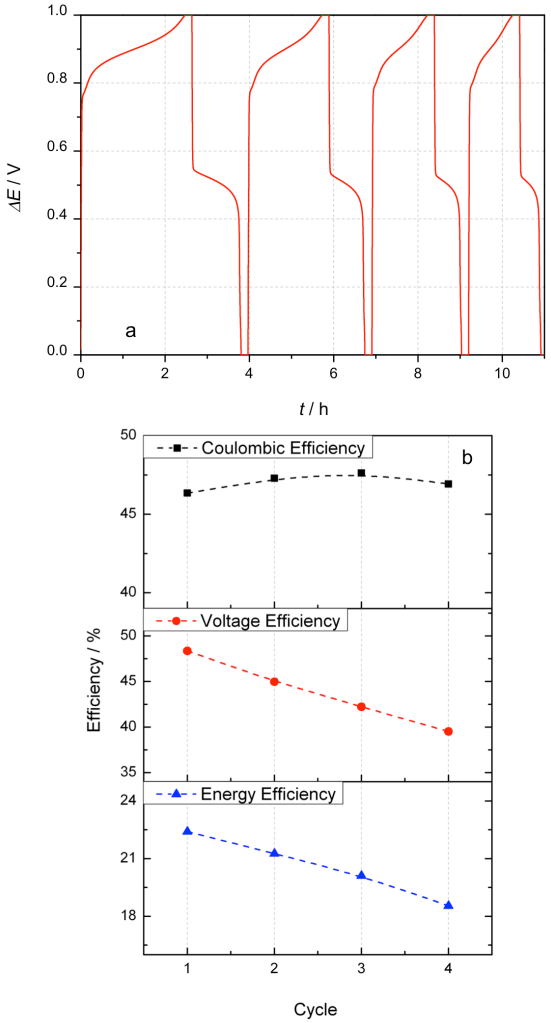

Figure 4.2 – Charge–discharge curves and b) Efficiencies of V3V3 RFB at current density of 1 $mA{\cdot}cm^{-2}$ at 20 $ml{\cdot}min^{-1}$.

4.2.7 Solar battery characterization

The photoelectrochemical cell used in the present study is based on previous design[166], and shown in Figure 4.3. The distance between membrane and each pho-

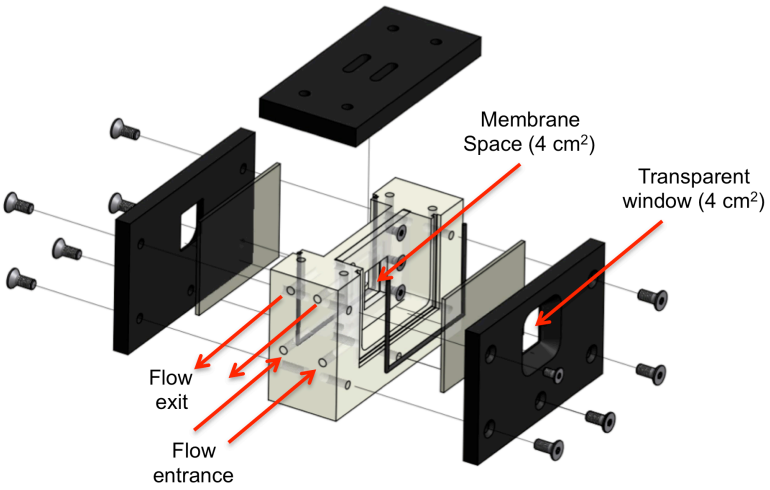

Figure 4.3 – Home-made solar redox flow battery cell design.

toelectrode was 1 cm and a Nafion^{TM} NM 117 membrane served as separator. The photoelectrodes were placed as close as possible (~ 1 mm) from the transparent window to minimize the light absorption from the electrolytes. The carbon felt counter-electrode was bonded to the graphite current collector plate with a carbonized resorcinol resin and no compression is thus needed for obtaining a good electrical contact. The carbonization/pyrolysis process is described elsewhere[167].

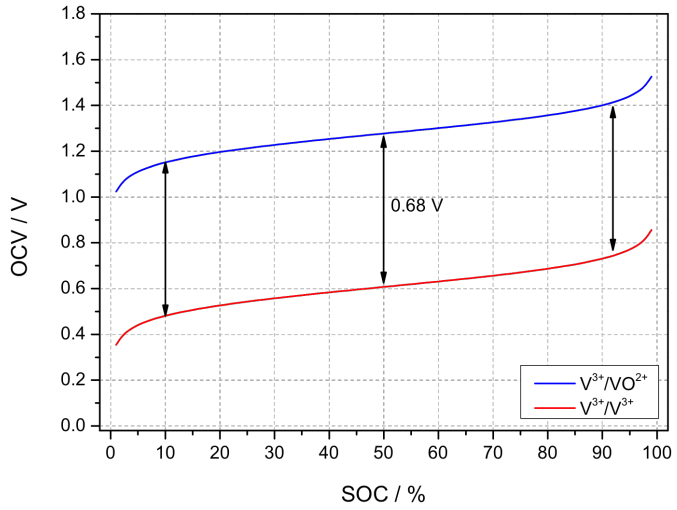

Figure 4.4 – Nernst equation for V^{3+}/V^{4+} and V^{3+}/V^{3+} configurations, according to reference 158.

For measurements at different SOC, the redox pairs were charged using an electrochemical cell equipped with two carbon felt electrodes. For example, for a standard all vanadium battery, comprising of initial redox species V^{3+} and VO^{2+} (Carbon Felt(s)|VO^{2+}, VO_2^+||V^{3+}, V^{2+}|Carbon Felt(s)), the battery was charged up to 1.2 V until a small current was observed (corresponding to 20 % SOC according to Nernst equation - Figure 4.4) and the electrolyte absorption spectra were measured. Using Beer–Lambert law[65], the concentration of the vanadium species with different oxidation states was

estimated and the experimental SOC computed. Given the high concentration of vanadium ions in solution, the electrolyte samples were diluted before determining the absorption.

The current-potential characteristic curves were recorded by linearly sweeping the potential using a ZENNIUM workstation. The measurements were performed in the dark and under simulated sunlight (Newport solar simulator, 150 W Xe lamp, AM 1.5 G, 1000 $W \cdot m^{-2}$) at a scan rate of 10 $mV \cdot s^{-1}$ in a two-electrode configuration. The light beam was calibrated with a c-Si photodiode. For stability measurements, no external bias was applied and the photocurrent response was recorded over time. No hydrogen or oxygen bubbles were observed during the experiments.

4.2.8 Tandem system

To test a tandem configuration of a CdS photoanode with a dye-sensitized solar cell (DSC), a DSC was fabricated as described elsewhere[168]. Briefly, cleaned FTO glasses were immersed in a 40 mM $TiCl_4$ (99.9 % Sigma-Aldrich) aqueous solution at 70 °C, for 20 min. Then, the samples were coated with porous TiO_2 layer by screen printing a commercial TiO_2 paste (Tiscreen printi from Solaronix), followed by drying at 80 °C for 20 minutes. Finally, the samples were annealed at 500 °C for 15 min in an infrared electrical oven (Nabertherm Gmbh model GF75. After, samples were again treated with 40 mM $TiCl_4$ aqueous solution and annealed at 500 °C for 15 min. The counter electrodes were made from the same cleaned FTO glass, after being drilled with two holes of 1 mm diameter. A commercial platinum based paste (Platisol T/SP from Solaronix®) was applied on the glass substrate by screen-printing followed by annealing at 400 °C for 15 minutes. Both electrodes were then sealed using a laser assisted glass frit method described elsewhere[169]. Dye (1 mM N719 dye solution) was recirculated for 10 hours, electrolyte was inserted in the cell (Iodolyte Z-150 from Solaronix) and the holes sealed using a glass lamella glued to the substrate using a thermo-plastic sealant (Surlyn®, DuPont). In order to insert the DSC inside the electrolyte, the entire cell edge was protected with epoxy resin resistant to high temperatures (Pattex Nural 22). The DSC was placed in the back of the photoanode, with which was connected in series using an electrical wire. The characteristic curves were obtained for both stand-alone DSC and tandem system.

4.3 Results and Discussion

4.3.1 CdS Photoanodes

Electrodeposited CdS films were 200 nm thick, compact and homogeneous (Figure 4.5a). The surface morphology of the samples is nanostructured with cauliflower-like features as small as 50 nm (Figure 4.5b). Depending on the deposition potential, dif-

ferent morphologies were obtained (Figure 4.6) and the cauliflower-like nanostructured surface was obtained with a deposition potential of -0.8 V. The increased roughness is associated with a better photoactivity of the photoanode[14] and in tests this cauliflower-like nanostructure yielded the best photocurrent performance. The films revealed good adhesion to the FTO glass, imperative for a good electrical performance.

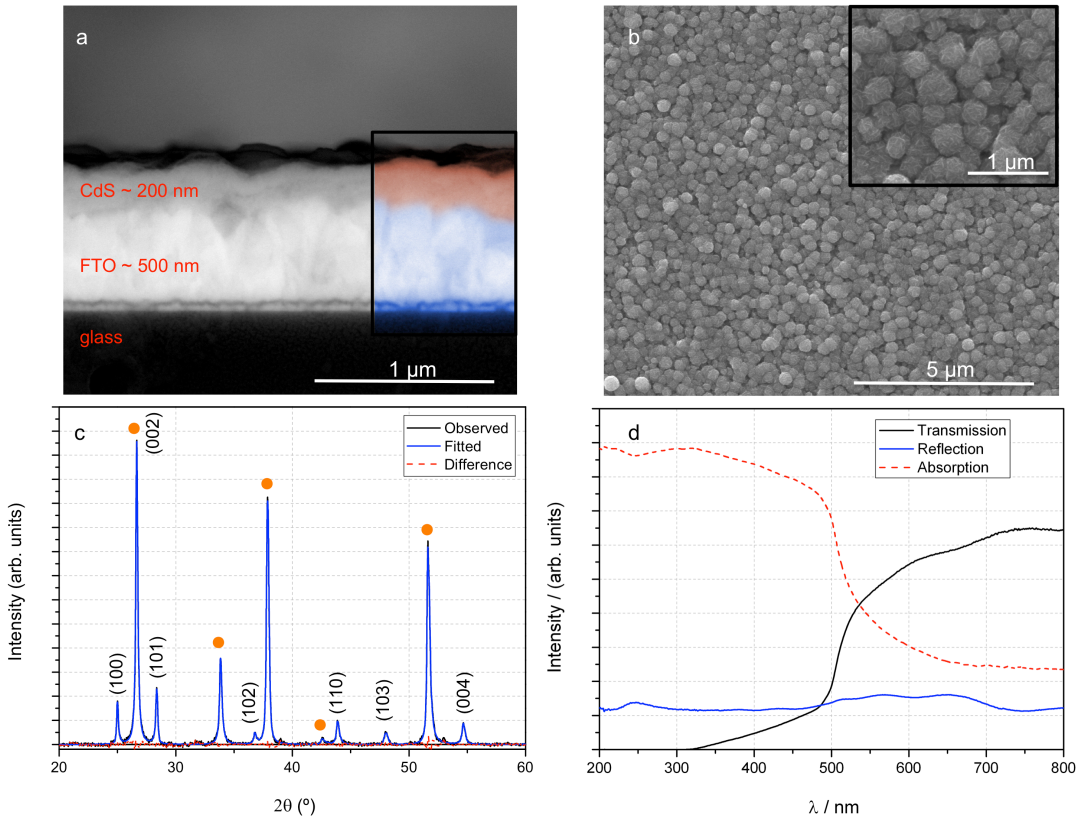

Figure 4.5 – Cross-sectional a) and surface b) SEM micrograph of a CdS photoanode. Inset shows an amplified view of the surface; c) X-ray diffraction patterns of CdS photoanode. Different crystalline phases are marked with the corresponding miller indexes. Orange circles mark the TCO diffraction peaks; d) The UV–VIS spectra of CdS thin films.

The CdS layer was characterized by X-ray diffraction - Figure 4.5c; literature values are shown as reference – Table 4.1[161]. Each peak was fitted with a Lorentzian function to assess the grain size using Scherer's equation[136]. The fit and difference to measured curves are plotted to verify the quality of the fitting. XRD spectra of CdS films indicate a nanocrystalline size of about 10 nm. Given the small thickness of the samples, the underlying FTO peaks are also visible and are identified in the spectra.

UV–VIS spectrophotometry, shown in Figure 4.5d, was performed to investigate the optical absorption of the films in the range of 200 nm - 800 nm. It can be observed that these films exhibit very good light absorption below 500 nm and it transmits most of the light in the 600-800 nm range.

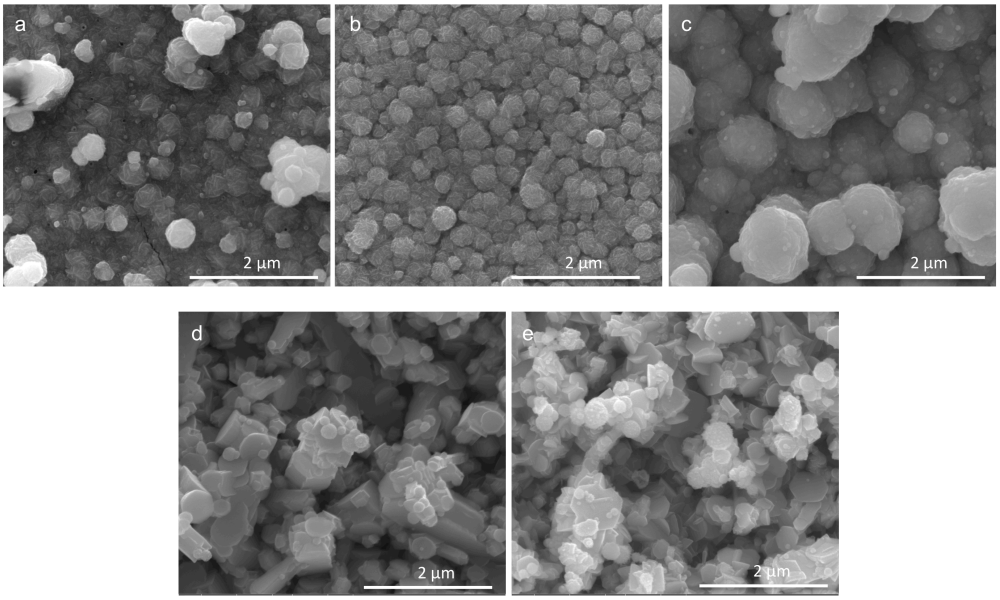

Figure 4.6 – CdS films deposited at different potentials with respect to reference electrode saturated Ag/AgCl: a) -0.75 V, b) -0.8 V, c) -0.85 V, d) -0.9 V and e) -0.95 V.

Table 4.1 – Structural parameters calculated from the XRD patterns and literature values for the diffracting planes[161].

(*h k l*) crystal system	2θ	
	XRD	**Literature values**
1 0 0	24.911	24.983
0 0 2	26.591	26.590
1 0 1	28.309	28.416
1 0 2	36.686	35.310
1 1 0	43.874	43.922
1 0 3	47.969	45.454
0 0 4	54.664	55.629

4.3.2 Battery Solar Charge

The selected electrolyte for the solar RFB were vanadium aqueous solutions:

$$V^{3+}+H_2O \rightarrow VO^{2+}+e^{-}+2H^{+} \quad E^0_{ox}= -0.337\ V_{NHE} \tag{4.1}$$

$$V^{3+}+e^{-} \rightarrow V^{2+} \quad E^0_{red}= -0.255\ V_{NHE} \tag{4.2}$$

This configuration is named V3/V3 from now on. These vanadium species exhibit a standard cell potential of E^0 = 0.6 V_{NHE} (Figure 4.4). Also, V^{3+}/V^{2+} redox pair is pH independent (Figure 4.7) offering the possibility to adjust the open circuit voltage (OCV) changing the electrolyte pH up to 2 for better band energy tuning; above this pH some vanadium species may start precipitating. In this work, pH was set to 0 to avoid precipitation and maximize energy density, at the expense of system stability. The OCV was experimentally measured using a carbon-felt electrode on cathode and anode sides, at different SOC values; it was done by applying a constant potential until a small residual current was observed.

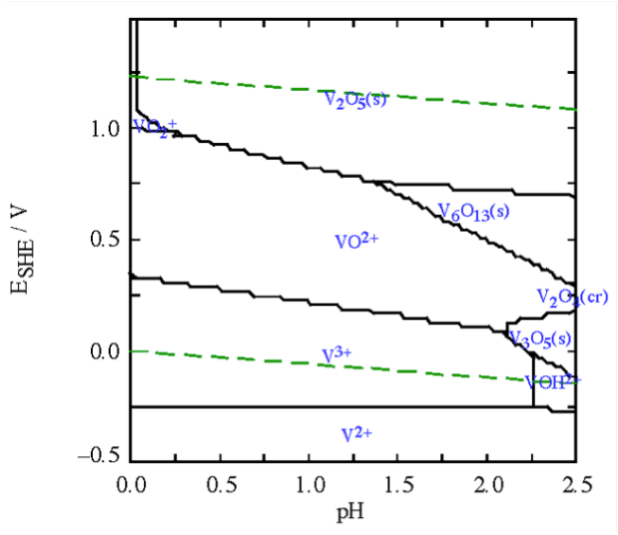

Figure 4.7 – Pourbaix diagram for V^{3+} at T = 25 °C, for $[V^{3+}]$ = 0.4 M. Generated using Medusa (http://www.kemi.kth.se/medusa/).

Under AM 1.5 illumination, the as-deposited bare CdS produced an unbiased photocurrent as high as 0.47 mA·cm^{-2} in a nitrogen-purged 0.4 M V^{3+} redox pair in 2 M H_2SO_4, for completely discharged V3/V3 cell - Figure 4.8; data shown are from top performing batches. The dark current was negligible up to 0.2 V. Preliminary experiments with a 1.6 M vanadium solution presented smaller photocurrents (~ 0.3 mA·cm^{-2}) attributed to the electrolyte darker color. The photocurrent onset is at -0.73 V - sufficient to charge the battery up to 90 % SOC without external bias, according to Nernst equation (Figure 4.4).

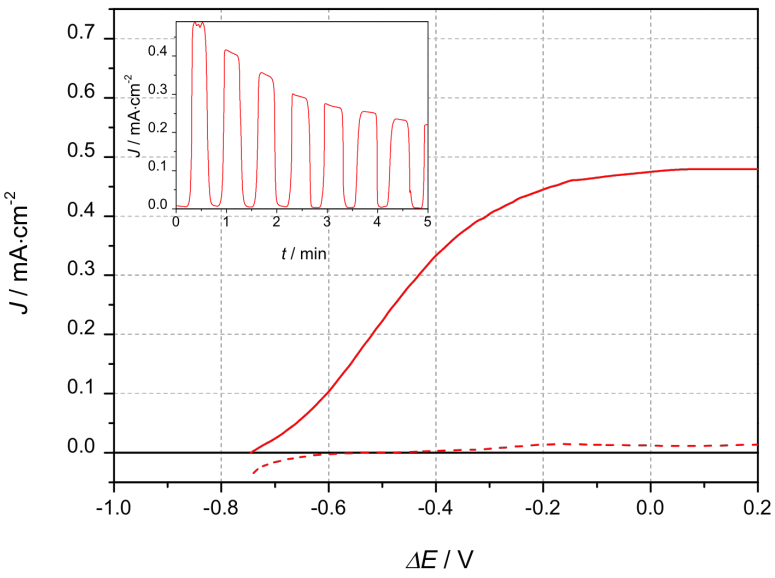

Figure 4.8 – a) Photocurrent–photovoltage characteristics under 1.5 AM light and dark conditions (in 0.4 M V3/V3 / 2 M H_2SO_4 electrolyte) of the best performing CdS photoanodes. Inset shows stability.

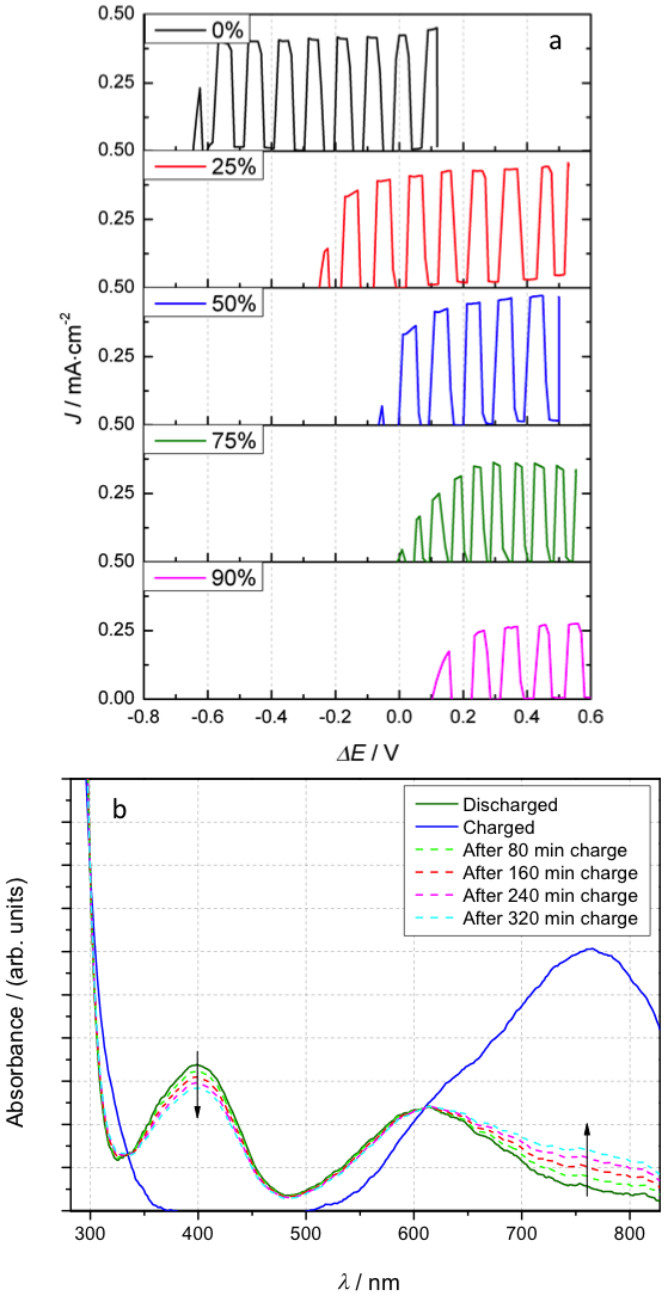

Figure 4.9 – a) Photocurrent–photovoltage characteristics under chopped 1.5 AM light CdS photoanode at different SOC values in V3/V3; b) Absorption spectra of V^{3+}-VO^{2+} mixtures at different SOC and for the parent V^{3+} and VO^{2+} solutions.

To confirm the possibility of unbiased charging battery, photocurrent characteristic curves were obtained at different SOCs (Figure 4.9a). Given the high concentration of vanadium ions in solution, the redox reactions kinetics remained mostly the same across the different SOC, and small differences in fill factors and plateau photocurrents are attributed to sample-to-sample variation. Only after 75 % SOC a decrease in photocurrent is observed which was attributed to a depletion of V^{3+} ions at the surface of the photoelectrode and counter-electrode. A shift in the onset is observed as the battery

charges. This shift fits perfectly with the Nernst equation: as the battery charges a built in chemical potential is created which requires more voltage to charge the battery further. For this reason, an initial low onset is required to charge the battery to high SOC.

The charging state of the battery was assessed by spectrophotometry. A fully charged and discharged redox pair sample was analyzed and the absorption spectra were according to literature: V^{3+} showed absorption peaks at 400 nm and 600 nm and VO^{2+} solution at 760 nm, Figure 4.9b. Starting from a complete discharged state, the battery was charged during equal time intervals at 0 V bias, under continuous 1.5 AM illumination, using several CdS samples. Absorption spectra of the anolyte were taken at each interval and a clear change from V^{3+} to VO^{2+} is observed over time.

The charging was confirmed from the absorption data assuming a linear relationship between concentration and the 760 nm absorption peak of VO^{2+} [65]. From Lambert-Beer law, using 18.46 as VO^{2+} molar absorptivity at 760 nm, the produced amount of VO^{2+} was estimated. After passing $\sim$ 0.6 C through the photoanode under continuous illumination, an amount of 0.13 mM of VO^{2+} was computed (total electrolyte volume of 14 ml). A conversion rate of $\sim$ 0.1 mM·h^{-1} for VO^{2+} was estimated.

4.3.3 Overlayers

To improve performance it was attempted to coat the photoelectrode with an overlayer. Here it is important that it has a staggered type-II band offset when interfaced with CdS. This ensures that charge carriers are injected in the correct direction for the desired reactions i.e. holes to the electrolyte and electrons to the counter electrode. This is the case of some n-type semiconductors with sufficiently low conduction band edge. Secondly, the layer should have a catalytic activity that promotes the charging reaction (Equation 4.1). Finally, no corrosive side reactions should occur at potentials within the bandgap potential range or at least have sufficiently low corrosion kinetics. Among n-type semiconductors CdSe and TiO_2meets these criteria and were selected to be tested.

Table 4.2 summarizes the PEC response produced by the two protected photoelectrodes. The maximum photocurrent corresponds to the photocurrent density at 0 V during the linear sweep voltammetry, corrected by the dark current. The stability was assessed over 5 min with chronoamperometric measurements at 0 V and chopped light. The final photocurrent density (J) was compared with the initial photocurrent density (J_0).

Table 4.2 – Summary of PEC performance for the different ALD layers investigated.

Sample ID	Anode/Cathode	Configuration	J at 0 V (mA·cm^{-2})	J/J_0 after 5 min at 0 V (%)
1	Anode	2oo nm CdS	0.47	46
2	Anode	2oo nm CdS/200 nm CdSe	1.4	86
3	Anode	2oo nm CdS/20 nm CdSe[a)]	0.66	42
4	Anode	TiO_2 [b)]/2oo nm CdS/200 nm CdSe	0.12	63
5	Cathode	2oo nm CdS/200 nm CdSe/100 nm TiO_2 [c)]	-1.9	47
6	Anode	2oo nm CdS/200 nm CdSe/100 nm TiO_2 [c)]	0.4	26

[a)]back illumination; [b)]deposited from TiO_2 paste; [c)]deposited using atomic layer deposition

TiO_2 is a well-tested material as a protective layer for other semiconductors[32,142,170], as well as for CdS[171]. It is stable in a wide range of pH values in aqueous environments and it can be deposited in a conformal and dense layer by atomic layer deposition. Despite previous reports using TiO_2 as protective layer of CdS, the low E_{VB} of TiO_2 (Figure 4.10) imposes an undesired potential step for holes diffusion to the redox pair, thus a resistive behavior is observed. In an attempt to reduce the resistive behavior, very thin layers of TiO_2 (5 nm) were tested, however, without improved performance (results not shown).

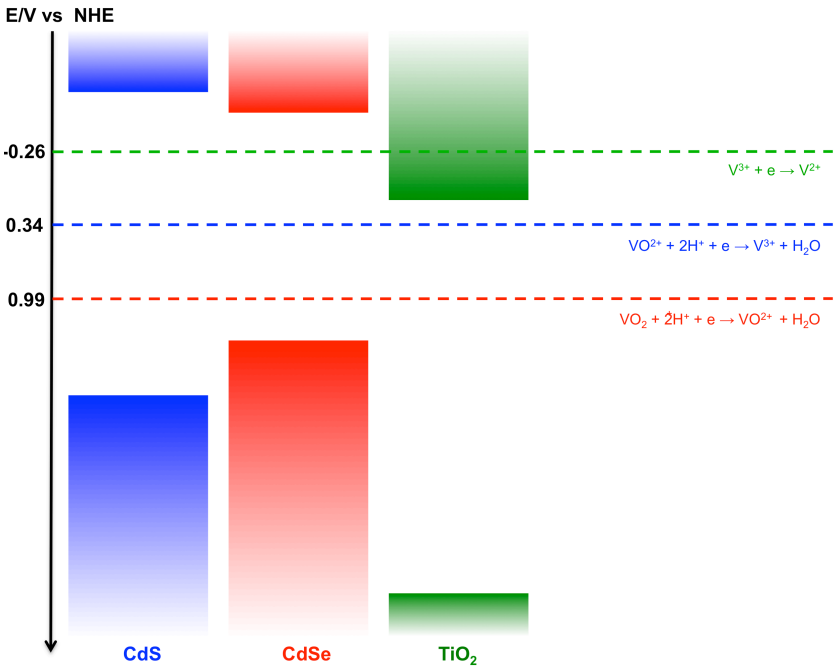

Figure 4.10 – A generalized band position diagram for the multilayer photocathode and redox levels of the involved chemical reactions.

CdSe, on the other hand, creates a favorable potential step when in contact with CdS[172]. In fact, CdS/CdSe structure is widely studied[161,173–175]. With a band gap of 1.7 eV, good conductivity and light absorption, CdSe has been studied for improving both CdS onset potential and photocurrent. Also, anodic decomposition potential[52] lies below the vanadium oxidation potential implying that CdSe should be more stable than CdS in vanadium electrolytes[161,172,173].

The optimized CdS/CdSe photoelectrode showed an onset at -0.67 V and a photocurrent of 1.4 $mA{\cdot}cm^{-2}$ at 0 V bias (Figure 4.11). CdSe protected samples displayed better stabilities (up to 5 minutes); but given the extreme pH conditions this still needs to be improved. A stable device can be achieved using sacrificial reagents[176] in the electrolyte but it is not the scope of this work, which solely intends to demonstrate the charge of the vanadium battery with no bias.

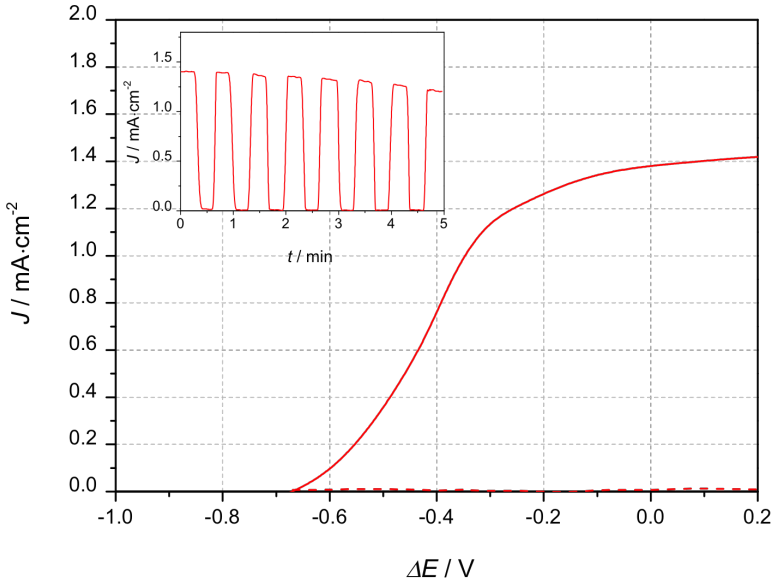

Figure 4.11 – Photocurrent-photovoltage characteristics of the best performing CdS/CdSe sample. Inset shows stability.

4.3.4 Tandem System

The open circuit potential of a RFB is directly related to the energy density it can provide. Open circuit potentials depend on different parameters according to Nernst equation but the standard redox potential is the predominant factor. Most of the commercial redox flow batteries have open circuit potentials over 1 V. The tested photoelectrodes provide insufficient photopotential to charge such a RFB without external bias. The necessary extra voltage can be obtained with a tandem system, placing a PV cell aligned with the photoelectrode[11,13,19]. The PV cell at the back of the photoanode generates an extra bias that is added to the photovoltage of the photoelectrode, provided that enough light reaches the photoanode through the PV cell. A schematic representation of the proposed system is given in Figure 4.12a. The selected PV technology was a dye sensitized solar cell since it can be made semi-transparent and it is fabricated from low cost and environmentally safe components. The semiconductor samples with lower onset potential were selected, in this case CdS.

As a higher energy density battery the following redox pairs were selected (named V3/V4 from now on):

$$VO^{2+} + H_2O \rightarrow VO_2^{+} + e^{-} + 2H^{+} \quad E^0_{ox} = -0.991\ V_{NHE} \tag{4.3}$$

$$V^{3+} + e^{-} \rightarrow V^{2+} \quad E^0_{red} = -0.255\ V_{NHE} \tag{4.4}$$

The DSC cell used had 4 cm^2 active area with an open circuit potential of 0.66 V, a short circuit current of $\sim$ 2.7 $mA{\cdot}cm^{-2}$ and a fill factor of 41 % – see Figure 4.13a; a CdS photoanode matching the useful area of the DSC, 4 cm^2, was prepared. The low current

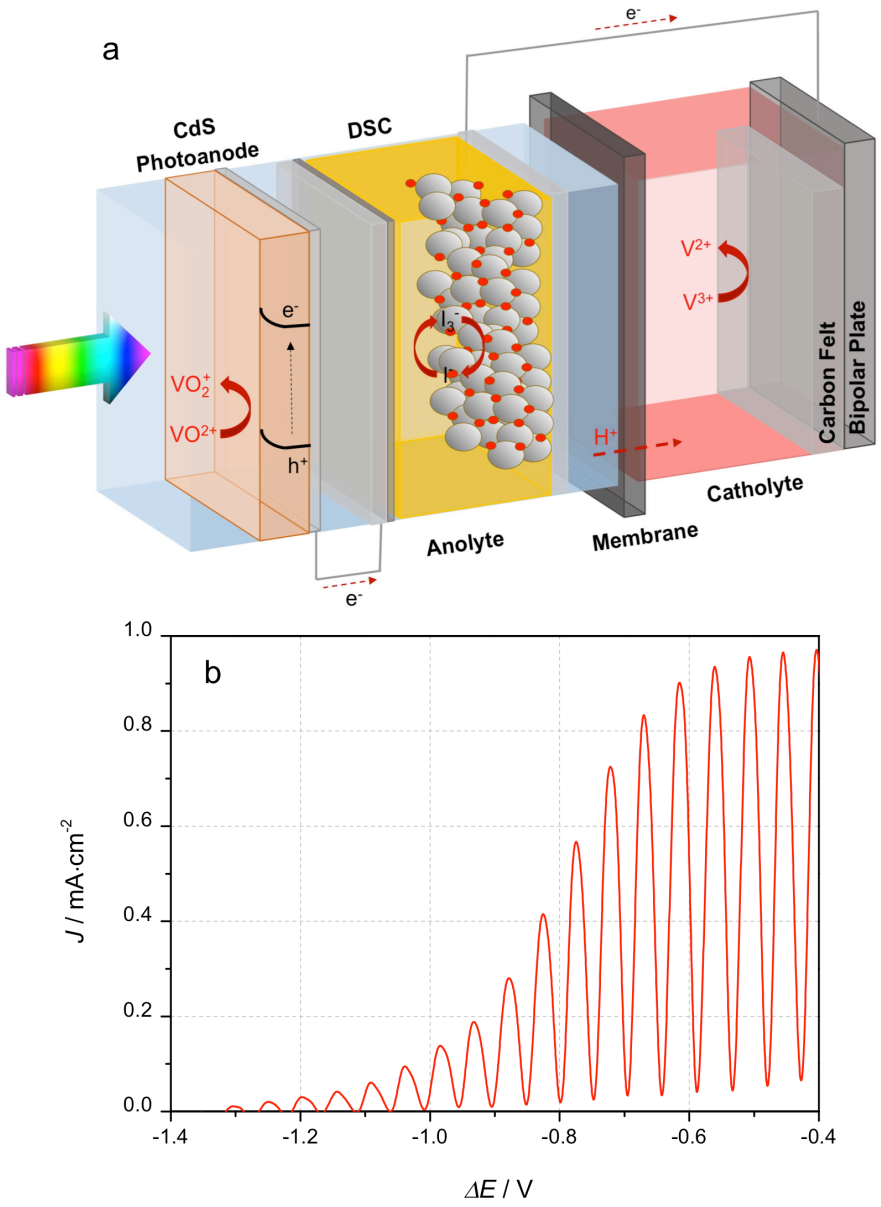

Figure 4.12 – a) Schematic representation of a tandem device comprising a DSC and a CdS photoanode to charge a vanadium RFB; Photocurrent–photovoltage characteristics of a tandem system composed by c) CdS(s)/DSC|VO^{2+}, VO_2^{+}||V^{3+}, V^{2+}|Carbon Felt(s).

density of the DSC cell was attributed to the thin, semitransparent, photoelectrode while the low fill factor was assigned to the large active area that promotes recombination[168]. The selected dye was N719 (Solaronix), which gives a reddish color to the DSC and high absorption across the visible range.

Given that the DSC has the widest absorption range – Figure 4.5d and 4.13b – The DSC was placed on the backside of the photoanode. This configuration originated higher photocurrents, in the range of 1 mA·cm^{-2} and photopotentials ca. 1.3 V (Figure 4.12b); a SOC of 70 % could be achieved.

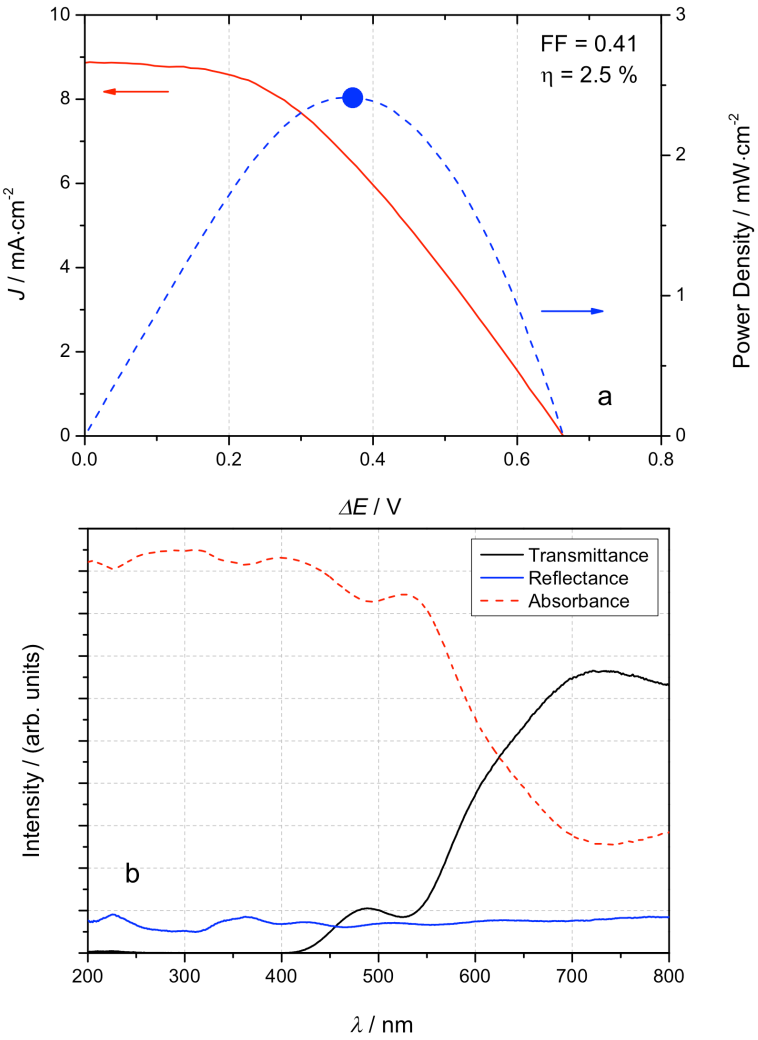

Figure 4.13 – a) Experimental results J–V and power curves; b) The UV–VIS absorption spectra of the DSC.

4.4 Conclusions

In this work the possibility of storing solar energy in a simple way using a vanadium redox flow battery and a CdS photoanode is demonstrated; unbiased charged of a solar-RFB (CdS(s)|V^{3+}, VO^{2+}||V^{3+}, V^{2+}|Carbon Felt(s), E^0 = 0.6 V_{NHE}) was achieved. A good semiconductor/electrolyte match was achieved allowing the unbiased solar charge of a RFB up to high SOC. CdSe protective over layer had a twofold increase with photocurrents up to 1.4 mA·cm^{-2} with no external bias. A tandem system battery using a dye-sensitized solar cell was also studied to provide necessary photovoltage to charge a standard all vanadium redox flow (DSC/CdS(s)|VO^{2+}, VO_2^{+}||V^{3+}, V^{2+}|Carbon Felt(s), E^0 = 1.2 V_{NHE}); in this configuration, the observed photocurrent was 1 mA·cm^{-2}.

Given the acidic nature of the electrolytes (pH ~ 0), the photoanodes are still limited by their long-term stability. To improve further the performance of the proposed solar-RFB system, the CdS/CdSe junction and CdS should be further optimized to

produce more reproducible photoelectrodes displaying higher photopotentials, currents and stability. Another option is reduced graphene oxide, that have been proven useful in minimizing CdS photocorrosion[177]. It is anticipated that new approaches will be proposed and photoelectrodes able to delivery higher current densities and photopotentials will be soon available. For example, organic alkaline electrolytes allow the use of stable semiconductors such as hematite.

CHAPTER 5

Solar Charging of an Alkaline Redox Flow Battery by a Surface Modified Hematite Photoanode

In this chapter the first solar alkaline redox flow battery using low cost and environmentally safe materials is demonstrated. The redox pairs consist of ferrocyanide and anthraquinone-2,7-disulphonate in sodium hydroxide solution yielding a cell potential of 0.74 V. Photovoltage enhancement strategies are demonstrated for the ferrocyanide-hematite junction by employing an annealing treatment and depositing an organic layer of conductive polymer polyaniline on the electrode surface thereby combating electron-hole recombination.

This chapter is adapted from the accepted work:
J. Azevedo[‡] and K. Wedege[‡], A. Khataee, A. Bentien and A. Mendes, *Angewandte Chemie International Edition*, DOI: 10.1002/anie.201602451. [‡]These two authors made equal contribution to this paper.

The author contributed to the planning and execution of all the experiments described in this chapter, except: redox flow cell tests which were carried out by Khataee, A.; Anthraquinone cyclic voltammetry measurements and prolonged illumination UV test which were carried by Wedege, K. The author was also involved on the discussion and interpretation of all results, as well as on the preparation of the manuscript.

5.1 Background

In the previous chapter, the solar charge of a RFB is described. Given the acidic nature of the vanadium redox pair used, the stability of the semiconductor was very limited. Therefore it is clear that low-cost and safe solar RFB future developments need to go through aqueous, non-acidic electrolytes where the most promising low-bandgap metal oxide semiconductors can be used, given the right energy levels of the redox couples. Examples include materials such as Cu_2O, $BiVO_4$ or $\alpha - Fe_2O_3$, which are materials already under investigation as photoelectrodes for water splitting[31,178,179].

Organic alkaline electrolytes might provide the answer as they are cheaper, efficient and allow using a wider range of semiconductors. In this chapter, a potential future

solar energy conversion technology with combined storage is investigated. The main principles are illustrated in Figure 5.1: A photoelectrochemical/redox flow (PEC/RF) cell is built from a hematite photoanode immersed in ferrocyanide solution and a graphite felt counter electrode immersed in anthraquinone-2,7-disulphonate (AQDS) solution separated by a cation conductive Nafion^{TM}-117 membrane. Upon illumination of the photoanode, electron/hole pair generation takes place in the hematite and holes move to the hematite surface oxidizing ferrocyanide through reaction 5.1 [180]:

$$Fe(CN)_6^{4-} + h^+ \rightarrow Fe(CN)_6^{3-} \quad E^{0'} = -0.49\ V_{NHE} \tag{5.1}$$

where $E^{0'}$ is the formal electrochemical potential for the reaction. Meanwhile AQDS is reduced on the other side through reaction 5.2:

$$AQDS + 2e^- + 2Na^+ \rightarrow AQDSNa_2 \quad E^{0'} = -0.25\ V_{NHE} \tag{5.2}$$

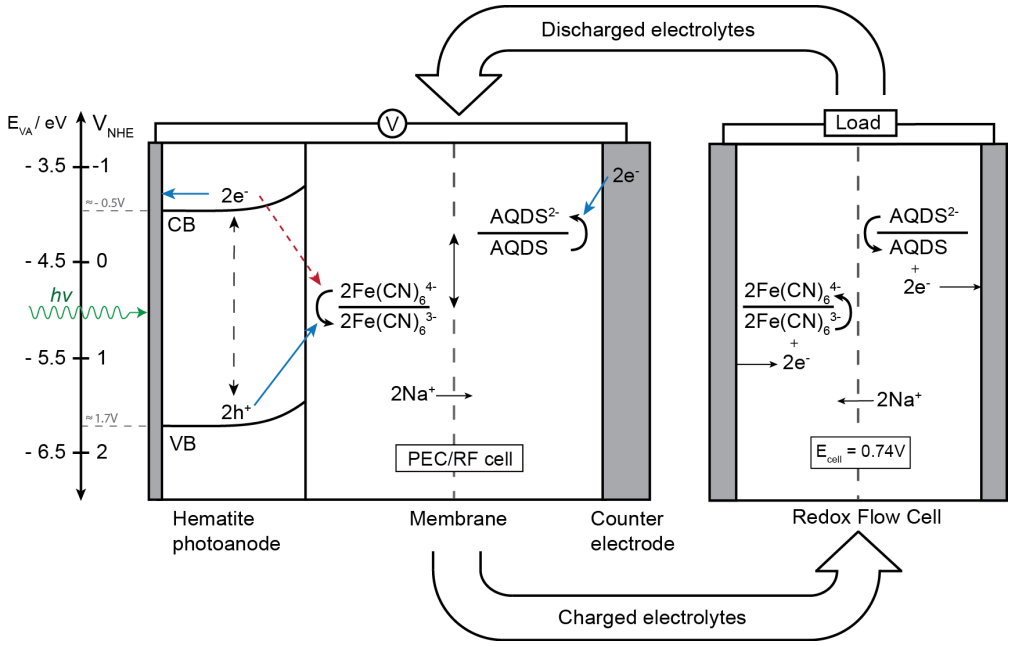

Figure 5.1 – Energy diagram of the PEC/RF cell for solar charging of redox pairs connected to a RF cell for discharge. Desired electron-hole pathways under light exposure are shown with full blue arrows. Undesirable back-electron transfer is shown in red dotted arrows.

In the photo-induced redox reactions the photon energy is converted and stored directly as electrochemical energy. The process produces ferricyanide $Fe(CN)_6^{3-}$ and $AQDS^{2-}$ that correspond to charged species in a RFB and, when needed, can be converted into electricity in an RF cell as outlined in Figure 5.1.

The energy levels of the conduction and valence band of hematite under alkaline condition are found to be around -0.5 V_{NHE} and +1.7 V_{NHE}, respectively [5]. With the potentials given in Equation 5.1 and 5.2, it is seen that the energy levels of the redox couples are in between those of the band gap of hematite, which is the primary

requirement for unbiased photoelectrochemical charging under sunlight illumination. Herein it is shown that the hematite–ferrocyanide junction provides enough photovoltage to oxidize/reduce the ferrocyanide/AQDS redox pairs and thereby charge the redox flow battery unbiased.

However, due to overpotentials the practical photovoltage generated by hematite turns out to be lower than expected[181]. In the hematite-ferrocyanide SCLJ, the limiting factor is known to be back electron recombination meaning that photo-generated electrons tend to reduce already produced ferricyanide[180], but no previous report on how to solve this issue has been reported. This work shows for the first time that a new polyaniline surface modified hematite photoanode actively decreases the back electron recombination and thereby improves the direct solar charging of the proposed RFB.

When this work started there were no reports on alkaline RFBs. Recently the performance of an alkaline RFB utilizing ferrocyanide and a similar anthraquinone species, 2,6-dihydroxyanthraquinone, was reported with impressively high power density and stability[81]. The introduction of organic redox species in alkaline environments into the flow battery technology is regarded as representing a major leap forward giving "*scope for developing flow cells with very low costs, high efficiencies at practical power densities, simplicity of operation, and inherent safety*"[182]. This highlights the relevance of research into solar energy storage by direct solar charging of RFB redox pairs creating an ideally grid-independent energy technology. It can be viewed as analogous to PEC water splitting coupled with hydrogen fuel cells, which is an active field of research[5,14]. Nonetheless, despite the great potential of PEC water splitting as future storable and renewable energy source, key challenges in particular with respect to obtain higher solar conversion efficiency remain. The sluggish kinetics of water oxidation[179] still present a major challenge for this field of research, which is a limitation that is bypassed with the use of fast redox couples like ferrocyanide in this work. Bard *et al.* reported an alkaline RFB using iron and cobalt complexes[159] indicating another possible research direction for aqueous (solar) RFBs and both findings highlight the relevance of shifting to higher pH environments.

The selected photoelectrode is hematite (α-Fe_2O_3), which has been extensively studied as a photoanode and is perceived as a promising material for PEC water splitting due to its low band gap (E_g = 1.9-2.2 eV, CB ~ -0.5 V_{NHE} and VB ~ 1.7 V_{NHE} at pH 14), high stability in alkaline media and low cost[5,180,183]. While chemically unstable in acidic solutions at most relevant potentials, hematite is stable in solutions of pH > 7, where photoelectrochemical corrosion is minor[5,183].

In this chapter, a new alkaline RFB is described. The iron complex ferro/ferricyanide ($Fe(CN)_6^{4-}/Fe(CN)_6^{3-}$) is a single-electron redox couple, which is electrochemically reversible under alkaline conditions and with a formal redox potential of $E^{0'}$ = 0.49 V_{NHE} at pH 13[180]. AQDS is used as the catholyte, as it has a suitable formal redox potential $E^{0'}$ = -0.25 V_{NHE} at pH > 10[76]. Unassisted solar charge is demonstrated up to 12.1 % SOC. Back electron recombination is identified as a major obstacle to achieve higher

unassisted SOC. A solution using a thermal treatment in combination with a conductive polymer is also presented with positive results.

5.2 Experimental details

5.2.1 Hematite photoanodes preparation

Thin and compact hematite photoanodes were prepared using spray pyrolysis technique, as described elsewhere[184]. Briefly, FTO conductive glass substrates (Solaronix TCO22-7, Switzerland) were carefully cleaned and heated to 500 °C on a heating plate. An underlayer of TEOS was deposited using a glass atomizer with a precursor solution of 10 % tetraethyl orthosilicate (Sigma-Aldrich) in ethanol solution (10 mL per 18 cm^2). After naturally cooling to room temperature, the substrates were re-heated to 500 °C and sprayed with 70 mL per 24 cm^2 of a 10 mM iron acetylacetonate (Fluka) solution in ethanol. The spraying was done by a spraying nozzle system (Spraying Systems Co. model SU J4B-SS) using a stainless steel pressurized tank and a pressure inside the tank of approximately 1 bar (by atmospheric air) from a height of 20 cm above 8 samples of 1 x 3 cm^2 (1 mL of solution was sprayed every 45 seconds). After deposition, the samples were maintained at 500 °C for 30 min and allowed to cool to room temperature. One end of the FTO/glass was protected to allow applying a silver electrical contact.

5.2.2 Hematite post synthetic annealing

Hematite samples were annealed using a modified pressure annealing method based on previous work[142]. Simply, the as-synthesized sampled were placed in a Teflon-lined autoclave inside a small open glass flask. 0.2 mL 10 mM iron acetylacetonate solution in ethanol were placed outside the flask and the autoclave was heated to 140 °C for 5.5 hours using a 350 °C/h heating ramp and left to cool in the oven. This treatment promotes surface defect patching[142].

5.2.3 Polyaniline electrodeposition

Polyaniline was deposited onto already annealed samples due to a visibly more homogeneous layer on these samples instead of untreated hematite. The procedure is based on a previous report[185]. Briefly, a hematite sample was placed as the working electrode in a 3-electrode glass cell filled with 0.2 M aniline (Sigma-Aldrich) in 0.5 M H_2SO_4 solution and with a Pt-wire counter electrode and sat. Ag/AgCl reference electrode (Metrohm, Switzerland). The electrodeposition was done by applying a constant positive current of 5 $\mu A \cdot cm^{-2}$ for 5 min using an Autolab potentiostat (Metrohm, NOVA 1.10.3 software) – Figure 5.2. A fresh solution of aniline was used for each deposition. The samples were washed with distilled water and subsequently immersed in 1 M NaOH and washed again. Just after deposition the color on TCO glass was green, but after

NaOH treatment it turned purple, (typical in an emeraldine structure) – Figure 5.2. The thickness of the film was estimated to 15 nm by assuming 100 % current efficiency and an aniline density of 1.0217 g/cm^3.

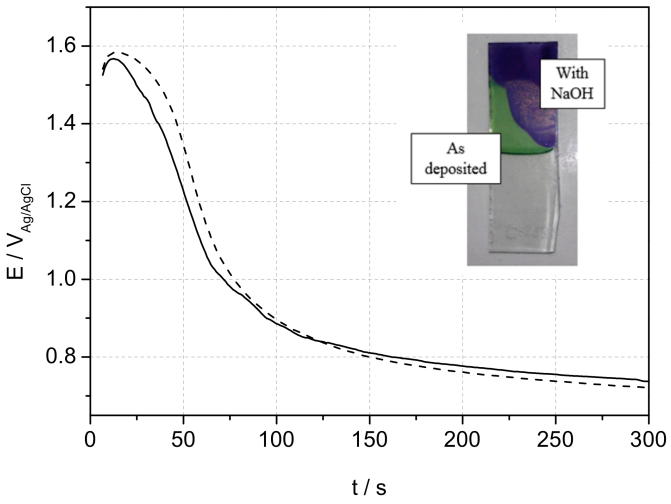

Figure 5.2 – Potential as a function of time when performing the polyaniline electrodeposition for two representative hydrothermally treated samples; (inset) Polyaniline deposition (20 min, 5 μA·cm^{-2}) on TCO glass after dipping half the sample in 1 M NaOH.

5.2.4 Cyclic voltammetry and charging/discharging in redox flow cell

The cyclic voltammograms of AQDS (Combi-Blocks, Inc. QA-7372) and potassium ferrocyanide (Sigma-Aldrich) were recorded in a 3 electrode glass cell with an Autolab potentiostat (Metrohm, NOVA 1.10.3 software) using a 3 mm freshly polished glassy carbon electrode (Chemical Instruments) as the working electrode, Pt-wire counter electrode and sat. Ag/AgCl (Metrohm, Switzerland) as reference electrode. The solutions of 1 mM AQDS or ferrocyanide in 1 M NaOH were purged with nitrogen before measurements.

The RF cell charging/discharging experiments were conducted in a single flow cell shown in Figure 5.3. The RF cell is based on a Fraunhofer cell (RF25-015-T and RF25-014-N, 25 cm^2) and consists of carbon felt electrodes, bipolar plates, current collectors and a cation exchange membrane. In order to facilitate current collection, solid copper plates were employed. Graphite plates were used as bipolar plates. Carbon felt was used as electrodes on both sides of the cell. Nafion-117 was adopted as a cation exchange membrane and PTFE gaskets were used for sealing the cell assembly. To assemble the cell, current collectors were screwed together by 4-11 bolts with bipolar plates, electrodes and gaskets in between. For circulating the electrolytes (100 ml on both sides) through the cell, 2 DDA pumps at a flow rate of 25 mL/min with Teflon tubing were utilized. Anolyte and catholyte were composed of 0.1 M AQDS in 1 M NaOH and 0.2 M $K_4Fe(CN)_6$ in 1 M NaOH, respectively and purged with nitrogen before use. Charge/discharge studies were carried out under constant current of 0.5 A, upper limit of

1.2 V during charge and lower limit of 0.2 V during discharge. An Aim-TTi QPX1200SP 1200 watt DC Power Supply was used for charging and an Aim-TTi LD400P 400 Watt Programmable DC Electronic Load for discharging the cell. A multimeter was used to measure the voltage.

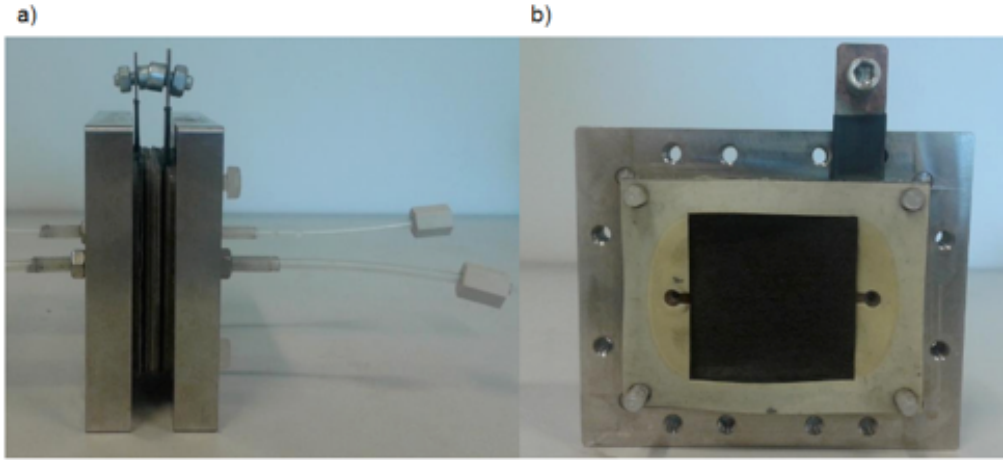

Figure 5.3 – a) Assembled cell, side-view and b) carbon felt and gaskets inside the cell.

5.2.5 Photoelectrochemical cells

The photooxidation of ferrocyanide was studied using a small PEC cell – cappuccino cell – as described elsewhere[5]. The cell was filled with 0.2 M $K_4Fe(CN)_6$ (Sigma-Aldrich) in 1 M NaOH with varying concentration of $K_3Fe(CN)_6$ (Sigma-Aldrich) in a three-electrode configuration. A Pt wire was used as counter electrode and 3 M Ag/AgCl as reference electrode (Chemical Instruments, UK). The cell has a 7 mm front quartz window and the sample was placed 5 mm from the window in a sample holder. These tests eliminate the influence of the AQDS in the PEC/RF with two half-cells.

The photoelectrochemical performance of the hematite photoanodes with redox pairs ferrocyanide|ferricyanide||AQDS|$AQDS^{2-}$ was measured in an open PEC cell (Figure 5.4a) with a transparent window in a 2-electrode setup making it possible to measure the absolute battery potential. The photoelectrochemical cell is the same as described in chapter 4 and is shown in Figure 5.4a, alongside with the electrolytes. Hematite or graphite felt plates (Sigracell) were used as the working electrode in one cell chamber and counter/reference electrode was short-circuited in the other chamber and connected to a graphite felt plate in the solution. The hematite area was reduced to 1 cm^2 by masking the samples with tape. The operating conditions in all experiments were as follows: starting anolyte was 0.1 M AQDS (Combi-Blocks, Inc. QA-7372) in 1 M NaOH and starting catholyte was 0.2 M $K_4Fe(CN)_6$ in 1 M NaOH.

The SOC is the degree of electrochemical transformation of the redox couples on both sides of the battery resulting in a certain battery voltage according to the Nernst equation. The PEC cell was charged to different SOC by applying a fixed potential,

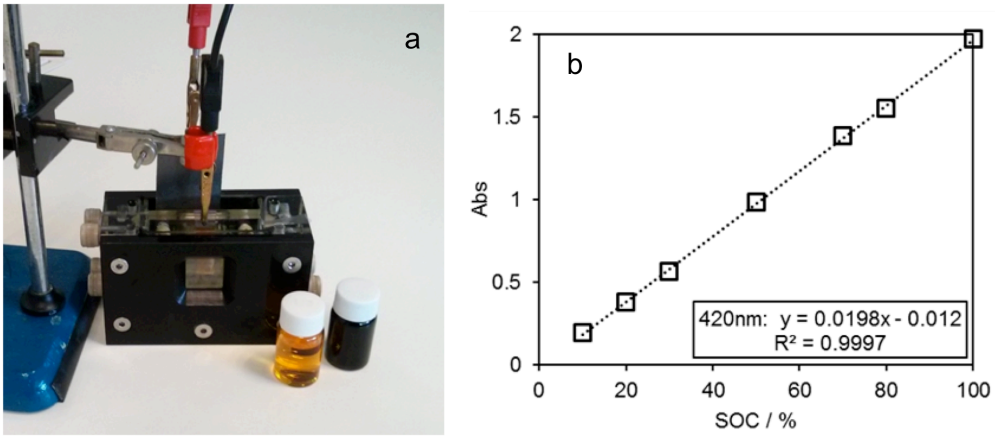

Figure 5.4 – a) PEC battery cell and b) UV Standard curve for 0.2 M ferrocyanide/ferricyanide solution in 1 M NaOH diluted 100 times for peaks at 420 nm referenced to 1 M NaOH

according to Nernst equation, until only residual current was measured. The charge was conducted using graphite felt electrodes at the anode and at the cathode sides. When each SOC was achieved, the electrode at the anode side was exchanged by the hematite photoelectrode to measure the photoresponse in the PEC/RF cell arrangement. The AQDS solution was bubbled 10 min with nitrogen in the beginning and after each new SOC was reached. The yellow color of the ferro/ferricyanide solution (10 % SOC) and the red color of the AQDS solution is seen in the two flasks (Figure 5.4a). The SOC was determined in three ways: measuring the OCV before recording the *J-E* curves of each sample, measuring the OCV after recording the *J-E* curves and by measuring the UV absorbance of the ferrocyanide solution at 420 nm (Figure 5.4b). For photoresponse experiments, a solar simulator Newport 67005 or Newport 94011A with AM 1.5 air mass filter was calibrated to 1 sun (100 $mW \cdot cm^{-2}$) with a c-Si photodiode (Newport). Current-potential linear sweeps (positive direction) were recorded at a scan rate of 10 $mV \cdot s^{-1}$ and with a resolution of 5 mV. The potential was controlled with a ZENNIUM workstation (Zahner Elektrik, Germany) or a CHI660E (Chemical Instruments).

The PEC water splitting performance of hematite samples in the same half cell system as previously described in using 1 M NaOH as electrolyte (pH 13) or 0.1 M phosphate buffer (pH 7.6).

5.2.6 Optical and morphological characterization

Absorption spectra of the samples were measured and the average absorption from 300-600nm is 58 %. UV-VIS spectra of hematite samples were measured using a Shimatzu UV-3600 UV-VIS-NIR spectrophotometer, equipped with a 150 mm integrating sphere and using $BaSO_4$ as 100 % reflectance standard. A QUANTA-FEI field emission scanning electron microscope (FE-SEM) was used to evaluate the morphology of the samples.

5.2.7 Prolonged illumination UV test

To ascertain that the photoelectrochemical process indeed does produce ferricyanide in the PEC/RF cell, a hematite sample was left in the battery under illumination starting from 0 % SOC for 7 h. The absorption from a sample of the ferri/ferrocyanide solution was measured at different times, as the ferricyanide absorbs at 420 nm as opposed to ferrocyanide. As a control, a 0 % SOC ferrocyanide solution was also left in the light in a separate transparent container with similar area/volume ration as in the battery and the absorbance measured. The absorbance of the control sample increases at just below 400 nm due to a photo-induced side reaction, but was stable during the whole test and with absorbance significantly lower than for the test in the PEC/RF cell using hematite.

The UV spectra were measured with reference to a 0 % SOC solution of ferrocyanide in 1 cm path length quartz cuvettes.

5.3 Results and Discussion

5.3.1 Surface Modification

In the current work it is shown that the hematite-ferrocyanide junction provides enough photovoltage to photo-oxidize the ferrocyanide while reducing the AQDS to a certain SOC. For improving the attainable photovoltage of the hematite-ferrocyanide junction, two surface treatments were attempted. Hematite photoanodes were prepared by spray pyrolysis on conductive glass in batches of 8 samples and data is reported for two batches, A and B, for three kinds: i) bare; ii) annealed and; iii) annealed with a thin layer of electrodeposited polyaniline on top, hereafter denoted “coated”. Low temperature steam annealing has earlier shown improvement in photoelectrochemical response of photoelectrodes due to patching of surface defects[142]. Polyaniline has been reported with both TiO_2 and WO_3 photoelectrodes[185,186] but not with $\alpha - Fe_2O_3$. None of the surface treatments produce discernable changes in SEM images of the samples or in absorption spectra (Figure 5.5 and 5.6, respectively).

The redox flow cell of ferrocyanide and AQDS in 1 M NaOH was characterized concerning cyclic voltammograms (CV) and cycling capacity and the results are shown in Figure 5.7. As seen from the CVs in Figure 5.7a, the redox couples show good electrochemical reversibility and the redox potentials are as expected from previous reports[76,180]. The battery charge–discharge cycles were tested in a 25 cm^2 single RF cell. Ten cycles are shown in Figure 5.7b. High coulombic efficiency of around 98 % is observed in Figure 5.7c and energy efficiency of around 75 %. The charging and discharging capacities are plotted as well. The overall RF cell performance is good as would be expected based on the recent alkaline anthraquinone/ferrocyanide battery report[81].

Figure 5.8a shows the photocurrent density (J) as function of the applied potential

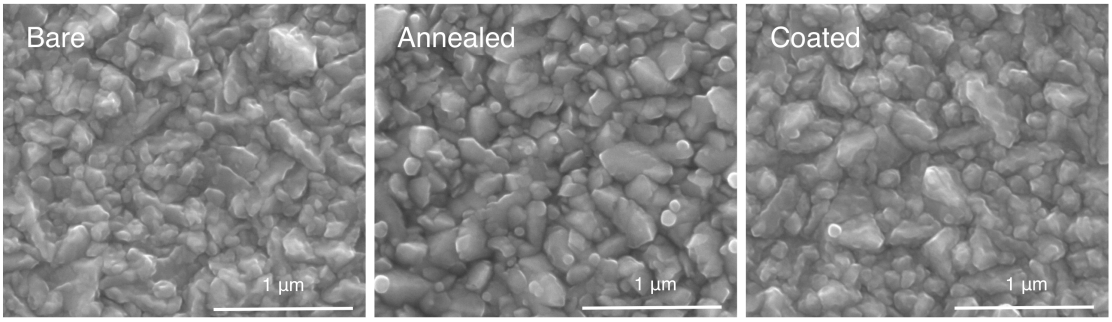

Figure 5.5 – SEM top view of different prepared samples a) bare b) annealed and c) coated.

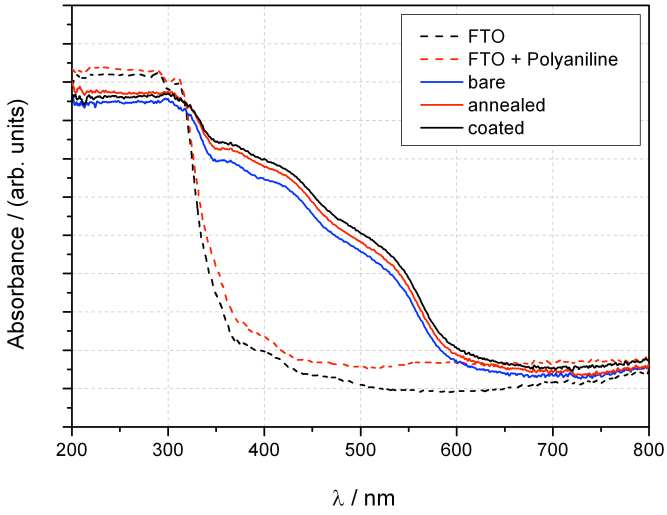

Figure 5.6 – Absorption measurements for bare TCO glass polyaniline directly on TCO glass, bare, annealed and coated sample.

(*E*) for three representative surface treated hematite samples. The responses were measured in a three-electrode arrangement in only ferri/ferrocyanide solution, under 1 sun illumination. The photo-induced oxidative (positive) current starts around -0.15-0.05 V_{NHE} (hereafter denoted photocurrent onset potential $E_{on,photo}$) depending on the sample and dark oxidative current onset ($E_{on,dark}$) after 0.4 V_{NHE} for the bare and annealed sample and after 0.6 V_{NHE} for the coated.

Figure 5.8b shows the average $E_{on,photo}$ for different hematite samples as a function of $Fe(CN)_6^{3-}$ concentration. It is seen that both surface treatments shifts $E_{on,photo}$ shifts towards a more negative potential, in particular for the coated samples. $E_{on,dark}$ generally shifts to more positive potentials for coated samples. This indicates both an overall increased photovoltage and a higher available voltage for oxidation of ferrocyanide[187]. The photovoltage decreases with increasing ferricyanide concentration, more precisely 122 mV per decade change in concentration for bare and annealed samples and 73 mV for coated samples, since with higher electron-acceptor concentration (ferricyanide) the probability of electrons recombining with the acceptor increases, which is a significant limitation of this system[180].

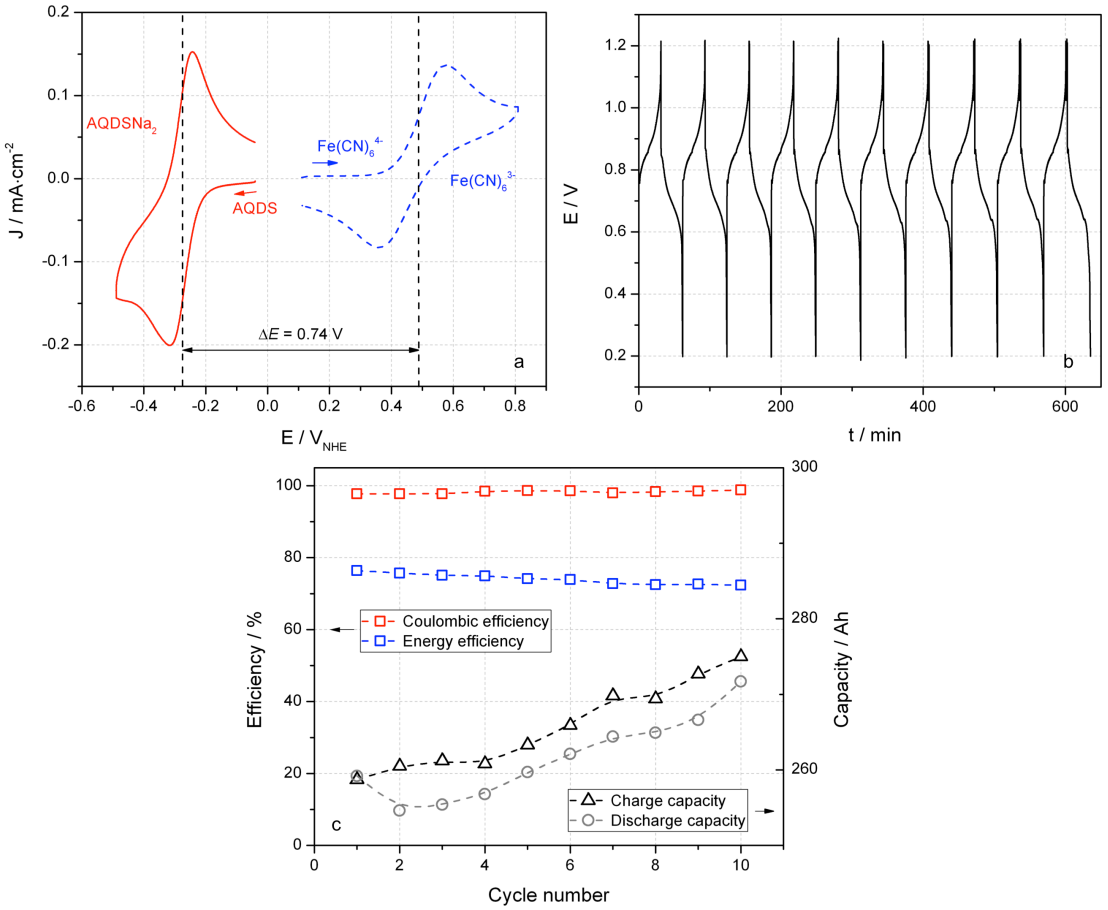

Figure 5.7 – a) CVs of AQDS (red line) and $Fe(CN)_6^{4-}$ (blue line) 1 mM in 1 M NaOH at scan rate 100 mV·s^{-1} on a GC electrode; b) Charge-discharge curves in a 25 cm^2 RF cell with a constant current density of 20 mA·cm^{-2} and redox pair concentration 0.1M AQDS and 0.2M ferrocyanide in 1 M NaOH; c) Efficiency data for the 10 cycles in b).

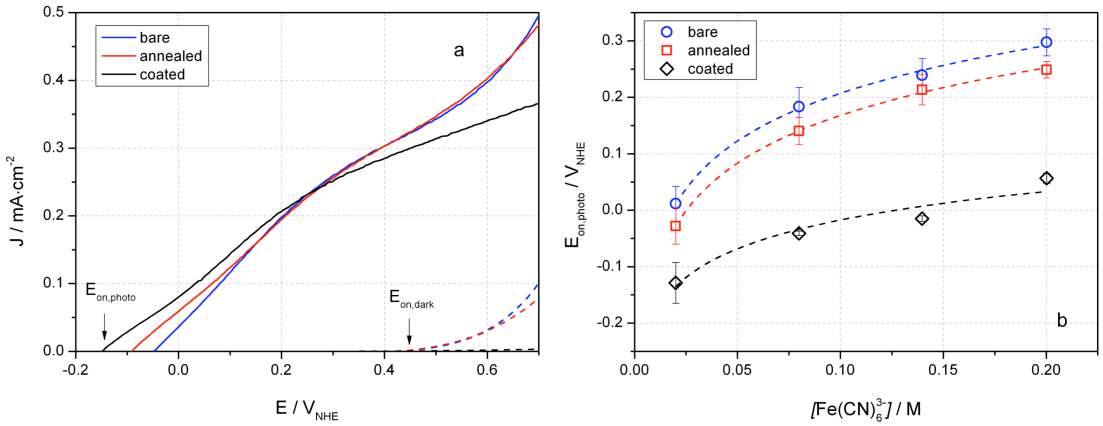

Figure 5.8 – a) *J-E* curves under 1 sun illumination (left) and in the dark (right) in the three-electrode PEC cell for 3 surface treated hematite samples from batch A in 0.2 M $K_4Fe(CN)_6$, 1 M NaOH. b) Average $E_{on,photo}$ and standard deviation for all samples from batch A from *J-E* measurements with varying $Fe(CN)_6^{3-}$ concentration and a constant concentration of 0.2 M $K_4Fe(CN)_6$ and semi-logarithmic fits with slopes 122 mV (bare, R^2 = 0.997), 122mV (annealed, R^2 = 0.999) and 73 mV (coated, R^2 = 0.936), respectively.

5.3.2 Onset Improvement

The photoresponse of bare and coated hematite samples were recorded in a PEC cell in a two-electrode configuration using ferrocyanide on the anode and AQDS on the cathode side. The *J-E* response of a representative bare hematite photoanode in the PEC cell at different SOCs is shown in Figure 5.9a. Here, the oxidative photocurrent has an onset of about -300 mV and is still observed with 0.07 $mA{\cdot}cm^{-2}$ at 0 V and corresponds to unbiased solar PEC/RF cell charging. As the SOC increases to above 10 %, $E_{on,photo}$ is observed at a slightly positive potential and unbiased photocharging no longer take place. Just before dark current onset the photocurrent is 0.10 $mA{\cdot}cm^{-2}$. In Figure 5.9b the *J-E* responses of a representative coated sample illustrate the effect of the surface treatment with polyaniline. The surface modified sample shows better fill-factor, earlier $E_{on,photo}$ and higher photovoltage seen from the later onset of dark current[187].

The magnitude of the photocurrent is comparable to reported values of around 0.2 $mA{\cdot}cm^{-2}$ for the ferrocyanide-hematite junction[180,188]. In Figure 5.9c the average $E_{on,photo}$ and $E_{on,dark}$ for different hematite samples, bare and coated, in the PEC cell is shown as a function of SOC. From semi-logarithmic regressions, the calculated intersection of $E_{on,photo}$ with the x-axis (SOC) in Figure 5.9c is interpreted as the maximum unbiased SOC possible and is 9.4 % for the untreated samples and 12.1 % for the surface treated samples, as can also be seen in Table 5.1. Generally it is noted that while batch-to-batch and sample-to-sample variation is significant (as also reported elsewhere), all results are consistent in terms of the general trends[180].

In Figure 5.9a and b it is clear that the photocurrent decreases with higher SOC. This is expected, owing to a lower concentration of the hole-acceptor species (ferrocyanide) and decreasing transparency of the electrolyte. The favorable effect of the polyaniline coating illustrated in Figure 5.8 is less clear in the PEC/RF cell tests of Figure 5.9 and Table 5.1. In Table 5.1, the slopes of the semi-logarithmic regressions of around 100 mV for both samples in the light and 70 mV in the dark show the opposite effect of the one observed in Figure 5.8, though a higher unbiased SOC can be reached for the coated samples. It is attributed to increased ohmic losses in the cell and the overvoltage associated with the AQDS reduction[76]. Furthermore, the Nernst contribution to the battery redox potentials shifts the relative positions of ferro/ferricyanide and AQDS further apart. This possibly causes the AQDS half- cell potential to shift critically close to the conduction band edge of hematite.

Calculating the half-cell potential for the AQDS side at 99.0 % SOC gives a potential of -0.31 V_{NHE}. Consequently, considering Figure 5.1, there should still be a favourable potential step for the reduction of around 200 mV, though it is significantly smaller than at, for example, 1.0 % SOC where the AQDS half-cell potential is -0.19V_{NHE} indicating a potential step of around 300 mV.

While it is clear from the data shown in Figure 5.8 that $E_{on,photo}$ of the ferrocyanide-

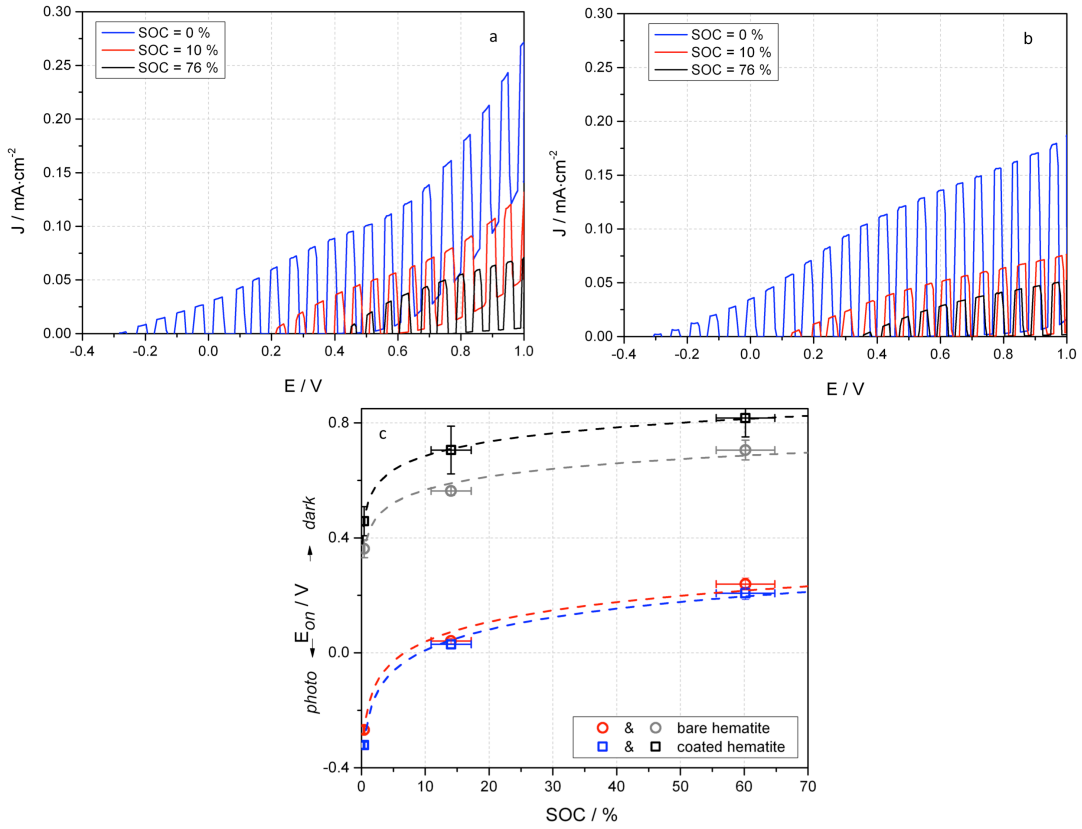

Figure 5.9 – a)+b) *J-E* chopped (1 sun illumination/dark) curves recorded in the PEC cell at different SOC for two representative samples from batch B a) bare and b) coated at a recording interval of 5 mV at scan rate of 10 mV·s^{-1}. c) Average $E_{on,photo}$ (red and blue) and $E_{on,dark}$ (black and grey) for bare hematite samples (circles) and coated (squares) with standard deviation obtained from chopped *J-E* curves recorded in the PEC cell and semi-logarithmic regressions (see Table 5.1).

Table 5.1 – Data for semi-logarithmic fits from Figure 5.9c.

Fit (E_{on} = slope·ln(SOC) + b)	Slope / mV	R^2	Max unbiased SOC / %
$E_{on,photo}$ - bare	99	0.988	9.4
$E_{on,photo}$ - coated	105	0.998	12.1
$E_{on,dark}$ - bare	67	0.981	-
$E_{on,dark}$ - coated	72	0.999	-

hematite junction is decreased by the surface treatments and especially the polyaniline layer, this effect is less clear in the RF cell tests due in part to increased ohmic losses in the cell and the overvoltage associated with the AQDS reduction (quasireversible redox reaction)[76]. Testing surface treated hematite samples for PEC water splitting in 1 M NAOH showed no perceivable change in photovoltage - Figure 5.10.

It is clear from Figure 5.8 that both surface treatments improve the photovoltage, the polyaniline coating most significantly. Low temperature steam annealing has earlier shown improvement in photoelectrochemical response of photoelectrodes due to patching of surface defects[142]. It also provides a smoother hematite layer for more homogeneous polyaniline deposition. Polyaniline is a conjugated polymer with extended Π-conjugated electron system previously used as a sensitizer in TiO_2 PV devices

for its electrical, optical and photoelectric properties[186,189]. It has also earlier been integrated with a WO_3 photoelectrode, changing the photoelectrochemical behavior significantly[185]. Recently, ferrocyanide has been studied as a hole-collector for hematite photoanodes with the aim of elucidating the properties and limitations of hematite photoanodes[180,188]. It was shown, that the most important recombination mechanism is the back-electron transfer of the photo-generated electrons into the ferricyanide $Fe(CN)_6^{3-}$ as illustrated in Figure 5.1 (red dotted arrow). The photovoltage was found to decrease with increasing ferricyanide concentration in a semi-logarithmic manner (slope 147 mV) consistent with the semi-logarithmic fits reproduced in Figure 5.8b, but with different slopes. This means that 147 mV of photovoltage is lost for every decade increase in ferricyanide concentration, here corresponding to the charged species in the flow battery and thus unavoidable. In Figure 5.8b, the photovoltage loss is 122 mV for bare and annealed samples and for the coated hematite sample only 73 mV. Thus, while annealing shifts $E_{on,photo}$ to more negative potentials, it does not change the back-electron recombination; however, the polyaniline coating does.

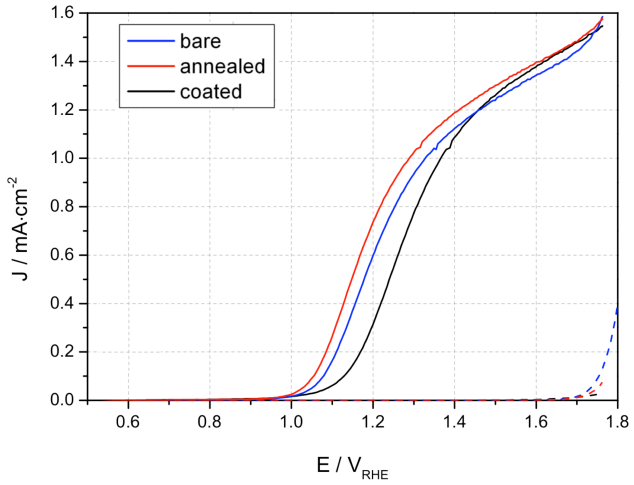

Figure 5.10 – *J-E* curves for water splitting in 1 M NaOH in the light and in the dark for hematite bare sample, annealed and coated – samples from the same batch.

An explanation as to why polyaniline actively reduces the back electron recombination with ferrocyanide can be found in literature and the principle is illustrated in Figure 5.11, which is adapted from a report where a polyaniline coated TiO_2 photoelectrode shows increased photodegradation of methylene blue[186]. Polyaniline absorbs visible light, since it has a fundamental absorption transition $\Pi \rightarrow \Pi^*$ corresponding to intramolecular charge transfer excitation, at 600 nm[189,190]. This transition is represented in Figure 5.11 together with hematite's band positions. The lowest unoccupied molecular orbital (LUMO), which is more negative in energy than the hematite conduction band, prevents back electron injection to ferrocyanide whilst maintaining a favorable energy step for holes to move from the valence band to the highest occupied molecular orbital (HOMO). For light to be absorbed by hematite, the polyaniline layer had to be very thin

so it is hypothesized that some electrons can still tunnel through the polyaniline layer and thus the back electron transfer is not completely inhibited. An optimization of the thickness could further improve this result.

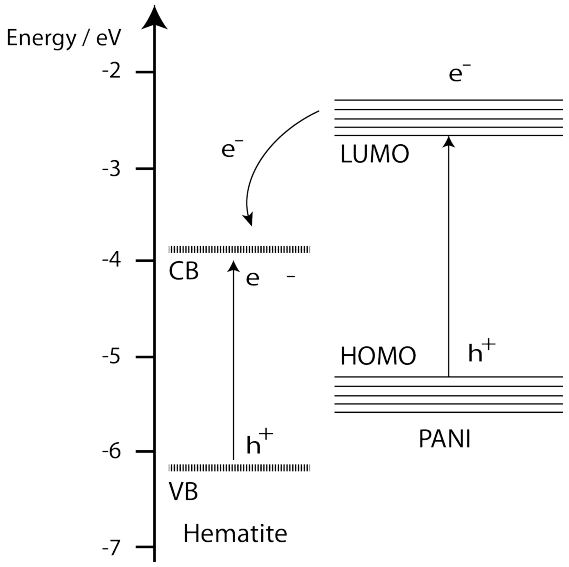

Figure 5.11 – Illustration of possible mechanism for increased electron harvesting in the hematite-PANI photoelectrode under visible light illumination (Adapted from 186).

5.3.3 Efficiency

The incident-solar-to-chemical conversion efficiency of a coated hematite sample was determined by recording the photoelectrochemical response in the PEC/RF cell as reported elsewhere[187] and the result is seen in Figure 5.12. The maximum efficiency is around 0.08 % at a current density of 0.27 $mA \cdot cm^{-2}$. In Figure 5.13a absorption spectra for the ferrocyanide side of the PEC cell for prolonged illumination test are shown to ensure that the observed photocurrent is inherent to ferricyanide production. An increase in absorption at 420 nm corresponding to the production of ferricyanide indicates that the RF cell is indeed being solar charged. Figure 5.13b represents a control test with no semiconductor to show that in fact, the absorption of ferrocyanide does not change in time without the electrical contribution from hematite.

The current work can thus be viewed as a proof-of-concept of a solar RFB that is stable, cheap and safe. Future investigations in new redox pairs, use of other low-cost phototoelectrodes such as Cu_2O or $BiVO_4$ or tandem photoelectrode systems, which have been widely described, may lead to higher efficiencies and feasible solar charged redox flow batteries[13,40,191,192]. For surface treatments, other conducting polymers such as polyacetylene and polyphenylene could be tested with other photoelectrodes in other electrolyte systems.

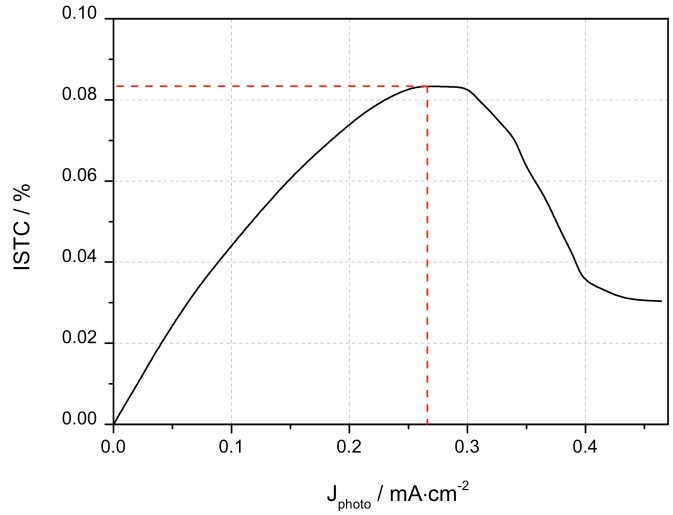

Figure 5.12 – Incident solar-to-chemical conversion efficiency of a coated hematite sample as a function of current density.

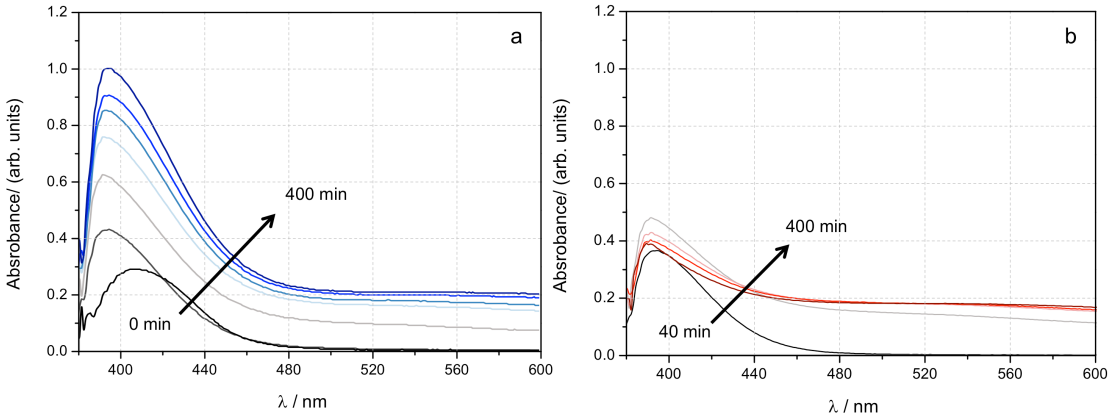

Figure 5.13 – a) The absorbance of the ferrocyanide side of the PEC/RF cell as a function of unbiased solar charging time of 40-400 min under 1 sun illumination. b) The absorbance of a 0 % SOC solution ferrocyanide left under 1 sun illumination in a separate transparent container (cuvette) with same light area-to-volume ratio for the same time as a).

5.4 Conclusions

In summary it is shown that it is possible to directly solar charge ferrocyanide/anthraquinone redox pairs for an alkaline RFB with a hematite photoanode in a photoelectrochemical process creating a solar RFB using only stable and low cost materials. Surface treatments of the hematite photoanodes have shown improved performance in terms of ferrocyanide oxidation photovoltage, which should be broadly applicable to other photoanode materials. The solar energy storage approach described here opens up many new possibilities with respect to variation of redox pairs and photoelectrodes. Specially the use of organic redox pairs in alkaline, aqueous media offers a wide range of possibilities in future fully organic solar redox flow batteries given the many possibilities of tailoring properties through manipulation of functional groups.

CHAPTER 6

Ultra-long Fe nanowires by pulsed electrodeposition with full filling of alumina templates

This chapter is dedicated to the electrodeposition of iron nanowires in porous anodic alumina templates. The effect of electrolyte molar concentration, temperature and stirring, pulse shape and barrier layer thickness on the deposition quality was investigated to potentially increase the template filling and the nanowires length. The electrodeposition temperature and current density were also found to be determinant parameters affecting NWs crystallography. A methodology of surface response design of experiment was conducted to retrieve the optimum values for the deposition parameters. With the determined optimized process, we were able to obtain filling ratios up to 93 % and aspect ratios over 10 times higher than previous reports for an alternating current method. These nanowires will be used in the synthesis of complex nanostrutures in Chapter 7.

This chapter is adapted from the published works:

- J. Azevedo, C. T. Sousa, A. Mendes and J. P. Araujo, *Journal of Nanoscience and Nanotechnology*, 2012, 12, 9112–9117.
- J. Azevedo, C. T. Sousa, J. Ventura, A. Apolinario, A. Mendes and J. P. Araujo, *Materials Research Express*, 2014, 1, 015028.

The author contributed to the planning and execution of all the experiments described in this chapter. The author was also involved on the discussion and interpretation of all results, as well as on the preparation of the manuscript.

6.1 Background

Vertically aligned magnetic nanowires (NWs) are expected to play a major role in future nanotechnologies for their high aspect ratio, small-size and quantum effects that can greatly modify the physical and chemical properties from their bulk counterparts. In the case of iron (Fe) NWs, such properties generated great interest for a wide

range of applications, such as high-density perpendicular magnetic recording media, chemical and biological sensors and microelectromechanical systems[193–197]. Within the numerous methods of fabrication, template assisted deposition within PAA has been widely used to prepare large arrays of vertically oriented metallic NWs[198–201]. The ability to tailor the PAA template morphology, combined with the simplicity and low cost of the electrodeposition methods available to fill them, makes this technique ideal for industrial applications. Although the electrodeposition of Fe NWs in PAA templates dates back 20 years[201], the main problem concerning the uniform filling of long templates remains unsolved. To our knowledge, only low thickness (few micrometers) templates have been used to fabricate Fe NWs and with filling fractions far from 100 %.

The electrodeposition process, uses an electrical current to reduce cations in solution to metal forming a metallic coating[202]. Using PAA as template presents a challenge because the interface between the metallic aluminum substrate and the nanopores is a thick layer of alumina ($\sim$ 52 nm if standard oxalic acid anodization conditions are used). Alumina is a good dielectric material[203], and storing the electric charge creates an electrical field that blocks the current flow[200]. There are two approaches to overcome this limitation depending whether the applied electric current is constant (DC) or alternate (AC). The first, to avoid charging the dielectric barrier, requires the removal of the bottom insulator, and therefore of the Al substrate, followed by the deposition of a metallic contact (usually Au)[114,195,197,204–206]. This method presents major disadvantages such as an elaborate fabrication procedure and the difficulty to manipulate templates thinner than 20 μm[205]. On the other hand, AC methods only require the reduction of the barrier layer thickness (δ_b) to perform deposition, given the alternate polarization pulse that allows discharging the alumina capacitance. The most common approach to reduce δ_b is to perform a pore widening process in a bath containing phosphoric acid (H_3PO_4) at 30 $^\circ$C[193,195,207–209]. For the particular case of the electrodeposition of Fe NWs, both methods have been reported. However, achieving large pore fillings in PAA templates thicker than few micrometers either required a too laborious process (DC) or was limited by hydrogen formation, due to the high cathodic potentials and the slow diffusion transport of the ionic species inside the PAA pores (AC)[210].

Recent results demonstrated[137,200,211–213] that pulsed electrodeposition (PED), is an excellent alternative to the two previous methods. In PED, the reduction of the PAA barrier layer is not performed by chemical etching, which isotropically attacks the alumina, hence reducing the wall and barrier layer thickness alike, usually leading to low PAA homogeneity. This method allows reducing the barrier layer thickness without changing the diameter of the main pore[137,200]. Using a non-steady-state anodization we were able to accurately tune δ_b by controlling the final anodization voltage. By exponentially reducing the anodization potential, δ_b is significantly reduced, achieving nominal values as low as $\sim$ 4 nm for anodization potential $\approx$ 3 V, giving origin to a dendritic structure at the bottom of the template without changing the characteristic

PAA nanopore dimensions. This enables current to flow through such small insulating layer[137]. Also, in contrast with typical square wave AC deposition, a modulated electric pulse is applied and a rest pulse is introduced to counterbalance the slow ionic diffusion and restore the metallic ions concentration at the deposition interface, leading to a more uniform NW growth[136,137,200,210].

In this work, for the first time, we address the influence and optimization of the main pulsed electrodeposition parameters (current density and rest pulse duration; electrolyte temperature, molar concentration and stirring; and barrier layer thickness) on the Fe NWs fabrication aiming uniform filling of long membranes. Afterwards, a cross parameter study was performed, allowing us to reach the optimum pore filling conditions with which templates with 20 μm length are almost completely filled (93 %), preserving high pore filling values up to 50 μm.

6.2 Experimental Details

6.2.1 Porous Anodic Alumina Membranes Fabrication

PAA templates were fabricated from Alfa Aesar high purity 0.25 mm thick Al foil (99.997 %). Each Al foil was rinsed in acetone, ethanol and distilled water. Immediately prior to anodization, the Al foils were individually electropolished in a stirred 10 °C bath of perchloric acid, $HClO_4$, and ethanol, C_2H_5OH, (volume ratio 1 : 4) at 20 V during 2 minutes, to reduce surface roughness and create nanopatterns for posterior pore nucleation[214]. Finally, the substrates were rinsed in ethanol, followed by deionized water and dried in air.

In order to fabricate highly vertically oriented PAA templates a two-step anodization process was used[215]. First anodizations were carried out in 0.3 M oxalic acid, $(COOH)_2$, at 40 V and 2 °C, during 24 h, using a Keithley 2400 power supply. The formed alumina template was then removed in a mixture of 0.4 M phosphoric acid, H_3PO_4, and 0.2 M cromic acid, H_2CrO_4, at 70 °C for 12 h. A second anodization was performed with the same conditions as the first one with a rate of $\sim$ 42 nm/min. For the individual studies the template thickness was chosen to be 10 μm. Immediately before electrodeposition, δ_b was reduced by applying an exponentially decreasing voltage from 40 V down to the desired potential[137]. More details on PAA templates can be found in Appendix A.

6.2.2 Iron Electrodeposition

A sequence of three different pulses was applied using a Keithley 2400 power supply. Firstly, a negative current density (10 - 510 mA·cm^{-2}) is applied for 8 ms to deposit the metal inside the PAA pores. Then a discharge pulse is applied during 2 ms with a voltage corresponding to the last applied potential drop of the δ_b defined in the barrier layer thinning process. This positive polarization pulse discharges the capacitance of

the barrier layer and interrupts the electric field at the deposition interface after each deposition pulse. It has been further reported that this pulse repairs discontinuities in the barrier layer and improves its homogeneity[200]. Finally, a rest pulse is applied allowing repositioning the ions in the deposition interface. The electrolyte used was a mixture of x g/L iron(II) sulfate heptahydrate, $FeSO_4 \cdot 7H_2O$, 45 g/L boric acid, H_3BO_3, and 1 g/L ascorbic acid,$C_6H_8O_6$, where x was systematically varied between 2.78 g/L and 278 g/L. The pH value of the electrolyte was maintained at 2.4 – 3.0.

The factors considered to optimize the Fe PED were the electrolyte molar concentration (C), temperature (T) and stirring, rest pulse duration (t_{rest}) and deposition pulse current density (j) and δ_b with standard values of 0.43 M, 20 °C, 0 rpm, 0.7 s, 70 mA·cm^{-2} and 10.4 nm, respectively[136,137,200,201,209,216]. Given the large number of factors, statistical methods were employed to reduce the number of experiments necessary to understand the influence and cross influence of the variables. Response surface methods (RSMs) are a combination of statistical design of experiments tools effective to study responses via sophisticated optimization models[217]. The RSM analysis was achieved with JMP 9 software[218] using a central composite design (CCD) to fit second order polynomials, which represent the effect of the operating conditions on the process response. The model parameters were obtained by the least square method[219] and are represented in Table 6.1 together with their levels. PED was monitored using a Keithley 2400 power supply connected to a personal computer by a GPIB interface.

Table 6.1 – CCD values and respective levels.

Factor	Level		
	-1	**0**	**1**
C (M)	0.01	0.5	1
T (°C)	5	20	40
Stirring (rpm)	0	100	200
t_{rest} (s)	0.3	0.7	1.2
δ_b (nm)	4	10	17
j (mA·cm^{-2})	10	75	125

6.2.3 Sample Characterization

A QUANTA-FEI field emission scanning electron microscope (FE-SEM), was used to evaluate the filled percentage (f_p) of the samples after ion milling ($\sim$ 500 nm) to remove the excess of material deposited on top of the PAA template. For each sample at least three different top areas were analyzed to obtain a more representative f_p value. The mean value and deviation are represented in the figures. The statistical count of f_p was performed using an open source software for image analysis[160]. In each sample, three randomly selected regions of the surface were observed to infer a representative f_p. The template thickness of each sample was determined by cross section FE-SEM images.

The samples were folded up to 180º to break the PAA template and the cracks were observed. The crystalline structure of the samples was analyzed XRD in a Siemens Bruker AXS D5000 diffractometer in the $\theta - 2\theta$ geometry using the Cu – K_α line with wavelength λ = 1.540593 Å. Magnetization measurements were performed using a Superconducting Quantum Interference Device (SQUID) magnetometer from Quantum Design.

6.3 Results and Discussion

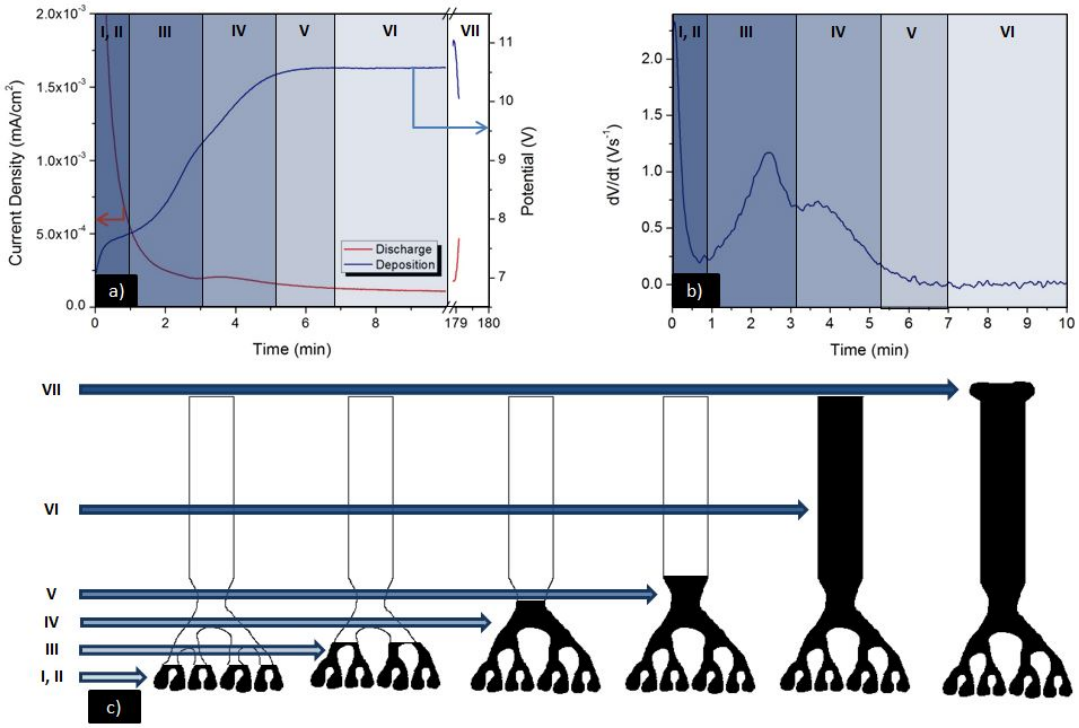

Figure 6.1 – Stages of nanowire growth embedded in PAA template: (a) V_{dep} and j_{dis}, (b) dV_{dep}/dt and (c) layout of the stages of nanowires growth.

One of the advantages of PED is the ability to control live the deposition stage - Figure 6.1a to c. Seven different regimes can be identified in deposition potential, V_{dep}, and discharge current density, j_{dis}, curves all ascribed to distinct stages of PAA filling. As the last dendritic generations are almost instantly filled due to the large nucleation sites they are not distinguishable (represented by stages I and II with and increase of 7.1 to 7.8 V over the first 60 seconds). The area shift being more significant to the following dendritic generation, it is already clear the filling effect on the deposition curve with an increase of the V_{dep} to 9.5V in 120s, in stage III (twice the previous generation filling time). The last generation of dendrites is represented by stage V corresponding to an increase in V_{dep} to 10.5V in 134 s. After the dendrites filling, a small decrease in the V_{dep} is associated with the cone-like pore filling (Stage V). Afterwards the stem pore is

filled with a nearly constant potential during $\sim$ 170 min. This particular PAA template had 10 μm length. When the NWs reach the top of the template, a sudden decrease in V_{dep} is observed accompanied with a noise enlargement. Observing dV_{dep}/dt profile the different filling stages are more evident (see Figure 6.1b). Each dendrite generation transition is accompanied by a minimum in the potential derivative. Considering the PAA template resistance with a corresponding resistivity a minimum value of dV_{dep}/dt corresponds to a larger pore area. Along each generation, D_p decreases before it increases again in the next generation. So the pore area shifts from maximum to minimum when the pores branch, which is in accordance with Figure 6.1b.

The study of the deposition parameters was performed in two steps: first an experimental individual study of each parameter to understand its direct influence on the deposition quality; then, a cross influence of the parameters was studied through RSM.

6.3.1 Rest Pulse Duration

The t_{rest} is one of the three regimes in pulsed electrodeposition (the other two are discharge and deposition)[200]. This period serves has a rest time for the ion concentration to recover after a deposition pulse. In this way a homogenous concentration along each pore before a new deposition pulse is guaranteed. This pulse also improves the homogeneity of the deposition and limits the hydrogen evolution[200].

Given the importance of t_{rest} in electrodeposition[200,210] we studied its influence on the deposition quality (herein measured by the PAA pore filling percentage) from 0.3 to 1.2 s. By monitoring V_{dep} the electrodeposition is controlled in real time. Observing Figure 6.2 different regimes are identified: first, the dendrites are filled (associated with the increase in V_{dep}) as the effective area of deposition in the dendrite region is larger than the stem pore region (associated with the nearly constant V_{dep}). As the template begins to fill, the NWs start to emerge from the pores, forming mushroom-like caps, which coalesce into a metallic thin film at the surface, the electrodeposition area increases very rapidly and V_{dep} decreases and presents a typical noise (see Figure 6.2).

Lower t_{rest} results in higher effective deposition time per pulse. Therefore it would be expected that the time necessary for the NWs to reach to top of the PAA template (filling point) would increase linearly with t_{rest}. In fact, up to 0.9 s the filling point increases. For 1.2 s the filling point is lower which can be associated with some NWs reaching the top quickly given the heterogeneity of the deposition[137]. To evaluate the deposition quality in response to t_{rest}, SEM images were analyzed and some reference t_{rest} values are presented in Figure 6.3 and the deposition quality evaluated, for each sample (see Figure 6.4).

A maximum is observed at 0.6 s with a filled percentage of 91.9 %. For low t_{rest} values ($\leq$ 0.5 s), only a few pores presented a complete filling and a formation of hydrogen bubbles on the PAA was observed (region I). Given the slow rate of diffusion

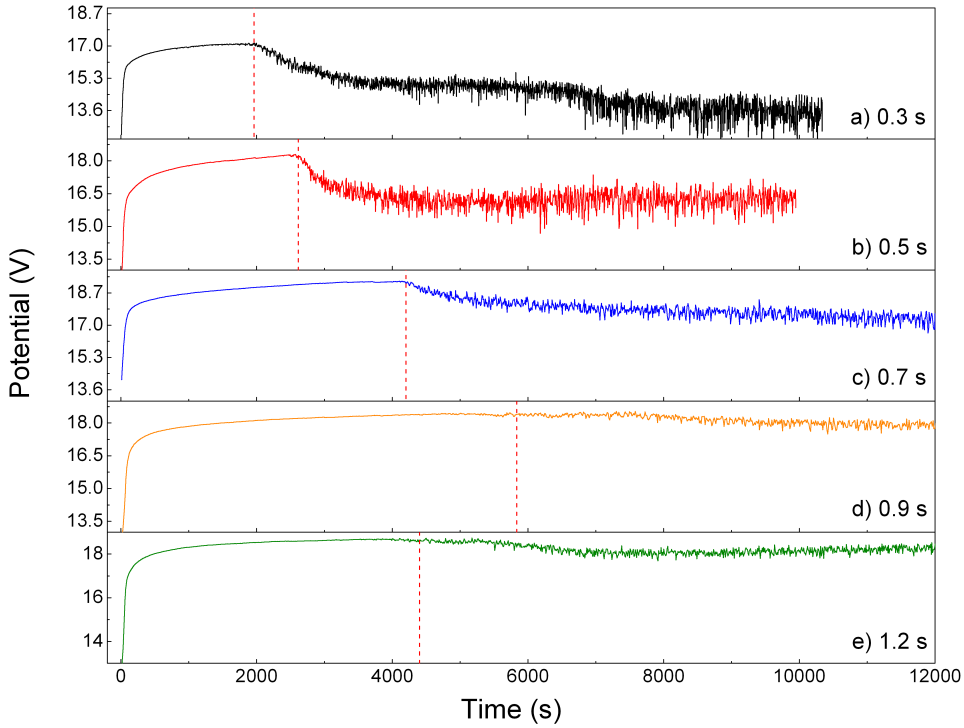

Figure 6.2 – Deposition profiles taken during the electrodeposition: a) 0.3 s, b) 0.5 s, c) 0.7 s, d) 0.9 s and e) 1.2 s. For each curve the point where the NWs reach the top of the template is marked (red line).

of the Fe ions, the reduction of the concentration near the nucleation sites lead to a heterogeneous filling. The fact that 0.3 s and 0.5 s present a more pronounced noise (see Figure 6.2) is indicative that not all NWs reached the top of the template simultaneously, i.e., of a inhomogeneous growth of the NWs. As t_{rest} increases, above a threshold value ($\sim$ 0.55 s), the Fe concentration is replenished and a uniform NWs growth is observed[210]. During the deposition, the PAA is exposed to the electrolyte chemical attack that damages the template. Therefore, as t_{rest} further increases, so does the template exposure to the electrolyte, which will inevitably affect the deposition quality, here represented as a decrease in the template filling ratio. These results are in well agreement with nickel PED in PAA templates[200].

The rest pulse also has an influence of the deposit morphology. The structure and phase composition of the sample was determined by XRD (see Figure 6.5). XRD allowed identifying the iron phase in the NWs. The mean crystalline diameter (D) was estimated using the (110) Bragg reflection. For that purpose the Scherrer's equation was used[220]:

$$D = \frac{k\lambda}{\beta cos(\theta)} \tag{6.1}$$

where θ is the diffraction angle, β is the full-width at half maximum, k is the shape factor (0.9 was used) and λ is the wavelength of the incident X-ray. From the obtained values

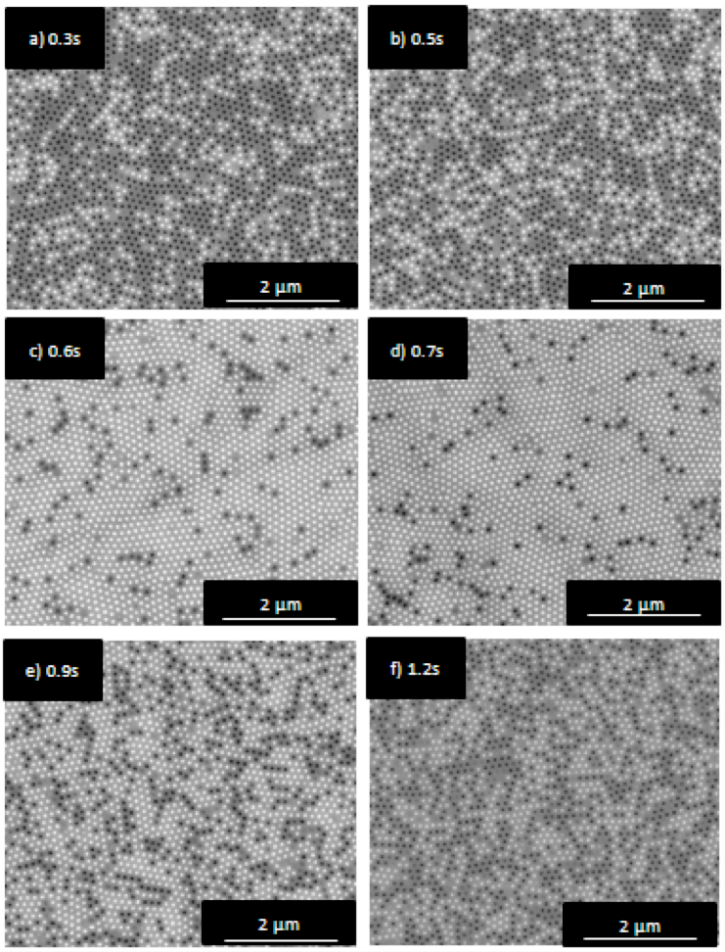

Figure 6.3 – Top SEM images of electrodeposited PAA templates with iron in different rest pulse durations: a) 0.3 s, b) 0.5 s, c) 0.6 s, d) 0.7 s, e) 0.9 s and e) 1.2 s.

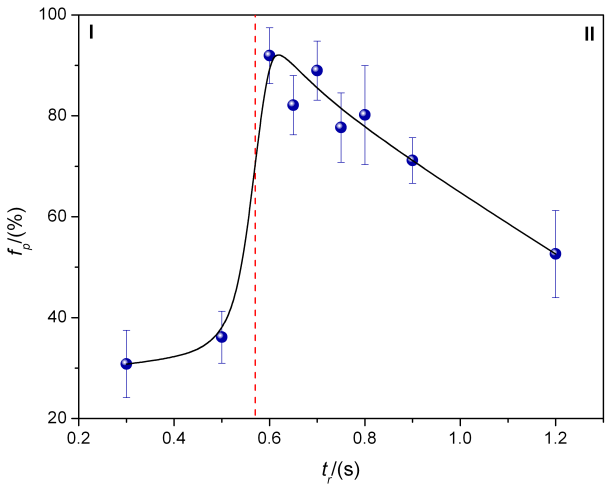

Figure 6.4 – Filled percentage dependence on rest pulse duration. The solid line is a guide to the eye.

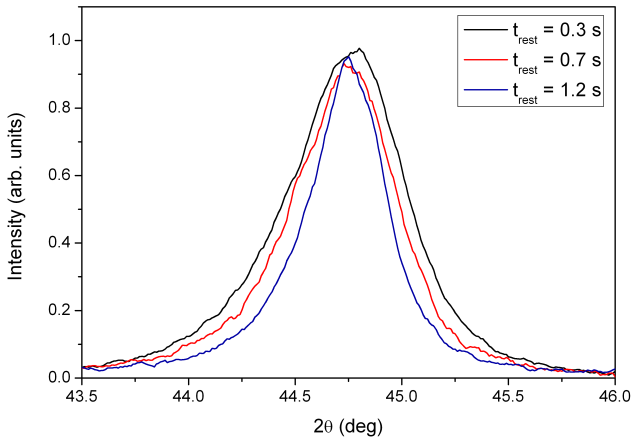

Figure 6.5 – X-ray diffraction pattern of the Fe NWs in an amorphous alumina matrix for different rest pulse durations. The Bragg reflection corresponds to 110.

an overall increase is observed (see Figure 6.6) compatible with the lower effective deposition rate. The decrease of the grain for t_{rest} = 0.9 s needs further research in order to clarify its nature.

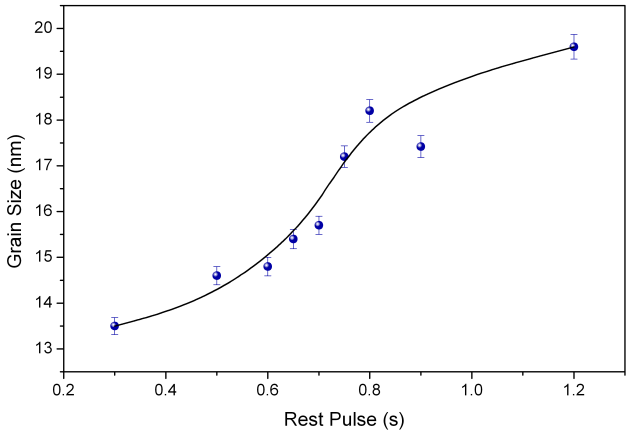

Figure 6.6 – Grain size dependence on rest pulse duration. The solid line is a guide to the eye.

In this simulation, the optimum time for the rest pulse duration was simulated in order to secure a homogeneous concentration at the bottom of each pore. The COMSOL Multiphysics software was used for obtaining the transport of diluted species[221]. The model used is based on the geometry presented in Figure 6.7. A single pore was simulated to maintain a reasonable number of degrees of freedom. In the beginning of the simulation, the whole domain is at the initial condition of 0.43 M (Fe ion concentration in the electrolyte). The deposition occurs only at the bottom of the pore were a depletion of the iron ions concentration takes place during a deposition pulse.

This negative flux, applied during the deposition pulses was determined based on

the applied current density (70 mA·cm^{-2}). Giving that $FeSO_4 \cdot 7H_2O$ contains Fe^{2+} ions it takes two electrons for each deposited iron ion (assuming a 100 % efficiency). The total number of deposited ions per second was estimated to be 0.203 mol·s^{-1}·m^{-2}.

As the reservoir of electrolyte compared to a single pore is practically infinite, a constant concentration was set above the pore. After a deposition pulse, the concentration tends to normalize inside the pore. The concentration and concentration gradient where monitored in the bottom of the pore during several PED pulses. From Figure 6.8, it is clear that 0.7 s is enough for the concentration homogenization in the pores. Above this threshold, the concentration along the nanopores is saturated at the initial value of 0.43 M. For values lower than 0.7 s the concentration rapidly decreases along the pore. Given the approximation degree of the simulation, we can only infer the real behavior of the concentration with t_{rest}. The influence of non-accounted parameters, could be the reason for the optimum value in the simulation ($\sim$ 0.7 s) being different from the experimental results ($\sim$ 0.6 s).

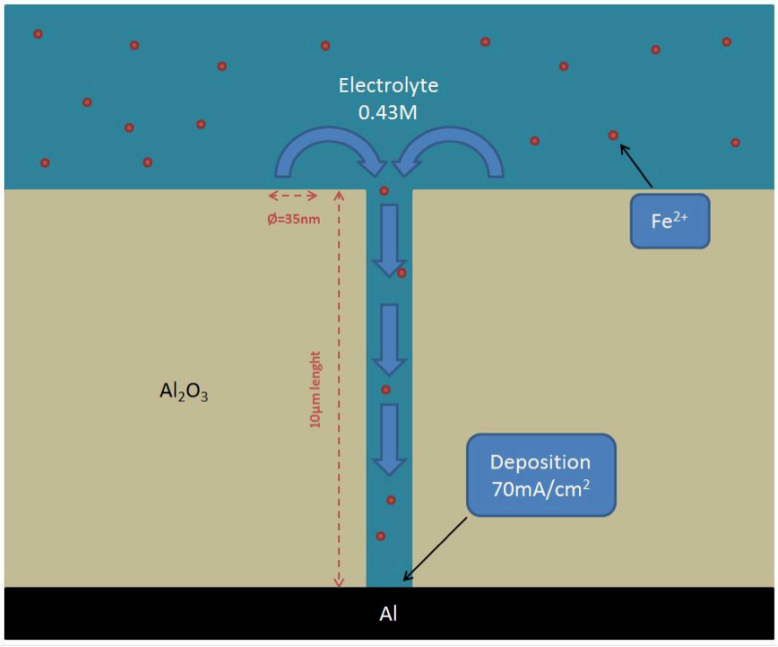

Figure 6.7 – Geometry and conditions used in the simulation.

6.3.2 Electrolyte Molar Concentration

The electrodeposition was carried out in an iron (II) sulfate bath, as it produces deposits that are smooth and can be operated at room temperature, in contrast with the ferrous chloride-calcium chloride bath[202]. As reported by Gadad *et al.*[222], the use of Fe^{2+} electrolytes without H_3BO_3 leads to deposits containing significantly higher amounts of oxygen. Also, H_3BO_3 can act as a buffer to the hydrogen generation at the cathode, increasing the smoothness, compactness and continuity of the NWs[193,223,224].

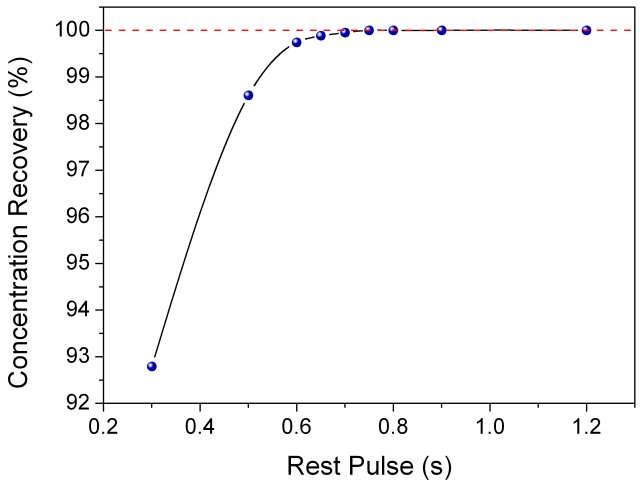

Figure 6.8 – Concentration before each deposition pulse for different rest pulse durations.

Since in nanopore structures, the electrodeposition is diffusion limited according to Fick's law[224], the bulk molar concentration of $FeSO_4 \cdot 7H_2O$ was varied in the range of 0.01 to 1 M, in order to study the influence of Fe^{2+} concentration in the electrodeposition efficiency. Figure 6.9a shows the initial electrodeposition potential measured during the first electrodeposition pulse (8 ms), which corresponds to the deposition of the first metallic atomic layers at the pore bottom (V_0) as a function of C. As the concentration of the electrolyte increases, an initial steady decrease of V_0 is visible, from 26 V for 0.01 M to 8 V for 0.25 M. In this range there are not sufficient ions for a uniform deposition and a higher potential needs to be applied to increase the electric field assisted diffusion in order to maintain the fixed current density. This potential corresponds to the applied bias

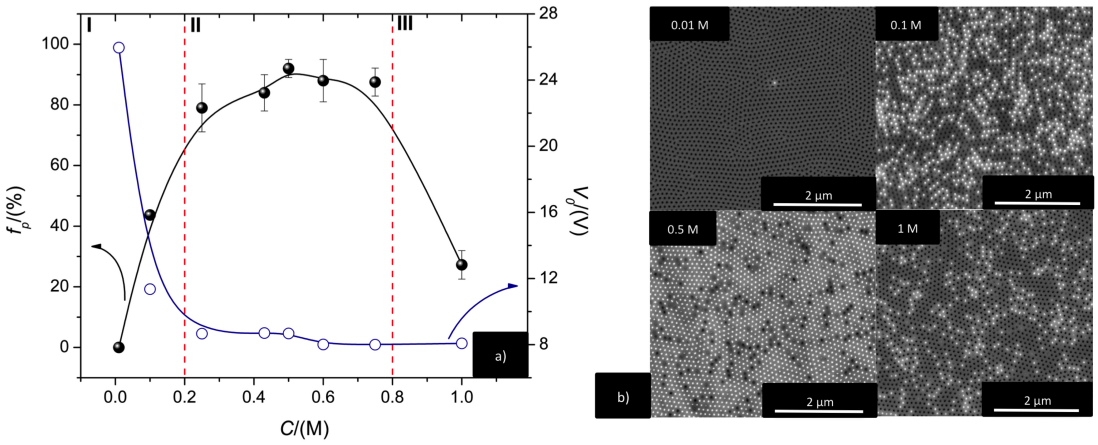

Figure 6.9 – (a) Effect of $FeSO_4 \cdot 7H_2O$ concentration on f_p and V_0. The PED parameters used are the standard values (T, stirring, t_{rest}, j and δ_b of 20 °C, 0 rpm, 0.7 s, 70 mA·cm^{-2} and 10.4 nm, respectively). The solid lines are a guide to the eye. (b) Surface SEM images of samples electrodeposited at 0.01 M, 0.1 M, 0.5 M and 1 M.

to fix the current density at a predefined value. It can be seen that the potential increases with the solution concentration decrease. When an iron ion reaches the interface of the alumina barrier it is reduced to metal iron and the electron transfer allows for the current to flow. To have a constant current density, a certain potential needs to be applied to reduce the ions and overcome the thin insulator alumina layer. If there are not sufficient available ions to be reduced the potential starts to increase to force the electrons through the system and maintain the current density. In this regime, the ionic concentration is rapidly depleted near the pore bottom and the growth is less compact following the electric field direction (vertical) instead of a more homogeneous growth given by a typical diffusion-controlled process[224,225]. These irregularities in the NWs morphology during their growth reflects on lower f_p values (< 50 %), as shown in Figure 6.9.

As the ionic species concentration increases, the electrodeposition becomes a diffusion controlled process and the deposits are smooth and compact. Figure 6.9 shows an optimum range of C values is then observed between 0.25 M and 0.75 M, with a f_p maximum of 92 % at 0.5 M. For higher C values (third regime, Figure 6.9; above 0.8 M) the decrease in f_p can be attributed to the solubility of Fe-O-H being exceeded more easily, associated with the oxides formation, and hydrogen evolution[197,222]. The pores are then blocked, causing an inefficient electrolyte renewal at the electrolyte/NW interface and the deposition efficiency decreases. The obtained experimental results can be observed in the SEM images (Figure 6.9b).

6.3.3 Temperature

Deposition temperature is one of the key features to obtain highly uniform growth of the NWs[197,225,226], so the effect of deposition temperature (between 5 °C and 40 °C) in f_p was here also studied. For temperatures below 5 °C the solution precipitated very quickly, covering the PAA surface and thus inhibiting the deposition, while for T > 40 °C a strong H_2 evolution was observed which hinders the electrodeposition, specially if the formed gas bubble are large enough to completely block the pores.

The f_p values, for different temperatures, are presented in Figure 6.10a, together with the electrodeposition time at which a film started to be deposited on the surface of the PAA membrane (filling time). The electrodeposition rate (Figure 6.10a) increases for temperatures above 20 °C (for 40 °C it is 5 times faster than for 20 °C), but the lower f_p values beyond this point indicate an irregular NW growth.

It is clearly seen that the overall f_p of the Fe NWs is significantly enhanced as the deposition temperature is decreased down to 20 °C. These low temperatures lead to a slow ion diffusion (Einstein-Stokes equation[227]) inside the PAA pores and consequently reduce the heterogeneity of NW growth[212,225,228]. Therefore, below the 20 °C threshold the deposition is smooth and regular and f_p reaches a stable value around 80 % (regime I, Figure 6.10). However, this stability is related with the balance between the high length uniformity and electrolyte precipitation that for temperatures below 5 °C starts to inhibit

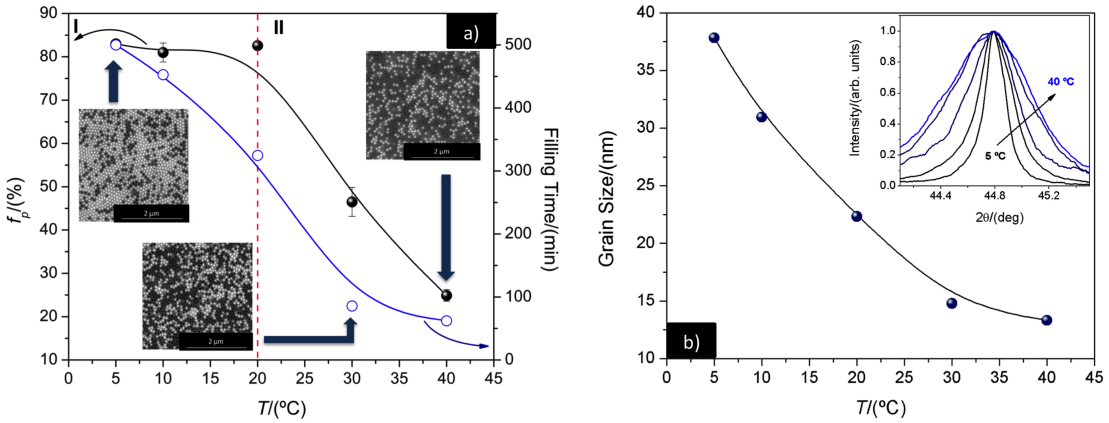

Figure 6.10 – (a) f_p and filling time dependence on electrodeposition temperature with corresponding surface SEM images. The PED parameters used are the standard values (C, stirring, t_{rest}, j and δ_b of 0.43 M , 0 rpm, 0.7 s, 70 mA·cm^{-2} and 10.4 nm, respectively). The solid lines are a guide to the eye; (b) Grain size *vs* temperature and Fe (110) Bragg diffraction peak (inset) for different electrodeposition temperature. Error bars contained within experimental points. The solid line is a guide to the eye.

electrodeposition.

Ion diffusion speed increases with temperature and so does the deposition rate (see Figure 6.10a). As ions are more readily available in the cathode, native defects in the alumina barrier will have major influence in the electrodeposition given that the deposition is no longer diffusion limited. Small imperfections in the alumina barrier and pore structure along the PAA template lead to different local current densities and a heterogeneous material deposition[229]. Therefore, the faster growing pores eventually reach the top of the template and block their neighbors by growing over the adjacent pores in a mushroom-like structure[213], leading to f_p values as low as 25 %. The heterogeneous j distribution can be verified by XRD measurements where high temperatures produce smaller grain sizes, associated with higher j [Figure 6.10b; determined using the Scherrer's equation].

6.3.4 Stirring

We tested the influence of stirring in f_p and V_0, by introducing a teflon fan in the electrolyte solution and turn it at different rpm (Figure 6.11). This way the bulk electrolyte outside the PAA was stirred. For low stirring velocities (regime I, Figure 6.11), f_p values are high (~ 80 %) with average $\overline{V_0}$ = 10.2 V. However, when one increases the stirring velocity above 50 rpm, V_0 increases and f_p decreases abruptly (from 80 % to 0 %).

To our knowledge, the influence of stirring on the deposition quality in PAA templates has never been studied. Although it was expected that stirring would benefit the homogenization of the electrolyte, thus improving the electrodeposition quality, in the case of electrodeposition inside the PAA pores it is clear that stirring has a negative effect. Ren *et al.*[228] reported the same behavior for the electroplating of Ni thin films. They argued that Ni was electrodeposited in several steps with the intermediate formation of

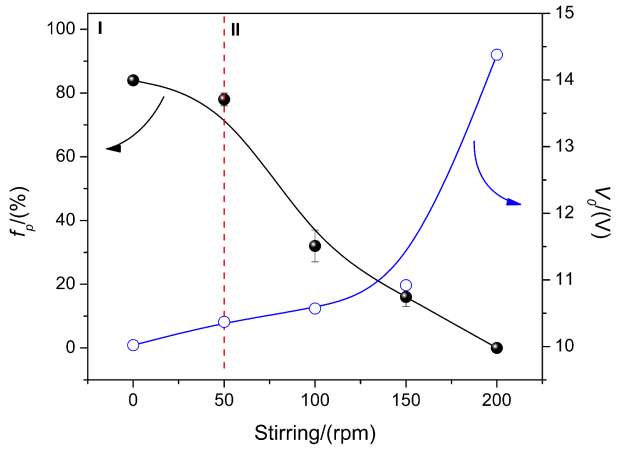

Figure 6.11 – Dependence of f_p and V_0 on stirring velocity. The PED parameters used are the standard values (C, T, t_{rest}, j and δ_b of 0.43 M, 20 °C, 0.7 s, 70 mA·cm^{-2} and 10.4 nm, respectively). The solid lines are a guide to the eye.

adsorbed Ni(OH). With stirring, the admission of H^+ is hindered, creating conditions for the accumulation of adsorbed Ni(OH). The same thing is likely to be occurring in our experiments, as Fe electrodeposition is believed to also proceed in a two-step process with the intermediate formation of absorbed Fe(OH)[222]. Further studies should be made to completely understand the influence of stirring in the electrodeposition of Fe in PAA templates.

For very high stirring speeds, the hydrodynamic conditions at the alumina surface become irregular and the rotation is strong enough to deplete the electrolyte in the center of the sample so that only the outer areas were filled, although at low f_p.

6.3.5 Barrier Layer Thickness

The bottom layer thickness determines the electron flow during electrodeposition, that enables the ion reduction and consequent deposition. We therefore studied the influence of δ_b on the Fe NWs deposition quality by varying the barrier layer thickness from 4 to 17 nm (corresponding to 3 V and 13 V, respectively).

Figure 6.12a shows the deposition curves for different samples, where the maximum potential value in each curve (corresponding to the final stage of ramifications filling) is marked (t_d). For very low δ_b, the electric current distribution in the PAA pores is very sensitive to small thickness variations. Then, a small portion of the pores will be supplied with enough current to rapidly grow, reaching the top of the template and blocking the neighboring ones. This can be observed in Figure 6.12a where, for δ_b = 3.9 nm, the potential is still increasing (dendritic filling of the slow growing NWs) when the typical noise corresponding to the deposition on top of PAA appears (rapidly growing NWs).

For high δ_b values, the resistance that the alumina barrier offers the electron flow is increased. Thus, upon a constant j pulse and given the fluctuations in the thickness of the oxide layer, some pores suffer dielectric breakdown and j is immediately distributed

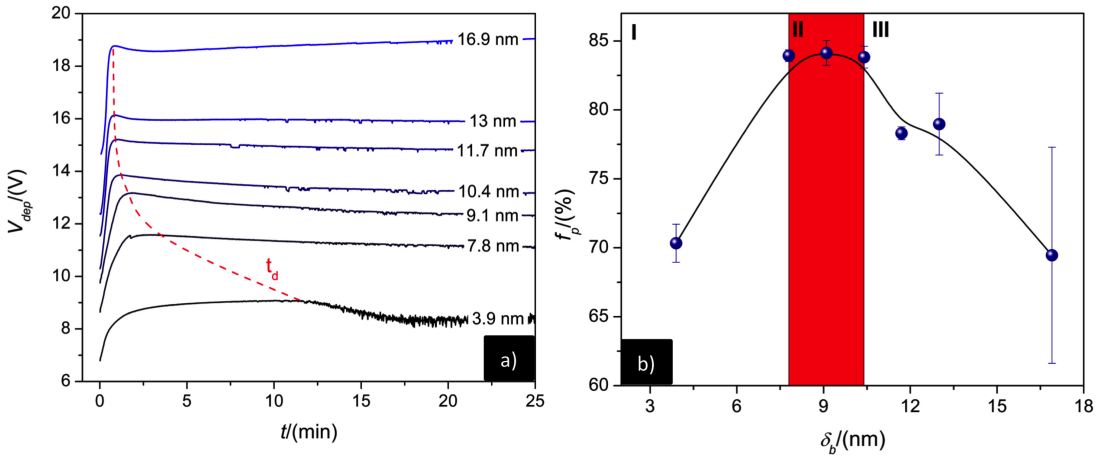

Figure 6.12 – (a) Deposition profiles for different δ_b and corresponding dendrites filling times (t_d); (b) Dependence of f_p with δ_b. The PED parameters used are the standard values (C, T, stirring, t_{rest}, j of 0.43 M, 20 °C, 0 rpm, 0.7 s and 70 mA·cm^{-2}, respectively). The solid lines are a guide to the eye.

to the resulting low resistance channels. Contrarily to the low δ_b value cases, this time only a few pores will actually start to fill, although at very high rates, giving rise to low t_d values. Since δ_b has random fluctuations, the f_p values largely vary from site to site, as observed in different surface areas of the same sample by SEM, inserting an associated error in the measurements. Figure 6.12b shows f_p as a function of δ_b, where an optimum regime (8 nm < δ_b < 10 nm) is observed with $f_p \sim 85$ %, below and above which it declines abruptly. These results are in good agreement with previous studies for Ni NWs, where an optimum value was observed at ~ 10 nm[137].

6.3.6 Deposition Pulse Current Density

The applied j during the deposition pulse will determine the number of available electrons to reduce the Fe^{2+} ions in the electrolyte. Hence, it will also establish the deposition rate and concentration depletion at the end of each deposition pulse. Furthermore, it is a crucial parameter to obtain a good barrier layer stability and prevent dielectric breakdowns. Therefore, a set of j values was tested, ranging from 10 to 510 mA·cm^{-2}.

Figure 6.13a shows deposition profiles at different j values. The time that it takes for the NWs to reach the top of the template decreases with increasing j, as the rate of Fe reduction is enhanced, being also very clear in the first stages of deposition (inset). In Figure 6.13b we observe that V_0 follows the expected linear relation with j (Ohm's law) from low j values up to 125 mA·cm^{-2} (low j regime). Since every experiment was conducted in the same conditions, the reproducibility of the quality of the template can be evaluated from this result, as the resistivity of the barrier layer and electrolyte remains constant[229]. For higher j, deviations from the linear trend are observed.

The f_p for different j values is presented in Figure 6.14a. The existence of the two different regimes is here also clear, with a threshold at 125 mA·cm^{-2}. In the low j regime

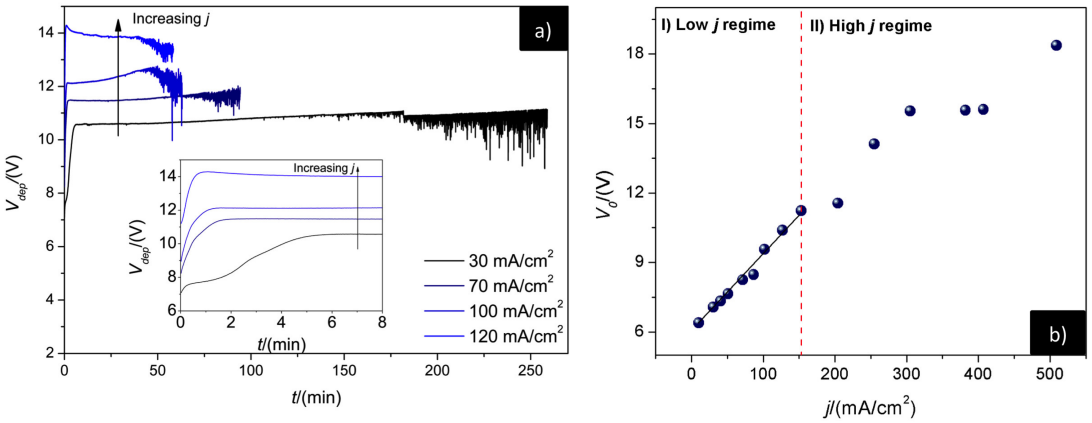

Figure 6.13 – (a) Deposition profiles, with increasing *j*, taken during electrodeposition (initial stages are shown in detail in the inset); (b) V_{dep} dependence on *j*. The PED parameters used are the standard values (*C*, *T*, stirring, t_{rest}, and δ_b of 0.43 M, 20 °C, 0 rpm, 0.7 s and 10.4 nm, respectively).

a rapid increase of the filling percentage from f_p~ 20 % (at 40 mA·cm^{-2}) to f_p> 90 % (at 70 mA/cm^2) is seen. Above this value a saturation is reached with a maximum of f_p= 95 % encountered for 117 mA·cm^{-2}. For *j* higher than 125 mA·cm^{-2}, f_p presents a random behavior and low reproducibility. Nevertheless, an overall increasing tendency is observed, from f_p of 12 % to 93 % at 152 mA·cm^{-2} and 510 mA·cm^{-2}, respectively.

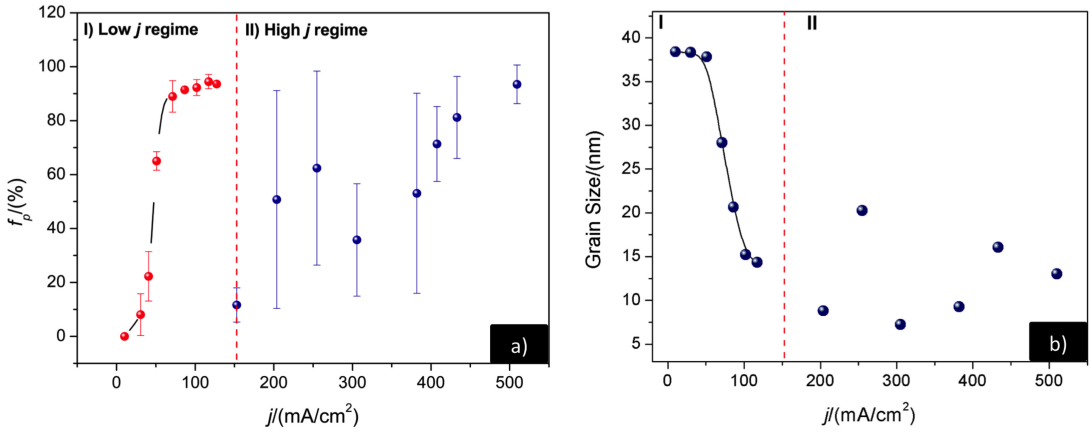

Figure 6.14 – (a) Filled percentage dependence on the current density; (b) Grain size *vs j*. Error bars contained within experimental points. The PED parameters used are the standard values (*C*, *T*, stirring, t_{rest}, and δ_b of 0.43 M, 20 °C, 0 rpm, 0.7 s and 10.4 nm, respectively). The solid lines are a guide to the eye.

In the low *j* regime, one expects that with increasing current, more pores are filled since electrons are readily available. For very low currents, f_p is also low as the deposition is slow and template exposure to the electrolyte also increases, affecting the deposition quality. As *j* increases, the deposition becomes more regular as the majority of the pores receive enough current for a good homogeneous growth. A saturation regime is observed from 70 to 125 mA·cm^{-2}, with a maximum f_p = 94 %, given that the depletion of Fe^{2+} at the pores bottom becomes a predominant factor as *j* increases,

i.e. more electrons are available for the reduction reaction but there are no ions to be reduced.

For high *j* values, several factors start to became predominant, such as pH fluctuations, H_2 evolution and even dielectric breakdown in the alumina barrier due to excessive local current[200,206]. In these situations, given the heterogeneity between pore impedances[229], the current distribution will be uneven and a preferential growth in a fraction of the template is observed. The lower limit of this regime presents the lowest f_p. It is the point where dielectric breakdown occurs in the barrier layer creating low resistance channels for the electrons to flow, limiting the current access in most of the PAA pores. As *j* increases, so does the number of pores that suffer dielectric breakdown and that will be efficiently deposited, thus the rising trend. Since the alumina barrier layer is the major resistive component (by three orders of magnitude)[229], very small variations in δ_b will have a major impact in the *j* distribution. Thus, dielectric breakdown depends on the fluctuations in δ_b, giving rise to the large error bars. This is also observed in the V_0 variations shown in Figure 6.13b which are due to the random nature of the pore bottom dielectric breakdown distribution in the PAA membrane. When extremely high *j* values are used most of the pores suffer a breakdown and higher f_p are observed.

The previous conclusions are supported by a grain size analysis. The increase of *j* in the low *j* regime leads to a smooth decrease of the grain size Figure 6.14b)[220]. However, in the high *j* regime the grain size does not follow any definitive trend. The high *j* values used and consequent dielectric breakdown of the barrier layer lead to non-homogeneous current distributions and different local *j*-values, during pore filling, compared to the nominal value due to the fluctuations in the nominal thickness of the barrier layer.

From magnetic measurements, we were also able to obtain the saturation moment of each sample and, combined with the deposition total time, to determine the deposition rate of at 0.34 $ng \cdot cm^2 \cdot s^{-1} \cdot mA^{-1}$.

6.3.7 Cross Parameter influence

After understanding all the primary effects of the electrodeposition parameters, a response surface methodology was implemented to assess the optimum set of parameters for a complete PAA filling. In this work, CCD was selected as it is the most used method to fit second order models. As mentioned previously, optimum variable ranges were pre-selected to enhance the precision of the statistical method. For 6 factors and 2 central points the CCD method indicates 46 runs.

From the analysis of variance (ANOVA) of the model, it was verified that all model parameters p-values are smaller than 0.005 making their contribution for the response of the system significant. An optimum set of deposition conditions was determined and is presented in Table 6.2, together with the optimum experimental conditions, obtained from the previous individual studies. The statistical trends for each parameter are

Table 6.2 – Optimum electrodeposition parameters obtained from RSM analysis and experimental results.

Parameter	RSM Analysis	Individual Experimental Results
δ_b (nm)	9.1	9
Stirring, (rpm)	0	0
t_r (s)	0.82	0.6
j (mA·cm^{-2})	94	125
C (M)	0.55	0.5
T (°C)	12	20

represented in Figure 6.15 corresponding to a maximum statistical value of f_p = (104±12) %.

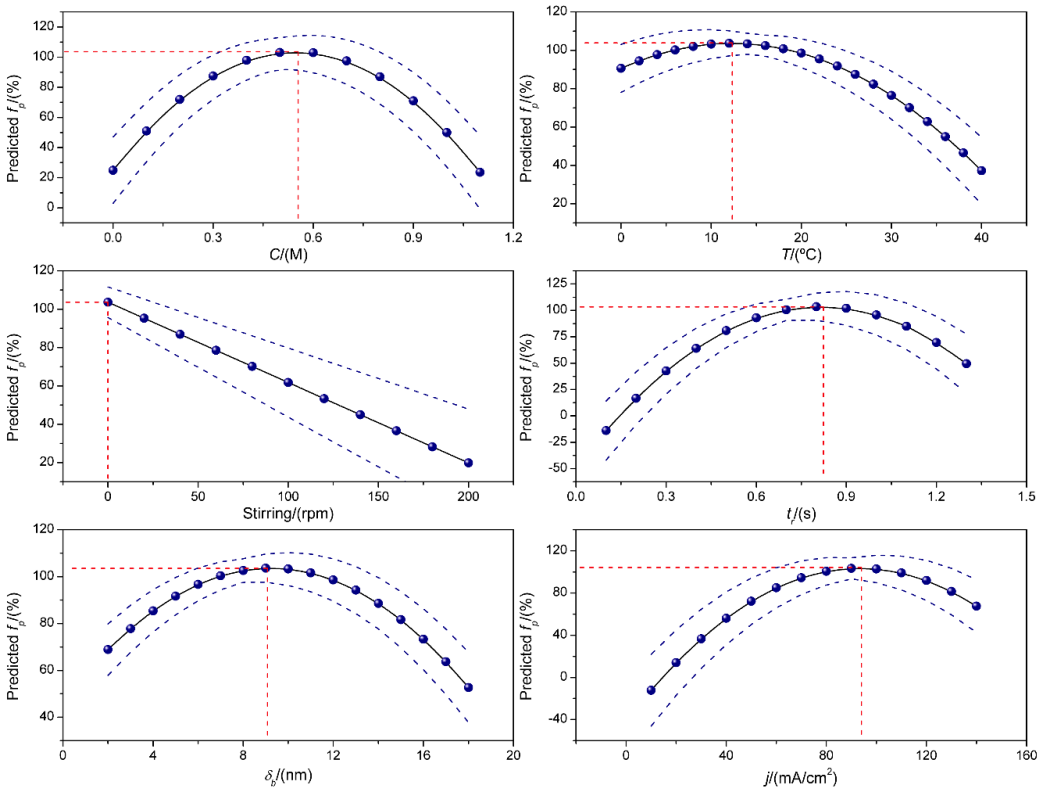

Figure 6.15 – Prediction profiles for each studied electrodeposition parameter and corresponding confidence intervals (blue dashed lines). For each parameters, the desirability plot is presented under the prediction profile. The solid lines are a guide to the eye and the dashed lines represent the confidence intervals.

The maximum of f_p is predicted to occur for parameters values given in Table 6.2. The optimum values obtained from the individual studies are in accordance with the RSM analysis, which was expected. With these optimum set of parameters, the limits of f_p were tested for different template lengths and compared with the initial reference values (Figure 6.16a). For lengths up to 20 μm the PAA is filled up to 93 %. For higher lengths, f_p steadily decreases down to 77 % for 50 μm length. Nevertheless, the growth of the NWs remains highly homogeneous very close to 50 μm as can be seen in the

cross section image of a 50 μm sample (Figure 6.16b). In the last few micrometers of the template, as the first NWs reach the surface of the template, they start to cover the adjacent pores preventing a complete template filling (Figure 6.16c). Although for low thicknesses the nominal f_p values are similar in all the used sets of parameters, as the PAA length increases it is notorious the improvement in the deposition homogeneity for the RSM results. Using the best deposition parameters we eliminated the pore blocking problems that arise in the last few micrometers. A 55 μm template was used and the last 5 μm were milled after deposition to study the growth homogeneity in 50 μm lenght. The result is presented in Figure 6.16a by a red star, with a f_p of 89 %. The SEM image can be observed in Figure 6.16d being this the highest filling ratio reported for AC or PED methods, opening a new window of opportunities for the fast fabrication of long, organized NWs.

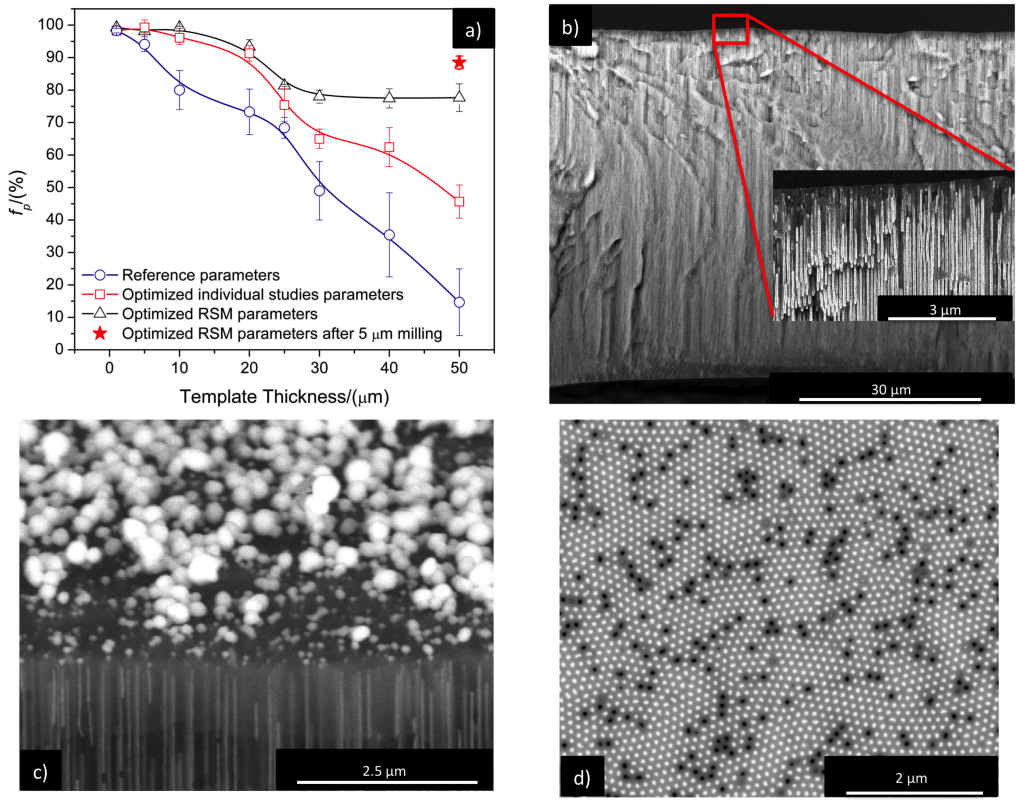

Figure 6.16 – (a) Filled percentage dependence on template thickness for reference, optimized from individual studies and RSM optimized parameters. The solid line is a guide to the eye.; (b) SEM cross section image of a 50 μm PAA filled sample; (c) top view without milling: the white mushroom structures correspond to the deposits once the nanowires reach the template surface; (d) SEM top view image of a 50 μm PAA filled sample after 5 μm milling.

6.4 Conclusions

In this work, we show for the first time the application of the pulsed electrodeposition as the simplest method to fabricate vertically aligned iron nanowire arrays with extreme homogeneity up to 50 μm. We performed a systematic study on the influence of several pulsed electrodeposition parameters in the deposition quality of Fe nanowires. The results reveal that electrolyte molar concentration, temperature, stirring, rest pulse duration, barrier layer thickness and current density have significant impacts on f_p. Each parameter was investigated and optimized from an initial set of reference values.

We show the importance of a cross parameter optimization to achieve very thick homogeneous nanowire arrays, something that was not shown before. With a RSM analysis the optimum set of values was predicted as follows: barrier layer thickness of 9.1 nm, 0 rpm stirring, rest pulse duration of 0.82 s, deposition pulse current density of 94 mA/cm^2, electrolyte molar concentration of 0.55 M and temperature of 12 °C. With this set of parameters, highly homogeneous filled templates were obtained with f_p up to 93 % for 20 μm. Also, high filling ratios are reported for very thick templates (50 μm) using alternate current methods. It is the first report of such excellent homogeneities in alternating current reports, for iron or any material.

CHAPTER 7

High Surface Area Double Walled Hematite Nanotubes

This chapter is dedicated to the fabrication and study of a double walled hematite nanotube structure. A new method to fabricate new double walled nanotube (NT) structure was developed. The approach is based on the electrodeposition of metallic Fe nanowires in porous alumina templates followed by a selective chemical etching with phosphoric acid and dichromic acid and an annealing at 600 °C in air. Hematite nanotubes with high degree of uniformity along the structure were obtained by applying this procedure. STEM analysis revealed that almost imperceptible bridges connect the thinner (2-3 nm) inner and outer walls. Chemical composition and atomic structure were assessed and a core-shell structure of iron-hematite was found in accordance with magnetic measurements. The high versatility of this novel method was demonstrated showing that it should be broadly applicable to several materials. Through pore modulation, more complex double walled nanotubes were created with diameter variation along the tube.

This chapter is adapted from the work under preparation for Advanced Functional Materials (J. Azevedo, M.P. Fernandez-Garcia, C. Magen, A. Mendes, J.P. Araujo and C.T. Sousa)

The author contributed to the planning and execution of all the experiments described in this chapter, except: STEM measurements that were conducted by Magen, C; Ni nanotubes were fabricated by Sousa, C.T. The author was also involved on the discussion and interpretation of all results, as well as on the preparation of the manuscript.

7.1 Background

Iron oxides have attracted much interest for their potential application in nanotechnology[230–233]. In particular hematite (α-Fe_2O_3), being the most stable form among several Fe oxide phases[234], is of significant scientific and technological importance for its wide potential in applications in catalysis/photocatalysis[24], gas sensors[235] and drug delivery[236]. For many applications, α-Fe_2O_3 materials are nanostructured to increase

the surface area for better reaction kinetics at the surface[107], light absorptivity[106] or electronic conductivity[237]. It is clear that nanostructuring and easy low-cost large-scale production methods are essential challenges in which researchers need to focus on so that the full potential of this material is exploited.

Various α-Fe_2O_3 nanostructures with different morphologies such as nanoparticles[183], nanowires[94,238] and nanotubes (NTs)[99,239] have already been successfully synthesized. Nanostructures of particular interest are double walled NTs as they offer high surface areas in different zones, such as inner and outer interfaces, which are important for more complex functionalization.

Recently a tube-in-tube α-Fe_2O_3 nanostructure was fabricated through a two-step hydrothermal process[240]. These structures are an opportunity for constructing complex nanodevices but the synthesis method reported so far is limited by diverse structure formation and attainable dimensions. It is known that the fundamental properties of nanostructures can be tuned through morphology and size, so precise structure adjustment is of utmost importance[99,116]. To gain more control over the different dimensions of the synthesized nano-objects, template assisted methods are advantageous. Some reports have been published on the synthesis of α-Fe_2O_3 NTs obtained through template assisted methods[124,241], but no report of a double walled NT structure has been made using such methods. Moreover, the reported nanostructures were relatively wide in diameter (> 100 nm), decreasing the attainable surface area.

An inexpensive fabrication of large arrays of α-Fe_2O_3 NTs with a unique designed architecture (i.e., crystalline double walled NTs) grown on porous alumina templates with controllable dimensions is here described. For the first time 1D Fe nanostructures grown inside an PAA templates were converted into the desired α-Fe_2O_3 phase with double walled NT morphology by combining a simple chemical etching and annealing route. The versatility of the developed method was demonstrated through it application to NWs with several dimensions and geometries and also to NWs of other materials, like Ni.

7.2 Experimental details

7.2.1 Sample preparation

Arrays of metallic Fe NWs were fabricated as described previously - Chapter 6. Briefly, high purity thick Al foil was rinsed and electropolished to reduce surface roughness and create nanopatterns for posterior pore nucleation. The Al foils were subjected to a two-step anodization process to create a PAA template. The first one in 0.3 M oxalic acid, $(COOH)_2$, at 40 V and 2 °C. Secondly, in order to obtain high aspect ratio NWs, a second anodization was carried out during 20 h (corresponding to 50 μm template thickness). Before electrodeposition, the anodization potential was lowered to 8 V to form dendritic channels[200]. Pulsed electrodeposition was employed to fill the template with Fe NWs

and electrodeposition conditions were optimized previously. A mixture of 153 g·L^{-1} Fe (II) sulfate heptahydrate, $FeSO_4 \cdot 7H_2O$, 45 g·L^{-1} boric acid, H_3BO_3, and 1 g·L^{-1} ascorbic acid, $C_6H_8O_6$, was used as precursor for electrodeposition at 94 mA·cm^{-2}. Completely filled porous alumina templates were obtained at the end of the process. To ensure that no Fe film was left on the surface of the template, a mechanical polishing was made using alumina powder.

To demonstrate the versatility of the fabrication process Ni double walled NTs were made together with modulated NTs to assess the control over the morphology of the NTs (see Appendix B for details). Both Ni NWs fabrication process and alumina modulation were adapted from previous works[137,242]. Briefly, the modulated template was fabricated using three different anodization potential ramps (80 V to 140 V in 36 s; 140 V to 160 V in 0 s and 160 V for 0.2 s). Ni was electrodeposited using a Watts bath, composed of 1.14 M $NiSO_4 \cdot 6H_2O$, 0.19 M $NiCl_2 \cdot 6H_2O$ and 0.73 M H_3BO_3. The pH value of the electrolyte was maintained at 4.0-5.0 and its temperature was kept constant at 40 °C. Deposition current was 70 mA·cm^{-2}.

The alumina template was dissolved in an aqueous solution of phosphoric acid, 0.4 M H_3PO_4 and dichromic acid, 0.2 M $H_2Cr_2O_7$ at 60 °C (removal rate: 50 nm/min) for several hours. The NWs were dispersed in an ultrasound bath. After the complete removal of the alumina template, the NWs were washed in ethanol. The dispersed NWs were then annealed in air at 600 °C for 6 h (heating rate of 2°C/min).

7.2.2 Sample Characterization

The morphology and surface topography of the samples were characterized using a high-resolution scanning electron microscope (FEI Quanta 400 FEG ESEM) with a through-the-lens detector for secondary electrons. The acceleration voltage was 15 keV while an in-lens detector was employed with a working distance of about 10 mm. Cross-sectional images were acquired from freshly cleaved samples. STEM was performed in an FEI Titan 60-300 operated at 300 kV and equipped with an aberration corrector for the probe. STEM spectrum imaging combining high angle annular dark field (HAADF) imaging and electron energy loss spectroscopy was used for the local chemical analysis of the NTs. Chemical line profiles and maps of the NTs were obtained from these STEM-EELS spectrum images by integrating the O-K and Fe $L_{2,3}$ edges intensity after after background extrapolation and subtraction.

The crystalline structure of the samples was analyzed by XRD in a Rigaku MiniFlex 600 diffractometer in the $\theta - 2\theta$ geometry using the Cu – Kα line with wavelength λ = 1.540593 Å. The spectra were acquired by moving the detector between $2\theta = 20°$ and $2\theta = 80°$ at a scan rate of 0.5 deg·min^{-1} with a step width of 0.04°. The spectra peaks were fitted using Lorentzian function to determine the average grain size according to Scherrer equation, as described elsewhere[136]. Reflection patterns were matched to reference values - Table 7.1 and 7.2. To measure the crystalline structure of the Fe NWs

inside the template, the Al substrate was removed to eliminate its contribution. For that, the samples were submerged in 0.5 M $CuCl_2$ and and 2.8 M HCl solution.

Table 7.1 – Structural parameters of α-Fe calculated from the XRD patterns and literature values for the diffracting planes.

(*h k l*) crystal system	2θ	
	XRD	**Literature values**
1 1 0	44.674	44.72
2 0 0	65.073	65.09

Table 7.2 – Structural parameters of α-Fe_2O_3 calculated from the XRD patterns and literature values for the diffracting planes.

(*h k l*) crystal system	2θ	
	XRD	**Literature values**
0 1 2	24.186	24.15
1 0 4	33.119	33.16
1 1 0	35.622	35.63
1 1 3	40.944	40.86
2 0 2	43.393	43.51
0 2 4	49.562	49.46
1 1 6	54.268	54.07
1 2 2	57.743	57.61
2 1 4	62.640	62.44
3 0 0	64.186	64.00
1 0 10	72.175	71.96
2 2 0	75.732	75.45

Raman spectra were determined on a LabRAM by Jobin-Yvon micro-sampling with an excitation line 633 nm of He-Ne laser at 100x amplification. To avoid sample damaging the laser power was 10 mW. Gratings of 1800 gr/mm were used. The measurements were from 200 to 1200 cm^{-1} using a 100 μm slit. Each measurement was done over 30 s at two different places in each sample to assure a correct spectra. The samples were placed in a low-susceptibility plastic sample holder for measurements. X-ray absorption spectroscopy measurements at the Fe K-edge in transmission were developed at the XAFS beam line of the Elettra synchrotron with an energy range of 6812 – 7969 eV. An Fe metal foil spectrum was also recorded to callibrate energy. For each sample three spectra were acquired for statistics with an integration time of 5.00 s. The experimental XANES spectrum of the sample was normalized at high energy after background subtraction to eliminate thickness dependence. In order to quantify the composition of each sample, the spectra were fitted with reference Fe/Fe oxide absorption curves using specifically made software.

Magnetization measurements were performed using a Quantum Design Superconducting Quantum Interference Device (SQUID) magnetometer from Quantum Design. Magnetization as a function of temperature [M(T) curves] were measured in the temperature range 10 – 320 K under an applied field of 100 Oe. Before the zero-field-cooled (ZFC) magnetization measurements (M_{ZFC}), the samples were cooled from room temperature to 10 K in zero applied magnetic field. Afterwards, the magnetic field was

applied and the magnetization $M_{ZFC}(T)$ was measured while warming. For the field-cooled (FC) measurements, the samples were cooled in the presence of the same magnetic applied field and magnetization was measured as a function of temperature while warming under the same field. Magnetization isotherms as a function of magnetic field [M(H) curves] were measured up to 50 kOe at selected temperatures from 5 K to 350 K.

7.3 Results and Discussion

7.3.1 Double walled hematite nanotubes

Crystalline Fe NWs were grown inside PAA templates into pores of 35 nm diameter, typical from oxalic acid self-organized regime anodization (Figure 7.1a). The deposition was highly homogeneous and lengths of 50 μm was used to achieve large aspect ratio (> 1.4×10^3). A thin Fe film was formed at the top of the alumina template and, to expose the tips of the NWs, mechanical polishing was employed[241]. Cross section SEM images revealed no defects along the alumina template and each wire appeared continuous and homogeneous (Figure 7.1b).

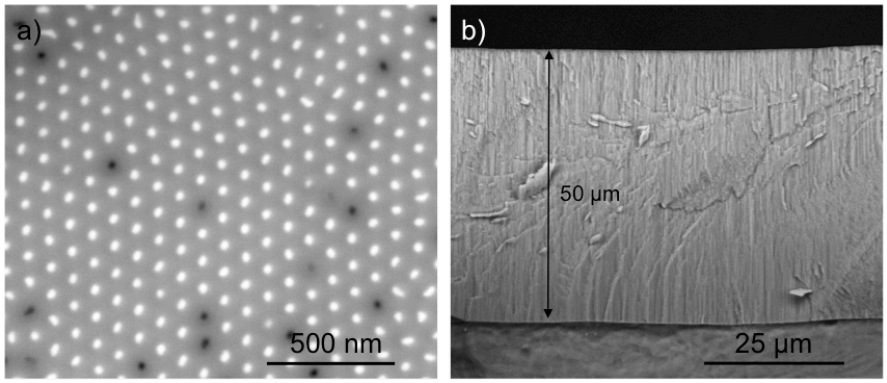

Figure 7.1 – (a) Top view SEM images showing the high-density of Fe nanowire array. (b) Cross section reveals the vertical alignment of the NWs.

The structure and phase composition of the samples were determined by X-ray diffraction (Figure 7.2). The positions of all Bragg reflections in Fe NWs coincide with the Bragg reflections characteristic of the metallic α-Fe phase. Metallic Fe NWs show a preferential bcc-structure and only two peaks (110) and (200), can be found in the patterns. From the most intense peak (110) the grain size is estimated at 17.8 nm.

The Bragg reflections of the Fe NWs after template removal are broader than in template and also the ratio between the intensity of the two peaks decreases. This is explained by the lightly texture along (110) direction of the Fe NWs grown in highly aligned pores of the PAA template.

The etching solution used in the template removal is widely used to remove electrodeposited materials from alumina templates as it is an alumina etching targeted

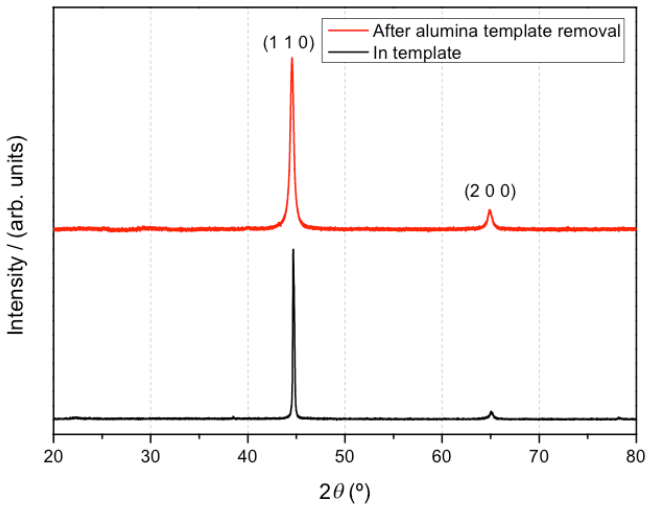

Figure 7.2 – X-ray diffraction patterns with corresponding layer Bragg reflections of nanoparticles in template and after alumina template removal. Peak values were compared to reference – Table 7.1.

solution[243]. Nevertheless, experience shows that it corrodes certain oxides, but at a much lower rate. After dissolving the alumina templates the remaining NWs were annealed at 600 °C in air for 6 h. These conditions are known to be optimum for α-Fe_2O_3 phase formation[239].

The morphology of the obtained nanostructures was analyzed by STEM and a double walled nanotube structure was observed - Figure 7.3a. The compositional line profiles of this double walled NTs were measured and the Fe and O signals variation is consistent with the double walled structure - Figure 7.3b. The dimensions of the tubes were assessed from the compositional profiles and the distance between inner and outer tubes is 4 nm with corresponding diameters of 20 nm and 45 nm. Inner and outer walls have different thicknesses (8 nm and 4 nm, respectively), which is 5 times thinner than previous reports, providing a much larger surface-to-volume ratio[240]. The NTs bottom ends (designated as the side originally adjacent to the Al foil before removing the alumina template) were dissolved during the alumina chemical etching, so no dendritic structure was present and most NTs were opened at both ends. The inner and outer tubes do not appear to be connected at any specific point and only very thin connection bridges were observed - Figure 7.3c. Very thin walls are interesting for different applications due to the quantum confinement effects[116].

The composition and crystallography of the NTs was assessed by different techniques. Raman spectroscopy was performed on reference samples of the most common Fe oxides (maghemite, magnetite and hematite) - Figure 7.4a. The NT modes positioned at 221, 285, 397, 602 and 645 nm in the spectrum (Figure 7.4b) all are indexed to the characteristic bands of α-Fe_2O_3 confirming that the NTs are constituted of only one Fe oxide phase – α-Fe_2O_3[244]. The XRD pattern of the NTs is shown in Figure 7.4c. All α-Fe_2O_3 Bragg reflections are identified. The spectra were fitted with hematite and

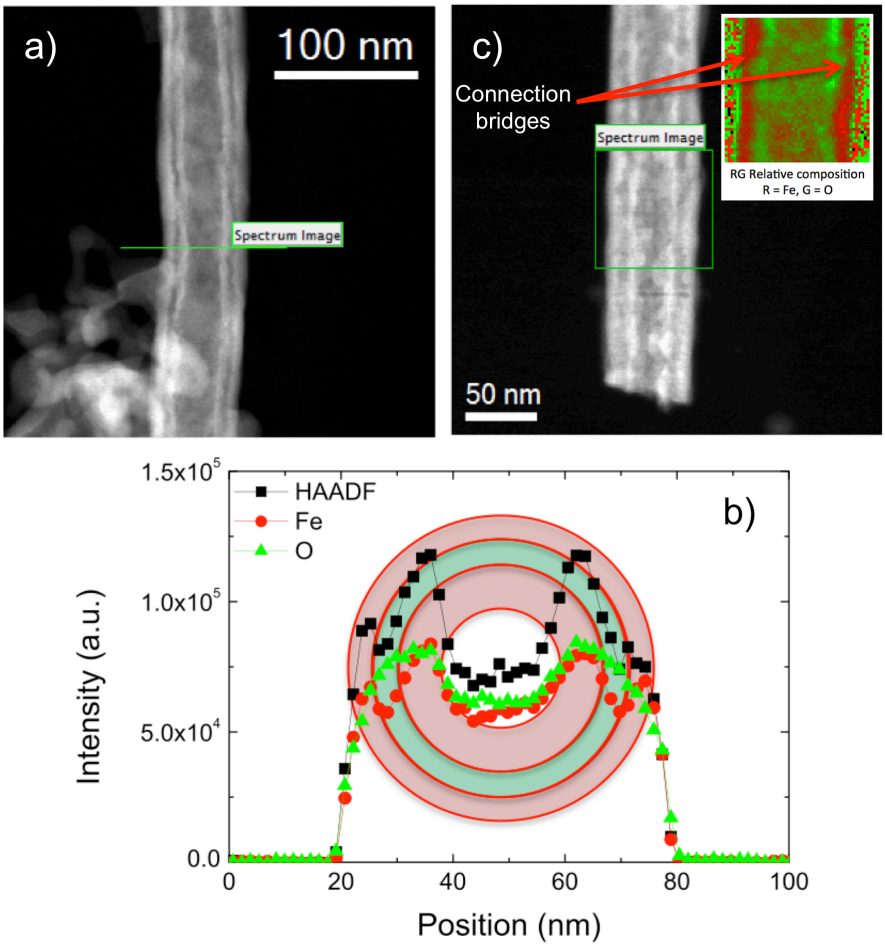

Figure 7.3 – a) STEM side-view image of a single double walled nanotube; (b) STEM-EELS chemical profile across α-Fe_2O_3 double wall NT along the green line in a); c) STEM side-view of another double walled nanotube with composition on inset.

iron (PDF Card No.: 9012706 and 2101169) and are in great accordance with the α-Fe_2O_3 spectra. Quantitative analysis, based on relative intensity ratio method, indicates a composition of 93.3 % α-Fe_2O_3 and 6.7 % Fe. All X-ray peaks can be indexed to a α-Fe_2O_3 R-3C hexagonal cell with lattice constants of a = b = 5.0380 Å and c = 13.7662 Å. The grain size was determined using Scherrer equation and is 11.5 nm.

To confirm the composition of the nanostructures in a precise manner, X-ray absorption spectroscopy, technique selective to atomic species, was used. The existence of Fe hydrooxides (goethite or ferrihydrite) and magnetite and maghemite was discarded by both XRD and Raman spectrometry and therefore, only hematite was considered for the experimental analysis of XANES. In Figure 7.5 the experimental Fe K-edge XANES spectrum of the sample is shown together with those of α-Fe and α-Fe_2O_3. In order to simulate the experimental data, we have performed a weighted sum of two XANES subspectra corresponding to α-Fe and α-Fe_2O_3. It can be observed that the simulated spectrum, with 90 % α-Fe_2O_3 and 10 % α-Fe, reproduces the shape, energy position of the different spectral features, their relative energy separation and intensity ratio when

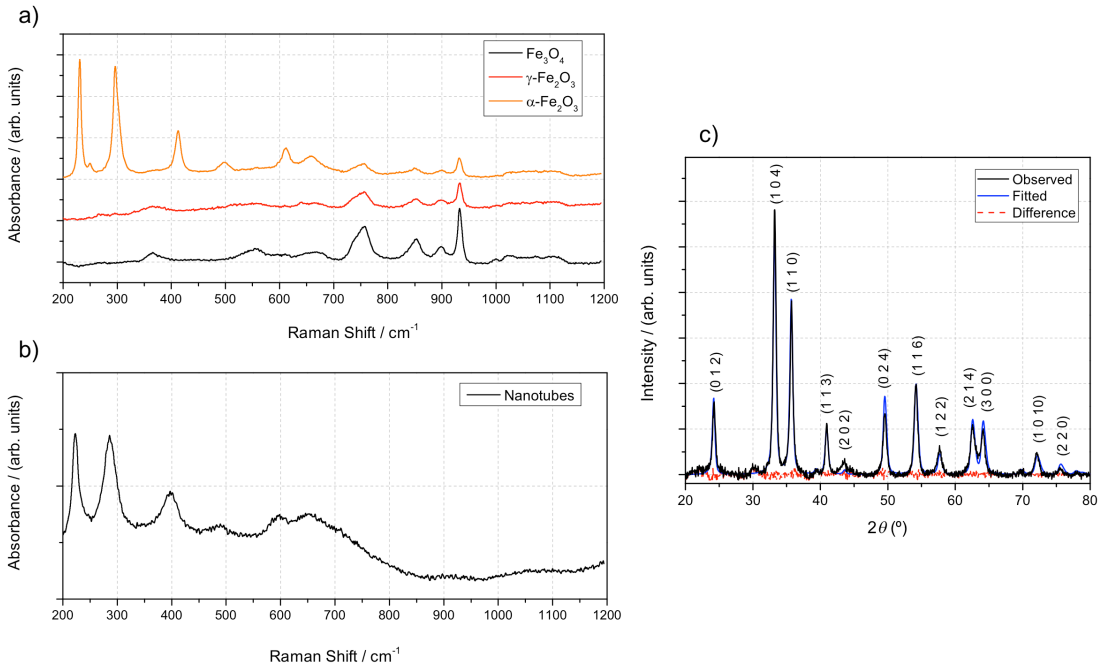

Figure 7.4 – a) Raman spectra of three most common iron oxide phases; b) Raman spectra of double walled nanotubes (peaks fit well with hematite); c) X-ray diffraction patterns of double walled nanotubes. Different crystalline phases of α-Fe_2O_3 are marked with the corresponding miller indexes. Peak values were compared to reference – Table 7.2.

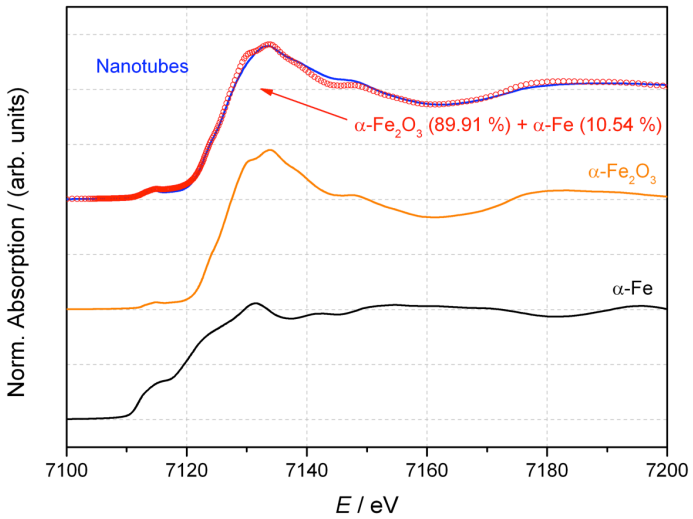

Figure 7.5 – Experimental Fe K-edge XANES spectrum for double walled nanotube sample (orange line) measured at room temperature together with the fit (blue circles) - see text. A weighted sum of Fe (10.54 %) and α-Fe_2O_3 (89.91 %) was employed to describe the experimental XANES of the sample. The spectra of α-Fe_2O_3 (red) and α–Fe (black) that were employed for the weighted sum (see text) are also shown at the bottom for clarity.

a mixture of α-Fe and α-Fe_2O_3 is considered. This result is in accordance with the XRD composition estimation.

7.3.2 Magnetic properties

Figure 7.6 shows the M(T) curve of double wall α-Fe/α-Fe_2O_3 NTs annealed at 600 °C.

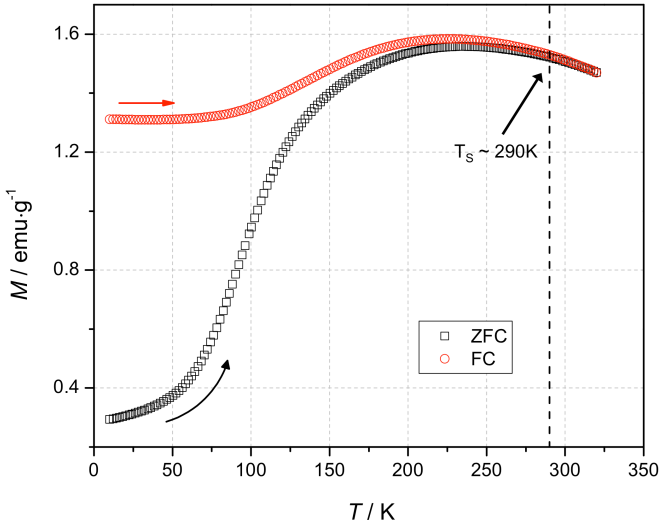

Figure 7.6 – Magnetization versus temperature after zero field cooling (ZFC) and field cooling (FC) conditions of the double walled NTs. Both were taken under a magnetic field of 100 Oe. Arrows indicate the measurement direction in reference to temperature variation. The dotted vertical line show the T_S.

As previously discussed, the obtained double wall NTs only contain 10 % of Fe. However it is known that a small percentage of iron on a nanostructure *shadows* magnetic hematite contribution (antiferromagnetic (AF) bellow the Morin transition, T_M = 260 K and weak ferromagnetic above T_M)[245] which has saturation magnetization M_S (hematite) = 0.5 emu·g^{-1} whereas M_S (iron) = 217.6 emu·g^{-1})][246]. Comparing the M_{FC} and M_{ZFC} curves two different features can be observed: both curves collapse above a saturation temperature T_S = 290 K and a broad maximum value on M_{ZFC} is observed at $T < T_S$, that can be associated to the blocking temperature ($T_B \sim 234$ K). The broad maximum of the M_{ZFC} magnetization suggests that there is a distribution of blocking temperatures rather than a unique and well-defined value for T_B. This indicates that a broad distribution of energy barriers is present due to the distribution of nanograin sizes. Bellow T_S, irreversibilities are observed with $M_{ZFC} < M_{FC}$ and increasing gap with decreasing temperature indicating that the largest Fe-grains remain blocked even up to 290 K. M_{FC}(T) also shows a plateau at low-temperatures that can be associated with the freezing of iron oxide magnetic moments leading to a disordered magnetic state and/or dipolar interaction[247]. The irreversibility at $T < T_S$ is another consequence of the freezing state in the spin-glass hematite shell at low temperatures frequently present in the interfaces of Fe-oxide or α–Fe phases[248].

Representative hysteresis loops $M(H)$ obtained at 5, 50, 100, 150, 200, 250, 300 and 350 K are shown in Figure 7.7a. It is clear that the saturation magnetization decreases with the temperature. The linear increase of the magnetization for high magnetic fields is associated to the AF contribution of the α-Fe_2O_3[249]. Figure 7.7b show the coercive

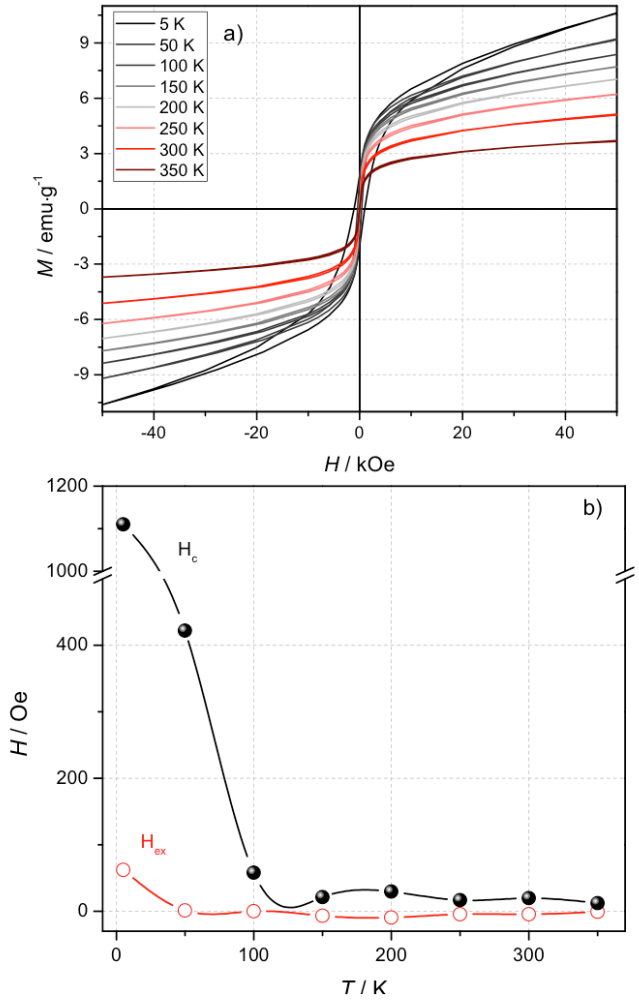

Figure 7.7 – a) Hysteresis loops measured at several temperatures; b) Temperature dependence of H_{ex} and H_c obtained from *M(H)* hysteresis loops.

field (H_c) and the exchange bias field (H_{ex}). These were calculated using the H_{right} and H_{left} (positive and negative magnetic field values, where the magnetization goes through zero in the hysteresis loops) as[250]:

$$H_c = \frac{\left(H_{right} - H_{left}\right)}{2}$$

$$H_{ex} = -\frac{\left(H_{right} + H_{left}\right)}{2}$$

H_c decreases with temperature indicating the existence of blocked nanograins at room temperature. The hysteresis loops are shifted to negative magnetic field values due to an exchange bias (EB) effect. H_{ex} decreases from 62 Oe at 5 K to approximately zero around 50 K (Figure 7.7b). This EB effect, in the same temperature range as the plateau in the $M_{FC}(T)$ curve, is attributed to the magnetic coupling between AFM α-Fe_2O_3 and a FM α-Fe phases with common interfaces[247]. Thus, it can be assumed that

the NTs present a concentric core-shell structure, with a metallic α-Fe core surrounded by a shell of α-Fe_2O_3 [251].

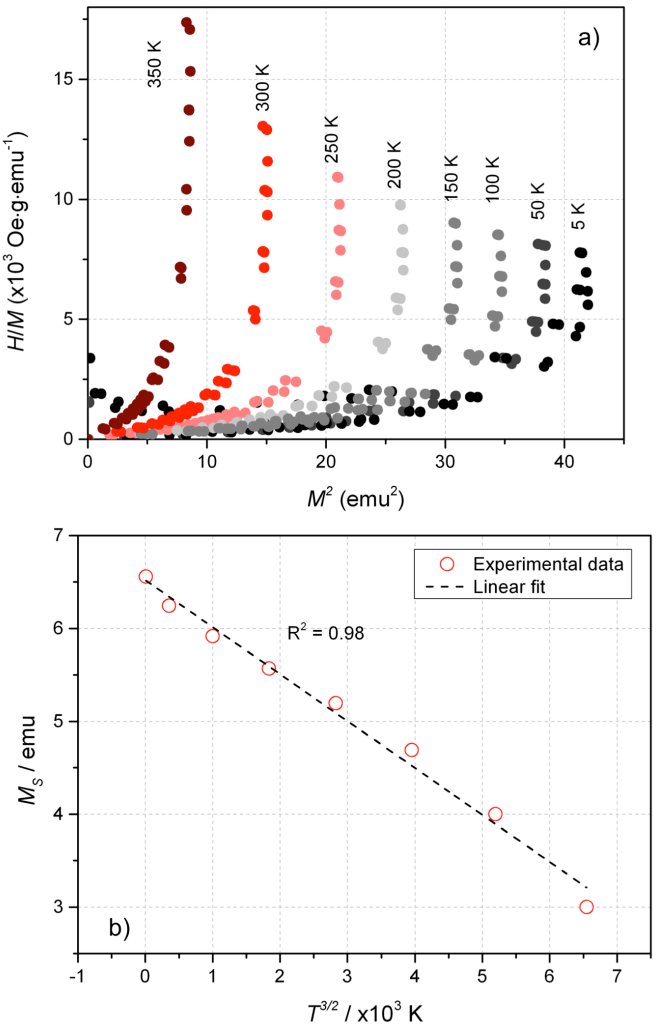

Figure 7.8 – a) Arrott plots for double wall NTs in the temperature range of 5 – 350 K; b) temperature dependence of spontaneous magnetization (The solid line shows the fit to Bloch's $T^{3/2}$ law).

Figure 7.8a displays the isothermal magnetization curves under *H* up to 50 kOe and in the temperature range of 5 – 350 K, where the data is depicted in an Arrott plot (*H*/*M* vs. M^2). From this plot a spontaneous magnetization can be extracted extrapolation the linear region of each curve to intercept the x-axis. The Bloch´s $T^{3/2}$ law was successfully applied for an extended range of temperature - Figure 7.8b. Within the parabolic magnon band structure the magnetic moment varies as $T^{3/2}$ for localized magnetic moment systems, in agreement with Bloch's theoretical prediction for the 3D Heisenberg-type ferromagnet[253]. Therefore the FM contribution of iron dominates the magnetization behavior.

7.3.3 Growth Mechanism

The formation mechanism of the double walled NTs is here explained in a step-by-step study, conducted by analyzing the morphology and crystallography of the samples at various stages – Figure 7.9.

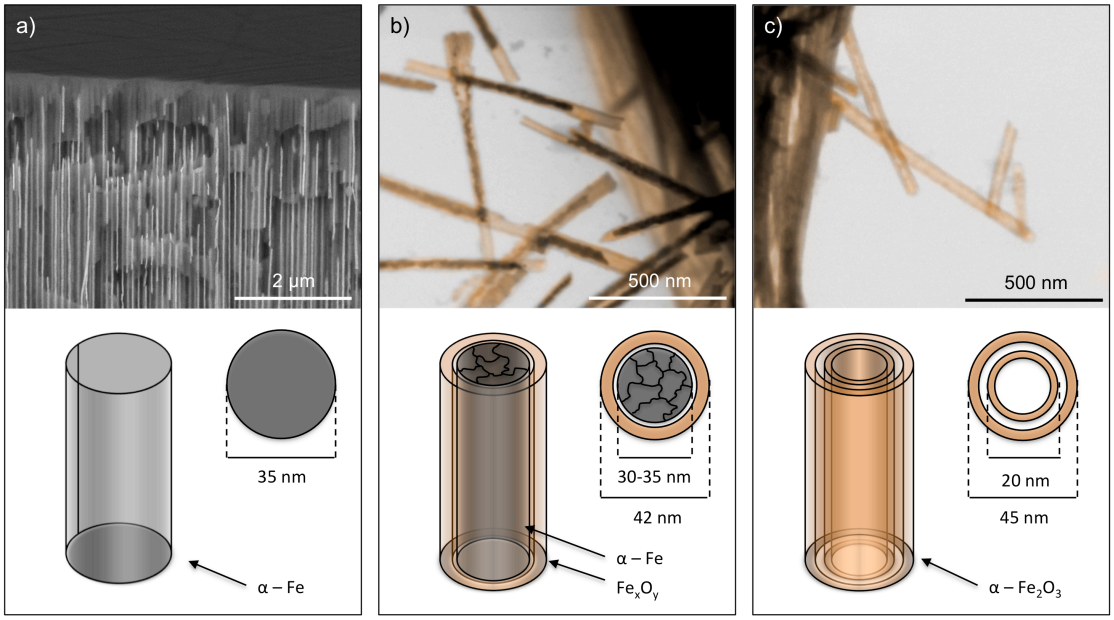

Figure 7.9 – Morphology evolution of the nanostructures: SEM and STEM images of the products obtained a) as prepared in template, b) after template removal and c) after annealing.

Firstly, the as-deposited α-Fe sample has typical structure of NWs fabricated through template-assisted electrodeposition with no visible morphology defects (Figure 7.9a). After several hours of alumina template removal, the NWs are converted into a core-shell structure with a very thin and smooth outer layer and a granular nucleus (Figure 7.9b). The outer radius of ~42 nm is larger than the previous 35 nm imposed by the alumina template, which indicates an oxidation of Fe accompanied with an expansion from oxygen incorporation. The nucleus preserves a radius between 30-35 nm indicating that it should be the non-oxidized electrodeposited α-Fe. XRD of the sample after alumina template removal (Figure 7.2) indicates the presence of α-Fe and no trace of Fe oxide. The absence of Fe oxide phases is attributed to the amorphous nature of the outer wall that only crystallizes after annealing at high temperatures. The Bragg reflections associated with Fe are also broader than in template. This is explained by the highly organized vertical nature of the template that disappears once the later is removed.

Based on the morphology and crystallography evolution, we propose a dissolution-based mechanism for the transformation of NW to core-shell structure. Jia *et al.* demonstrated that α-Fe_2O_3 ellipsoid like structures in the presence of phosphate ions promote a selective dissolution of the structure, preserving both the outer walls and several low-energy sites across the vertical axis[240]. This dissolution resulted in tube-in-tube structures. In this study, it is proposed that when submerged for long times in

aqueous solution, the α-Fe nanowires start to oxidize. A similar dissolution then occurs in the presence of phophate ions (from the etching solution used for alumina removal) removing the high-energy sites from the surface of the NWs. This dissolution preserves the granular structure of the deposited Fe NWs in the core and a smooth oxide outer tube - Figure 7.9c. The flat top surface of the NWs enables a high reproducible product when compared to previous hydrothermal synthesis[240].

The final double walled NT structure was formed after sintering at high temperatures. Two smooth and adjacent tubes are formed with almost imperceptible connection between both. The outer diameter increased once more indicating a more complete oxidation of the structure. The granular core change to a smooth oxide tube is related to a different mechanism. Annealing of Fe NWs in template was performed and no indication of tube formation was observed, as reported elsewhere[124]. But if the annealing is performed on core-shell nanoparticles, which are dispersed, the oxygen intake and Fe diffusion create a second NT. This transformation can be explained by the Kirkendall effect which leads to the formation of voids in the Fe core during oxidation creating a tube[254]. Recrystallization makes the inner tube smooth, which is confined by the outer NT formed previously. STEM images show very tenuous connection between both and it is here hypothesized that many small connections must exist to prevent both tubes to collapse.

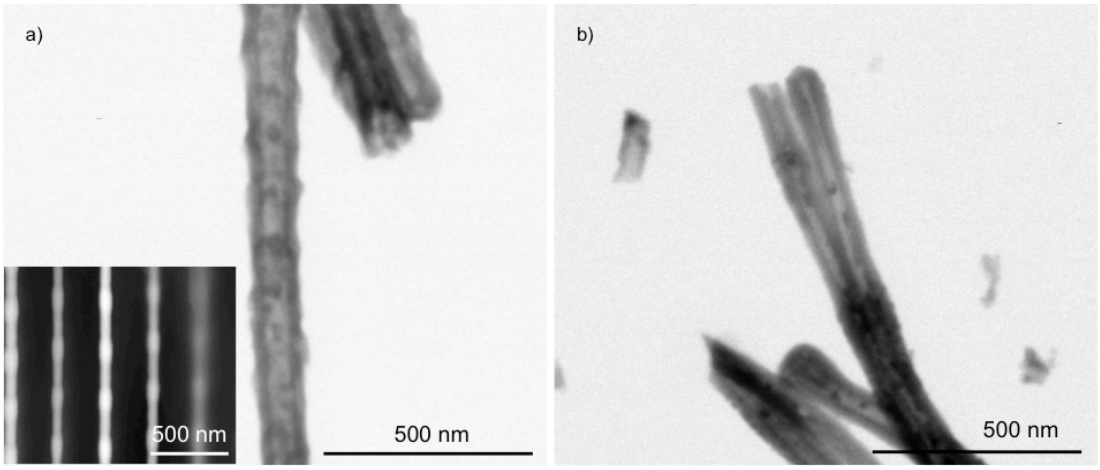

Figure 7.10 – STEM images of a) modulated Fe NTs (inset shows SEM image of original Fe NW, prior to annealing); b) Ni NTs formed using the same technique.

The proposed new methodology demonstrates that, if the annealing stage is pre-formed after the NWs are immersed in a phosphate containing solution a double walled NT can be formed in a reproducible manner. Given that the template dictates the initial shape of the NW, a variety of aspect ratios should be obtained. Presently, various porous alumina templates are being tested with larger and smaller diameters. With recent advances in porous alumina template control, it is even possible to use modulated template for more complex applications, as described in Appendix B – Figure 7.10a[242,255]. This method can also be directly applied to other metals, such as nickel,

where NTs can be formed from NWs – Figure 7.10b. Optimal conditions for double walled Ni NTs is also being investigated.

7.4 Conclusions

In this work, a simple and low cost method to synthesize high aspect ratio double walled hematite NTs is reported. The formation mechanism of these structures is studied in detail and the proposed technique may be used to create other oxide complex architectures, as demonstrated. A precise composition of the structures was assessed by combining x-ray diffraction and Fe K-edge x-ray absorption spectroscopy. The NTs are composed of hematite with small percentage of iron. Magnetic measurements are in accordance with this composition.

In the future, these high surface area α – Fe_2O_3 NTs will be implemented as PEC photoelectrode (for both solar water splitting as well as solar RFB) using simple fabrication methods such as previous described [256].

CHAPTER 8

Main Conclusions and Perspectives

In this chapter the main conclusions and achievements accomplished throughout this thesis are presented and an outlook on the future perspectives is discussed.

Direct contact of Cu_2O with aqueous solutions promote its photocorrosion making this semiconductor impracticable for photoelectrochemical (PEC) devices. The instability of Cu_2O as photocathode for solar water splitting is addressed by searching for homogeneous and defect free protective layers. To improve the quality of previously reported overlayers a novel simple low-cost post-synthetic treatment was developed. Post-synthetic annealing under steam atmosphere was optimized for Cu_2O/AZO/TiO_2 (where AZO stands for aluminum doped zinc oxide) composite photocathodes and 10 % photocurrent loss over its initial value during more than 50 h of light chopping (biased at 0 V vs. reversible hydrogen electrode - V_{RHE}) was achieved. Transmission electron microscopy (TEM) analysis shows a smoothness of the TiO_2 surface and the absence of cracks in the overlayer, providing a better protection for the underlying Cu_2O. This treatment was tested with two different co-catalysts (RuO_x and Pt) and both yielded better stabilities with the steam treated samples. In the process of achieving record-breaking stabilities, the critical importance of morphological changes of the surface in generating these high-stable photocathodes was uncovered.

To further improve the stability of Cu_2O, alternative overlayers were tested and it was observed that ALD deposited SnO_2 is a promising candidate overlayer for stabilizing photocathodes for hydrogen evolution. SnO_2 protected Cu_2O was optimized and the performance and stability were proved to be influenced by the film thickness, post-deposition steam treatment, and the nature of the heterojunction interface. This work also revealed the versatility of the steam treatment to materials different from TiO_2. The optimized device exhibited great stability, maintaining 90 % of its initial photocurrent after 57 h of sustained photoelectrochemical water reduction. Better interface properties were observed compared to Cu_2O/TiO_2, were an intermediate layer of AZO was necessary. To the best of our knowledge, this study represents the first demonstration of SnO_2 as a photocathode protection layer, and these findings should be widely applicable on other photoelectrode devices. Extremely thin intermediate layers (at the atomic scale) were explored revealing important improvements in the photocathode device.

To avoid some limitations of solar water splitting, such as sluggish kinetics or gaseous fuels storage, a new solar energy harvesting and storage solution was ex-

plored. The innovative concept developed at LEPABE (Prof. Adélio Mendes) and Aarhus University (Prof. Anders Bentien) was implemented for the first at these laboratories over the course of this thesis. In this work the possibility of storing solar energy in a simple way using a vanadium redox flow battery and a CdS photoanode was demonstrated; unbiased charged of a solar redox flow battery (RFB) (CdS(s)|V^{3+}, VO^{2+}||V^{3+}, V^{2+}|Carbon Felt(s), E^0 = 0.6 V_{NHE}) was achieved. Different strategies to improve the low CdS stability were explored and CdSe protective over layer had a twofold increase with photocurrents up to 1.4 mA·cm^{-2} . A tandem system battery using a dye-sensitized solar cell (DSC) was also studied to provide the necessary photovoltage to charge a standard all vanadium redox flow (DSC/CdS(s)|VO^{2+}, VO_2^{+}||V^{3+}, V^{2+}|Carbon Felt(s), E^0 = 1.2 V_{NHE}); in this configuration, the observed photocurrent was 1 mA·cm^{-2}.

For practical applications, non-acidic electrolytes combined with stable and efficient semiconductors are required. Nevertheless, alkaline RFBs are only recently being studied. A new RFB was developed based on anthraquinone-2,7-disulphonate and ferrocyanide redox pairs. This new battery displayed high energy and coulombic efficiencies. It was shown that it is possible to directly solar charge ferrocyanide/anthraquinone redox pairs in an alkaline RFB with a hematite photoanode, which is low cost and stable. Although ferrocyanide is a known hole-scavenger, which ameliorates surface defects problems in hematite, as battery charges and ferricyanide is produced, back electron recombination limits the performance of this device. Novel surface treatments of the hematite photoanodes, based on pressure annealing and organic polymer coating, showed improved performance in terms of ferrocyanide oxidation photovoltage, which should be broadly applicable to other photoanode materials. Specially the use of organic redox pairs in alkaline, aqueous media offers a wide range of possibilities in future fully organic solar redox flow batteries given the many possibilities of tailoring properties through the manipulation of functional groups.

Many different techniques have been reported to produce a wide range of different nanostrutures of several semiconductors. One of the most explored semiconductor for nanostrutured PEC applications is $\alpha - Fe_2O_3$. But not all preparation methods are practical, as they require either expensive equipments or many fabrication steps. For this reason a new low cost and effective $\alpha - Fe_2O_3$ nanostructure fabrication method was studied based on the conversion of nanowires (NWs) into nanotubes (NTs). The application of pulsed electrodeposition to fabricate vertically aligned Fe nanowire arrays with extreme homogeneity was shown. A systematic study on the influence of several pulsed electrodeposition parameters revealed that electrolyte molar concentration, temperature, stirring, rest pulse duration, barrier layer thickness and current density have significant impacts on filling percentage. The importance of a cross parameter optimization to achieve very thick homogeneous nanowire arrays was revealed, something that was not shown before. With a RSM approach the optimum set of factors was predicted as follows: barrier layer thickness of 9.1 nm, without stirring, rest pulse duration of 0.82 s, deposition pulse current density of 94 mA/cm^2, electrolyte

molar concentration of 0.55 M and temperature of 12 °C. With this set of parameters, high filling ratios are reported for very thick templates (50 μm) using alternate current methods.

Using a simple and low-cost fabrication method, it was shown the possibility of synthesis of double walled hematite nanotubes using porous anodic alumina templates to control the overall morphology of the nanotubes. The features of these structures were assessed by STEM revealing diameters smaller than 50 nm and wall thicknesses less than 10 nm, in addition to an imperceptible connection between inner and outer nanotube walls. The crystallography and composition was evaluated precisely revealing a single iron oxide phase - hematite - together with small amount of metallic iron. Furthermore, magnetic properties were characterized revealing an exchange bias effect typical of the coexistence of an antiferromagnetic and a ferromagnetic phases with common interfaces, rising from the presence of a core containing non-oxidized α-Fe surrounded by a shell of α-Fe_2O_3. Isothermal magnetization curves reinforce the presence of both an antiferromagnetic and ferromagnetic phases. Finally, the growth mechanism of these double walled nanotubes is revealed. A synergetic combination of a chemical attack and an annealing on metallic nanowires allows the fabrication of double walled oxide nanotubes with controlled morphology. In summary, a novel method to fabricate double walled nanotubes is described and studied step-by-step. This method to fine tune the morphology of the nanostructures using alumina template modulation and, given that the physical properties of the nanoparticles can be greatly influenced by their feature size, the modulation of double walled nanotubes might shed new light into novel applications such as catalysis or sensors. The material chosen for this work was hematite, for its broad range of applications, but it was also demonstrated the possibility of using nickel oxide instead and should be broadly applicable to other materials.

Based on the results obtained throughout this thesis, some of the most interesting future works that can be developed are here proposed.

- Further studies of Cu_2O should include the identification of the mechanism of slow degradation, optimization of the heterojunctions for improved performance, and exploration of photocathode operation in acidic or alkaline solutions, which are desirable for complete devices.

- Development of new organic RFB, with competitive efficiencies and energy densities, is an important goal for electricity storage, not just for solar energy storage. Further studies of organic redox pairs will also improve the tunability of semiconductor/electrolyte energy levels.

- Other semiconductors should also be tested. In particular, Ta_3N_5 is expected to good performance and stability in ferrocyanide with photocurrents up to 7 $mA{\cdot}cm^{-2}$ [257]. Initially Ta foils will be used to demonstrate an efficient solar-RFB using Ta_3N_5 and afterwards the semiconductor will be deposited on a conductive

transparent substrate.

- The development of a numerical model for solar RFBs would allow a deeper understanding of the underlying phenomena and improve future device designs, from material selection and configuration to cell design and operation conditions.
- New cell designs for solar RFBs that take advantage of electrolyte flow, minimize internal resistance, are leak free and compact will also be necessary for bringing this technology to the commercial level. A new design was already developed during this thesis and is currently being tested.
- Implementation of the new double walled NTs in PEC devices should be made. A possible way to apply these structures is using simple reported methods based of reduced graphene oxide as supporting electrode.
- During this thesis, high surface area three dimensional structures were synthesized - see Appendix C. These novel structures can be used as templates to create highly organized and self-supporting nano materials. If a core of a conductive material (such as a metal or conductive oxide) is used and then covered by a light-absorbing semiconductor, a core shell structure could be achieved with charge extraction capabilities. In particular, if gold is used, plasmonic effect could be used to further enhance efficiency. Undergoing numerical simulations show that by using localized surface plasmon-induced near-field enhancement, light trapping by scattering could enhance hematite light absorption in the 500 - 650 nm by a factor of 3.

List of Publications

Several contributions were made to the scientific community, directly related to the work developed in the present thesis, including 18 oral communications, 5 poster presentations, 1 book chapter and the several publications. This thesis is based on the following publications:

1. **J. Azevedo**, C.T. Sousa, A. Mendes and J.P Araújo; Influence of the rest pulse duration in pulsed electrodeposition of iron nanowires. Journal of Nanoscience and Nanotechnology, Volume 12, 2012 Pages 9112-9117

2. **J. Azevedo**, C.T. Sousa, J. Ventura, A. Apolinário, A. Mendes and J.P. Araújo; Ultra-long Fe nanowires by pulsed electrodeposition with full fill of alumina templates. Materials Research Express, Volume 1, 2014 Page 015028-1 - 015028-16

3. **J. Azevedo**, S.D. Tilley, M. Stefik, P. Dias, C.T. Sousa, A. Mendes, J.P. Araújo and M. Grätzel; On the Stability Enhancement of Cuprous Oxide Water Splitting Photocathodes by Low Temperature Steam Annealing. Energy and Environmental Science, Volume 7, 2014 Page 4044 - 4052

4. **J. Azevedo**, T. Seipp, J. Burfeind, C.T. Sousa, A. Bentien, J. Araújo, A. Mendes; Unbiased solar energy storage: Photoelectrochemical redox flow battery. Nano Energy, Volume 22, 2016 Page 396 - 405.

5. **J. Azevedo**, S.D. Tilley, M. Schreier, M. Stefik, C. Sousa, J. Araújo, A. Mendes, M. Grätzel, M.T. Mayer; Tin Oxide as Stable Protective Layer for Composite Cuprous Oxide Water-Splitting Photocathodes. Nano Energy, Volume 24, 2016 Page 10 - 16.

6. **J. Azevedo**, K. Wedege, A. Khataee, A. Mendes, A. Bentien; Direct Solar Charging of an Organic–Inorganic, Stable, and Aqueous Alkaline Redox Flow Battery with a Hematite Photoanode. Angewandte Chemie International Edition (DOI: 10.1002/anie.201602451)

7. **J. Azevedo**, M.P. Fernandez-Garcia, C.T. Sousa, A. Apolinário, J.M. Teixeira, A. Mendes and J.P. Araújo; High Surface Area Double Walled Hematite Nanotubes (under preparation)

Publications related to but not included in the thesis (the proponent's contribution is briefly explained for each work):

1. M.P. Fernandez-Garcia, J. Agostinho Moreira, A.M. Pereira, G.N.P. Oliveira, **J. Azevedo**, J. Oliveira, M.R.Chaves, D. Mota, C.T. Sousa, J.M. Teixeira, A.M.L. Lopes, M.M.R Costa, J.S. Amaral, T.M. Mendonca, V.A. KhonchenKo, V.H. Rodrigues, P.B. Alvares, A. Mendes, J.G. Correia, V.S. Amaral, A. Almeida, J.B. Sousa, J.P. Araujo; Synchrotron radiation experiments on multiferroic, magnetocaloric and magnetic nanostructured materials. Ciência e Tecnologia dos Materiais, Volume 24, 2012 Pages 128-133. (contributed with iron oxide XANES measurments used to study the oxidation of iron nanowires inside porous alumina templates)

2. S.D. Tilley, M. Schreier, **J. Azevedo**, M. Stefik, M. Grätzel; Ruthenium Oxide Hydrogen Evolution Catalysis on Composite Cuprous Oxide Water Splitting Photocathodes. Advanced Functional Materials, Volume 24, Issue 3, 2014 Pages 303 - 311. (contributed with sample preparation and characterization, ruthenium oxide thickness optimization and impedance measurements.)

3. A. Apolinário, P. Quitério, C.T. Sousa, M. Proença, **J. Azevedo**, M. Susano, S. Moraes, P. Lopes, J. Ventura and J.P. Araújo; Bottom-up nanofabrication using self-organized porous templates; Invited, Journal of Physics: Conference series, Volume 534, 2014 Page 012001-1 - 012001-10. (contributed with experimental results on pulsed electrodeposition in porous anodic alumnina templates)

4. P. Dias, M. Schreier, S.D. Tilley, J. Luo, **J. Azevedo**, L. Andrade, D. Bi, A. Hagfeldt, A. Mendes, M. Grätzel, M.T. Mayer; Transparent Cuprous Oxide Photocathode Enabling a Stacked Tandem Cell for Unbiased Water Splitting. Advanced Energy Materials, 2015 Page 1501537. (contributed with the development of a new electrodeposition process of Cu_2O on conductive glass that, after optimization, made possible the fabrication of efficient transparent photocathodes and the first tandem device comprising Cu_2O)

5. C.T. Sousa, D. Leitao, A. Apolinario, M. Proenca, **J. Azevedo**, J. Ventura and J.P. Araujo; Dendritic nanostructures grown in hierarchical branched pores. Nanotechnology Research Journal, Volume 7, 2014 Page 123. (contributed with a section on energy applications of dendritic nanostrutures)

6. C.T. Sousa, D. Leitao, A. Apolinario, M. Proenca, **J. Azevedo**, J. Ventura and J.P. Araujo; Invited Book Chapter for Nova publishers: Dendritic nanostructures grown in hierarchical branched pores, 2014 ISBN: 978-1-63321-383-8. (contributed with a section on energy applications of dendritic nanostrutures)

7. A.Apolinário, C.T. Sousa, A.M.Pereira, M.P.Fernandez, G. Oliveira, **J. Azevedo**, J. Ventura, L. Andrade, A.M. Mendes and J. P. Araújo; Magnetic and structural study of anodic iron oxide nanotubes (under preparation). (contributed with assistance in data interpretation)

8. A.Apolinário, P. Dias, **J. Azevedo**, C.T. Sousa, L. Andrade, A.M. Mendes and J. P. Araújo; Hematite photoanodes for photoelectrochemical water splitting prepared by ion beam deposition (under preparation). (contributed with experience planning, sample fabrication and characterization)

Nevertheless, several collaborations also took place, resulting in 7 oral communications, 1 poster presentations, and the following publications:

1. **J. Azevedo**, João Coelho, Graham Hungerford, N. Sooraj Hussain; Lasing transition ($^4F_{3/4} \rightarrow {}^4I_{11/2}$) at 1.06 μm in neodymium oxide doped lithium boro tellurite glass. Physica B: Condensed Matter, Volume 405, Issue 22, 2010, Pages 4696-4701. (contributed with experimental planning, sample preparation and characterization, as well as manuscript preparation)

2. João Coelho, **J. Azevedo**, Graham Hungerford, N. Sooraj Hussain; Luminescence and decay trends for NIR transition ($^4I_{13/2} \rightarrow {}^4 I_{15/2}$) at 15 μm in Er^{3+} doped LBT glasses. Optical Materials, Volume 33, Issue 8, 2011, Pages 1167-1173. (contributed with experimental planning, sample preparation and characterization, as well as manuscript preparation)

3. J.M. Teixeira, J.D. Costa, J. Ventura, M.P. Fernández-García, **J. Azevedo**, J.P. Araújo, J.B. Sousa, P. Wisniowski, S. Cardoso, P.P. Freitas; Giant intrinsic thermomagnetic effects in thin MgO magnetic tunnel junctions. Applied Physics Letters, Volume 102, Issue 21, 2013 Pages 212413-1 - 212413-3. (contributed with numerical simulation script development)

4. J.D. Costa, P. Quitério, A. Apolinário, C. T. Sousa, **J. Azevedo**, J. Ventura, L. Andrade, A.M. Mendes, and J.P. Araújo; The effect of electrolyte re-utilization in the growth rate and morphology of TiO_2 nanotubes. Materials Letters, Volume 171, 2016 Pages 224 - 227. (contributed with literature review as well as data interpretation)

Bibliography

[1] D. Abbott, Keeping the Energy Debate Clean: How Do We Supply the World's Energy Needs?, Proceedings of the IEEE 98 (1) 42–66. doi: 10.1109/JPROC.2009.2035162.

[2] C. A. Grimes, O. K. Varghese, S. Ranjan, Light, Water, Hydrogen: The Solar Generation of Hydrogen by Water Photoelectrolysis, 1st Edition, Springer, 2007.

[3] F. Trieb, Concentrating Solar Power for the Mediterranean Region, Tech. rep. (Jul. 2005).

[4] M. Skunik-Nuckowska, K. Grzejszczyk, P. J. Kulesza, L. Yang, N. Vlachopoulos, L. Häggman, E. Johansson, A. Hagfeldt, Integration of solid-state dye-sensitized solar cell with metal oxide charge storage material into photoelectrochemical capacitor, Journal of Power Sources 234 (C) (2013) 91–99. doi: 10.1016/j.jpowsour.2013.01.101.

[5] R. van de Krol, M. Gratzel, Photoelectrochemical Hydrogen Production, Springer Science & Business Media, 2011.

[6] T. N. Murakami, N. Kawashima, T. Miyasaka, A high-voltage dye-sensitized photocapacitor of a three-electrode system, Chemical Communications (26) (2005) 3346. doi:10.1039/b503122b.

[7] N. S. Lewis, Light work with water., Nature 414 (6864) (2001) 589–590. doi: 10.1038/414589a.

[8] M. Schreier, P. Gao, M. T. Mayer, J. Luo, T. Moehl, M. K. Nazeeruddin, S. D. Tilley, M. Gratzel, Efficient and selective carbon dioxide reduction on low cost protected Cu_2O photocathodes using a molecular catalyst, Energy & Environmental Science 8 (2015) 855–861. doi:10.1039/C4EE03454F.

[9] F. Studt, I. Sharafutdinov, F. Abild-Pedersen, C. F. Elkjær, J. S. Hummelshøj, S. Dahl, I. Chorkendorff, J. K. Nørskov, Discovery of a Ni–Ga catalyst for carbon dioxide reduction to methanol, Nature Chemistry 6 (4) (2014) 320–324. doi: 10.1038/nchem.1873.

[10] G. Ghadimkhani, N. R. de Tacconi, W. Chanmanee, C. Janaky, K. Rajeshwar, Efficient solar photoelectrosynthesis of methanol from carbon dioxide using hybrid CuO–Cu_2O semiconductor nanorod arrays, Chemical Communications 49 (13) (2013) 1297. doi:10.1039/c2cc38068d.

[11] Gurudayal, D. Sabba, M. H. Kumar, L. H. Wong, J. Barber, M. Gratzel,

N. Mathews, Perovskite-Hematite Tandem Cells for Efficient Overall Solar Driven Water Splitting, Nano Letters 15 (6) (2015) 3833–3839. doi: 10.1021/acs.nanolett.5b00616.

[12] S. Choudhary, S. Upadhyay, P. Kumar, N. Singh, V. R. Satsangi, R. Shrivastav, S. Dass, Nanostructured bilayered thin films in photoelectrochemical water splitting – A review, International Journal of Hydrogen Energy 37 (24) (2012) 18713–18730. doi:10.1016/j.ijhydene.2012.10.028.

[13] F. F. Abdi, L. Han, A. H. M. Smets, M. Zeman, B. Dam, R. van de Krol, Efficient solar water splitting by enhanced charge separation in a bismuth vanadate-silicon tandem photoelectrode, Nature Communications 4 (2013) 1–18. doi: 10.1038/ncomms3195.

[14] S. D. Tilley, M. Cornuz, K. Sivula, M. Gratzel, Light-Induced Water Splitting with Hematite: Improved Nanostructure and Iridium Oxide Catalysis, Angewandte Chemie International Edition 49 (36) (2010) 6405–6408. doi: 10.1002/anie.201003110.

[15] T. Lopes, L. Andrade, A. M. Mendes, Solar Energy Sciences and Engineering Applications, CRC Press, 2013. doi:10.1201/b15507-11.

[16] J. Luo, Z. Li, S. Nishiwaki, M. Schreier, M. T. Mayer, P. Cendula, Y. H. Lee, K. Fu, A. Cao, M. K. Nazeeruddin, Y. E. Romanyuk, S. Buecheler, S. D. Tilley, L. H. Wong, A. N. Tiwari, M. Gratzel, Targeting Ideal Dual-Absorber Tandem Water Splitting Using Perovskite Photovoltaics and $CuIn_xGa_1 - xSe_2$ Photocathodes, Advanced Energy Materials 5 (24) (2015) n/a–n/a. doi:10.1002/aenm.201501520.

[17] J. Brillet, M. Cornuz, F. L. Formal, J.-H. Yum, M. Gratzel, K. Sivula, Examining architectures of photoanode–photovoltaic tandem cells for solar water splitting, Journal of Materials Research 25 (01) (2011) 17–24. doi: 10.1557/JMR.2010.0009.

[18] P. Bornoz, F. F. Abdi, S. D. Tilley, B. Dam, R. van de Krol, M. Graetzel, K. Sivula, A Bismuth Vanadate–Cuprous Oxide Tandem Cell for Overall Solar Water Splitting, The Journal of Physical Chemistry C 118 (30) (2014) 16959–16966. doi:10.1021/jp500441h.

[19] X. Shi, K. Zhang, K. Shin, M. Ma, J. Kwon, I. T. Choi, J. K. Kim, H. K. Kim, D. H. Wang, J. H. Park, Unassisted photoelectrochemical water splitting beyond 5.7 % solar-to-hydrogen conversion efficiency by a wireless monolithic photoanode/dye-sensitised solar cell tandem device, Nano Energy 13 (C) (2015) 182–191. doi: 10.1016/j.nanoen.2015.02.018.

[20] M. G. Walter, E. L. Warren, J. R. McKone, S. W. Boettcher, Q. Mi, E. A. Santori, N. S. Lewis, Solar Water Splitting Cells, Chemical Reviews 110 (11) (2010) 6446–6473. doi:10.1021/cr1002326.

[21] Z. Chen, T. F. Jaramillo, T. G. Deutsch, A. Kleiman-Shwarsctein, A. J. Forman, N. Gaillard, R. Garland, K. Takanabe, C. Heske, M. Sunkara, E. W. McFarland, K. Domen, E. L. Miller, J. A. Turner, H. N. Dinh, Accelerating materials development for photoelectrochemical hydrogen production: Standards for methods, definitions, and reporting protocols, Journal of Materials Research 25 (01) (2011) 3–16. doi:10.1557/JMR.2010.0020.

[22] A. Fujishima, K. Honda, Electrochemical Photolysis of Water at a Semiconductor Electrode, Nature 238 (5358) (1972) 37–38. doi:10.1038/238037a0.

[23] J. Y. Kim, J.-W. Jang, D. H. Youn, G. Magesh, J. S. Lee, A Stable and Efficient Hematite Photoanode in a Neutral Electrolyte for Solar Water Splitting: Towards Stability Engineering, Advanced Energy Materials 4 (13) (2014) n/a–n/a. doi:10.1002/aenm.201400476.

[24] L. Steier, I. Herraiz-Cardona, S. Gimenez, F. Fabregat-Santiago, J. Bisquert, S. D. Tilley, M. Gratzel, Understanding the Role of Underlayers and Overlayers in Thin Film Hematite Photoanodes, Advanced Functional Materials 24 (48) (2014) 7681–7688. doi:10.1002/adfm.201402742.

[25] F. Le Formal, M. Gratzel, K. Sivula, Controlling Photoactivity in Ultrathin Hematite Films for Solar Water-Splitting, Advanced Functional Materials 20 (7) (2010) 1099–1107. doi:10.1002/adfm.200902060.

[26] P. J. Boddy, Oxygen evolution on semiconducting TiO_2, Journal of The Electrochemical Society 115 (2) (1968) 199–203. doi:10.1149/1.2411080.

[27] G. Wang, H. Wang, Y. Ling, Y. Tang, X. Yang, R. C. Fitzmorris, C. Wang, J. Z. Zhang, Y. Li, Hydrogen-Treated TiO_2 Nanowire Arrays for Photoelectrochemical Water Splitting, Nano Letters 11 (7) (2011) 3026–3033. doi:10.1021/nl201766h.

[28] T. Zhu, M. N. Chong, E. S. Chan, Nanostructured Tungsten Trioxide Thin Films Synthesized for Photoelectrocatalytic Water Oxidation: A review, ChemSusChem 7 (11) (2014) 2974–2997. doi:10.1002/cssc.201402089.

[29] T. W. Kim, K. S. Choi, Nanoporous $BiVO_4$ Photoanodes with Dual-Layer Oxygen Evolution Catalysts for Solar Water Splitting, Science 343 (6174) (2014) 990–994. doi:10.1126/science.1246913.

[30] J. Luo, S. D. Tilley, L. Steier, M. Schreier, M. T. Mayer, H. J. Fan, M. Gratzel, Solution Transformation of Cu_2O into $CuInS_2$ for Solar Water Splitting, Nano Letters 15 (2) (2015) 1395–1402. doi:10.1021/nl504746b.

[31] C. G. Morales-Guio, S. D. Tilley, H. Vrubel, M. Gratzel, X. Hu, Hydrogen evolution from a copper(I) oxide photocathode coated with an amorphous molybdenum sulphide catalyst, Nature Communications 5 (2014) 3059. doi:10.1038/ncomms4059.

[32] S. D. Tilley, M. Schreier, J. Azevedo, M. Stefik, M. Graetzel, Ruthenium Oxide Hydrogen Evolution Catalysis on Composite Cuprous Oxide Water–Splitting Photocathodes, Advanced Functional Materials 24 (3) (2014) 303–311. doi: 10.1002/adfm.201301106.

[33] G. Riveros, J. Vásquez, H. Gómez, T. Makarova, D. Silva, R. E. Marotti, E. A. Dalchiele, Single-step electrodeposition of polycrystalline CdSe microwire arrays: structural and optical properties, Applied Physics A 90 (3) (2007) 423–430. doi: 10.1007/s00339-007-4318-9.

[34] D. J. Peña, J. K. N. Mbindyo, A. J. Carado, T. E. Mallouk, C. D. Keating, B. Razavi, T. S. Mayer, Template Growth of Photoconductive Metal−CdSe−Metal Nanowires, The Journal of Physical Chemistry B 106 (30) (2002) 7458–7462. doi:10.1021/jp0256591.

[35] Y. Yin, Z. Jin, F. Hou, Enhanced solar water-splitting efficiency using core/sheath heterostructure CdS/TiO_2 nanotube arrays, Nanotechnology 18 (49) (2007) 495608. doi:10.1088/0957-4484/18/49/495608.

[36] M. K. Arora, A. Sinha, S. N. Upadhyay, Active cadmium sulfide photocatalysts for hydrogen production from water, Industrial & engineering chemistry research 37 (10) (1998) 3950–3955. doi:10.1021/ie970617y.

[37] S. S. K. Ma, T. Hisatomi, K. Maeda, Y. Moriya, K. Domen, Enhanced Water Oxidation on Ta_3N_5 Photocatalysts by Modification with Alkaline Metal Salts, Journal of the American Chemical Society 134 (49) (2012) 19993–19996. doi: 10.1021/ja3095747.

[38] H. X. Dang, N. T. Hahn, H. S. Park, A. J. Bard, C. B. Mullins, Nanostructured Ta_3N_5 Films as Visible-Light Active Photoanodes for Water Oxidation, The Journal of Physical Chemistry C 116 (36) (2012) 19225–19232. doi:10.1021/jp307369z.

[39] A. Duret, M. Gratzel, Visible light-induced water oxidation on mesoscopic α-Fe_2O_3 films made by ultrasonic spray pyrolysis., The Journal of Physical Chemistry B 109 (36) (2005) 17184–17191. doi:10.1021/jp044127c.

[40] A. Paracchino, V. Laporte, K. Sivula, M. Gratzel, E. Thimsen, Highly active oxide photocathode for photoelectrochemical water reduction., Nature Materials 10 (6) (2011) 456–461. doi:10.1038/nmat3017.

[41] D. H. Kim, S. H. Yoo, K. S. An, H. S. Yoo, Y. Kim, Chemical Vapor Deposition of Ga_2O_3 Thin Films on Si Substrates, Buletin-Korean Chemical Society 23 (2) (2002) 225–228.

[42] L. Steier, J. Luo, M. Schreier, M. T. Mayer, T. Sajavaara, M. Gratzel, Low-Temperature Atomic Layer Deposition of Crystalline and Photoactive Ultrathin Hematite Films for Solar Water Splitting., ACS Nano 9 (12) (2015) 11775–11783. doi:10.1021/acsnano.5b03694.

[43] R. Wick, S. D. Tilley, Photovoltaic and Photoelectrochemical Solar Energy Conversion with Cu_2O, The Journal of Physical Chemistry C 119 (47) (2015) 26243–26257. doi:10.1021/acs.jpcc.5b08397.

[44] S. S. Wilson, J. P. Bosco, Y. Tolstova, D. O. Scanlon, G. W. Watson, H. A. Atwater, Interface stoichiometry control to improve device voltage and modify band alignment in ZnO/Cu_2O heterojunction solar cells, Energy & Environmental Science 7 (2014) 3606–3610. doi:10.1039/C4EE01956C.

[45] A. F. Wright, J. S. Nelson, Theory of the copper vacancy in cuprous oxide, Journal of Applied Physics 92 (10) (2002) 5849. doi:10.1063/1.1516620.

[46] O. Porat, I. Riess, Defect chemistry of $Cu_{2-y}O$ at elevated temperatures. Part I: Non-stoichiometry, phase width and dominant point defects, Solid State Ionics 74 (3-4) (1994) 229–238. doi:10.1016/0167-2738(94)90215-1.

[47] N. L. Peterson, C. L. Wiley, Diffusion and point defects in Cu_2O, Journal of Physics and Chemistry of Solids 45 (3) (1984) 281–294. doi:10.1016/0022-3697(84)90033-7.

[48] B. K. Meyer, A. Polity, D. Reppin, M. Becker, P. Hering, P. J. Klar, T. Sander, C. Reindl, J. Benz, M. Eickhoff, C. Heiliger, M. Heinemann, J. Bläsing, A. Krost, S. Shokovets, C. Müller, C. Ronning, Binary copper oxide semiconductors: From materials towards devices, physica status solidi (b) 249 (8) (2012) 1487–1509. doi:10.1002/pssb.201248128.

[49] M. Hara, T. Kondo, M. Komoda, S. Ikeda, J. N. Kondo, K. Domen, M. Hara, K. Shinohara, A. Tanaka, Cu_2O as a photocatalyst for overall water splitting under visible light irradiation, Chemical Communications (3) (1998) 357–358. doi:10.1039/a707440i.

[50] A. Paracchino, J. C. Brauer, J.-E. Moser, E. Thimsen, M. Graetzel, Synthesis and Characterization of High-Photoactivity Electrodeposited Cu_2O Solar Absorber by Photoelectrochemistry and Ultrafast Spectroscopy, The Journal of Physical Chemistry C 116 (13) (2012) 7341–7350. doi:10.1021/jp301176y.

[51] A. Paracchino, N. Mathews, T. Hisatomi, M. Stefik, S. D. Tilley, M. Gratzel, Ultrathin films on copper(i) oxide water splitting photocathodes: a study on performance and stability, Energy & Environmental Science 5 (9) (2012) 8673. doi:10.1039/c2ee22063f.

[52] S. Chen, L.-W. Wang, Thermodynamic Oxidation and Reduction Potentials of Photocatalytic Semiconductors in Aqueous Solution, Chemistry of Materials 24 (18) (2012) 3659–3666. doi:10.1021/cm302533s.

[53] W. Anaf, O. Schalm, K. Janssens, K. De Wael, Understanding the (in)stability of semiconductor pigments by a thermodynamic approach, Dyes and Pigments 113 (C) (2015) 409–415. doi:10.1016/j.dyepig.2014.09.015.

[54] O. V. Marchenko, S. V. Solomin, The future energy: Hydrogen versus electricity, International Journal of Hydrogen Energy 40 (10) (2015) 3801–3805. doi: 10.1016/j.ijhydene.2015.01.132.

[55] J. R. McKone, N. S. Lewis, H. B. Gray, Will Solar-Driven Water-Splitting Devices See the Light of Day?, Chemistry of Materials 26 (1) (2014) 407–414. doi: 10.1021/cm4021518.

[56] A. Z. Weber, M. M. Mench, J. P. Meyers, P. N. Ross, J. T. Gostick, Q. Liu, Redox flow batteries: a review, Journal of Applied Electrochemistry 41 (10) (2011) 1137–1164. doi:10.1007/s10800-011-0348-2.

[57] A. Pedersen, Status and recommendations for RD&D on energy storage technologies in a Danish context.

[58] E. Sum, M. Skyllas-Kazacos, A study of the V(II)/V(III) redox couple for redox flow cell applications, Journal of Power Sources 15 (2-3) (1985) 179–190. doi: 10.1016/0378-7753(85)80071-9.

[59] H. Zhou, H. Zhang, P. Zhao, B. Yi, A comparative study of carbon felt and activated carbon based electrodes for sodium polysulfide/bromine redox flow battery, Electrochimica Acta 51 (28) (2006) 6304–6312. doi: 10.1016/j.electacta.2006.03.106.

[60] K. J. Kim, S.-W. Lee, T. Yim, J.-G. Kim, J. W. Choi, J. H. Kim, M.-S. Park, Y.-J. Kim, A new strategy for integrating abundant oxygen functional groups into carbon felt electrodes for vanadium redox flow batteries, Scientific Reports 4 (2014) 6906. doi:10.1038/srep06906.

[61] B. Li, M. Gu, Z. Nie, X. Wei, C. Wang, V. Sprenkle, W. Wang, Nanorod Niobium Oxide as Powerful Catalysts for an All Vanadium Redox Flow Battery, Nano Letters 14 (1) (2014) 158–165. doi:10.1021/nl403674a.

[62] B. Li, M. Gu, Z. Nie, Y. Shao, Q. Luo, X. Wei, X. Li, J. Xiao, C. Wang, V. Sprenkle, W. Wang, Bismuth Nanoparticle Decorating Graphite Felt as a High-Performance Electrode for an All-Vanadium Redox Flow Battery, Nano Letters 13 (3) (2013) 1330–1335. doi:10.1021/nl400223v.

[63] X. Ma, H. Zhang, C. Sun, Y. Zou, T. Zhang, An optimal strategy of electrolyte flow rate for vanadium redox flow battery, Journal of Power Sources 203 (2012) 153–158. doi:10.1016/j.jpowsour.2011.11.036.

[64] M. Rychcik, M. Skyllas-Kazacos, Characteristics of a new all-vanadium redox flow battery, Journal of Power Sources 22 (1) (1988) 59–67. doi: 10.1016/0378-7753(88)80005-3.

[65] D. N. Buckley, X. Gao, R. P. Lynch, N. Quill, M. J. Leahy, Towards Optical Monitoring of Vanadium Redox Flow Batteries (VRFBs): An Investigation of the

Underlying Spectroscopy, Journal of The Electrochemical Society 161 (4) (2014) A524–A534. doi:10.1149/2.023404jes.

[66] K. W. Knehr, E. Agar, C. R. Dennison, A. R. Kalidindi, E. C. Kumbur, A Transient Vanadium Flow Battery Model Incorporating Vanadium Crossover and Water Transport through the Membrane, Journal of The Electrochemical Society 159 (9) (2012) A1446–A1459. doi:10.1149/2.017209jes.

[67] C. Yin, Y. Gao, S. Guo, H. Tang, A coupled three dimensional model of vanadium redox flow battery for flow field designs, Energy 74 (C) (2014) 886–895. doi:10.1016/j.energy.2014.07.066.

[68] E. Kjeang, B. T. Proctor, A. G. Brolo, D. A. Harrington, N. Djilali, D. Sinton, High-performance microfluidic vanadium redox fuel cell, Electrochimica Acta 52 (15) (2007) 4942–4946. doi:10.1016/j.electacta.2007.01.062.

[69] A. Parasuraman, T. M. Lim, C. Menictas, M. Skyllas-Kazacos, Review of material research and development for vanadium redox flow battery applications, Electrochimica Acta 101 (2013) 27–40. doi:10.1016/j.electacta.2012.09.067.

[70] D. You, H. Zhang, J. Chen, A simple model for the vanadium redox battery, Electrochimica Acta 54 (27) (2009) 6827–6836. doi:10.1016/j.electacta.2009.06.086.

[71] D. P. Scamman, G. W. Reade, E. P. L. Roberts, Numerical modelling of a bromide–polysulphide redox flow battery, Journal of Power Sources 189 (2) (2009) 1220–1230. doi:10.1016/j.jpowsour.2009.01.071.

[72] D. P. Scamman, G. W. Reade, E. P. L. Roberts, Numerical modelling of a bromide-polysulphide redox flow battery. Part 2: Evaluation of a utility-scale system, Journal of Power Sources 189 (2) (2009) 1231–1239. doi:10.1016/j.jpowsour.2009.01.076.

[73] P. Zhao, H. Zhang, H. Zhou, B. Yi, Nickel foam and carbon felt applications for sodium polysulfide/bromine redox flow battery electrodes, Electrochimica Acta 51 (6) (2005) 1091–1098. doi:10.1016/j.electacta.2005.06.008.

[74] B. Huskinson, J. Rugolo, S. K. Mondal, M. J. Aziz, A high power density, high efficiency hydrogen–chlorine regenerative fuel cell with a low precious metal content catalyst, Energy & Environmental Science 5 (9) (2012) 8690–8698. doi:10.1039/c2ee22274d.

[75] M. Skyllas-Kazacos, M. H. Chakrabarti, S. A. Hajimolana, F. S. Mjalli, M. Saleem, Progress in Flow Battery Research and Development, Journal of The Electrochemical Society 158 (8) (2011) R55. doi:10.1149/1.3599565.

[76] B. Huskinson, M. P. Marshak, C. Suh, S. Er, M. R. Gerhardt, C. J. Galvin, X. Chen, A. Aspuru-Guzik, R. G. Gordon, M. J. Aziz, A metal-free organic-inorganic aqueous flow battery, Nature 505 (7482) (2015) 195–198. doi:

10.1038/nature12909.

[77] M. H. Chakrabarti, R. Dryfe, Organic Electrolytes for Redox Flow Batteries, Journal of the Chemical Society of Pakistan 29 (2007) 294–300.

[78] S. Er, C. Suh, M. P. Marshak, A. Aspuru-Guzik, Computational design of molecules for an all-quinone redox flow battery, Chemical Science 6 (2015) 885–893. doi:10.1039/C4SC03030C.

[79] T. Wilke, D. Schricker, J. Rolf, K. Kleinermanns, Solar Water Splitting by Semiconductor Nanocomposites and Hydrogen Storage with Quinoid Systems, Open Journal of Physical Chemistry 02 (04) (2012) 195–203. doi:10.4236/ojpc.2012.24027.

[80] E. A. Cepeda, M. Diaz, Solubility of anthracene and anthraquinone in acetonitrile, methyl ethyl ketone, isopropol alcohol and their mixtures, Fluid Phase Equilibria 121 (1) (1995) 267–272. doi:10.1016/0378-3812(96)03000-2.

[81] K. Lin, Q. Chen, M. R. Gerhardt, L. Tong, S. B. Kim, L. Eisenach, A. W. Valle, D. Hardee, R. G. Gordon, M. J. Aziz, M. P. Marshak, Alkaline quinone flow battery., Science 349 (6255) (2015) 1529–1532. doi:10.1126/science.aab3033.

[82] P. H. Raven, Biology of Plants, Worth Publishers, Inc., 2004.

[83] M. Sharon, P. Veluchamy, C. Natarajan, D. Kumar, Solar rechargeable battery—principle and materials, Electrochimica Acta 36 (7) (1991) 1107–1126. doi:10.1016/0013-4686(91)85097-Q.

[84] M. Yu, W. D. McCulloch, D. R. Beauchamp, Z. Huang, X. Ren, Y. Wu, Aqueous Lithium–Iodine Solar Flow Battery for the Simultaneous Conversion and Storage of Solar Energy, Journal of the American Chemical Society 137 (26) (2015) 8332–8335. doi:10.1021/jacs.5b03626.

[85] M. Yu, X. Ren, L. Ma, Y. Wu, Integrating a redox-coupled dye-sensitized photoelectrode into a lithium-oxygen battery for photoassisted charging, Nature Communications 5 (2014) 1–17. doi:10.1038/ncomms6111.

[86] D. Liu, Z. Wei, C.-j. Hsu, Y. Shen, F. Liu, Efficient Solar Energy Storage Using A TiO_2/WO_3 Tandem Photoelectrode in An All-vanadium Photoelectrochemical Cell, Electrochimica Acta 136 (2014) 435–441. doi:10.1016/j.electacta.2014.05.129.

[87] Z. Wei, D. Liu, C. Hsu, F. Liu, All-vanadium redox photoelectrochemical cell: An approach to store solar energy, Electrochemistry Communications 45 (2014) 79–82. doi:10.1016/j.elecom.2014.05.018.

[88] P. Roy, S. Berger, P. Schmuki, TiO_2 Nanotubes: Synthesis and Applications, Angewandte Chemie International Edition 50 (13) (2011) 2904–2939. doi:10.1002/anie.201001374.

[89] C. Valsecchi, A. G. Brolo, Periodic metallic nanostructures as plasmonic chemical

sensors., Langmuir 29 (19) (2013) 5638–5649. doi:10.1021/la400085r.

[90] D. O'Carroll, D. Iacopino, G. Redmond, Luminescent Conjugated Polymer Nanowire Y-Junctions with On-Branch Molecular Anisotropy, Advanced Materials 21 (10-11) (2009) 1160–1165. doi:10.1002/adma.200801723.

[91] P. Krogstrup, H. I. Jørgensen, M. Heiss, O. Demichel, J. V. Holm, M. Aagesen, J. Nygard, A. F. i. Morral, Single–nanowire solar cells beyond the Shockley–Queisser limit, Nature Photonics 7 (4) (2013) 306–310. doi:10.1038/nphoton.2013.32.

[92] Z. Zhang, R. Dua, L. Zhang, H. Zhu, H. Zhang, P. Wang, Carbon-Layer-Protected Cuprous Oxide Nanowire Arrays for Efficient Water Reduction, ACS Nano 7 (2) (2013) 1709–1717. doi:10.1021/nn3057092.

[93] L. Wang, W. Mao, D. Ni, J. Di, Y. Wu, Y. Tu, Direct electrodeposition of gold nanoparticles onto indium/tin oxide film coated glass and its application for electrochemical biosensor, Electrochemistry Communications 10 (4) (2008) 673–676. doi:10.1016/j.elecom.2008.02.009.

[94] Y. Fu, J. Chen, H. Zhang, Synthesis of Fe_2O_3 nanowires by oxidation of iron, Chemical Physics Letters 350 (5) (2001) 491–494. doi:10.1016/S0009-2614(01)01352-5.

[95] C.-J. Jia, L.-D. Sun, Z.-G. Yan, L.-P. You, F. Luo, X.-D. Han, Y.-C. Pang, Z. Zhang, C.-H. Yan, Single-Crystalline Iron Oxide Nanotubes, Angewandte Chemie International Edition 44 (28) (2005) 4328–4333. doi:10.1002/anie.200463038.

[96] J. Hou, Z. Wang, C. Yang, H. Cheng, S. Jiao, H. Zhu, Cobalt-bilayer catalyst decorated Ta_3N_5 nanorod arrays as integrated electrodes for photoelectrochemical water oxidation, Energy & Environmental Science 6 (11) (2013) 3322. doi:10.1039/c3ee41854e.

[97] C. M. Payne, L. J. E. Anderson, J. H. Hafner, Novel Plasmonic Structures Based on Gold Nanobelts, The Journal of Physical Chemistry C 117 (9) (2013) 4734–4739. doi:10.1021/jp3080089.

[98] J. Moir, N. Soheilnia, P. O'Brien, A. Jelle, C. M. Grozea, D. Faulkner, M. G. Helander, G. A. Ozin, Enhanced Hematite Water Electrolysis Using a 3D Antimony-Doped Tin Oxide Electrode, ACS Nano 7 (5) (2013) 4261–4274. doi:10.1021/nn400744d.

[99] S. K. Mohapatra, S. E. John, S. Banerjee, M. Misra, Water Photooxidation by Smooth and Ultrathin α-Fe_2O_3 Nanotube Arrays, Chemistry of Materials 21 (14) (2009) 3048–3055. doi:10.1021/cm8030208.

[100] O. Khaselev, A Monolithic Photovoltaic-Photoelectrochemical Device for Hydrogen Production via Water Splitting, Science 280 (5362) (1998) 425–427. doi:

10.1126/science.280.5362.425.

[101] K. L. Hardee, Semiconductor Electrodes, Journal of The Electrochemical Society 123 (7) (1976) 1024. doi:10.1149/1.2132984.

[102] Y. Lin, G. Yuan, S. Sheehan, S. Zhou, D. Wang, Hematite-based solar water splitting: challenges and opportunities, Energy & Environmental Science 4 (12) (2011) 4862. doi:10.1039/c1ee01850g.

[103] R. J. Atkinson, A. M. Posner, J. P. Quirk, Adsorption of potential-determining ions at the ferric oxide-aqueous electrolyte interface, The Journal of Physical Chemistry 71 (3) (1967) 550–558. doi:10.1021/j100862a014.

[104] J. R. Bolton, Solar photoproduction of hydrogen: A review, Solar Energy 57 (1) (1996) 37–50. doi:10.1016/0038-092X(96)00032-1.

[105] M. P. Dare-Edwards, J. B. Goodenough, A. Hamnett, P. R. Trevellick, Electrochemistry and photoelectrochemistry of iron(III) oxide, Journal of the Chemical Society, Faraday Transactions 1 79 (9) (1983) 2027. doi:10.1039/f19837902027.

[106] K. Sivula, F. Le Formal, M. Gratzel, Solar Water Splitting: Progress Using Hematite (α-Fe_2O_3) Photoelectrodes, ChemSusChem 4 (4) (2011) 432–449. doi:10.1002/cssc.201000416.

[107] Y. Ling, G. Wang, D. A. Wheeler, J. Z. Zhang, Y. Li, Sn-doped hematite nanostructures for photoelectrochemical water splitting, Nano Letters 11 (5) (2011) 2119–2125. doi:10.1021/nl200708y.

[108] K. Itoh, J. O. Bockris, Stacked thin-film photoelectrode using iron oxide, Journal of Applied Physics 56 (3) (1984) 874–876. doi:10.1063/1.334028.

[109] J. Brillet, M. Gratzel, K. Sivula, Decoupling feature size and functionality in solution-processed, porous hematite electrodes for solar water splitting, Nano Letters 10 (10) (2010) 4155–4160. doi:10.1021/nl102708c.

[110] J. A. Glasscock, P. R. F. Barnes, I. C. Plumb, N. Savvides, Enhancement of Photoelectrochemical Hydrogen Production from Hematite Thin Films by the Introduction of Ti and Si, The Journal of Physical Chemistry C 111 (44) (2007) 16477–16488. doi:10.1021/jp074556l.

[111] A. Kay, I. Cesar, M. Gratzel, New Benchmark for Water Photooxidation by Nanostructured α-Fe_2O_3 Films, Journal of the American Chemical Society 128 (49) (2006) 15714–15721. doi:10.1021/ja064380l.

[112] K. Sivula, R. Zboril, F. Le Formal, R. Robert, A. Weidenkaff, J. Tucek, J. Frydrych, M. Gratzel, Photoelectrochemical Water Splitting with Mesoporous Hematite Prepared by a Solution-Based Colloidal Approach, Journal of the American Chemical Society 132 (21) (2010) 7436–7444. doi:10.1021/ja101564f.

[113] L. Vayssieres, N. Beermann, S.-E. Lindquist, A. Hagfeldt, Controlled Aqueous

Chemical Growth of Oriented Three-Dimensional Crystalline Nanorod Arrays: Application to Iron(III) Oxides, Chemistry of Materials 13 (2) (2001) 233–235. doi:10.1021/cm001202x.

[114] A. Mao, G. Y. Han, J. H. Park, Synthesis and photoelectrochemical cell properties of vertically grown α-Fe_2O_3 nanorod arrays on a gold nanorod substrate, Journal of Materials Chemistry 20 (11) (2010) 2247–2250. doi:10.1039/b921965j.

[115] R. van de Krol, Y. Liang, J. Schoonman, Solar hydrogen production with nanostructured metal oxides, Journal of Materials Chemistry 18 (20) (2008) 2311. doi:10.1039/b718969a.

[116] L. Vayssieres, C. Sathe, S. M. Butorin, D. K. Shuh, J. Nordgren, J. Guo, One-Dimensional Quantum-Confinement Effect in α-Fe_2O_3 Ultrafine Nanorod Arrays, Advanced Materials 17 (19) (2005) 2320–2323. doi:10.1002/adma.200500992.

[117] H. E. Prakasam, O. K. Varghese, M. Paulose, G. K. Mor, C. A. Grimes, Synthesis and photoelectrochemical properties of nanoporous iron (III) oxide by potentiostatic anodization, Nanotechnology 17 (17) 4285. doi:10.1088/0957-4484/17/17/001.

[118] Z. Zhang, M. F. Hossain, T. Takahashi, Self-assembled hematite (α-Fe_2O_3) nanotube arrays for photoelectrocatalytic degradation of azo dye under simulated solar light irradiation, Applied Catalysis B: Environmental 95 (3-4) (2010) 423–429. doi:10.1016/j.apcatb.2010.01.022.

[119] C. Sanchez, K. D. Sieber, G. A. Somorjai, The photoelectrochemistry of niobium doped α-Fe_2O_3, Journal of Electroanalytical Chemistry and Interfacial Electrochemistry 252 (2) (1988) 269–290. doi:10.1016/0022-0728(88)80216-X.

[120] R. Shinar, J. H. Kennedy, Photoactivity of doped α-Fe_2O_3 electrodes, Solar Energy Materials 6 (3) (1982) 323–335. doi:10.1016/0165-1633(82)90038-7.

[121] X. Guo, L. Wang, Y. Tan, Hematite nanorods Co-doped with Ru cations with different valence states as high performance photoanodes for water splitting, Nano Energy 16 (2015) 320–328. doi:10.1016/j.nanoen.2015.07.005.

[122] A. Kleiman-Shwarsctein, Y.-S. Hu, A. J. Forman, G. D. Stucky, E. W. McFarland, Electrodeposition of α-Fe_2O_3 Doped with Mo or Cr as Photoanodes for Photocatalytic Water Splitting, The Journal of Physical Chemistry C 112 (40) (2008) 15900–15907. doi:10.1021/jp803775j.

[123] K. M. H. Young, T. W. Hamann, Enhanced photocatalytic water oxidation efficiency with $Ni(OH)_2$ catalysts deposited on α-Fe_2O_3 via ALD, Chemical Communications 50 (63) (2014) 8727. doi:10.1039/C4CC02598A.

[124] A. Mao, K. Shin, J. K. Kim, D. H. Wang, G. Y. Han, J. H. Park, Controlled Synthesis of Vertically Aligned Hematite on Conducting Substrate for Photoelectrochemical

Cells: Nanorods versus Nanotubes, ACS Applied Materials & Interfaces 3 (6) (2011) 1852–1858. doi:10.1021/am200407t.

[125] E. R. Kötz, S. Stucki, Ruthenium dioxide as a hydrogen-evolving cathode, Journal of Applied Electrochemistry 17 (6) (1987) 1190–1197. doi:10.1007/BF01023602.

[126] R. T. Downs, M. Hall-Wallace, The American Mineralogist crystal structure database, American Mineralogist 88 (1) (2003) 247–250.

[127] H. Solache-Carranco, G. Juarez-Diaz, M. Galvan-Arellano, J. Martinez-Juarez, R. Romero-Paredes, R. Pena-Sierra, Raman scattering and photoluminescence studies on Cu_2O (2008) 421–424doi:10.1109/ICEEE.2008.4723375.

[128] W. F. Zhang, Y. L. He, M. S. Zhang, Z. Yin, Q. Chen, Raman scattering study on anatase TiO_2 nanocrystals, Journal of Physics D: Applied Physics 33 (8) (2000) 912–916. doi:10.1088/0022-3727/33/8/305.

[129] M. Reiners, K. Xu, N. Aslam, A. Devi, R. Waser, S. Hoffmann-Eifert, Growth and Crystallization of TiO_2 Thin Films by Atomic Layer Deposition Using a Novel Amido Guanidinate Titanium Source and Tetrakis-dimethylamido-titanium, Chemistry of Materials 25 (15) (2013) 2934–2943. doi:10.1021/cm303703r.

[130] S. Park, B. L. Clark, D. A. Keszler, J. P. Bender, J. F. Wager, T. A. Reynolds, G. S. Herman, Low-temperature thin-film deposition and crystallization, Science 297 (5578) (2002) 65–65. doi:10.1126/science.1072009.

[131] D. R. G. Mitchell, G. Triani, Z. Zhang, Hydrothermal crystallization of amorphous titania films deposited using low temperature atomic layer deposition, Thin Solid Films 516 (23) (2008) 8414–8423. doi:10.1016/j.tsf.2008.04.052.

[132] A. I. Kontos, I. M. Arabatzis, D. S. Tsoukleris, A. G. Kontos, M. C. Bernard, D. E. Petrakis, P. Falaras, Efficient photocatalysts by hydrothermal treatment of TiO_2, Catalysis Today 101 (3-4) (2005) 275–281. doi:10.1016/j.cattod.2005.03.003.

[133] O. Lupan, T. Pauporté, Hydrothermal treatment for the marked structural and optical quality improvement of ZnO nanowire arrays deposited on lightweight flexible substrates, Journal of Crystal Growth 312 (16-17) (2010) 2454–2458. doi:10.1016/j.jcrysgro.2010.05.022.

[134] K. Murakami, M. Rommel, B. Hudec, A. Rosová, K. Hušeková, E. Dobročka, R. Rammula, A. Kasikov, J. H. Han, W. Lee, S. J. Song, A. Paskaleva, A. J. Bauer, L. Frey, K. Fröhlich, J. Aarik, C. S. Hwang, Nanoscale Characterization of TiO_2 Films Grown by Atomic Layer Deposition on RuO_2 Electrodes, ACS Applied Materials & Interfaces 6 (4) (2014) 2486–2492. doi:10.1021/am4049139.

[135] J. Azevedo, C. T. Sousa, J. Ventura, A. Apolinário, A. M. Mendes, J. P. Araujo, Ultra-long Fe nanowires by pulsed electrodeposition with full filling of alumina templates, Materials Research Express 1 (1) (2014) 015028. doi:

10.1088/2053-1591/1/1/015028.

[136] J. Azevedo, C. T. Sousa, A. M. Mendes, J. P. Araujo, Influence of the Rest Pulse Duration in Pulsed Electrodeposition of Fe Nanowires, Journal of Nanoscience and Nanotechnology 12 (12) (2012) 9112–9117. doi:10.1166/jnn.2012.6769.

[137] C. T. Sousa, D. C. Leitao, M. P. Proença, A. Apolinário, J. G. Correia, J. Ventura, J. P. Araujo, Tunning pore filling of anodic alumina templates by accurate control of the bottom barrier layer thickness, Nanotechnology 22 (31) (2011) 315602–315607. doi:10.1088/0957-4484/22/31/315602.

[138] V. Pore, A. Rahtu, M. Leskelä, M. Ritala, T. Sajavaara, J. Keinonen, Atomic Layer Deposition of Photocatalytic TiO_2 Thin Films from Titanium Tetramethoxide and Water, Chemical Vapor Deposition 10 (3) (2004) 143–148. doi:10.1002/cvde.200306289.

[139] Y. Mao, J. He, X. Sun, W. Li, X. Lu, J. Gan, Z. Liu, L. Gong, J. Chen, P. Liu, Y. Tong, Electrochemical synthesis of hierarchical Cu_2O stars with enhanced photoelectrochemical properties, Electrochimica Acta 62 (2012) 1–7. doi:10.1016/j.electacta.2011.10.106.

[140] M. Wang, L. Sun, Z. Lin, J. Cai, K. Xie, C. Lin, p–n Heterojunction photoelectrodes composed of Cu_2O-loaded TiO_2 nanotube arrays with enhanced photoelectrochemical and photoelectrocatalytic activities, Energy & Environmental Science 6 (4) (2013) 1211. doi:10.1039/c3ee24162a.

[141] Z. Zhang, P. Wang, Highly stable copper oxide composite as an effective photocathode for water splitting via a facile electrochemical synthesis strategy, Journal of Materials Chemistry 22 (6) (2012) 2456. doi:10.1039/c1jm14478b.

[142] J. Azevedo, L. Steier, P. Dias, M. Stefik, C. T. Sousa, J. P. Araujo, A. M. Mendes, M. Gratzel, S. D. Tilley, On the stability enhancement of cuprous oxide water splitting photocathodes by low temperature steam annealing, Energy & Environmental Science 7 (2014) 4044–4052. doi:10.1039/C4EE02160F.

[143] B. Seger, D. S. Tilley, T. Pedersen, P. C. K. Vesborg, O. Hansen, M. Gratzel, I. Chorkendorff, Silicon protected with atomic layer deposited TiO_2: durability studies of photocathodic H_2 evolution, RSC Advances 3 (48) (2013) 25902. doi:10.1039/c3ra45966g.

[144] S. J. Ikhmayies, Properties of Amorphous SnO_2 Thin Films, Prepared by Thermal Evaporation, International Journal of Materials and Chemistry 2 (4) (2012) 173–177. doi:10.5923/j.ijmc.20120204.10.

[145] L. Tan, L. Wang, Y. Wang, Hydrothermal Synthesis of SnO_2 Nanostructures with Different Morphologies and Their Optical Properties, Journal of Nanomaterials 2011 (1) (2011) 1–10. doi:10.1021/jp036741e.

[146] M. A. Yıldırım, Y. Akaltun, A. Ateş, Characteristics of SnO_2 thin films prepared by SILAR, Solid State Sciences 14 (9) (2012) 1282–1288. doi: 10.1016/j.solidstatesciences.2012.07.012.

[147] J. Hu, Y. F. Zhu, Q. Liu, Y. B. Gao, R. G. Du, C. J. Lin, SnO_2 Nanoparticle Films Prepared by Pulse Current Deposition for Photocathodic Protection of Stainless Steel, Journal of The Electrochemical Society 162 (4) (2015) C161–C166. doi: 10.1149/2.0451504jes.

[148] M. G. Kast, L. J. Enman, N. J. Gurnon, A. Nadarajah, S. W. Boettcher, Solution-Deposited F:SnO_2/TiO_2 as a Base-Stable Protective Layer and Antireflective Coating for Microtextured Buried-Junction H2-evolving Si Photocathodes, ACS Applied Materials & Interfaces 6 (24) (2014) 22830–22837. doi: 10.1021/am506999p.

[149] M. Stefik, M. Cornuz, N. Mathews, T. Hisatomi, S. Mhaisalkar, M. Gratzel, Transparent, Conducting Nb:SnO_2 for Host–Guest Photoelectrochemistry, Nano Letters 12 (10) (2012) 5431–5435. doi:10.1021/nl303101n.

[150] P. Dai, W. Li, J. Xie, Y. He, J. Thorne, G. McMahon, J. Zhan, D. Wang, Forming Buried Junctions to Enhance the Photovoltage Generated by Cuprous Oxide in Aqueous Solutions, Angewandte Chemie International Edition 53 (49) (2014) 13493–13497. doi:10.1002/anie.201408375.

[151] Y. S. Lee, D. Chua, R. E. Brandt, S. C. Siah, J. V. Li, J. P. Mailoa, S. W. Lee, R. G. Gordon, T. Buonassisi, Atomic Layer Deposited Gallium Oxide Buffer Layer Enables 1.2 V Open-Circuit Voltage in Cuprous Oxide Solar Cells, Advanced Materials 26 (27) (2014) 4704–4710. doi:10.1002/adma.201401054.

[152] S. Hu, N. S. Lewis, J. W. Ager, J. Yang, J. R. McKone, N. C. Strandwitz, Thin-Film Materials for the Protection of Semiconducting Photoelectrodes in Solar-Fuel Generators, The Journal of Physical Chemistry C 119 (43) (2015) 24201–24228. doi:10.1021/acs.jpcc.5b05976.

[153] H. Chen, T. N. Cong, W. Yang, C. Tan, Y. Li, Y. Ding, Progress in electrical energy storage system: A critical review, Progress in Natural Science 19 (3) (2009) 291–312. doi:10.1016/j.pnsc.2008.07.014.

[154] S. Licht, G. Hodes, R. Tenne, J. Manassen, A light-variation insensitive high efficiency solar cell, Nature 326 (6116) (1987) 863–864. doi:10.1038/326863a0.

[155] W. Wang, Q. Luo, B. Li, X. Wei, L. Li, Z. Yang, Recent Progress in Redox Flow Battery Research and Development, Advanced Functional Materials 23 (8) (2012) 970–986. doi:10.1002/adfm.201200694.

[156] B. Yang, L. Hoober-Burkhardt, F. Wang, G. K. Surya Prakash, S. R. Narayanan, An Inexpensive Aqueous Flow Battery for Large-Scale Electrical Energy Storage Based on Water-Soluble Organic Redox Couples, Journal of The Electrochemical

Society 161 (9) (2014) A1371–A1380. doi:10.1149/2.1001409jes.

[157] P. Alotto, M. Guarnieri, F. Moro, Redox flow batteries for the storage of renewable energy: A review, Renewable and Sustainable Energy Reviews 29 (2014) 325–335. doi:10.1016/j.rser.2013.08.001.

[158] K. W. Knehr, E. C. Kumbur, Open circuit voltage of vanadium redox flow batteries: Discrepancy between models and experiments, Electrochemistry Communications 13 (4) (2011) 342–345. doi:10.1016/j.elecom.2011.01.020.

[159] N. Arroyo-Curras, J. W. Hall, J. E. Dick, R. A. Jones, A. J. Bard, An Alkaline Flow Battery Based on the Coordination Chemistry of Iron and Cobalt, Journal of The Electrochemical Society 162 (3) (2014) A378–A383. doi:10.1107/S0108270189000016.

[160] W. S. Rasband, ImageJ, http://rsb.info.nih.gov/ij/.

[161] C. Lu, L. Zhang, Y. Zhang, S. Liu, G. Liu, Fabrication of CdS/CdSe bilayer thin films by chemical bath deposition and electrodeposition, and their photoelectrochemical properties, Applied Surface Science 319 (2014) 278–284. doi:10.1016/j.apsusc.2014.08.158.

[162] G. Sasikala, R. Dhanasekaran, C. Subramanian, Electrodeposition and optical characterisation of CdS thin films on ITO-coated glass, Thin Solid Films 302 (1) (1997) 71–76. doi:10.1016/S0040-6090(96)09582-X.

[163] M. Takahashi, S. Hasegawa, M. Watanabe, T. Miyuki, S. Ikeda, K. Iida, Preparation of CdS thin films by electrodeposition: effect of colloidal sulfur particle stability on film composition, Journal of Applied Electrochemistry 32 (4) (2002) 359–367. doi:10.1023/A:1016325211708.

[164] E. Fatás, Electrochemical Deposition of CdS Thin Films on Mo and Al Substrates, Journal of The Electrochemical Society 131 (10) (1984) 2243. doi:10.1149/1.2115233.

[165] F. Goto, K. Shirai, M. Ichimura, Defect reduction in electrochemically deposited CdS thin films by annealing in O_2, Solar Energy Materials and Solar Cells 50 (1) (1998) 147–153. doi:10.1016/S0927-0248(97)00136-0.

[166] T. Lopes, P. Dias, L. Andrade, A. M. Mendes, An innovative photoelectrochemical lab device for solar water splitting, Solar Energy Materials and Solar Cells 128 (C) (2014) 399–410. doi:10.1016/j.solmat.2014.05.051.

[167] S. C. Rodrigues, R. Whitley, A. M. Mendes, Preparation and characterization of carbon molecular sieve membranes based on resorcinol–formaldehyde resin, Journal of Membrane Science 459 (C) (2014) 207–216. doi:10.1016/j.memsci.2014.02.013.

[168] J. Maçaira, L. Andrade, A. M. Mendes, Modeling, simulation and design of

dye sensitized solar cells, RSC Advances 4 (6) (2014) 2830–2844. doi: 10.1039/C3RA46295A.

[169] F. Ribeiro, J. Maçaira, R. Cruz, J. Gabriel, L. Andrade, A. M. Mendes, Laser assisted glass frit sealing of dye-sensitized solar cells, Solar Energy Materials and Solar Cells 96 (C) (2012) 43–49. doi:10.1016/j.solmat.2011.09.009.

[170] X. Li, P. S. Bassi, P. P. Boix, Y. Fang, L. H. Wong, Revealing the Role of TiO_2 Surface Treatment of Hematite Nanorods Photoanodes for Solar Water Splitting., ACS Applied Materials & Interfaces 7 (31) (2015) 16960–16966. doi: 10.1021/acsami.5b01394.

[171] A. S. Aliev, M. N. Mamedov, M. T. Abbasov, Photoelectrochemical properties of TiO_2/CdS heterostructures, Inorganic Materials 45 (9) (2009) 965–967. doi: 10.1134/S0020168509090039.

[172] Y.-L. Lee, C.-F. Chi, S.-Y. Liau, CdS/CdSe Co-Sensitized TiO_2 Photoelectrode for Efficient Hydrogen Generation in a Photoelectrochemical Cell, Chemistry of Materials 22 (3) (2010) 922–927. doi:10.1021/cm901762h.

[173] S. Cheng, W. Fu, H. Yang, L. Zhang, J. Ma, H. Zhao, M. Sun, L. Yang, Photoelectrochemical Performance of Multiple Semiconductors (CdS/CdSe/ZnS) Cosensitized TiO_2 Photoelectrodes, The Journal of Physical Chemistry C 116 (3) (2012) 2615–2621. doi:10.1021/jp209258r.

[174] H.-S. Rao, W.-Q. Wu, Y. Liu, Y.-F. Xu, B.-X. Chen, H.-Y. Chen, D. Kuang, C.-Y. Su, CdS/CdSe co-sensitized vertically alignedanatase TiO_2 nanowire arrays for efficientsolar cells, Nano Energy 8 (2014) 1–8. doi:10.1016/j.nanoen.2014.05.003.

[175] Y.-F. Xu, W.-Q. Wu, H.-S. Rao, H.-Y. Chen, D. Kuang, C.-Y. Su, CdS/CdSe co-sensitized TiO_2 nanowire-coated hollow Spheres exceeding 6 % photovoltaic performance, Nano Energy 11 (2015) 621–630. doi:10.1016/j.nanoen.2014.11.045.

[176] X. Wang, G. Liu, G. Q. Lu, H.-M. Cheng, Stable photocatalytic hydrogen evolution from water over ZnO-CdS core-shell nanorods, International Journal of Hydrogen Energy 35 (15) (2010) 8199–8205. doi:10.1016/j.ijhydene.2009.12.091.

[177] Y. Tang, X. Hu, C. Liu, Perfect inhibition of CdS photocorrosion by graphene sheltering engineering on TiO_2 nanotube array for highly stable photocatalytic activity, Physical Chemistry Chemical Physics 16 (2014) 25321–25329. doi: 10.1039/C4CP04057K.

[178] T. W. Kim, K.-S. Choi, Improving Stability and Photoelectrochemical Performance of $BiVO_4$ Photoanodes in Basic Media by Adding a $ZnFe_2O_4$ Layer, The Journal of Physical Chemistry Letters 7 (3) (2016) 447–451. doi: 10.1021/acs.jpclett.5b02774.

[179] M. Barroso, S. R. Pendlebury, A. J. Cowan, J. R. Durrant, Charge carrier trapping,

recombination and transfer in hematite (α-Fe_2O_3) water splitting photoanodes, Chemical Science 4 (7) (2013) 2724–2734. doi:10.1039/c3sc50496d.

[180] B. M. Klahr, T. W. Hamann, Current and Voltage Limiting Processes in Thin Film Hematite Electrodes, The Journal of Physical Chemistry C 115 (16) (2011) 8393–8399. doi:10.1021/jp200197d.

[181] F. Le Formal, N. Tétreault, M. Cornuz, T. Moehl, M. Gratzel, K. Sivula, Passivating surface states on water splitting hematite photoanodes with alumina overlayers, Chemical Science 2 (4) (2011) 737–743. doi:10.1039/C0SC00578A.

[182] M. S. Lavine, A solution for scalable-flow batteries, Science 349 (6255) (2015) 1500–1502. doi:10.1126/science.349.6255.1500-l.

[183] D. K. Bora, A. Braun, E. C. Constable, “In rust we trust”. Hematite – the prospective inorganic backbone for artificial photosynthesis, Energy & Environmental Science 6 (2) (2013) 407. doi:10.1039/c2ee23668k.

[184] P. Dias, A. Vilanova, T. Lopes, L. Andrade, A. M. Mendes, Extremely Stable Bare Hematite Photoanode for Water Splitting, (to be submitted) (2016) 1–45.

[185] C. Janaky, N. R. de Tacconi, W. Chanmanee, K. Rajeshwar, Electrodeposited Polyaniline in a Nanoporous WO_3 Matrix: An Organic/Inorganic Hybrid Exhibiting Both p- and n-Type Photoelectrochemical Activity, The Journal of Physical Chemistry C 116 (6) (2012) 4234–4242. doi:10.1021/jp211698j.

[186] F. Wang, S. Min, Y. Han, L. Feng, Visible-light-induced photocatalytic degradation of methylene blue with polyaniline-sensitized TiO_2 composite photocatalysts, Superlattices and Microstructures 48 (2) (2010) 170–180. doi:10.1016/j.spmi.2010.06.009.

[187] H. Dotan, N. Mathews, T. Hisatomi, M. Gratzel, A. Rothschild, On the Solar to Hydrogen Conversion Efficiency of Photoelectrodes for Water Splitting, The Journal of Physical Chemistry Letters 5 (19) (2014) 3330–3334. doi:10.1021/jz501716g.

[188] B. Klahr, S. Gimenez, F. Fabregat-Santiago, J. Bisquert, T. W. Hamann, Electrochemical and photoelectrochemical investigation of water oxidation with hematite electrodes, Energy & Environmental Science 5 (6) (2012) 7626. doi:10.1039/c2ee21414h.

[189] K. M. Molapo, P. M. Ndangili, R. F. Ajayi, G. Mbambisa, S. M. Mailu, N. Njomo, M. Masikini, P. Baker, E. I. Iwuoha, Electronics of Conjugated Polymers (I): Polyaniline, Int. J. Electrochem. Sci 7 (2012) 11859–11875.

[190] G. G. Wallace, G. M. Spinks, L. A. P. Kane-Maguire, P. R. Teasdale, Conductive Electroactive Polymers: Intelligent Polymer Systems, 3rd Edition, CRC Press, 2008.

[191] J. Y. Kim, G. Magesh, D. H. Youn, J.-W. Jang, J. Kubota, K. Domen, J. S.

Lee, Single-crystalline, wormlike hematite photoanodes for efficient solar water splitting., Scientific Reports 3 (2013) 2681. doi:10.1038/srep02681.

[192] J. Brillet, J.-H. Yum, M. Cornuz, T. Hisatomi, R. Solarska, J. Augustyński, M. Graetzel, K. Sivula, Highly efficient water splitting by a dual-absorber tandem cell, Nature Photonics 6 (12) (2012) 824–828. doi:10.1038/nphoton.2012.265.

[193] D. Borissov, S. Isik-Uppenkamp, M. Rohwerder, Fabrication of Iron Nanowire Arrays by Electrodeposition into Porous Alumina, The Journal of Physical Chemistry C 113 (8) (2009) 3133–3138. doi:10.1021/jp809202h.

[194] A. Jagminas, K. Mažeika, J. Reklaitis, V. Pakštas, D. Baltrūnas, Annealing effects on the transformations of Fe nanowires encapsulated in the alumina template pores, Materials Chemistry and Physics 115 (1) (2009) 217–222. doi:10.1016/j.matchemphys.2008.11.052.

[195] S. Yang, H. Zhu, D. Yu, Z. Jin, S. Tang, Y. Du, Preparation and magnetic property of Fe nanowire array, Journal of Magnetism and Magnetic Materials 222 (1) (2000) 97–100. doi:10.1016/S0304-8853(00)00541-2.

[196] D. R. Cornejo, E. Padrón-Hernández, Study of magnetization process in ordered Fe nanowire arrays, Journal of Magnetism and Magnetic Materials 316 (2) (2007) e48–e51. doi:10.1016/j.jmmm.2007.02.023.

[197] V. Haehnel, S. Fähler, P. Schaaf, M. Miglierini, C. Mickel, L. Schultz, H. Schlörb, Towards smooth and pure iron nanowires grown by electrodeposition in self-organized alumina membranes, Acta Materialia 58 (7) (2010) 2330–2337. doi:10.1016/j.actamat.2009.12.019.

[198] M. Sun, G. Zangari, M. Shamsuzzoha, R. M. Metzger, Electrodeposition of highly uniform magnetic nanoparticle arrays in ordered alumite, Applied Physics Letters 78 (19) (2001) 2964–2966. doi:10.1063/1.1370986.

[199] A. Santos, L. Vojkuvka, J. Pallarés, J. Ferré-Borrull, L. F. Marsal, Cobalt and Nickel Nanopillars on Aluminium Substrates by Direct Current Electrodeposition Process, Nanoscale Research Letters 4 (9) (2009) 1021–1028. doi:10.1007/s11671-009-9351-5.

[200] K. Nielsch, F. Muller, A. Li, U. Gösele, Uniform nickel deposition into ordered alumina pores by pulsed electrodeposition, Advanced Materials 12 (8) (2000) 582–586. doi:10.1002/(SICI)1521-4095(200004)12:8<582::AID-ADMA582>3.0.CO;2-3.

[201] D. AlMawlawi, N. Coombs, M. Moskovits, Magnetic properties of Fe deposited into anodic aluminum oxide pores as a function of particle size, Journal of Applied Physics 70 (8) (1991) 4421–4425. doi:10.1063/1.349125.

[202] M. Schlesinger, M. Paunovic, Modern Electroplating, Wiley, 2011.

[203] I. Vrublevsky, A. Jagminas, J. Schreckenbach, W. A. Goedel, Electronic properties of electrolyte/anodic alumina junction during porous anodizing, Applied Surface Science 253 (10) (2007) 4680–4687. doi:10.1016/j.apsusc.2006.10.038.

[204] C. Ji, P. C. Searson, Synthesis and Characterization of Nanoporous Gold Nanowires, The Journal of Physical Chemistry B 107 (19) (2003) 4494–4499. doi:10.1021/jp0222200.

[205] L. Li, S. Pan, X. Dou, Y. Zhu, X. Huang, Y. Yang, G. Li, L. Zhang, Direct Electrodeposition of ZnO Nanotube Arrays in Anodic Alumina Membranes, The Journal of Physical Chemistry C 111 (20) (2007) 7288–7291. doi:10.1021/jp0711242.

[206] M. P. Proença, C. T. Sousa, J. Ventura, M. Vazquez, J. P. Araujo, Ni growth inside ordered arrays of alumina nanopores: Enhancing the deposition rate, Electrochimica Acta 72 (2012) 215–221. doi:10.1016/j.electacta.2012.04.036.

[207] J. Qin, J. Nogués, M. Mikhaylova, A. Roig, J. S. Muñoz, M. Muhammed, Differences in the Magnetic Properties of Co, Fe, and Ni 250−300 nm Wide Nanowires Electrodeposited in Amorphous Anodized Alumina Templates, Chemistry of Materials 17 (7) (2005) 1829–1834. doi:10.1021/cm047870q.

[208] B. Kalska-Szostko, E. Brancewicz, P. Mazalski, J. Sveklo, W. Olszewski, K. Szymanski, A. Sidor, Electrochemical Deposition of Nanowires in Porous Alumina, Acta Physica Polonica A 115 (2) (2009) 542–544.

[209] J. M. Baik, M. Schierhorn, M. Moskovits, Fe Nanowires in Nanoporous Alumina: Geometric Effect versus Influence of Pore Walls, The Journal of Physical Chemistry C 112 (7) (2008) 2252–2255. doi:10.1021/jp711621v.

[210] N. J. Gerein, J. A. Haber, Effect of ac Electrodeposition Conditions on the Growth of High Aspect Ratio Copper Nanowires in Porous Aluminum Oxide Templates, The Journal of Physical Chemistry B 109 (37) (2005) 17372–17385. doi:10.1021/jp051320d.

[211] J. Lee, S. Farhangfar, J. Lee, L. Cagnon, R. Scholz, U. Gösele, K. Nielsch, Tuning the crystallinity of thermoelectric Bi_2Te_3 nanowire arrays grown by pulsed electrodeposition, Nanotechnology 19 (36) (2008) 365701–365709. doi:10.1088/0957-4484/19/36/365701.

[212] L. Trahey, C. R. Becker, A. M. Stacy, Electrodeposited Bismuth Telluride Nanowire Arrays with Uniform Growth Fronts, Nano Letters 7 (8) (2007) 2535–2539. doi:10.1021/nl070711w.

[213] C. T. Sousa, A. Apolinário, D. C. Leitao, A. M. Pereira, J. Ventura, J. P. Araujo, Precise control of the filling stages in branched nanopores, Journal of Materials Chemistry 22 (7) (2012) 3110–3116. doi:10.1039/c2jm14828e.

[214] D. C. Leitao, A. Apolinário, C. T. Sousa, J. Ventura, J. B. Sousa, M. Vazquez,

J. P. Araujo, Nanoscale Topography: A Tool to Enhance Pore Order and Pore Size Distribution in Anodic Aluminum Oxide, The Journal of Physical Chemistry C 115 (17) (2011) 8567–8572. doi:10.1021/jp202336j.

[215] H. Masuda, K. Fukuda, Ordered Metal Nanohole Arrays Made by a Two-Step Replication of Honeycomb Structures of Anodic Alumina, Science 268 (5216) (1995) 1466–1468. doi:10.1126/science.268.5216.1466.

[216] Y. Peng, H.-L. Zhang, S.-L. Pan, H.-L. Li, Magnetic properties and magnetization reversal of α-Fe nanowires deposited in alumina film, Journal of Applied Physics 87 (10) (2000) 7405. doi:10.1063/1.373001.

[217] M. J. Anderson, P. J. Whitcomb, RSM Simplified - Optimizing Processes Using Response Surface Methods For Design Of Experiments, Productivity, Inc., 2005.

[218] JMP9, SAS Institute Inc. http://www.jmp.com/.

[219] M. Catarino, A. Ferreira, A. M. Mendes, Study and optimization of aroma recovery from beer by pervaporation, Journal of Membrane Science 341 (1-2) (2009) 51–59. doi:10.1016/j.memsci.2009.05.038.

[220] A. M. Rashidi, A. Amadeh, The effect of current density on the grain size of electrodeposited nanocrystalline nickel coatings, Surface and Coatings Technology 202 (16) (2008) 3772–3776. doi:10.1016/j.surfcoat.2008.01.018.

[221] C. Multiphysics, COMSOL Inc. http://www.comsol.com/.

[222] S. Gadad, T. M. Harris, Oxygen Incorporation during the Electrodeposition of Ni, Fe, and Ni-Fe Alloys, Journal of The Electrochemical Society 145 (11) (1998) 3699–3703. doi:10.1149/1.1838861.

[223] N. Zech, D. Landolt, The influence of boric acid and sulfate ions on the hydrogen formation in Ni-Fe plating electrolytes, Electrochimica Acta 45 (21) (2000) 3461–3471. doi:10.1016/S0013-4686(00)00415-1.

[224] H. Schlörb, V. Haehnel, M. S. Khatri, A. Srivastav, A. Kumar, L. Schultz, S. Fähler, Magnetic nanowires by electrodeposition within templates, physica status solidi (b) 247 (10) (2010) 2364–2379. doi:10.1002/pssb.201046189.

[225] S. Shin, B. H. Kong, B. S. Kim, K. M. Kim, H. K. Cho, H. H. Cho, Over 95 % of large-scale length uniformity in template-assisted electrodeposited nanowires by subzero-temperature electrodeposition, Nanoscale Research Letters 6 (1) (2011) 467–475. doi:10.1186/1556-276X-6-467.

[226] D. Ramírez, H. Gómez, G. Riveros, R. Schrebler, R. Henríquez, D. Lincot, Effect of Zn(II) Concentration on the Morphology of Zinc Oxide Nanorods During Electrodeposition on Very Thin Alumina Membrane Templates, The Journal of Physical Chemistry C 114 (35) (2010) 14854–14859. doi:10.1021/jp1056754.

[227] J. T. Edward, Molecular volumes and the Stokes-Einstein equation, Journal of

chemical education 47 (4) (1970) 261. doi:10.1021/ed047p261.

[228] X.-l. REN, Q.-f. WEI, Z. LIU, J. Liu, Electrodeposition conditions of metallic nickel in electrolytic membrane reactor, Transactions of Nonferrous Metals Society of China 22 (2) (2012) 467–475. doi:10.1016/S1003-6326(11)61200-4.

[229] G. Sharma, M. V. Pishko, C. A. Grimes, Fabrication of metallic nanowire arrays by electrodeposition into nanoporous alumina membranes: effect of barrier layer, Journal of Materials Science 42 (13) (2007) 4738–4744. doi:10.1007/s10853-006-0769-1.

[230] S. Laurent, D. Forge, M. Port, A. Roch, C. Robic, L. Vander Elst, R. N. Muller, Magnetic Iron Oxide Nanoparticles: Synthesis, Stabilization, Vectorization, Physicochemical Characterizations, and Biological Applications, Chemical Reviews 108 (6) (2008) 2064–2110. doi:10.1021/cr068445e.

[231] Y. Lu, Y. Yin, B. T. Mayers, Y. Xia, Modifying the Surface Properties of Superparamagnetic Iron Oxide Nanoparticles through A Sol−Gel Approach, Nano Letters 2 (3) (2002) 183–186. doi:10.1021/nl015681q.

[232] J. Park, E. Lee, N.-M. Hwang, M. Kang, S. C. Kim, Y. Hwang, J.-G. Park, H.-J. Noh, J. Y. Kim, J.-H. Park, T. Hyeon, One-Nanometer-Scale Size-Controlled Synthesis of Monodisperse Magnetic Iron Oxide Nanoparticles, Angew. Chem 117 (19) (2005) 2932–2937. doi:10.1002/ange.200461665.

[233] H. B. Wu, J. S. Chen, H. H. Hng, X. Wen David Lou, Nanostructured metal oxide-based materials as advanced anodes for lithium-ion batteries, Nanoscale 4 (8) (2012) 2526. doi:10.1039/c2nr11966h.

[234] M. Tadić, V. Kusigerski, D. Marković, N. Čitaković, M. Remškar, V. Spasojević, Morphological, structural and magnetic properties of α-Fe_2O_3 nanoparticles in an amorphous alumina matrix obtained by aqueous combustion method, Journal of Alloys and Compounds 486 (1-2) (2009) 839–843. doi:10.1016/j.jallcom.2009.07.077.

[235] B. Sun, J. Horvat, H. S. Kim, W.-S. Kim, J. Ahn, G. Wang, Synthesis of Mesoporous α-Fe_2O_3 Nanostructures for Highly Sensitive Gas Sensors and High Capacity Anode Materials in Lithium Ion Batteries, The Journal of Physical Chemistry C 114 (44) (2010) 18753–18761. doi:10.1021/jp102286e.

[236] A. K. Gupta, M. Gupta, Synthesis and surface engineering of iron oxide nanoparticles for biomedical applications, Biomaterials 26 (18) (2005) 3995–4021. doi:10.1016/j.biomaterials.2004.10.012.

[237] S. C. Warren, K. Voitchovsky, H. Dotan, C. M. Leroy, M. Cornuz, F. Stellacci, C. Hébert, A. Rothschild, M. Gratzel, Identifying champion nanostructures for solar water-splitting, Nature Materials 12 (7) (2013) 1–36. doi:10.1038/nmat3684.

[238] C. H. Kim, H. J. Chun, D. S. Kim, S. Y. Kim, J. Park, J. Y. Moon, G. Lee, J. Yoon, Y. Jo, M.-H. Jung, S. I. Jung, C. J. Lee, Magnetic anisotropy of vertically aligned α-Fe_2O_3 nanowire array, Applied Physics Letters 89 (22) (2006) 223103. doi: 10.1063/1.2393165.

[239] A. Apolinário, C. T. Sousa, A. M. Pereira, M. P. Fernandez, G. Oliveira, J. Azevedo, J. Ventura, L. Andrade, A. M. Mendes, A. J P, Magnetic and structural study of anodic iron oxide nanotubes, (to be submitted).

[240] C. J. Jia, L. D. Sun, Z. G. Yan, Y. C. Pang, L. P. You, C. H. Yan, Iron Oxide Tube-in-Tube Nanostructures, The Journal of Physical Chemistry C 111 (35) (2007) 13022–13027. doi:10.1021/jp073837q.

[241] J.-H. Lim, S.-G. Min, L. Malkinski, J. B. Wiley, Iron oxide nanotubes synthesized via template-based electrodeposition, Nanoscale 6 (10) (2014) 5289–5295. doi: 10.1039/C3NR06924A.

[242] W. Lee, J.-C. Kim, Highly ordered porous alumina with tailor-made pore structures fabricated by pulse anodization, Nanotechnology 21 (48) (2010) 485304. doi: 10.1088/0957-4484/21/48/485304.

[243] C. T. Sousa, D. C. Leitao, J. Ventura, P. B. Tavares, J. P. Araujo, A versatile synthesis method of dendrites-free segmented nanowires with a precise size control, Nanoscale Research Letters 7 (1) (2012) 168. doi:10.1186/1556-276X-7-168.

[244] A. M. Jubb, H. C. Allen, Vibrational Spectroscopic Characterization of Hematite, Maghemite, and Magnetite Thin Films Produced by Vapor Deposition, ACS Applied Materials & Interfaces 2 (10) (2010) 2804–2812. doi:10.1021/am1004943.

[245] J. B. Lee, H. J. Kim, J. Lužnik, A. Jelen, D. Pajić, M. Wencka, Z. Jagličić, A. Meden, J. Dolinšek, Synthesis and Magnetic Properties of Hematite Particles in a “Nanomedusa” Morphology, Journal of Nanomaterials 2014 (2014) 1–9. doi:10.1103/PhysRevB.61.6826.

[246] J. Crangle, G. M. Goodman, The magnetization of pure iron and nickel, Proceedings of the Royal Society of London. Series A, Mathematical and Physical Sciences 321 (1971) 477–491.

[247] M. P. Fernández-García, P. Gorria, J. A. Blanco, R. Boada, J. Chaboy, D. Schmool, J.-M. Grenèche, Microstructure and magnetism of nanoparticles with γ-Fe core surrounded by α-Fe and iron oxide shells, Physical Review B 81 (9). doi:10.1103/PhysRevB.81.094418.

[248] R. K. Zheng, G. H. Wen, K. K. Fung, X. X. Zhang, Training effect of exchange bias in γ−Fe_2O_3 coated Fe nanoparticles, Physical Review B 69 (21) (2004) 214431. doi:10.1103/PhysRevB.69.214431.

[249] R. M. Cornell, U. Schwertmann, The Iron Oxides, Structure, Properties, Reac-

tions, Occurrences and Uses, Wiley-VCH, 2007.

[250] Ò. Iglesias, X. Batlle, A. Labarta, Particle size and cooling field dependence of exchange bias in core/shell magnetic nanoparticles, Journal of Physics D: Applied Physics 41 (13) (2008) 134010. doi:10.1088/0022-3727/41/13/134010.

[251] M. P. Proença, J. Ventura, C. T. Sousa, M. Vazquez, J. P. Araujo, Exchange bias, training effect, and bimodal distribution of blocking temperatures in electrodeposited core-shell nanotubes, Physical Review B 87 (13) (2013) 134404. doi:10.1103/PhysRevB.87.134404.

[252] A. Aharoni, Introduction to the Theory of Ferromagnetism, Clarendon Press, 1996.

[253] C. Suchomski, C. Reitz, C. T. Sousa, J. P. Araujo, T. Brezesinski, Room Temperature Magnetic Rare-Earth Iron Garnet Thin Films with Ordered Mesoporous Structure, Chemistry of Materials 25 (12) (2013) 2527–2537. doi:10.1021/cm400999b.

[254] Y. Ren, W. K. Chim, S. Y. Chiam, J. Q. Huang, C. Pi, J. S. Pan, Formation of Nickel Oxide Nanotubes with Uniform Wall Thickness by Low-Temperature Thermal Oxidation Through Understanding the Limiting Effect of Vacancy Diffusion and the Kirkendall Phenomenon, Advanced Functional Materials 20 (19) (2010) 3336–3342. doi:10.1002/adfm.201000498.

[255] W. Lee, R. Ji, U. Gösele, K. Nielsch, Fast fabrication of long-range ordered porous alumina membranes by hard anodization, Nature Materials 5 (9) (2006) 741–747. doi:10.1038/nmat1717.

[256] K. S. Lee, S. Park, W. Lee, Y. S. Yoon, Hollow Nanobarrels of α-Fe_2O_3 on Reduced Graphene Oxide as High-Performance Anode for Lithium-Ion Batteries., ACS Applied Materials & Interfaces 8 (3) (2016) 2027–2034. doi:10.1021/acsami.5b10342.

[257] A. Ishikawa, T. Takata, J. N. Kondo, M. Hara, K. Domen, Electrochemical Behavior of Thin Ta_3N_5 Semiconductor Film, The Journal of Physical Chemistry B 108 (30) (2004) 11049–11053. doi:10.1021/jp048802u.

[258] M. P. Proença, Magnetism at the Nanoscale: Nanoparticles, Nanowires, Nanotubes and their Ordered Arrays, Ph.D. thesis, FCUP, Porto (Dec. 2012).

[259] C. T. Sousa, Development of Nanoporous Alumina Templates for Biotechnological Applications, Ph.D. thesis, Universidade do Porto, Porto (Dec. 2011).

[260] Resistive-Switching Memory Effects of NiO Nanowire/Metal Junctionsdoi:10.1021/ja101742f.

[261] Synthesis of Inorganic Solids Using Microwaves, Chemistry of Materials 11 (4) (1999) 882–895. doi:10.1021/cm9803859.

[262] A. Carretero Genevrier, N. Mestres, T. Puig, A. Hassini, J. Oró, A. Pomar, F. Sandiumenge, X. Obradors, E. Ferain, Single–Crystalline $La_{0.7}Sr_{0.3}MnO_3$ Nanowires by Polymer–Template–Directed Chemical Solution Synthesis, Advanced Materials 20 (19) 3672–3677. doi:10.1002/adma.200800487.

[263] A. V. Kabashin, P. Evans, S. Pastkovsky, W. Hendren, G. A. Wurtz, R. Atkinson, R. Pollard, V. A. Podolskiy, A. V. Zayats, Plasmonic nanorod metamaterials for biosensing, Nature Materials 8 (11) (2009) 867–871. doi:10.1038/nmat2546.

[264] G. Meng, Y. J. Jung, A. Cao, R. Vajtai, P. M. Ajayan, Controlled fabrication of hierarchically branched nanopores, nanotubes, and nanowires, Proceedings of the National Academy of Sciences 102 (20) (2005) 7074–7078.

[265] F. Li, Nanostructure of Anodic Porous Alumina Films of Interest in Magnetic Recording, Ph.D. thesis, University of Alabama (1998).

[266] A. J. Bard, Encyclopedia of Electrochemistry of the Elements, Journal of The Electrochemical Society 123 (10) (1976) 348C. doi:10.1149/1.2132649.

[267] K. Nielsch, Hochgeordnete Ferromagneticsche Nano-Stabensembles, Ph.D. thesis, Martin Luther Universität Halle Wittenberg (Sep. 2002).

[268] M. Proença, Nanoporous alumina membranes: Fabrication process and template growth of ordered nanotubes, Final year project (Universidade do Porto, 2008).

[269] K. Nielsch, J. Choi, K. Schwirn, R. B. Wehrspohn, U. Gösele, Self-ordering Regimes of Porous Alumina: The 10 % Porosity Rule, Nano Letters 2 (7) (2002) 677–680. doi:10.1021/nl025537k.

[270] A. Rajendra, B. J. Parmar, A. K. Sharma, H. Bhojraj, M. M. Nayak, K. Rajanna, Hard anodisation of aluminium and its application to sensorics, Surface Engineering 21 (3) (2005) 193–197. doi:10.1179/174329405X50000.

[271] S. Shingubara, K. Morimoto, H. Sakaue, T. Takahagi, Self-Organization of a Porous Alumina Nanohole Array Using a Sulfuric/Oxalic Acid Mixture as Electrolyte, Electrochemical and Solid-State Letters 7 (3) (2004) E15. doi:10.1149/1.1644353.

[272] S. Ono, M. Saito, M. Ishiguro, H. Asoh, Controlling Factor of Self-Ordering of Anodic Porous Alumina, Journal of The Electrochemical Society 151 (8) (2004) B473. doi:10.1149/1.1767838.

[273] S. Z. Chu, K. Wada, S. Inoue, M. Isogai, A. Yasumori, Fabrication of Ideally Ordered Nanoporous Alumina Films and Integrated Alumina Nanotubule Arrays by High-Field Anodization, Advanced Materials 17 (17) (2005) 2115–2119. doi:10.1002/adma.200500401.

[274] S. Ono, M. Saito, H. Asoh, Self-Ordering of Anodic Porous Alumina Induced by Local Current Concentration: Burning, Electrochemical and Solid-State Letters

7 (7) (2004) B21. doi:10.1149/1.1738553.

[275] S. Ono, M. Saito, H. Asoh, Self-ordering of anodic porous alumina formed in organic acid electrolytes, Electrochimica Acta 51 (5) (2005) 827–833. doi:10.1016/j.electacta.2005.05.058.

[276] D. J. Arrowsmith, A. W. Clifford, D. A. Moth, Fracture of anodic oxide formed on aluminium in sulphuric acid, Journal of Materials Science Letters 5 (9) (1986) 921–922. doi:10.1007/BF01729276.

[277] K. Wada, T. Shimohira, M. Yamada, N. Baba, Microstructure of porous anodic oxide films on aluminium, Journal of Materials Science 21 (11) (1986) 3810–3816. doi:10.1007/BF02431615.

[278] D. Losic, M. Lillo, D. Losic Jr., Porous Alumina with Shaped Pore Geometries and Complex Pore Architectures Fabricated by Cyclic Anodization, Small 5 (12) (2009) 1392–1397. doi:10.1002/smll.200801645.

[279] D. Losic, D. Losic, Preparation of Porous Anodic Alumina with Periodically Perforated Pores, Langmuir 25 (10) (2009) 5426–5431. doi:10.1021/la804281v.

[280] A. I. Fernández-Domínguez, O. Caballero-Calero, J. M. i. n, M. M. i. n.-G. a. lez, Ordered three-dimensional interconnected nanoarchitectures in anodic porous alumina, Nature Communications 5 (2014) 1–9. doi:10.1038/ncomms6130.

APPENDIX A

Porous Anodic Alumina Templates

A.1 Fabrication Process

A.1.1 Mild Anodization

In this section a brief explanation for the PAA templates fabrication methods is presented under mild anodization conditions. More detailed explanations can be found elsewhere[258,259]. This is an easy and cost effective method to grow uniform high aspect ratio nanostructures in a fast and well-controlled way. Several materials have already been prepared in nano-sized structures using PAA templates as mold[195,209,260–263]. This kind of templates are membranes with pores distributed along the thickness of the latter which are a result of a precise control of formation conditions allowing to manipulate the dimensions and distribution of the template. A high quality and organized template can thus be fabricated at a nanoscale. The PAA is widely used due to its high pore density disposed in ordered close-packed hexagonal arrays, easy fabrication method and the possibility to tailor pore diameter and length[264].

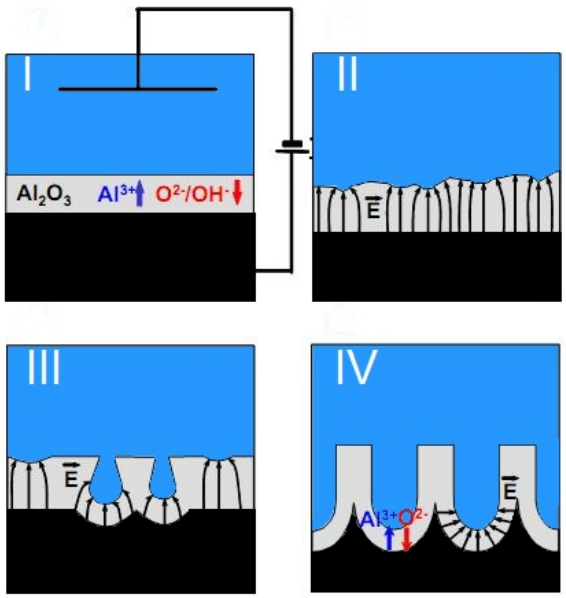

Figure A.1 – Illustration of the principal stages of pore formation in a nanoporous alumina membrane.

The spontaneous reaction leading to the formation of aluminum oxide in air can be ascribed to the large negative Gibb's free energy changes[265]

$$2Al(s) + \frac{3}{2}O_2(g) \rightarrow Al_2O_3(s) \quad \Delta G = -1582 \text{ kJ/mol}, \tag{A.1}$$

$$2Al(s) + 3H_2O(l) \rightarrow Al_2O_3(s) + 3H_2(g) \quad \Delta G = -871 \text{ kJ/mol}. \tag{A.2}$$

If aluminum is electrochemically anodized, an oxide grows at the anode electrode[266],

$$2Al(s) + 3H_2O(l) \rightarrow Al_2O_3(s) + 6H^+ + 6e^-, \tag{A.3}$$

and hydrogen evolves at the cathode,

$$6H^+ + 6e^- \rightarrow 3H_2(g). \tag{A.4}$$

At the anode, the forced (electrical field driven) oxide formation occurs at the metal/oxide interface by (electro)migration and (to a less extent) diffusion of O^{2-} and OH^- anions present in the electrolyte solution through the previously formed oxide-layer (Figure A.1). At the same time, oxide dissolution takes place at the electrolyte/oxide interface, with Al^{3+} entering the solution through the just formed oxide-layer.

Depending on several factors, in particular the electrolyte, two types of anodic films can be produced:

1. Barrier type films can be formed in completely insoluble electrolytes ($5 < pH < 7$), e.g., neutral boric acid, ammonium borate, tartrate, and ammonium tetraborate in ethylene glycol.;

2. Porous type films can be created in slightly soluble electrolytes such as sulfuric, phosphoric, chromic and oxalic acid.

For template assisted methods we are most interested in the latter.

The transient of the potentiostatic current density reflects the formation of barrier-type or porous- type porous alumina (see Figure A.2). In the case of the formation of porous films, the current density profiles (shown in Figure A.2) are typically observed[258,259,265,267]. First, the current density, j, decreases rapidly due to the formation of a non-conductive oxide barrier, as at the beginning of the process, the Al oxide thickness is very small (usually only $\sim$ 2 nm) (regime I, Figures A.1 and A.2). Then, it passes through a minimum value as the thickness of the barrier-layer reaches a threshold value (determined by the anodization conditions) and the onset of pore nucleation takes place (regime II, Figures A.1 and A.2). It then increases to arrive at a maximum value. At this point the pores start to grow where the irregularities on the surface that give rise to a field or/and temperature enhanced dissolution in the formed oxide (regime III, Figures A.1 and A.2). The damping observed in the curve corresponds to the "pore competition" during the self-organization process. At this phase some pores

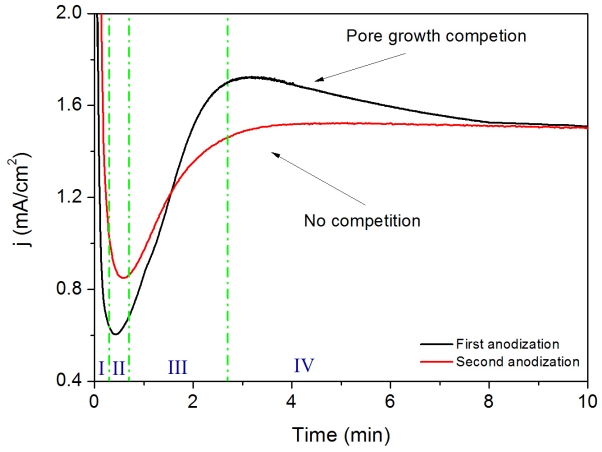

Figure A.2 – Current density transient monitored during a first and second anodization in 0.3 M oxalic acid at 2 °C and with a constant applied potential of 40 V.

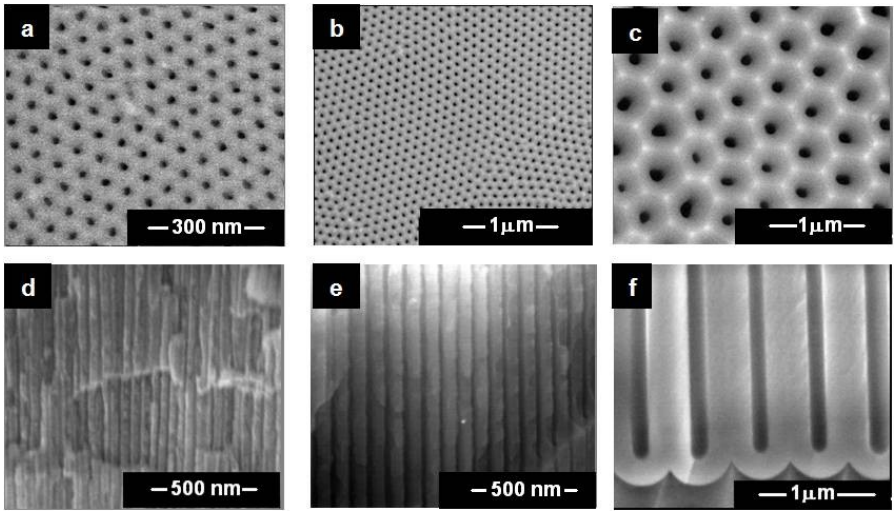

Figure A.3 – SEM images obtained with different acidic solutions: top surface and cross section images of anodizations with (a), (d) sulphuric acid; (b), (e) oxalic acid and (c), (f) phosphoric acid (Adapted from 268).

merge, inducing a slight decrease of the current density. If a first anodization was conducted previously, this is not observed as the pore growth is much more organized. Subsequently, it slightly decreases again. Finally, a steady current density remains which corresponds to the continuous growth of the porous alumina layer (regime IV, Figures A.1 and A.2).

Several previous studies revealed that self-ordered PAA structures can only be obtained under specific conditions. For example, structures with pore spacing of 50, 65, 100, 420 and 500 nm are fabricated at 19 V and 25 V in sulfuric acid, at 40 V in oxalic acid, and at 160 V and 195 V in phosphoric acid, respectively[258,259,265,267], as seen in Figure A.3. Nielsh *et al.*[269], also reported that a porosity of ~ 10 % is required to ensure that a moderated volume expansion and consequently, sufficient repulsive

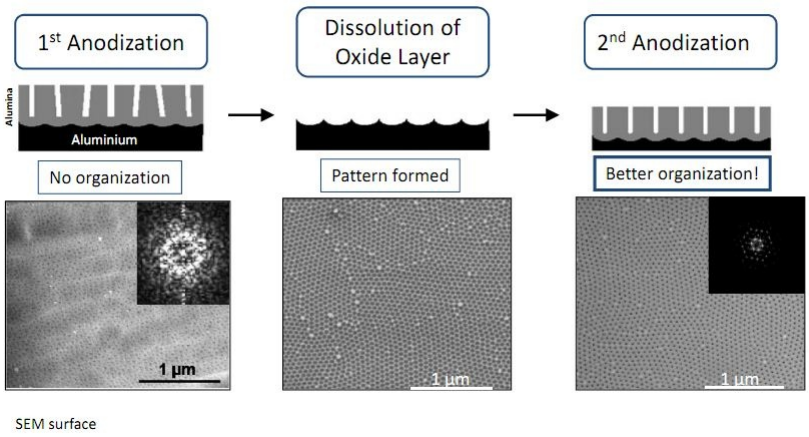

Figure A.4 – Schematic drawings of two step anodization method and correspondent SEM images.

forces among growing pores are present. As the porosity of a hexagonal geometry is given by:

$$P = \frac{2\pi}{\sqrt{3}}\left(\frac{r}{D_{int}}\right)^2 \tag{A.5}$$

where r is the pore radii and D_{int} the interpore distance.

Table A.1 summarizes the self-ordering conditions for the three mainly used anodization acids (sulphuric, oxalic and phosphoric). These electrolytes have different electrical conductivities and pH values, clearly leading to different self-ordered regimes. Figure A.3 shows top-view and cross-section SEM images of the PAA for second anodization in sulphuric, oxalic and phosphoric acids with the conditions of Table A.1: electrolyte concentration (C), electrode potential (U), temperature (T), pore diameter (D_p), interpore distance (D_{int}), bottom layer thickness (δ_b), porosity (P) and anodization rate (AR).

Table A.1 – Anodization conditions and pore characteristics.

Electrolyte	C (M)	U (V)	T (°C)	D_p (mm)	D_{int} (mm)	δ_b (nm)	P (%)	AR (μ/h)
H_2SO_4	0.3	25	2	20	65	34	10	2
$C_2O_4H_2$	0.3	40	4	35	105	50	10	2.5
H_3PO_4	0.1	195	1	100	200	250	9	2

A.1.1.1 Two-step anodization process

To improve the nanoporous organization, in 1995, Masuda and Fukuda proposed a simple method to obtain highly ordered PAA templates, without the need to resort to complicated and expensive lithographic techniques, called the two-step anodization [215]. They observed that after a long anodization process the Al substrate acquires a hexagonal arrays of pits at its surface due to the pore formation. By removing the oxide

layer formed in the first anodization this pattern can be observed (see Figure A.4) and performing a subsequent second anodization on the pre-pattern foil the pores will now preferentially nucleate on the depressions of the surface, with the pattern guiding effectively the nanopores growth. Such effect results on a highly ordered hexagonal porous structure (see Figure A.4).

With this simple method PAA templates with hexagonal monodomain size larger than 1 μm can be obtained. One has to be careful with the anodization time since, long anodizations lead to higher organization quality only to a certain point where the pH value at the pore bottom may lead to a deviation from the optimum self-order conditions[269]. This value is set to be around 24 h.

One more direct and easy way to infer the faster field-enhanced dissolution at the bottom of each pit in the second anodization is by observing the $j(t)$ curve of both first and second anodization. Figure A.2 shows the $j(t)$ curves corresponding to a first and a second anodization in 0.3 M oxalic acid, with U = 40 V and $T \simeq 4$ ºC (black and red lines, respectively). Notice that not only in the second anodization the rise after the minimum is faster, indicating that the pore nucleation is easier on the pre-textured Al but there is also no overshoot, associated with the competition among the growing nanopores as they grow directly over the pre-existent holes.

APPENDIX B

Alumina Template Pore Modulation

B.1 Hard anodization

For practical applications, simple and fast fabrication of highly ordered PAA templates with a wide range of D_p and D_{int} would be highly desirable. In consequence, the attention on HA processes, which were discovered in the early 1960's, was renewed. This type of processes are characterized by the use of sulphuric acid at relatively low temperatures and high current densities, and has been widely used for various industrial applications (for example, surface finishing of Al cookware, automobile engineering, textile machinery) by taking advantage of the high-speed oxide growth of 50-100 $\mu m \cdot h^{-1}$ [270].

The problem associated with HA is that when the anodization process is carried out outside the self-ordering regimes, the degree of spatial ordering decreases drastically. Applied voltages higher than the optimum value required to maintain stable anodization in a given electrolyte always result in 'breakdown' or 'burning' of the oxide film caused by catastrophic flow of electric current. Much research effort has been made in order to overcome this limitation [271–277]. Ono *et al.* found that domains of highly-ordered pore arrays occur in porous alumina film formed during breakdown [272]. More recently, Chu *et al.* reported the fabrication of self-ordered PAA templates in sulphuric acid solution under high anodization potentials and current densities of up to 70 V and 200 $mA \cdot cm^{-2}$, far from the MA regime but similar to the anodization conditions for HA [273]. Although the starting problem had been resolved there was still limitations in fabricating PAA membranes with a high aspect ratio (depth divided by the diameter) of nanopores above about 20.

In 2006 a new method for the fast fabrication of long-range ordered PAA membranes by HA was introduced by Lee *et al.* using oxalic acid and applying potentials of 100 - 150 V, which are more than three times higher than the voltage (40 V) used in conventional oxalic acid anodization [255]. In order to suppress breakdown effects caused by the high current densities and to enable uniform oxide film growth at a high voltage (> 100 V), they found that an oxide layer (thickness > 400 nm) should be formed on the surface of the Al substrate before carrying out the HA process. This protective layer was generated by the common MA process using oxalic acid 0.3 M at 40 V for $\sim$ 5 min. Then a soft

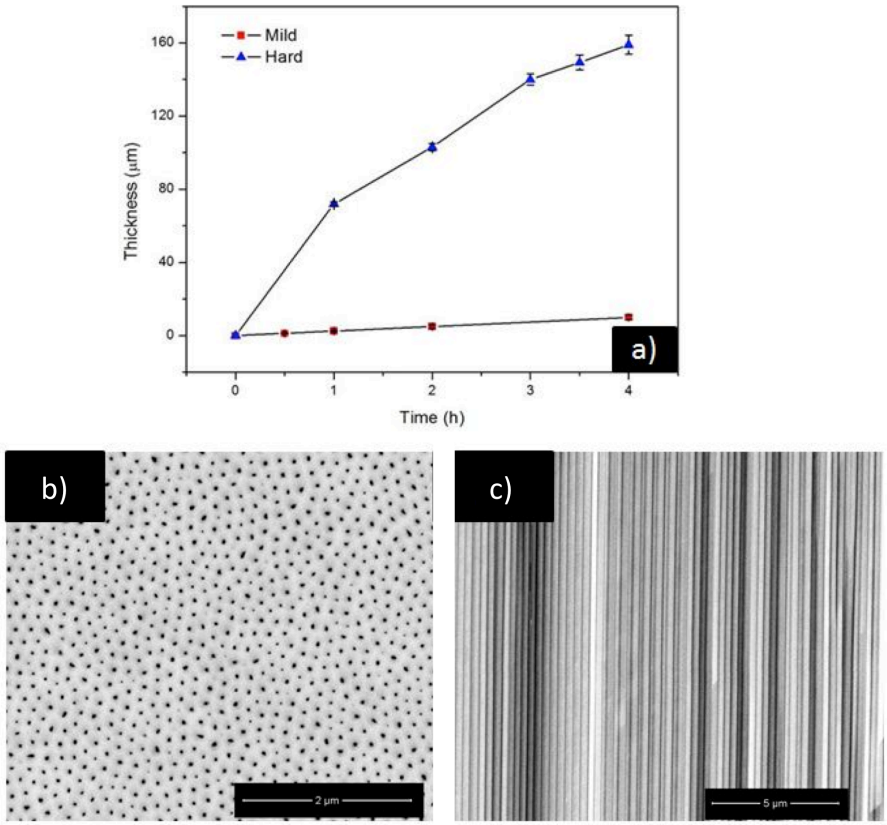

Figure B.1 – (a) Comparison between the thickness of PAA for MA (40 V) and HA (140 V) as a function of time, using oxalic acid; Top (b) and cross-section (c) SEM views of a PAA template made by HA at 140 V for 4 h.

transition to the HA regime was carried out by a slow increase in the voltage to the target values (100 - 150 V). Afterwards the HA process was maintained until the desired PAA template thickness was achieved. This way, highly vertically oriented PAA templates could be made much more faster than the MA anodization process. Figure B.1a shows that hard anodization can have a growth rate up to 32 times bigger than mild anodization. Figure B.1b and c shows that the organization of hard anodization can be as good as mild anodization.

B.2 Pore Modulation

It is known that D_{int} depends locally on U by the following relation[269]:

$$D_{int} = kU \tag{B.1}$$

where k is a proportionality constant of $\sim$ 2.5 nm/V for MA and $\sim$ 2.0 nm/V for hard anodization HA[255]. By alternating between these two regimes, pore modulation can be achieved.

Lee *et al.* introduced the pore modulation by completely alternating between MA and

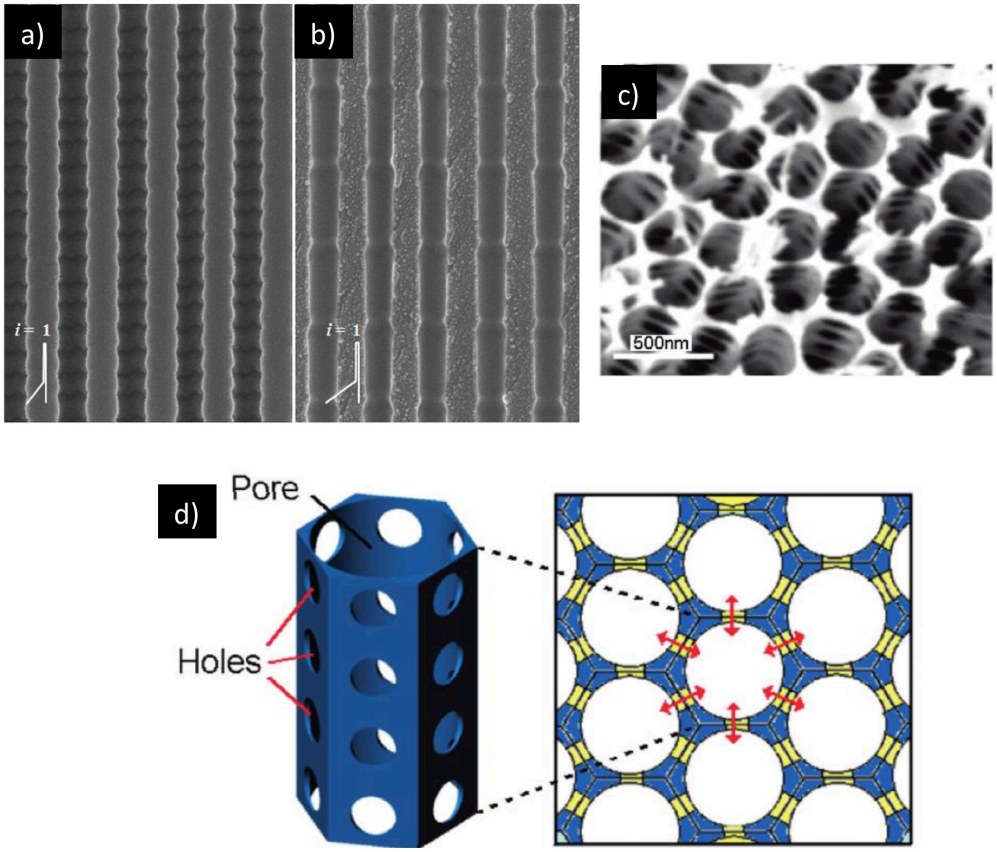

Figure B.2 – a) and b) 1D Pore modulation with different diameters (Extracted from 242); c) and d) 3D template (Extracted from 279).

HA conditions (changing the electrolyte, temperature and voltage)[255]. This method is complex as for each modulation the conditions need to be changed manually. Afterwards, new anodization procedures as pulsed anodization (PA) by Woo Lee *et al.*[242,255] or cyclic anodization by Dusan Losic *et al.*[278,279] greatly improved the pore modulation strategy. These processes can also be performed under potentiostatic or galvanostatic mode or with sulphuric or oxalic acid based electrolytes. These modulations could be used as both 1D or 3D templates – Figure B.2.

In this thesis, PAA templates with periodically modulated pore diameter along the pore axis have been synthesized by pulse anodization, using an in-house made setup[242]. In order to suppress breakdown effects caused by the high current densities a thin oxide layer is first created by anodizing the Al foil in oxalic acid, in MA conditions, for 5 min. Then, without changing the electrolyte, the potential is shifted at 0.6 $V \cdot s^{-1}$ to the desired values. The high potential regime is then maintained for the desired time. In respect to the tailoring of the PAA pores, a precise controlled pulse was applied, varying the potential as desired to obtain tailored PAA templates. The pulse shape is presented in Figure B.3. A LabVIEW program was developed to easily change the parameters. It allows to introduce four different potential values and four different ramps to change between values. It also allows to define the time to apply the pulses and it repeats the

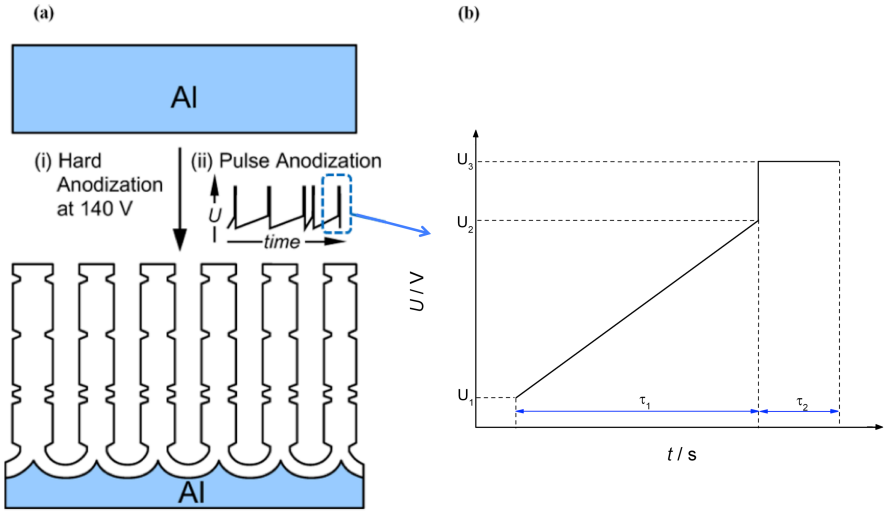

Figure B.3 – a) Pore modualted template abrication process and b) pulsed anodization pulse shape (Adapted from 242).

Table B.1 – Different pulses applied during anodization.

Sample	U1 (V)	U2 (V)	U3 (V)	t1 (s)	t2 (s)
1 to 8	80	140	160	**36-500**	0.2
9 to 15	**30-100**	140	160	144	0.2
15 to 21	80	140	160	144	**0.2-10**
22 to 26	80	**120-160**	160	144	0.2
27 to 33	80	140	**140-190**	400	0.2

pulse until the time runs out. In the end, a transition to a MA regime is performed (rate of 0.6 $V \cdot s^{-1}$) and a 40 V is applied for 1 min to stabilize the barrier layer at the bottom of the pores for barrier-layer thinning purposes and consequent PED electrodeposition.

Various sets of tailor pulse were applied as presented in Table B.1.

A typical *j* profile is presented in Figure B.4. Normally, current-time transients during a pulse anodization present sharp increases in current density as the potential changes (see Figure B.4a). The periodic changes in *j* result tailored pore in which the length of each segment is proportional to the integrated charge. Such pores present no branching or disorder. By changing the potential from high to lower values (HA to MA) *j* drops abruptly and then gradually increases with time to a steady value corresponding to the MA potential (called current recovery). This recovery time is associated with the barrier layer thickness decreasing gradually and/or to the slow dissolution of the oxide layer into the electrolyte[242]. The recovery current behavior is also noted (see Figure B.4b) where the later starts at an anodizing potential around 111 V. Therefore, the contribution of the potential below 112 V to the formation of anodic oxide can be ignored under the present electrochemical conditions[242]. At 125 V a decrease in *j* is observed possible due to the pore competition, as an increase in the pore diameter has occurred and consequently so did the stress between pores. As the pores rearrange themselves and due to the continuous increase in *U*, *j* increases once again. In Figure B.4a we also observe two different behaviors: The maximum *j* decreases over time in an exponential trend, and

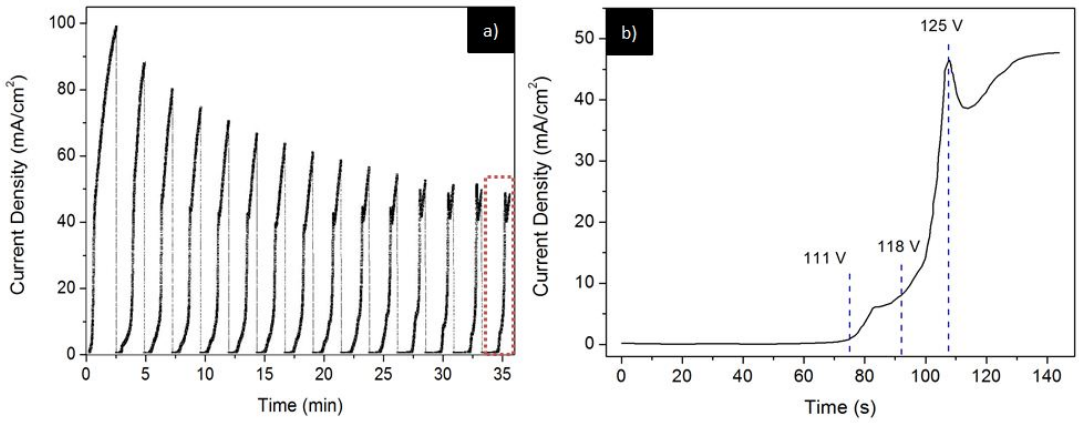

Figure B.4 – Current density profile of a series of tailor pulses (a) and the amplified view of one pulse (b) marked with a red rectangle. U_1 = 80 V; U_2 = 140 V; U_3 = 160 V; τ_1 = 144 s; τ_2 = 0.2 s.

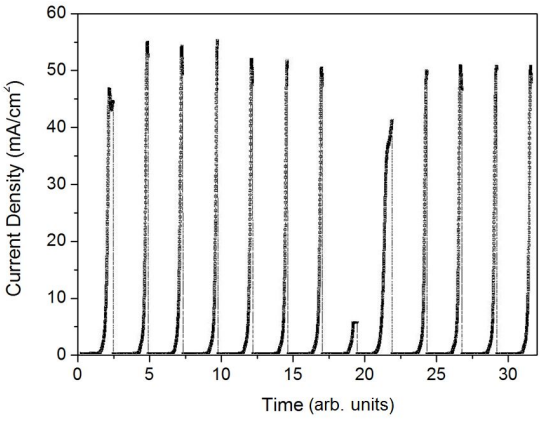

Figure B.5 – Current density profile of a series of tailor pulses for a prolonged time.

the point where the pore competition becomes visible (125 V in Figure B.4b) gets more pronounced over time.

We believe that a charge accumulation increases with time affecting the effective electric field at the pore base, thus changing the *j* maximum values. In fact, W. Lee *et al.*[255] reported that the effective electric field changes during the tailoring process. In order to test our theory we performed a more prolonged tailoring process to observe the *j* behavior (see Figure B.5). We observe that the *j* maximum is more stable after the initial pulses were applied (Figure B.4a) but at some point the *j* suffers a breakdown. Given the accumulation of charge, some defect could be formed not allowing the current to pass. During this time, the charge can discharge and in the next pulse the anodization returns to normal. This behavior can be observed several times if the tailoring pulses are applied for long times.

The length of PAA nanopores with a smaller D_p can be controlled by varying the time width τ_1, during which the recovery of current takes place. On the other hand, the length and the internal pore geometry of PAA nanopores with a larger diameter can be tuned by appropriately varying the pulse duration and the amplitude, which are defined by (τ_2,

Table B.2 – Range of different modulation features.

Smaller Diameter (nm)	Larger Diameter (nm)	Smaller Diameter length (nm)	Larger Diameter length (nm)
53 to 73	74 to 100	38 to 139	136 to 1459

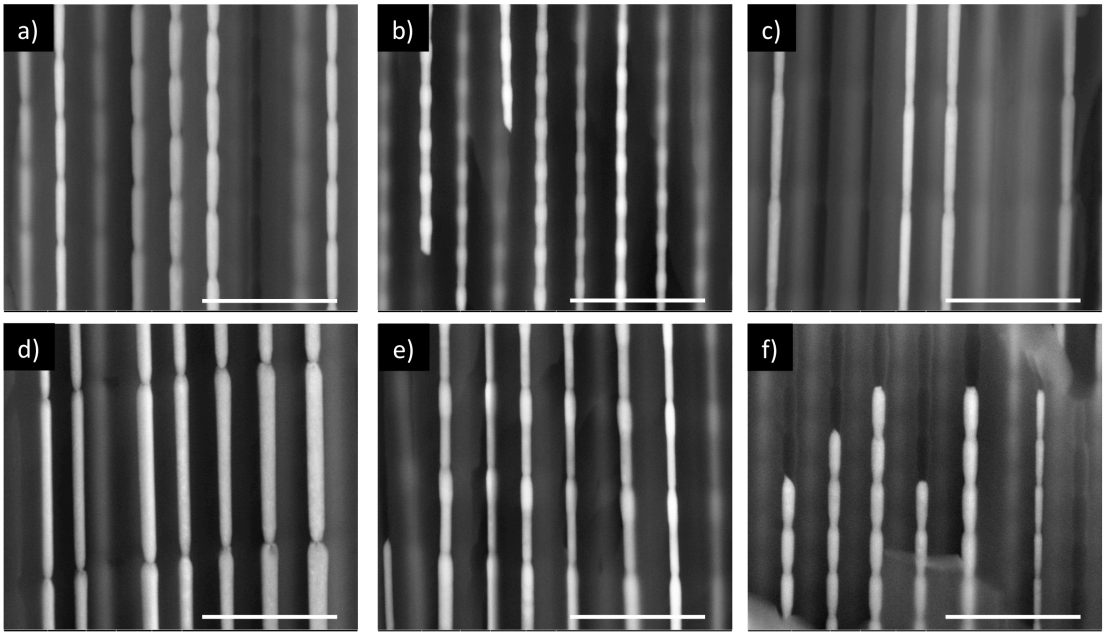

Figure B.6 – Different modulation patterns. U_1, U_2, U_3, τ_1 and τ_2 values are: a) 80, 140, 160, 144, 0.2; b) 80, 140, 160, 36, 0.2; c) 80, 140, 160, 200, 0.2; d) 80, 140, 160, 400, 0.2; e) 80, 140, 160, 144, 5; f) 50, 140, 160, 144, 0.2. Bar corresponds to 1 μm.

U_2 and U_3 respectively. In order to obtain better SEM images, the templates were filled with Fe NWs, as described in Chapter 6. The features of measured and are presented in Table B.2. Figure B.6 shows some different pore modulations that can be obtained.

APPENDIX C

Three-dimensional Template for Conductive Substrates

C.1 3D interconnected nanoporous alumina templates

Appendix B described how to control the shape, periodicity and size of the PAA modulations by periodically changing the anodization potential/current. This appendix summarizes the work performed on the optimization of pore modulation to achieve interconnected pores and fabricate three-dimensional nanoarchitectures. After a two step anodization process – described in appendix A – two additional steps are introduced: a modulation step in which anodization potential and current pulses are applied in sequence; followed by a third anodization step, again at a constant applied potential (the same as the one used for the first and second anodization processes). The applied pulses are represented in Figure C.1. To connect the pores at the wide diameter sections of the modulated pores, the pores are chemically etched for an optimized short period. SEM cross-sectional images of the resulting 3D interconnected pores are depicted in Figure C.1. By changing the anodization conditions different three dimensional templates can be fabricated - Figure C.2.

C.2 3D interconnected nanowire arrays

C.2.1 Au Nanowires

To create an interconnected structure, the template was filled with Au NWs. These were electrodeposited inside the modulated PAA template using Orosene 999 (Technic, Inc.) solution at -1.0 V (vs. the Ag/AgCl reference electrode). This lower deposition rate was selected to avoid damaging the template, as it is extremely fragile. Figure C.3 shows selected SEM images illustrating the interconnected array of Au NWs successfully obtained. The continuous thin films formed between modulations, as depicted in the SEM top right image in Figure C.3, formed in case of template breaking.

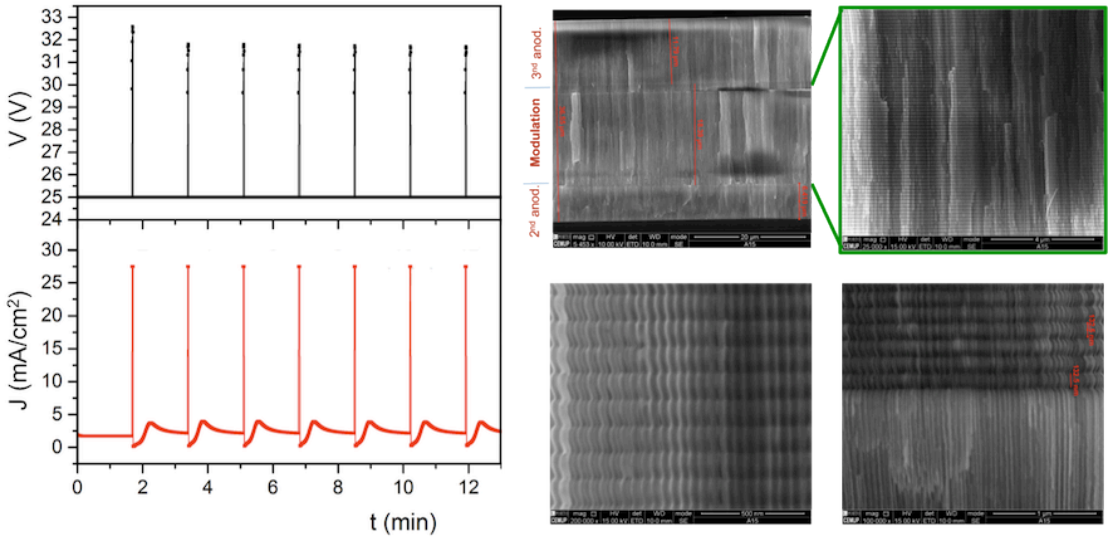

Figure C.1 – Sequence of the applied anodization potential/current pulses for the formation of diameter modulated pores. SEM cross-sectional images of the 3D interconnected nanoarchitectures formed in the nanoporous alumina templates.

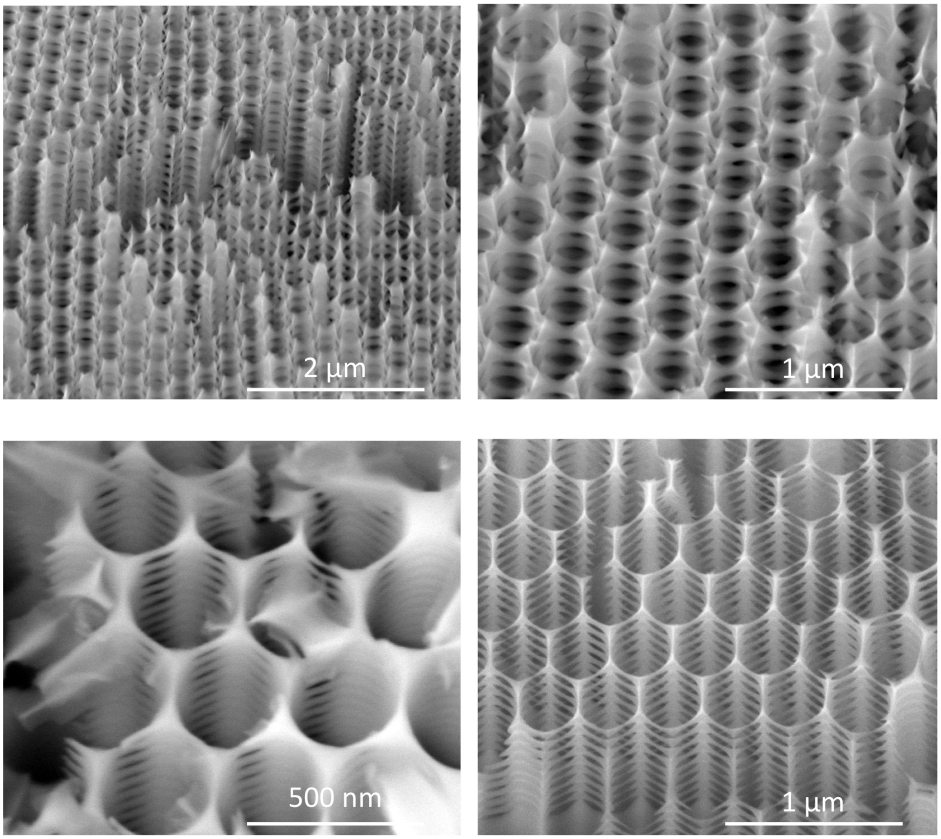

Figure C.2 – Different three dimensional templates.

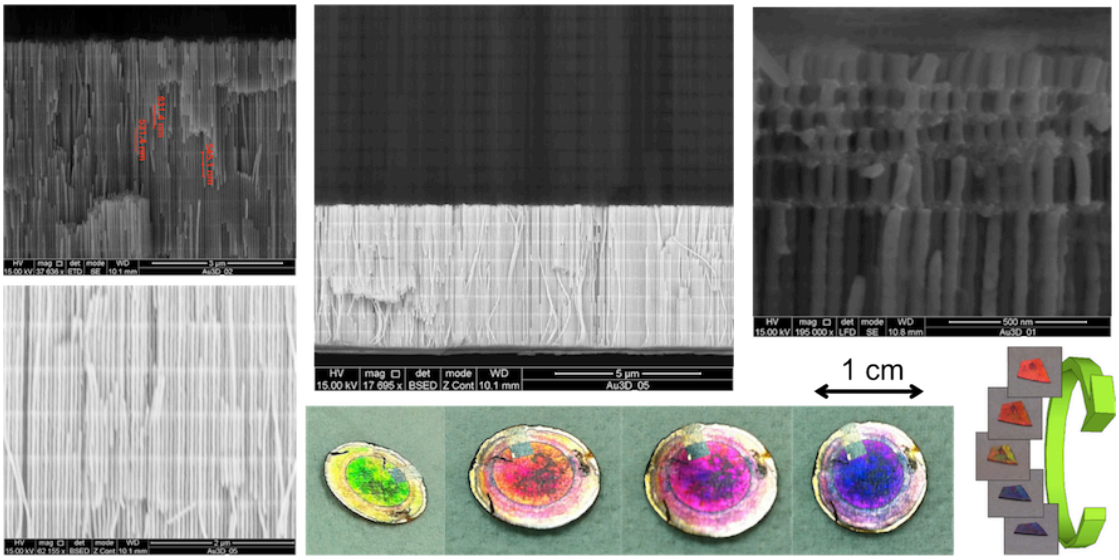

Figure C.3 – SEM cross-sectional images of 3D interconnected arrays of Au nanowires electrodeposited in 3D porous alumina templates, illustrating diameter modulations with different spacings and the breaking of the interconnected wires during deposition in some segments (upper right). At the bottom: photographs of the alumina membranes (around 1 cm in diameter) after the electrodeposition process in the central area (with around 0.5 cm in diameter) taken at different angles, illustrating the different optical reflections of the 3D interconnected network of nanowires. The scheme at the bottom right, extracted from reference 280, illustrates the same effect.

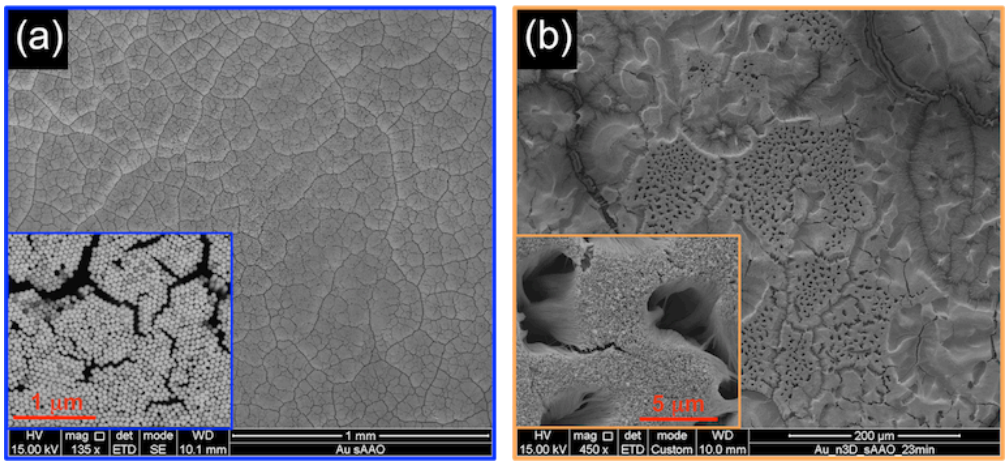

Figure C.4 – SEM top views of free-standing Au nanowire arrays after template removal: a) 3D interconnected NW arrays, and b) NW arrays with no interconnected structures.

C.2.2 Free-standing interconnected nanowire arrays

For solar cell applications, three-dimensional charge extraction structures and plasmonic substrates are important. Once coated with a semiconductor, a freestanding three-dimensional metallic structure becomes an improved photoelectrode. After a chemical etch the PAA was removed and the interconnected Au NWs isolated. These were found to maintain a compact network structure with vertical alignment (Figure C.4a). When comparing these results with free-standing NWs grown using non-

3D alumina templates (with the same pore diameter and interpore distances, but no modulations), the compact network structure was completely lost (Figure C.4b). This proves the importance of having an interconnected structure to support the NWs after template removal.